

AD-A284 212



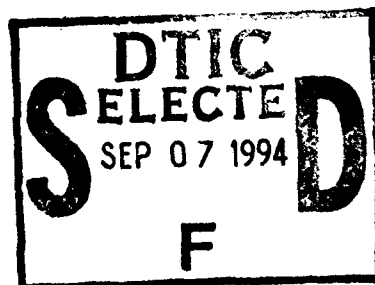
①

MODELING OF CLOUD/RADIATION PROCESSES FOR LARGE-SCALE CLOUDS AND TROPICAL ANVILS

Principal Investigator: K.N. Liou

Co-principal Investigators: S.C. Ou, S.K. Krueger, and Q. Fu

Department of Meteorology/CARSS
University of Utah
Salt Lake City, Utah, 84112



Final Report
1 November 1991 - 31 March 1994

31 May 1994

This document has been approved
for public release and sale; its
distribution is unlimited.

14698

94-29029



DTIC QUALITY INSPECTED 3

94 9 06 1 02

MODELING OF CLOUD/RADIATION PROCESSES FOR LARGE-SCALE CLOUDS AND TROPICAL ANVILS

Principal Investigator: K.N. Liou

Co-principal Investigators: S.C. Ou, S.K. Krueger, and Q. Fu

**Department of Meteorology/CARSS
University of Utah
Salt Lake City, Utah, 84112**

**Final Report
1 November 1991 - 31 March 1994**

31 May 1994

Accession For	
NTIS CRA&I	<input checked="" type="checkbox"/>
DTIC TAB	<input type="checkbox"/>
Unannounced	<input type="checkbox"/>
Justification	
By	
Distribution/	
Availability Codes	
Dist	Avail and/or Special
A-1	

REPORT DOCUMENTATION PAGE

1a. REPORT SECURITY CLASSIFICATION Unclassified		1b. RESTRICTIVE MARKINGS	
2a. SECURITY CLASSIFICATION AUTHORITY		3. DISTRIBUTION / AVAILABILITY OF REPORT Approval for public release; distribution unlimited A	
2b. DECLASSIFICATION / DOWNGRADING SCHEDULE		4. PERFORMING ORGANIZATION REPORT NUMBER(S)	
4. PERFORMING ORGANIZATION REPORT NUMBER(S)		5. MONITORING ORGANIZATION REPORT NUMBER(S) AFOSR-91-0039 94 0486	
6a. NAME OF PERFORMING ORGANIZATION Center for Atmospheric and Remote Sounding Studies	6b. OFFICE SYMBOL (if applicable) CARSS	7a. NAME OF MONITORING ORGANIZATION Air Force Office of Scientific Research	
6c. ADDRESS (City, State, and ZIP Code) Department of Meteorology/CARSS University of Utah Salt Lake City, Utah 84112		7b. ADDRESS (City, State, and ZIP Code) Bolling Air Force Base Washington, D.C. 20332	
8a. NAME OF FUNDING / SPONSORING ORGANIZATION	8b. OFFICE SYMBOL (if applicable)	9. PROCUREMENT INSTRUMENT IDENTIFICATION NUMBER	
8c. ADDRESS (City, State, and ZIP Code)		10. SOURCE OF FUNDING NUMBERS	
		PROGRAM ELEMENT NO 61102F	PROJECT NO 2310
		TASK NO CS	WORK UNIT ACCESSION NO
11. TITLE (Include Security Classification) Modeling of Cloud/Radiation Processes for Large-scale Clouds and Tropical Anvils			
12. PERSONAL AUTHOR(S) K.N. Liou, Q. Fu, S. Krueger, J.L. Lee, S.C. Ou, and Y. Takano			
13a. TYPE OF REPORT Final	13b. TIME COVERED FROM 11/01/91 TO 03/31/94	14. DATE OF REPORT (Year, Month, Day) 1994 May 31	15. PAGE COUNT
16. SUPPLEMENTARY NOTATION			
17. COSATI CODES		18. SUBJECT TERMS (Continue on reverse if necessary and identify by block number)	
FIELD	GROUP	Radiation Parameterization, Radiative Transfer, Cloud Model, Cumulus Ensemble, Cloud Microphysics Parameterization	
19. ABSTRACT (Continue on reverse if necessary and identify by block number) This final report includes five reprints and preprints of papers associated with the modeling of cloud/radiation processes for large-scale clouds and tropical anvils. These papers present (1) a three-dimensional large-scale cloud model for testing the role of radiative heating and ice phase processes, (2) parameterization of the radiative properties of cirrus clouds, (3) discussion of the scattering and absorption properties of ice crystals in relation to numerical modeling, (4) improvements of an ice-phase microphysics parameterization for use in cloud models, and (5) physical discussions on the interactions of radiation and convection in simulated tropical cloud clusters using a cumulus ensemble model.			
DTIC QUALITY INSPECTED 3			
20. DISTRIBUTION / AVAILABILITY OF ABSTRACT <input checked="" type="checkbox"/> UNCLASSIFIED/UNLIMITED <input type="checkbox"/> SAME AS RPT <input type="checkbox"/> DTIC USERS		21. ABSTRACT SECURITY CLASSIFICATION Unclassified	
22a. NAME OF RESPONSIBLE INDIVIDUAL Major James Kroll		22b. TELEPHONE (Include Area Code) (202) 767-5021	22c. OFFICE SYMBOL DM

Publications Acknowledging the AFOSR Grant (AFOSR-91-0039) Support

1 November 1991-31 March 1994

1. J.L. Lee, K.N. Liou, and S.C. Ou, 1992: A three-dimensional large-scale cloud model: Testing the role of radiative heating and ice phase processes. Tellus, 44A, 197-216.
2. Q. Fu, and K.N. Liou, 1993: Parameterization of the radiative properties of cirrus clouds. J. Atmos. Sci., 50, 2008-2025.
3. K.N. Liou, and Y. Takano, 1994: Light scattering by nonspherical particles: Remote sensing and climatic implications. Atmos. Res., 31, 271-298.
4. S.K. Krueger, Q. Fu, K.N. Liou, and H.N. Chin, 1994: Improvements of an ice-phase microphysics parameterization for use in numerical simulations of tropical convection. J. Appl. Meteor., 33, November.
5. Q. Fu, S.K. Krueger, and K.N. Liou, 1994: Interactions of radiation and convection in simulated tropical cloud clusters. J. Atmos. Sci., (submitted).

Accession For	
NTIS	CRA&I
DTIC	TAB
Unannounced	
Justification	
By	
Distribution /	
Availability Codes	
Dist	Avail and/or Special
A-1	

A three-dimensional large-scale cloud model: testing the role of radiative heating and ice phase processes

By J. L. LEE, K. N. LIOU and S. C. OU, *Department of Meteorology/CARSS, University of Utah, Salt Lake City, Utah 84112, USA*

(Manuscript received 23 September 1991; in final form 7 January 1992)

ABSTRACT

A time-dependent, three-dimensional, large-scale cloud model has been developed for the prediction of cloud cover, cloud liquid/ice water content (LWC/IWC), precipitation, specific humidity and temperature. Partial cloudiness is allowed to form when large-scale relative humidity is less than 100%. Both liquid and ice phases are included in the model. The liquid phase processes consist of evaporation, condensation, autoconversion and precipitation. The ice phase processes include heterogeneous nucleation to generate ice crystals, depositional growth to simulate Bergeron-Findeisen's process, sublimation to deplete ice crystals, and gravitational settling of ice crystals. The radiative transfer parameterization scheme is based on a broadband method and involves the transfer of infrared and solar radiation in clear and cloudy regions. The broadband infrared emissivity, reflectivity, and transmissivity for cirrus clouds, as well as the broadband solar absorption, reflection, and transmission values for low, middle and high clouds are computed based on the cloud LWC and IWC interactively generated by the cloud model. Large amounts of satellite data, including cloud cover climatology derived from the US-Air Force three-dimensional nephelometer (3DNEPH) and earth radiation budget (ERB), have been processed into formats appropriate for verification. The 96-h model simulations of cloud cover, outgoing long-wave radiation (OLR), and cloud LWC have been verified against data analyzed from 3DNEPH, ERB and the Nimbus-7 Scanning Multichannel Microwave Radiometer (SMMR) satellite observations, respectively. The predicted cloud IWC is compared to in situ observations as well as to results from other studies. The predicted cloud and radiation results compare well with those analyzed from satellite data. Numerical experiments are carried out with and without radiative heating and ice phase processes in the cloud formation scheme. The inclusion of radiative heating produces a significant change in temperature, cloud cover and total cloud water content, while the inclusion of ice phase processes generates a substantial change only in total cloud water content. If the cloud LWC is sufficiently large to initiate effective Bergeron-Findeisen's processes, the total cloud water content decreases, indicating that gravitational settling is an efficient mechanism in reducing the cloud IWC.

1. Introduction

Clouds regularly occupy about 50% of the sky. They are the most important regulators of the earth's radiation budget, i.e., the balance between net solar radiation and outgoing longwave radiation at the top of the atmosphere (TOA), by which the earth's climate is determined. On the one hand, clouds reflect a large portion of incoming solar radiation, producing a cooling effect referred to as the solar albedo effect. On the other, they trap the outgoing longwave radiation emitted from the earth, resulting in a warming effect referred to as

the IR greenhouse effect. Since the greenhouse and albedo effects are different in sign as well as magnitude, the existence of clouds may have a profound impact upon the sensitivity of climate to external perturbations, such as the increase of atmospheric carbon dioxide. In particular, cirrus clouds, which regularly cover about 20% of the globe, are optically thin and nonblack. The outcome of the greenhouse-versus-albedo effects is intrinsically modified by the radiative effects of nonblack cirrus (Liou, 1986).

Recognizing the importance of clouds in weather and climate processes, numerous

modeling efforts have been carried out to understand the relative significance of solar albedo and IR greenhouse effects involving clouds. In early models, the formation of clouds was very crude and lacked physical foundation. An arbitrary fractional amount of cloud was assigned to a given layer where large-scale condensation occurs. All the excessive water vapor was condensed and immediately precipitated onto the ground. As a result, there was no cloud water or cloud ice remaining in the clouds. These two elements are necessary for the calculation of cloud radiative effects. In climatic perturbation studies, Wetherald and Manabe (1988) assigned a cloud amount of 80% to condensation and found that cloud feedback processes enhance the sensitivity of the model climate to an increase in atmospheric carbon dioxide. This conclusion is in agreement with that drawn by Hansen et al. (1983). The features of cloud cover change obtained in these studies, as well as in that of Washington and Meehl (1984), are qualitatively similar.

Efforts have also been focused on improving the specification of the radiative properties of clouds and cloud parameterization schemes in GCMs to demonstrate the importance of cloud-radiation interaction to the simulation of atmospheric circulation. Ramanathan et al. (1983) demonstrated that refinement in radiative properties of non-black high cirrus emissivity significantly improves the model simulation of atmospheric temperatures as well as that of zonal mean winds. Slingo and Slingo (1988) reached the same conclusion in their study of cloud longwave radiative forcing. Using a GCM designed for medium range weather prediction, Liou and Zheng (1984) illustrated the importance of cloud and radiative processes to the maintenance of the Hadley circulation.

In order to incorporate interactive cloud and radiation processes in models, cloud liquid water content (LWC) and ice water content (IWC) are required for radiation calculations. The models must be able to generate LWC/IWC. This is the so-called prognostic method, which requires the additional prognostic equation(s) for the prediction of LWC/IWC. Sundqvist (1978) made the first attempt to develop a physically based prognostic large-scale cloud scheme for use in a GCM. In his approach, the cloud LWC is a prognostic variable determined by various source and sink terms which are parameterized in terms of associated

bulk quantities. Also partial cloudiness is allowed to exist when the large-scale relative humidity is less than 100%. Sundqvist (1981) incorporated the proposed cloud scheme into the European Centre for Medium Range Weather Forecasts (ECMWF) model and carried out a 5-day integration. The forecast and cloud amounts were compared with satellite photographs, which showed that the cloud patterns are reasonably well-simulated; the predicted cloud LWC is within the observational range. However, these studies did not include radiative effects and ice phase processes. The importance of including a more realistic and physically based parameterization for cloud parameters in GCMs has recently been articulated by Sundqvist (1988).

Mitchell et al. (1989) conducted a study of cloud feedback in the UK Meteorological Office GCM. A cloud liquid water budget equation was included in the model. However, ice clouds were not generated from the budget equation. Water cloud radiative properties are interactive in the model based on the schemes developed by Liou and Wittman (1979) for solar radiation and Stephens (1978) for IR radiation. Roeckner (1988) also included a water budget equation in the University of Hamburg GCM to undertake a study of the feedback processes involving clouds due to external radiative forcing. Smith (1990) incorporated a prognostic cloud water budget equation in a GCM and compared the simulated cloud and radiation fields with satellite observations.

Interactive cloud formation in a model setting would require a detailed consideration of the sources and sinks of water and ice particles. The inclusion of separate empirical equations for cloud LWC (e.g., Xu and Krueger, 1991), IWC (e.g., Heymsfield and Donner, 1990) and precipitation in the GCM (i.e., diagnostic approach) would appear to be extremely difficult and inconsistent with respect to the model physics. In order to understand the role of radiative heating and ice phase processes in the formation of large-scale clouds, we have developed a global stratiform cloud model that includes prognostic cloud LWC, IWC and precipitation equations as well as an interactive radiative transfer program. The wind fields required for the simulation are determined from a GCM. In Section 2, we describe a large-scale cloud model and an interactive radiation program. Section 3 contains bulk parameteriza-

tions of various sources and sinks for the cloud microphysical processes simulated in the model. Section 4 presents comparisons of model predictions and verification data, including a description of model input and verification data. Results on the numerical experiments on atmospheric radiation and ice phase processes are shown in Section 5. Finally, conclusions are given in Section 6.

2. Model description

2.1. Governing equations

We have developed a time-dependent, three-dimensional cloud-moisture model for the prediction of water vapor, cloud LWC, cloud IWC, precipitation and temperature. The first four variables are governed by the law of mass conservation. The latent heat exchanges during the phase transitions of water substances are determined by the first law of thermodynamics through the temperature field. The governing equations may be written as follows:

$$\begin{aligned} \frac{\partial}{\partial t} (\bar{\rho} T) + \frac{1}{a \cos \phi} \left[\frac{\partial}{\partial \lambda} (\bar{\rho} T \bar{u}) + \frac{\partial}{\partial \phi} (\bar{\rho} T \bar{v} \cos \phi) \right] \\ + \frac{\partial}{\partial z} (\bar{\rho} T \bar{w}) + \bar{\rho} \Gamma_a \bar{w} \\ = \bar{\rho} (\bar{Q}_c + \bar{Q}_R) - \frac{L_c}{C_p} \bar{E}_r + \frac{L_t}{C_p} \bar{S}_{BF} \\ - \frac{L_d}{C_p} \bar{S}_s + F_H^T + F_V^T, \end{aligned} \quad (2.1)$$

$$\begin{aligned} \frac{\partial}{\partial t} (\bar{\rho} \bar{q}_v) + \frac{1}{a \cos \phi} \left[\frac{\partial}{\partial \lambda} (\bar{\rho} \bar{q}_v \bar{u}) + \frac{\partial}{\partial \phi} (\bar{\rho} \bar{q}_v \bar{v} \cos \phi) \right] \\ + \frac{\partial}{\partial z} (\bar{\rho} \bar{q}_v \bar{w}) \\ = - \frac{C_p}{L_c} \bar{\rho} \bar{Q}_c + \bar{\rho} \bar{E}_r + \bar{S}_s + F_H^q + F_V^q, \end{aligned} \quad (2.2)$$

$$\begin{aligned} \frac{\partial}{\partial t} (\bar{\rho} \bar{q}_i) + \frac{1}{a \cos \phi} \left[\frac{\partial}{\partial \lambda} (\bar{\rho} \bar{q}_i \bar{u}) + \frac{\partial}{\partial \phi} (\bar{\rho} \bar{q}_i \bar{v} \cos \phi) \right] \\ + \frac{\partial}{\partial z} [\bar{\rho} \bar{q}_i (\bar{w} - \bar{w}_i)] \\ = \frac{C_p}{L_c} \bar{\rho} \bar{Q}_c - \bar{\rho} \bar{P} - \bar{S}_{BF} + F_H^q + F_V^q, \end{aligned} \quad (2.3)$$

$$\begin{aligned} \frac{\partial}{\partial t} (\bar{\rho} \bar{q}_i) + \frac{1}{a \cos \phi} \left[\frac{\partial}{\partial \lambda} (\bar{\rho} \bar{q}_i \bar{u}) + \frac{\partial}{\partial \phi} (\bar{\rho} \bar{q}_i \bar{v} \cos \phi) \right] \\ + \frac{\partial}{\partial z} [\bar{\rho} \bar{q}_i (\bar{w} - \bar{V}_T)] \\ = \frac{C_p}{L_d} \bar{\rho} \bar{Q}_i + \bar{S}_{BF} - \bar{S}_s + F_H^q + F_V^q, \end{aligned} \quad (2.4)$$

$$-\frac{\partial}{\partial z} (\bar{P}) = \bar{\rho} \bar{P} - \bar{\rho} \bar{E}_r. \quad (2.5)$$

In these equations, an overbar denotes the average of a variable over a grid space. The variables \bar{u} , \bar{v} , and \bar{w} are wind fields and are obtained from a GCM; λ and ϕ are the longitude and latitude, respectively; $\bar{\rho}$ is the air density, T the temperature, C_p the specific heat at constant pressure, Γ_a the adiabatic lapse rate, \bar{P} the precipitation flux, \bar{q}_v , \bar{q}_i , \bar{q}_1 , \bar{q}_2 the mixing ratios for water vapor, cloud water, and cloud ice, respectively, and L_c , L_d and L_t the latent heat of condensation, sublimation, and melting, respectively. Also in these equations, \bar{Q}_c , \bar{Q}_i and \bar{Q}_R represent the condensational heating rates for cloud water, cloud ice, and the radiative heating rate, respectively, \bar{P} is the rate of autoconversion from cloud droplets to raindrops, \bar{E}_r is the evaporation of rain water, \bar{S}_{BF} and \bar{S}_s are the rates of change of the mass of ice particles due to Bergeron-Findeisen's process and sublimation, respectively, and \bar{w}_i and \bar{V}_T are the bulk terminal velocities for cloud water and ice particles, respectively. The total precipitation including rain and snow in a unit area at the surface for a given time period Δt is given by: $-\Delta t [\bar{P} + \bar{\rho} q_i (\bar{w} - \bar{V}_T)] / \bar{\rho}_l$, where $\bar{\rho}_l$ is the liquid water density. In addition, the vertical eddy flux and horizontal diffusion terms have been denoted by F_V^x and F_H^x , respectively, where x can be T , q_v , q_i or q_1 .

The cloud cover, η , is derived based on an average of the specific humidities over clear and cloudy regions in the form

$$\bar{q} = \eta q_c + (1 - \eta) q_0, \quad (2.6)$$

where q_c and q_0 are, respectively, the specific humidity in the cloudy and clear regions. After rearranging terms, the cloud cover is given by

$$\eta = \frac{\bar{q}_v / \bar{q}_s - q_0 / \bar{q}_s}{q_c / \bar{q}_s - q_0 / \bar{q}_s}. \quad (2.7)$$

Here, we have introduced the grid-averaged saturation specific humidity, $\bar{q}_s(\bar{T})$, which is a function of the grid-averaged temperature, \bar{T} . For a stratiform cloud, the temperature within the cloud is approximately equal to the grid-averaged temperature, i.e., $q_c \approx \bar{q}_s(\bar{T})$. Thus,

$$\eta \approx \frac{(\bar{h} - h_0)}{(1 - h_0)}, \quad (2.8)$$

where $\bar{h} = \bar{q}_v / \bar{q}_s$ is the averaged relative humidity and $h_0 = q_0 / \bar{q}_s$ is referred to as the threshold relative humidity, which is a parameter to be prescribed to close the model equations.

The cloud cover expression in eq. (2.8) denotes a linear relation between the relative humidity and cloud cover. A similar empirical relation based on observations has been developed by Smagorinsky (1960) for use in GCMs (Fig. 1). For the present large-scale studies we have used the threshold relative humidity presented in Fig. 1 for the calculation of high, middle and low cloud covers.

With the introduction of the threshold relative humidity ($h_0 < 1$), partial cloudiness in the grid box is allowed when the large-scale relative humidity is less than 100%. The cloudy area and clear region in a grid box are denoted by η and $(1 - \eta)$, respectively. Condensation occurs in the cloudy area; evaporation takes place in the clear

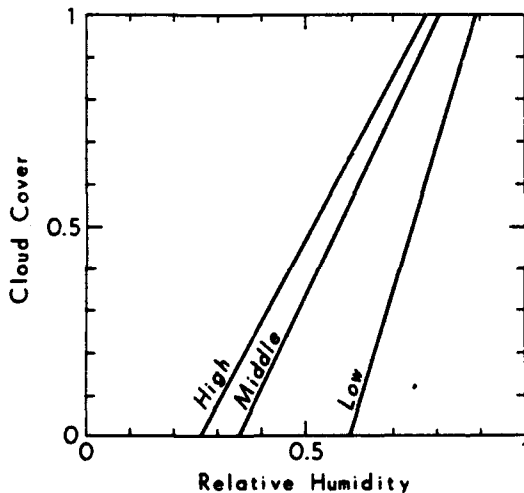


Fig. 1. Empirical relations between the low-, middle-, and high-cloud amount and relative humidity (Smagorinsky, 1960). The values of h_0 for low, middle, and high clouds are 0.6, 0.35, and 0.26, respectively.

region. Raindrops formed in a given layer are not subject to evaporation within that layer. Instead, raindrops that fall through this layer from higher clouds may evaporate in the clear region of the layer.

Since the averaged terminal velocity of cloud droplets is on the order of 1 cm/s, which is close to the large scale vertical velocity, we would expect that the terminal velocity of cloud droplets and vertical air motion roughly cancel each other in stratiform clouds. Therefore, vertical advection of cloud LWC in eq. (2.3) is omitted in the model calculations. The vertical eddy fluxes are calculated from a K -theory approach (Liou and Ou, 1983) and the diffusion terms in spherical coordinates are parameterized based on the methodology described by Washington and Williamson (1977). Because clouds are allowed to form only above the 0.925 σ -level, the turbulent fluxes involving clouds are not computed at the surface.

2.2. Cloud microphysical processes

The cloud microphysical processes simulated in the present cloud model are illustrated in Fig. 2. Both the liquid and ice phase processes are included, with the liquid phase on the left-hand side and ice phase on the right-hand side of the diagram. The liquid phase processes consist of condensation of water vapor into cloud liquid water at temperatures warmer than -40°C , conversion of cloud liquid water into rain water by means of autoconversion, and precipitation of rain water onto the ground. Evaporation of cloud and rain water increases the specific humidity.

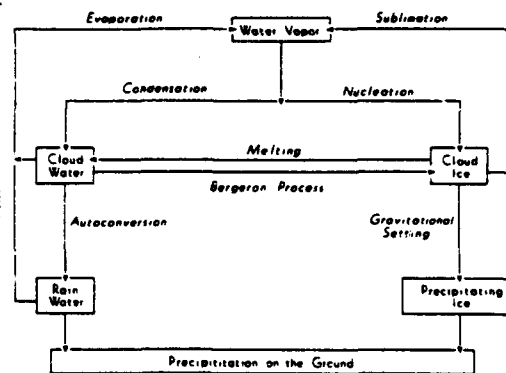


Fig. 2. Schematic display of the cloud microphysical processes simulated in the model.

The ice phase processes include both heterogeneous and homogeneous nucleations of water condensate to form cloud ice. Homogeneous nucleation occurs at temperatures colder than -40°C . Cloud ice is converted to precipitation ice by virtue of gravitational settling, in which the downward ice flux is calculated by integrating the mass and fall velocity of an individual ice crystal over the whole spectrum of ice crystals. The sublimation of cloud ice increases the specific humidity. At temperatures above the freezing point, the melting process converts cloud ice to cloud water.

An important link between the liquid and ice phases is the so-called Bergeron-Findeisen process. The saturation vapor pressure over ice is less than that over water. As a result, ice crystals grow by diffusion at the expense of the supercooled liquid cloud droplets. Once generated by ice nucleation, ice crystals grow by deposition due to Bergeron-Findeisen's process and are depleted by sublimation as well as the gravitational settling. Above the freezing point, clouds consist entirely of cloud water. In the region 0° to -40°C , cloud water and cloud ice may coexist. At temperatures below -40°C , cloud ice dominates because of homogeneous nucleation.

The formation of rimed crystals, such as graupel and hail, is not considered in this model since they occur more frequently in convective clouds than in large-scale stratiform clouds.

2.3. Numerical implementation

In the horizontal, the grid point space is characterized by 48 equally-spaced longitudinal points and 38 Gaussian latitudes, which is the same as the horizontal grid structures used in the Air Force Geophysics Laboratory (AFGL) GCM (Yang et al., 1989). We have used this model to provide the present cloud model with initial data and a wind field. The horizontal grid space in the model has been modified near the poles to maintain nearly constant geographical distances between the grid points. In the vertical, a 16-layer stretched z -coordinates is used in the cloud model.

The upstream scheme is utilized as a means of numerically differencing the horizontal and vertical advection terms. The scheme is conditionally stable and its stability criterion follows the Courant-Friedrichs-Levy (CFL) condition,

i.e., $C_{\max} \Delta t / \Delta S < 1$, where C_{\max} is the maximum velocity in the computational domain, Δt is the time step and ΔS is the grid size. This criterion is easily satisfied in large scale models. For example, in the vertical where $\bar{w}_{\max} \sim 10^0 \text{ cm/s}$, $\Delta t \sim 10^3$, and $\Delta S \sim 10^5 \text{ cm}$, the criterion is much less than 1. The time step used in this study is 30 minutes. We have carried out an experiment to investigate the required time step for radiation calculations. The results produced by using 30-min or 3-h time steps are practically the same. For this reason, the radiation calculations are updated every 3 h, i.e., the radiative heating rates are calculated every 3 hours at every horizontal grid point.

2.4. Radiative transfer parameterization

The radiative transfer parameterization program used in this study is based on a broadband method and involves the transfer of thermal IR and solar radiation in clear and cloudy regions. In a clear atmosphere, the entire IR spectrum is divided into five bands: three for H_2O , one for CO_2 , and one for O_3 absorption. The parameterizations of these broadband IR emissivities, which included H_2O and CO_2 overlap, were developed by Liou and Ou (1981) and Ou and Liou (1983). The solar spectrum consists of 25 bands: 6 for H_2O , 1 for CO_2 , which overlaps the H_2O 2.7- μm band, and 18 for O_3 .

In a cloudy atmosphere, low and middle clouds are treated as blackbodies in the IR radiative transfer calculation. The broadband IR emissivity, reflectivity, and transmissivity for high clouds, as well as the broadband solar absorption, reflection, and transmission values for low, middle, and high clouds, were computed based on the cloud LWC and IWC interactively generated by the cloud model. The cloud radiative properties were calculated, based on the parameterizations developed by Liou and Wittman (1979). Accuracy of all the aforementioned parameterization was verified via more comprehensive and exact radiative transfer calculations described by Ou and Liou (1988). In the parameterization, there are upper and lower limits for cloud LWP. For low clouds, for example, the limits are 600 and 40 g m^{-2} . In unusual circumstances where the predicted LWPs are larger or smaller than the preset limits, these preset values are used in the calculation of the solar radiative properties.

The radiative heating rate at level z is related to the divergence of the net fluxes and is given by

$$\frac{\partial T}{\partial t} = -\frac{1}{\rho C_p} (\Delta F / \Delta z), \quad (2.9)$$

where Δz is the model layer thickness and ΔF is the net radiative flux difference between the layer top and bottom. This equation applies to both IR and solar heating rate calculations with downward solar flux and upward IR flux defined as positive. For the transfer of solar radiation in a cloud layer, the net flux density decreases from the cloud top to the bottom because of cloud absorption and scattering. The absorbed radiant energy leads to the heating of the cloud layer. For black clouds (low or middle clouds), the IR radiative flux is proportional to the fourth power of the absolute temperature of the cloud. Since the atmospheric temperature usually decreases with height, the downward IR flux emitted by the atmosphere above a black cloud top is much smaller than that emitted upward by the black cloud. As a result, the net flux near the cloud top is greater than zero and leads to strong IR cooling in the region. Similarly, there is IR heating near the cloud bottom.

Specification of the overlap that occurs between cloud layers is required for the calculation of radiative transfer in a radiation model. In this study, the model-generated clouds are strapped into three cloud decks. Low, middle, and high clouds fill, respectively, layers (4, 5, 6), layers (7, 8), and layers (9, 10). The cloud cover for each deck of clouds is obtained by averaging model cloud covers as follows:

$$\eta_l = (\eta_4 + \eta_5 + \eta_6) / 3, \quad (2.10a)$$

$$\eta_m = (\eta_7 + \eta_8) / 2, \quad (2.10b)$$

$$\eta_h = (\eta_9 + \eta_{10}) / 2, \quad (2.10c)$$

where η_l , η_m and η_h denote deck cloud covers for low, middle, and high clouds, respectively.

To determine the total cloud amount, we have assumed that clouds overlap each other in a statistically random manner. Thus the total cloud cover is given by

$$\eta = 1 - (1 - \eta_l)(1 - \eta_m)(1 - \eta_h), \quad (2.11)$$

where η is the total cloud cover over a grid area.

We have also used maximum overlap scheme in the total cloud cover calculation. However, this scheme produces cloud cover results that significantly underestimate the observed values.

For partly cloudy conditions, the radiative heating/cooling rate at each model layer is obtained by linearly weighting the percentages of the total cloud cover, η , and clear portion, $(1 - \eta)$, in the form

$$\left(\frac{\partial T}{\partial t}\right)^{pc} = \eta \left(\frac{\partial T}{\partial t}\right)^c + (1 - \eta) \left(\frac{\partial T}{\partial t}\right)^{nc}, \quad (2.12)$$

where the superscripts pc , c , and nc represent partly cloudy, cloudy, and clear conditions, respectively.

3. Bulk parameterization of cloud microphysics

Since it is not practical in a large-scale cloud model to simulate detailed microphysical processes with respect to each individual cloud particle, we must relate these processes in terms of bulk quantities, which represent the various sources and sinks for cloud water substances.

3.1. Liquid phase

3.1.1. *Condensation.* In principle, condensation may be evaluated on the basis of microphysical cloud processes. However, for application to large-scale processes, clouds must be allowed to form in a grid box when the model relative humidity is much less than 1. For this reason, we have used the following scheme to compute condensation. Condensation occurs as a result of expanding air under saturation conditions and may be related to the time rate of change of the saturation vapor pressure. Consequently, the condensational heating rate may be derived from the first law of thermodynamics, the Clausius-Clapeyron equation and the hydrostatic approximation as follows:

$$\bar{Q}_c = \eta \Gamma_d \frac{\bar{q}_s(T)}{R_a} \left(\frac{LR_a - C_p R_v T}{C_p R_v T^2 + \bar{q}_s L^2} \right) \bar{w}, \quad (3.1)$$

where Γ_d is the dry adiabatic lapse rate, R_a is the gas constant for air, R_v is the gas constant for water vapor, L is the latent heat for liquid and vapor phases, and \bar{q}_s is the saturation vapor

pressure. The condensation is strongly dependent on the vertical velocity, \bar{w} . As saturated air rises, i.e., $\bar{w} > 0$, condensation takes place and cloud forms, while depletion of clouds occurs with descending saturated air. The present scheme differs from that developed by Sundqvist (1978) in that condensation and evaporation are computed explicitly.

3.1.2. Autoconversion. Autoconversion is a process through which small cloud droplets merge into large raindrops. The parameterization of autoconversion follows the simple exponential form developed by Sundqvist (1978):

$$\bar{P} = c_0 \bar{q}_1 \{1 - \exp[-(\bar{q}_1 / (\eta q_{1r}))^2]\}, \quad (3.2)$$

where c_0 denotes the typical time for the conversion of droplets to raindrops, and q_{1r} is a reference value of cloud LWC above which the conversion from cloud droplets to raindrops increases rapidly. These two values function in a manner similar to the rate of conversion and the accretion parameterization developed by Kessler (1969). We find that Sundqvist's and Kessler's parameterizations produce about the same results for the normal range of cloud LWC. Eq. (3.2) has been used in this study for its simplicity in large-scale cloud modeling.

3.1.3. Evaporation of raindrops. The evaporation of raindrops may be derived from the combination of the Fick law of mass diffusion and the Marshall-Palmer raindrop size distribution. The size distribution is assumed to remain the same throughout the whole process of evaporation. The raindrop evaporation rate is given by

$$\bar{E}_r = K_e (1 - \bar{h}) \bar{P}^{0.42}. \quad (3.3)$$

where the evaporation rate constant K_e is $1.785 \times 10^{-2} \bar{q}_1$.

3.2. Ice phase

The ice phase parameterizations include homogeneous/heterogeneous nucleation to generate ice crystals, depositional growth to simulate the Bergeron-Findeisen process, sublimation and melting of ice crystals, and gravitational settling to deplete the ice crystals. The Bergeron-Findeisen process occurs primarily at temperatures between 0° and -40°C , while below -40°C homogeneous nucleation dominates. The parameterizations of these source and sink terms are described below.

3.2.1. Homogeneous nucleation. Homogeneous nucleation takes place whenever condensation occurs at temperatures below -40°C . Homogeneous nucleation is analogous to the liquid water condensation process, and may be written in the form:

$$\bar{Q}_i = \eta \Gamma_d \frac{\bar{q}_s(\bar{T})}{R_s} \left(\frac{L_d R_s - C_p R_v \bar{T}}{C_p R_v \bar{T}^2 + \bar{q}_s L_i^2} \right) \bar{w}, \quad (3.4)$$

where L_d is the latent heat for ice and vapor phases.

3.2.2. Heterogeneous nucleation. Heterogeneous nucleation leads to the formation of ice crystals on active ice nuclei primarily at temperatures between 0° and -40°C . Based on the experimental work of Mason (1971) and Koenig and Murray (1976), it is assumed that the active ice-forming nuclei (IN) concentration may be expressed in terms of temperature as follows:

$$N = A_1 \exp \left\{ -\frac{\ln(10)}{A_2} \max[(T - T_0), T^*] \right\}, \quad (3.5)$$

where $A_1 = 1$, $A_2 = 4$, $T^* = 0^\circ\text{C}$, and T_0 is a threshold temperature, which is taken to be -20°C . Here, it is assumed that when the saturated air temperature is lower than T_0 , the total number of IN remains the same as that at T_0 .

The heterogeneous nucleation rate of ice crystals, S_h , is given by

$$S_h = m_0 \frac{dN}{dt}, \quad (3.6)$$

where m_0 is the mass of a newly nucleated ice crystal, prescribed as 10^{-11} g, which is equivalent to an ice sphere with a diameter of $2.77 \mu\text{m}$ (Koenig and Murray, 1976), and

$$\frac{dN}{dt} = \begin{cases} \frac{N_{t+\Delta t} - N_t}{\Delta t} & \text{if } T \geq -20^\circ\text{C} \\ 0 & \text{if } T < -20^\circ\text{C}. \end{cases} \quad (3.7)$$

Here, $N_{t+\Delta t}$ and N_t are the IN concentrations at consecutive time steps of $t + \Delta t$ and t , respectively.

3.2.3. Bergeron-Findeisen process. The Bergeron-Findeisen process transforms cloud water into cloud ice at temperatures between 0° and -40°C .

To simplify the complicated vapor diffusion equation, Koenig (1971) developed a simple equation to describe the crystal vapor diffusion growth rate as a function of mass. The equation is written as follows:

$$\frac{dm}{dt} = a_3 m^{a_4}, \quad (3.8)$$

where a_3 and a_4 are temperature-dependent parameters given in Koenig (1971), and m is the crystal mass in grams.

The bulk quantity of the ice crystal depositional rate, denoted as S_{BF} , may be derived from eq. (3.8) by multiplying both sides by N , as follows:

$$\bar{S}_{BF} = \frac{d}{dt} (\bar{\rho} \bar{q}_i) = \eta f_1 N^{1-a_4} a_3 (\bar{\rho} \bar{q}_i)^{a_4}, \quad (3.9)$$

where $f_1 = \bar{q}_i / (\bar{q}_l + \bar{q}_i)$ is the cloud liquid fraction serving as an adjustment factor, which allows for higher ice crystal growth rates with more cloud water. The growth is terminated if there is no cloud water to supply water vapor.

3.2.4. Sublimation and melting of ice crystals. Similar to the derivation for the evaporation of raindrops, we have developed the following equation for the rate of sublimation:

$$\bar{S}_s = 0.1037 (\bar{\rho} \bar{q}_s) (1 - \bar{h}) (\bar{\rho} \bar{q}_i)^{0.65}. \quad (3.10)$$

At temperatures above 0°C, cloud ice crystals are assumed to melt instantaneously.

3.2.5. Gravitational settling. Gravitational settling is an important sink for cloud IWC. Therefore, it is desirable to have a representative (mean-volume-weighted) downward flux of ice water. Following Starr and Cox (1985), the downward ice flux may be expressed as:

$$\bar{V}_T (\bar{\rho} \bar{q}_i) = \int_{L_{\min}}^{L_{\max}} n m v dL, \quad (3.11)$$

where n , m , and v are the ice crystal size distribution, mass and terminal velocity of an ice crystal, respectively, and L is the maximum dimension of an ice crystal. L_{\min} and L_{\max} are the minimum and maximum sizes of ice crystals. The cloud IWC may be further related to n and m as

$$\bar{\rho} \bar{q}_i = \int_{L_{\min}}^{L_{\max}} n m dL. \quad (3.12)$$

In order to calculate the downward ice flux, the size distribution, mass, and terminal velocity for the precipitating ice crystals need to be specifically expressed in terms of the maximum dimension of ice crystals.

The size distributions of ice crystals in mid-latitude cirrus clouds have been measured from aircraft using an optical probe (Heymsfield, 1977). Using these data, Heymsfield and Platt (1984) have averaged all spectra of crystals within every 5°C temperature interval ranging from -20°C to -60°C. The ice crystal size distributions in terms of the maximum dimension of ice crystals may then be parameterized for different temperature ranges in the form

$$n = a_n L^{b_n}, \quad (3.13)$$

where a_n and b_n are temperature dependent empirical coefficients.

The minimum length that the optical probe can measure is about 20 μm. Small ice crystals less than 20 μm in size could be missed by the measurement technique. Consequently, small ice crystal data were excluded from the analysis by Heymsfield and Platt (1984). For this reason, 20 μm is taken as the minimum length of ice crystals, L_{\min} , which is needed in the calculations of Eqs. (3.11) and (3.12).

3.2.6. Crystal mass and terminal velocity. The individual ice crystal mass, m , may be parameterized in terms of the maximum dimension of an ice crystal, L , as follows:

$$m = a_m L^{b_m}, \quad (3.14)$$

where m and L are in units of grams and μm, respectively. The constants a_m and b_m associated with various ice crystal habits are given in Heymsfield (1972).

The terminal velocity v (m/s) of an ice crystal of maximum dimension, L , (μm) is given by

$$v = a_v L^{b_v}, \quad (3.15)$$

where the constants a_v and b_v are dependent on the ice crystal habit and size as given in Starr and Cox (1985). These coefficients were derived at an ambient pressure of 400 mb. For an ice crystal at a given pressure p , Beard and Pruppacher (1969)

have suggested that its terminal velocity may be expressed by

$$v(p) = v(p_*) (p_*/p)^{1/3}, \quad (3.16)$$

where p_* denotes a reference pressure level, and $v(p_*)$ is the terminal velocity of a crystal at the reference level. To obtain the terminal velocity at any given pressure, we simply apply the pressure adjustment to the expression in eq. (3.15).

3.2.7. Downward ice flux. The ice crystal size distribution, ice crystal mass, and terminal velocity are all parameterized in terms of the maximum dimension. Thus, the downward ice flux may be obtained by analytically integrating eq. (3.11), provided that the size of the largest crystal, L_{\max} , is known. Since the lower limit, L_{\min} , is set to be $20 \mu\text{m}$, as stated previously, the upper limit (L_{\max}) may be determined from eq. (3.12) as follows: We first obtain $\bar{\rho}\bar{q}_i$ for the n th time step. Subsequently, eqs. (3.13) and (3.14) are substituted into eq. (3.12) to calculate L_{\max} . Having determined L_{\max} , the downward ice flux can then be computed from eq. (3.11) in the form

$$\begin{aligned} \mathcal{V}_T(\bar{\rho}\bar{q}_i) &= \frac{a_n a_m a_r}{b_n + b_m + b_r + 1} \\ &\times [L_{\max}^{(b_n + b_m + b_r + 1)} - L_{\min}^{(b_n + b_m + b_r + 1)}]. \end{aligned} \quad (3.17)$$

The downward flux is a function of L_{\max} , which in turn is a function of cloud IWC.

4. Model performance and verification

4.1. Model input and verification datasets

The atmospheric data generated from the AFGL spectral global model (Yang et al., 1989) analyzed at 1200 GMT 1–4 July 1979, were used as inputs to the cloud model. This period has been chosen because of the availability of cloud and radiation budget data that have been analyzed on a daily basis. The input data contain temperature, specific humidity, and wind fields (\bar{u} , \bar{v} , \bar{w}) at all 12 σ -layers in the atmosphere, plus the surface pressure and geopotential height. These analyses were carried out using a rhomboidal 15 (R15) truncation which corresponds to a horizontal resolution of 38 and 48 grid points in latitude and longitude, respectively. In the vertical, since the GCM-generated input data are available only at the σ -coordinate, it is necessary to perform

vertical interpolations to obtain these data in the z -coordinate.

The 3DNEPH cloud data sets have been determined from various satellite, aircraft and ground-based observational sources. Based on 3DNEPH analysis, the global cloud climatologies for January and July 1979 have been processed into appropriate formats for model verification (Koenig et al., 1987). The global distribution of cloud amounts on 1–4 July 1979 is derived from the above cloud climatologies and used as the verification dataset for the cloud cover simulated in the model.

It is important to recognize the limitation of 3DNEPH cloud analysis. A threshold method is employed to process satellite images to determine cloud cover by a threshold temperature. If an observed brightness temperature of a pixel is colder than the threshold temperature, then a cloudy condition is assigned to the pixel. Consequently, the cloud amount tends to be overestimated when the associated surface temperature is low, and underestimated when a temperature inversion is located in the region. This is evident from the fact that 3DNEPH over- and underestimates cloud amounts in the wintertime and summertime polar regions, respectively (Henderson-Sellers, 1986). However, several intercomparisons of the cloud cover between 3DNEPH and the other cloud retrieval techniques have been made (Koenig et al., 1987; Hughes, 1984). The 3DNEPH total cloud cover appears to be reliable, except in the polar regions where all satellite retrieval methodologies tend to fail. Additionally, the surface observational cloud climatology compiled by London (1957) is used as a complementary verification dataset for the polar regions.

The archived ERB flux data tapes for July, 1979, provided by the NASA ERB team (Kyle et al., 1990), are used to validate OLR produced by the model. Since ERB fields are strongly modulated by the radiative effects of clouds, including cloud cover and cloud LWC/IWC, they have been widely used in large-scale cloud model verifications (Slingo, 1987; Smith, 1990). Monthly mean distributions of liquid water have been derived from the Nimbus SMMR observations over the oceans for the period November 1978 to November 1979 (Prabhakara and Short, 1984). The liquid water estimate for July 1979 is applicable to the monthly average over an area approximately 3°

by 5°. The liquid water derived from satellite microwave channels includes vertically integrated amounts of liquid droplets in both clouds and rain. The liquid water verification data are confined to the oceans equatorward of 60° latitude. Over land and ice surfaces, due to the limitation of microwave techniques, there is no climatological liquid water data of global extent for comparisons.

Since there is no ground truth with which to compare, the accuracy of liquid water observations from SMMR is roughly estimated as 100 g/m², based on theoretical considerations (Prabhakara et al., 1983). However, by taking monthly averages, this accuracy may be improved to 50 g/m² (Prabhakara and Short, 1984).

4.2. Design of the verification and initial data

In the development of any parameterization scheme, the prediction results must be carefully verified to assess its performance. The large scale cloud model was integrated for 96 h with a time step of 30 min from the initial conditions taken at 1200 GMT on 1 July 1979. The wind fields are prescribed from a GCM. It is noted that cloud-radiation feedback to the dynamic structure is not accounted for in this study.

With input of the initial data and wind fields, the cloud model is capable of forecasting large-scale cloud cover and cloud LWC/IWC, which are interactively used in the radiation model. The radiation model computed OLR for comparison with the ERB satellite data. In this study, the interactive radiation computations are undertaken every 3 h, while the calculated heating/cooling rates are input in the cloud model at every time step during those 3 h.

The simulated cloud cover, OLR, cloud LWC and cloud IWC are verified against 3DNEPH cloud cover, ERB data, SMMR results, and in situ observations and other model studies, respectively. However, there are several problems which make the use of satellite observations in model verification not entirely straightforward. For instance, verification datasets such as 3DNEPH and ERB are based on the daily average over local time, while the output of the model simulation is the instantaneous global distribution. In order to allow intercomparisons to be made between the satellite observations and model simulations, we have to average the model predicted fields over local time in order to obtain daily averaged model results.

The analysis data on 12 GMT, 1 July 1979 for temperature and specific humidity are used as initial values to perform a 96-h model simulation. Data for the cloud LWC/IWC are not available for initial values on a global basis. At this point we do not have any physical means to provide the initial cloud LWC/IWC values. For this reason, we have set these values as zero, initially. Unless specified, all of the results including satellite observations and model simulation are averaged over 3–4 July 1979. That is, most of the results shown in this and latter sections are presented as a 2-day average of 3 and 4 July. The 2-day average of the model results circumvents the spin-up problem in the numerical simulations. Due to the limitation of the initial cloud LWC/IWC fields, the results for 1 and 2 July have not been included in the analysis and verification.

4.3. Model results and verification

In Fig. 3a, the model-predicted zonal mean total cloudiness, averaged over 3–4 July, is compared with the corresponding 3DNEPH cloud data. Differences between the two curves are generally within 10% of the total cloud cover except in the tropics, Arctic, and Antarctic areas.

As mentioned in Subsection 4.1, 3DNEPH under- and overestimates cloud covers in Arctic and Antarctic regions, respectively, during the Northern Hemisphere summer. Henderson-Sellers (1986) compared 3DNEPH monthly mean data with London's (1957) cloud climatology which is based on surface cloud observations. Since London's cloud climatology was compiled only for the Northern Hemisphere, the comparison is confined to the Northern Hemisphere. London's cloud climatology shows about 70% of total cloudiness in the summertime Arctic region and 40% in the wintertime. The 70% of total cloudiness in the Arctic is close to our model prediction in the area. This explains the differences between the predicted and 3DNEPH cloud cover in the Arctic and Antarctic regions.

The observed large cloudiness in the tropics is largely caused by tropical anvils, which originate from convective clouds. Since the present large-scale cloud model has been developed primarily for stratiform clouds, the simulated cloud cover in the tropics is underestimated, as is evident in Fig. 3a. Another shortcoming in the simulated cloud cover is the overestimation of cloud cover

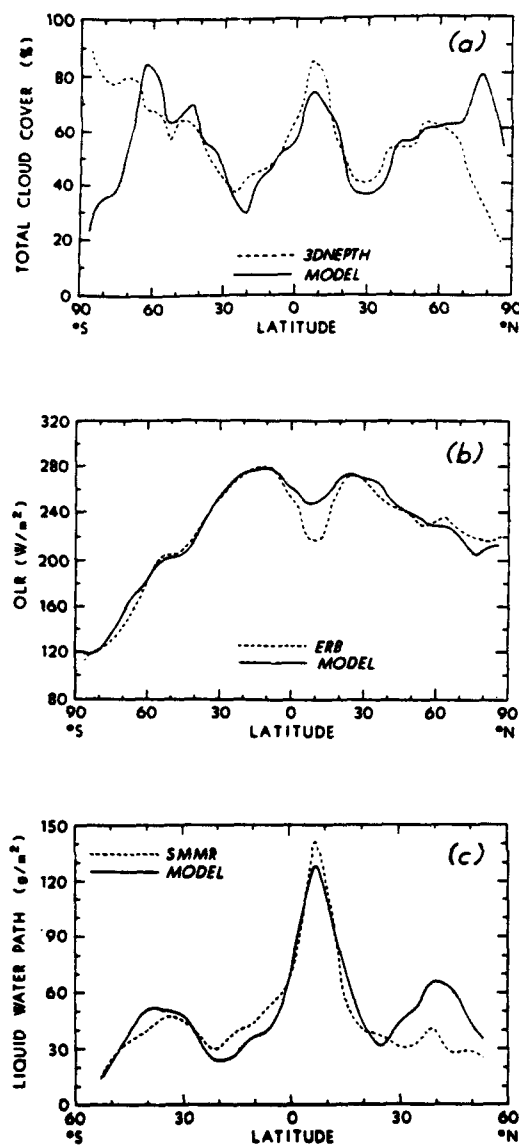


Fig. 3. (a) Comparison of zonal-mean total cloudiness between 3DNEPH and model simulated results averaged over the time period, 3–4 July 1979; (b) Comparison of the zonally averaged OLR computed from the model and derived from ERB data. The model results and ERB data are averaged over the time period, 3–4 July 1979; (c) Comparison of the zonal mean LWP in the simulation and from SMMR data. The SMMR results are taken from Prabhakara and Short (1984) for the monthly average of June 1979. Only the LWPs that are zonally averaged over the oceans are shown in the figure for both simulation and SMMR data.

near 60°S, where the absorbed solar radiation becomes smaller. As a result, strong radiative cooling is produced at the top of middle clouds, leading to a large increase of total cloudiness in the region. It appears that an improvement could be made if a dynamic instability feedback were allowed in the simulation. The simulated small cloud cover located at the subtropical highs in both hemispheres is realistic. Large cloudiness in the tropics is also predicted, although the 3DNEPH cloud data suggests that the predicted cloud cover is underestimated.

Fig. 3b reveals good agreement in OLR between the model simulation and ERB observation, with differences generally less than 10 W/m^2 , except in the tropics. The OLR in the tropics predicted from the model is 30 W/m^2 higher than that analyzed from the ERB data. This overestimation of OLR may be explained by the following two factors. First, the altitude of high clouds defined in the model is usually lower than the actual height of tropical anvils. Second, the simulated cloud cover in the tropics is underestimated. Both curves in Fig. 3b indicate two maxima located in the subtropics in both hemispheres with a minimum in the tropics. These two well-defined OLR maxima are associated with the subtropical highs, where small cloudiness coupled with high temperature produces large OLR. The minimum OLR in the tropics is related to the ITCZ region, where thick high clouds are abundant.

Data on cloud LWP are very limited. There are no observational LWP data on a daily basis with which to compare, nor are the zonal averaged values of LWP available for July of 1979. Since the time domain in this study is the very beginning of July, we have compared the predicted zonal mean LWP with the monthly averaged zonal mean data analyzed from SMMR for June, 1979. Fig. 3c shows the zonal mean LWP from model simulations and from SMMR measurements taken from Prabhakara and Short (1984). The zonally averaged LWPs over the oceans are shown in the figure. The zonal mean simulated cloud LWPs compare quite well with SMMR observations. Differences between the two are within 50 g/m^2 which is the uncertainty of SMMR data suggested by Prabhakara and Short.

The maximum LWP that occurs in the tropics is related to the ITCZ. The two well-defined local LWP maxima at mid-latitudes in both

hemispheres are associated with storm tracks. The minimum LWP is found in regions of subtropical highs with prevailing downward motions. The SMMR data show maximum values of about 140, 47, and 40 g/m² in the tropics and mid-latitudes, respectively. The corresponding values obtained from simulation are 130, 53, and 65 g/m², respectively. The ratio of maximum observed LWP in the tropics to that in the middle latitude is about 3 to 1. This ratio is about 2 to 1 based on the model simulation. This difference indicates that the model underestimates the cloud LWP in the tropics, where a significant amount of LWP observed by the SMMR is associated with convective clouds, which are not simulated in the present model. The simulated LWPs are larger than the observed values in the midlatitudes of the Northern Hemisphere. However, the differences are all within observational uncertainty.

We have also compared the predicted and observed cloud cover, OLR and LWP, in terms of the horizontal cross-sections to demonstrate the geographical distribution of cloud fields. Below is a brief discussion of these comparisons.

The major distinctive features of the geographical distribution of cloud cover in the observation and simulation include the following. First, a pronounced bright band of cloudiness extends along the ITCZ from 150°W to 90°E. Although the ITCZ cloud band is less pronounced in the simulation, the model reasonably predicts the bright cloud bands extending from the central Pacific to the central Atlantic, and into central Africa. Second, areas of small cloudiness associated with subtropical highs occur both north and south of the ITCZ and are clearly identified in both the observation and the simulation. The oceanic subtropical highs in the Atlantic and Pacific Oceans are also evident from the presence of small cloudiness over the regions. Third, in both the simulation and the observation, cloud bands are found over the east coast of South America, the southern and northern Pacific, and the Greenland Sea. The cloudiness over the east coast of North America is larger in the simulation than in the observation. Finally, the under- and overestimation of cloud cover is shown in the 3DNEPH data in the Arctic and Antarctic regions, respectively, for the Northern Hemisphere summer.

There are two distinct features on the OLR patterns. First, the well defined ITCZ and mon-

soon circulation are characterized by relatively small values of OLR. They are located over the equatorial western and eastern Pacific, the Atlantic and central Africa, as well as the monsoon area over India and Asia. The cloudiness in these regions is underestimated in the simulation. As a result, the OLR values in these regions are overestimated by the model. Second, the large values of OLR are associated with the subtropical highs located to the south and north of the ITCZ, due to the small cloudiness in the areas. Small OLR values are also evident in the mid-latitude storm tracks in the Northern Hemisphere. The simulated values of OLR in the Greenland Sea are smaller than observed values.

With respect to the geographical distribution of LWP, we have used for comparison the observed data taken from Prabhakara and Short (1984) in terms of the monthly averaged map for July 1979. A large amount of liquid water is shown in the ITCZ. However, in the subtropical highs of both hemispheres, liquid water is small. In the southern Pacific, the model simulates large LWPs, which are also evident in the observed values. In both the simulation and the observation, abundant liquid water is found over the Indian Ocean, and southeast and northeast Asia. In addition, the well-defined observed local LWP maxima near the east coasts of North, Central, and South America are well simulated by the model. The large amount of liquid water associated with the mid-latitude storm tracks near 50°S(N)–60°S(N) is not shown in the SMMR observation because the sea surfaces are largely covered by ice. In addition, the model simulates large amounts of liquid water over land in Central America, central Africa, India and southeast China. These results are not reported by the SMMR observation because of the inability of the microwave technique to function over land.

Since observed cloud IWC has not been available on the global scale, we qualitatively compare the model-predicted cloud IWC with values derived from aircraft measured data in cirrus, as well as with other model results. Based on aircraft measured data in mid-latitude cirrus over the United States, Heymsfield and Platt (1984) have derived the ice crystal size distribution and IWC as functions of temperature. Averaged cloud IWC varies from 0.001 g/m³ at temperatures below -40°C to about 0.02 g/m³ above this temperature. Similar cloud IWC values have also been simul-

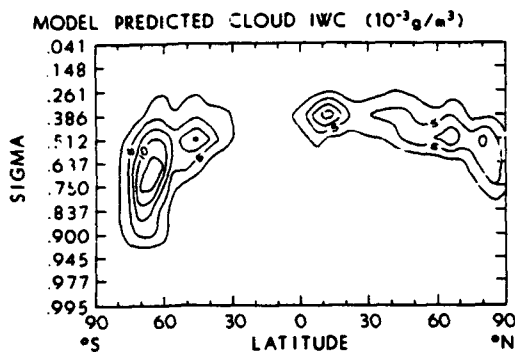


Fig. 4. The model simulations for zonal-mean cloud IWC with a contour interval of $2.5 \times 10^{-3} \text{ g/m}^3$.

ated from a cirrus cloud model by Starr and Cox (1985). The simulated cloud IWC, averaged over 3–4 July 1979, is shown in Fig. 4. The magnitude of the predicted cloud IWC is on the order of 0.01 g/m^3 , which is consistent with the other model studies and aircraft observed values in mid-latitude cirrus clouds.

The maxima cloud IWC are located along a temperature of about -15°C , at which the maximum rate of Bergeron-Findeisen's process occurs. The simulated cloud IWC decreases from about 0.01 g/m^3 near -15°C to 0.001 g/m^3 at temperatures below -40°C . The variations of cloud IWC with respect to the temperature obtained from the model are similar to those suggested by Heymsfield and Platt (1984). It is noted that the simulated cloud ice vanishes at temperatures warmer than the melting point, because the melting process converts ice crystals into water droplets. The simulated cloud IWC appears to depend more on temperature than on vertical velocity, which is most significant in the condensation process. The latitudinal distribution of cloud IWC appears to be realistic. In the wintertime Antarctic area, all clouds contain ice, while in the summertime Arctic region, only middle and high clouds are ice clouds. In the tropics, high clouds are largely composed of ice crystals.

5. The role of radiative heating and ice phase processes in cloud formation

In order to examine the effects of radiative heating fields and ice phase microphysics on the

large-scale cloud simulations, a set of numerical experiments has been carried out with and without the inclusion of radiative heating and ice phase processes. Below is a brief description of the experimental runs:

- CTRL: Control run which includes both radiation and ice-phase processes.
- EXP1: As in CTRL, but without radiative heating.
- EXP2: As in CTRL, but without the ice-phase processes.

All of the control and experimental runs have the same initial conditions and wind fields. The results are averaged over the same period, allowing inter-comparisons to be made between the control and experimental runs.

5.1. Control run

The control run is identical to the experiment described in Subsection 4.2. In that section, the computational results were illustrated in terms of the horizontal cross section. In this section, these results are shown in terms of the meridional cross section so that the vertical structure of cloud fields can be easily identified.

Figs. 5a and 5b show the zonally averaged cloud cover and cloud LWC predicted from the model CTRL. Cloud IWC predicted from CTRL has been shown in Fig. 4. Three cloud cover maxima are seen in the tropics and in the mid-high latitudes of both hemispheres. These maxima are due to large upward motions in these regions. Minima cloud covers occur in the regions of subtropical highs, which are directly related to downward motions. Because of the strong sinking motion of the Southern Hemisphere Hadley cell, cloud cover in the subtropical high of the Southern Hemisphere is smaller than that in the Northern Hemisphere counterpart.

The pattern of simulated cloud LWC in Fig. 5b is consistent with that illustrated in Fig. 5a. The three cloud LWC maxima, located in the tropics and mid-latitude storm tracks, correspond to large cloudiness in these regions. The cloud LWC minima associated with the subtropical highs are due to the prevailing downward motions in the regions. In the vertical, large cloud LWCs are associated with low and middle clouds. The maximum cloud LWC is located in the tropics, and two local maxima exist in mid-latitudes.

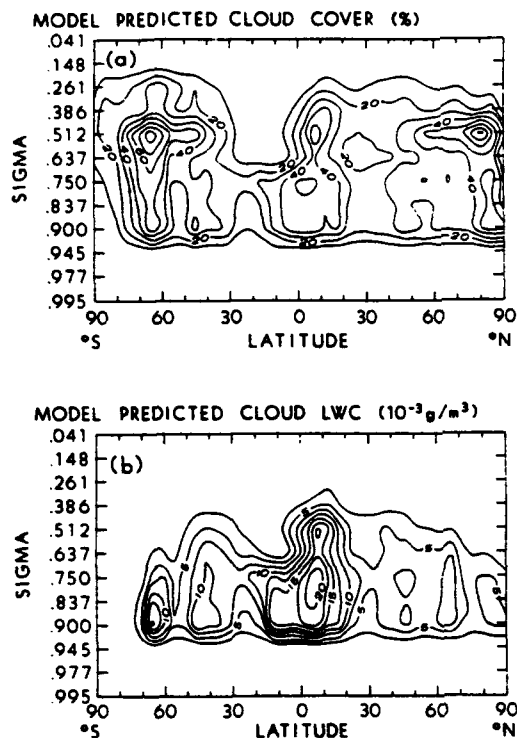


Fig. 5. The model predicted zonal mean fields of (a) cloud cover, and (b) cloud LWC. The model results are averaged over the time period, 3–4 July 1979.

5.2. Experiment on inclusion of radiative heating

Figs. 6–8 show the results from the experiments with and without the inclusion of radiative heating. These results are expressed in terms of the differences between two experiments (CTRL–EXP1).

Solar heating rate differences are illustrated in Fig. 6a. Solar radiation heats the atmosphere. As would be expected, the solar heating rates in July of the Northern Hemisphere are much larger than those of the Southern Hemisphere counterpart. There is no solar radiation within the Antarctic Circle because the sun does not rise above the horizon in this region during July. Two solar heating maxima with values of $\sim 2 \text{ K/day}$ are located at the tops of middle clouds in the Northern Hemisphere. Large solar heating rates within the Arctic Circle are due to long solar days. Large solar heating rates in the tropics are related to small solar zenith angles during the daytime. The large solar heating located in the upper atmosphere is associated with strong ozone absorption.

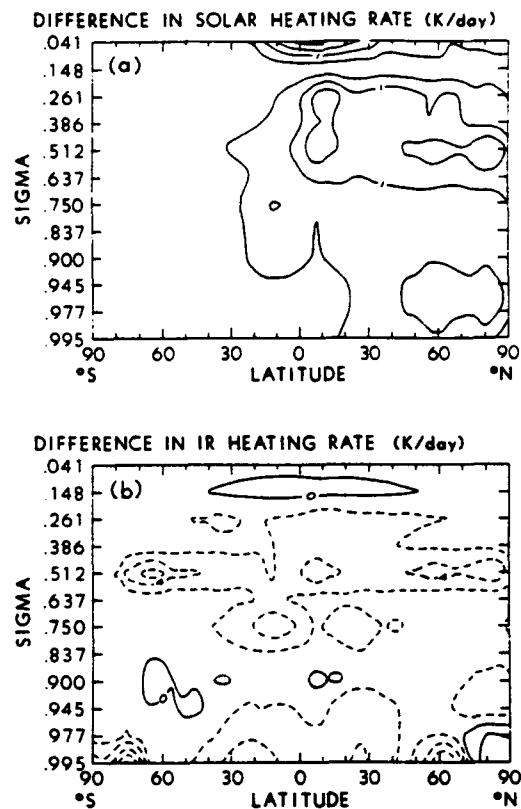


Fig. 6. Zonally averaged differences in (a) solar and (b) IR radiative heating rates. The differences are obtained by subtracting the results in EXP1 from those in CTRL. The contour intervals for solar and IR heating rates are 0.5 and 2 K/day, respectively.

Fig. 6b shows the IR heating rate differences. The most distinct feature in this figure is the strong IR cooling rates that occur at the middle cloud tops. This is because high clouds are considered to be nonblack in radiation calculations, while middle clouds are assumed to be blackbodies. As a result, the upward IR flux emitted by middle clouds is much stronger than the downward flux emitted by high clouds. Consequently, strong IR radiative cooling is generated at the tops of middle clouds.

The inclusion of IR radiative heating basically cools the atmosphere. However, if low cloudiness is sufficiently large to emit strong downward IR fluxes from the cloud base, weak IR heating may be produced beneath the cloud base. This explains the two regions of weak IR heating at the low

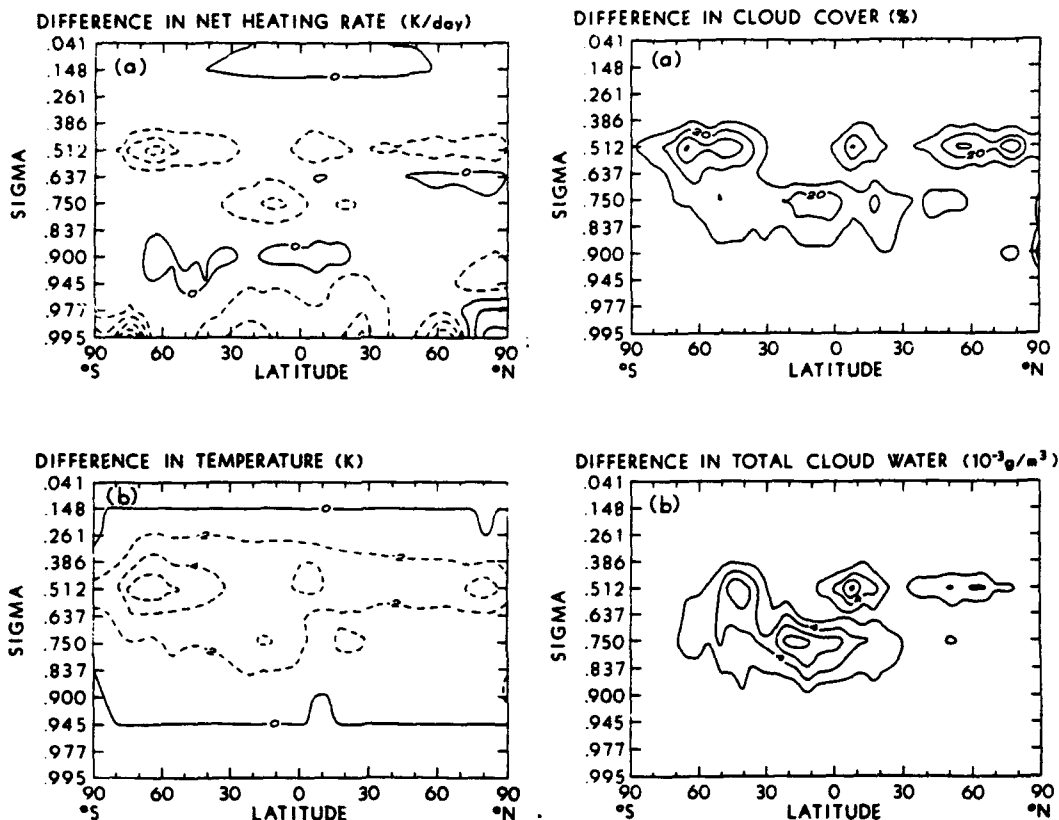


Fig. 7. As in Fig. 6, but for differences in (a) net heating rate and (b) temperature.

Fig. 8. As in Fig. 6, but for differences in (a) cloud cover and (b) total cloud water with contour intervals of 10% and $2 \times 10^{-3} \text{g/m}^3$, respectively.

cloud bottoms at 60°S and in the tropics. Two other weak IR heating rates, located in the upper tropical atmosphere and in the lower atmosphere in the Arctic, are associated with the areas of high ozone concentration and temperature inversion in the regions, respectively.

Fig. 7a shows net radiative heating rates. The inclusion of radiative processes in the model leads to the decrease of atmospheric temperature. As would be expected, the net radiative heating shows relatively large cooling at middle cloud tops and small cooling at cloud bottoms. However, there are weak heating rates in lower tropical atmospheres and in the Southern Hemisphere due to large low cloud cover over those regions. The strongest radiative cooling at the middle cloud top, located within the Antarctic Circle, is due to the

absence of solar radiation in the winter season. Relatively large cooling at the low cloud level within the Arctic area is associated with the temperature inversion in the region, while the large cooling near the surface layers in the equatorial region is due to the contribution of water vapor continuum absorption. It is noted that noticeable net radiative heating is located in the upper atmosphere in the Northern Hemisphere because of the ozone solar absorption in the region. The weak heating at the middle cloud level within the Arctic Circle is due to the absorption of solar radiation during long solar days.

Fig. 7b shows the temperature difference pattern. The inclusion of radiative heating decreases the atmospheric temperature which decreases more significantly for cloudy conditions than clear

sky. The largest temperature reduction occurs at the middle cloud top near 66.5°S , where the sun does not rise much above the horizon in the winter season. Temperature decreases are relatively small in the subtropical regions where small cloud amounts are located. These temperature changes, in turn, initiate all of the changes in the cloud fields such as cloud cover, cloud LWC, and cloud IWC.

Fig. 8a shows differences in cloud cover between the two experiments. The inclusion of radiative heating leads to an increase in cloud cover. Large increases occur at the middle cloud tops, at which large temperature decreases are located. The increases in low cloudiness are relatively small due to small radiative cooling associated with low clouds. However, there are two large increases of low cloud cover. One occurs in the tropics where a large amount of water vapor exists, while the other is in the Arctic area where a strong inversion is located.

Fig. 8b illustrates the differences in total cloud water content, i.e., cloud LWC plus IWC between CTRL and EXP1. Cloud water increases wherever cloud cover increases. As has been mentioned previously, the decrease of cloud temperature by radiative cooling increases the condensational rate and results in the increase of total cloud water. The large increase of cloud water occurs at the tops of middle and low clouds in the tropics, where strong radiative cooling is located.

5.3. Experiment on ice phase processes

Figs. 9a and 9b show the results from the experiments with and without the inclusion of ice-phase processes. The differences in temperature and cloud cover due to the inclusion of ice-phase processes are insignificant. Figure 9a illustrates the differences in cloud LWC between the cases with and without the inclusion of ice-phase processes. This figure shows little change in cloud LWC in the tropical low and middle clouds that contain primarily water droplets. Marked reductions of cloud LWC with ice processes included occur in low, middle, and high clouds within the Antarctic Circle, high clouds in the tropics, and middle and high clouds within the Arctic Circle. In these regions clouds are largely composed of ice crystals, which deplete the cloud LWC by virtue of Bergeron-Findeisen's process. Since there is no cloud IWC in EXP2, the differences in cloud IWC

are identical to cloud IWC shown in CTRL (see Fig. 4).

Fig. 9b shows the differences in total cloud water content. The increases of total cloud water when the ice phase is included indicate that the increase of ice crystals in clouds is larger than the reduction of cloud LWC. It follows that ice clouds in these regions are not entirely controlled by Bergeron-Findeisen's process.

In order to further examine the relationship between autoconversion and Bergeron-Findeisen's process on cloud formation, we have undertaken two more experimental runs with the autoconversion rate of $c_0 = 10^{-4} \text{ s}^{-1}$, which is five times smaller than what was used in the CTRL. A smaller autoconversion rate leads to the production of more cloud LWC, which in turn generates

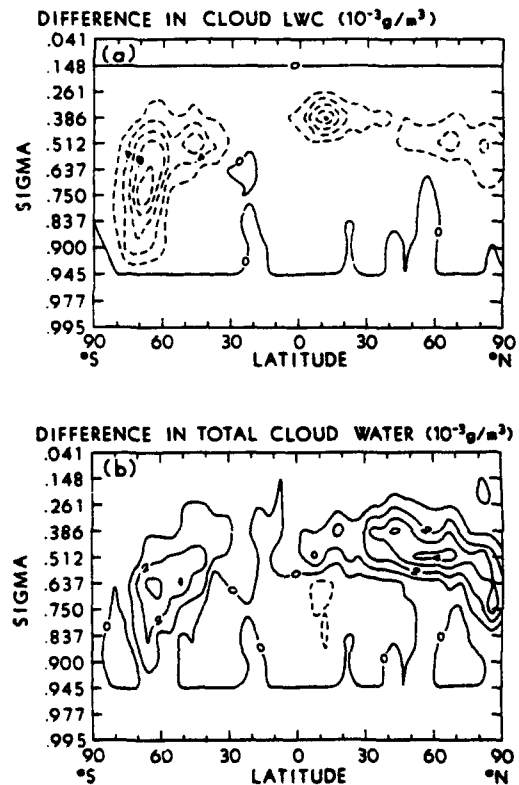


Fig. 9. Zonally averaged differences in (a) cloud LWC and (b) total cloud water. The differences are obtained by subtracting the results in EXP2 from those in CTRL. The contour intervals for cloud LWC and total cloud water are $2 \times 10^{-3} \text{ g/m}^3$ and 10^{-3} g/m^3 , respectively.

more cloud IWC through Bergeron-Findeisen's process. In the following two experimental runs, the first run is the same as CTRL with the smaller value of the autoconversion rate, i.e., $c_0 = 10^{-4}$; the second run is the same as the first run but without the ice phase processes.

Fig. 10a shows a pattern very similar to that in

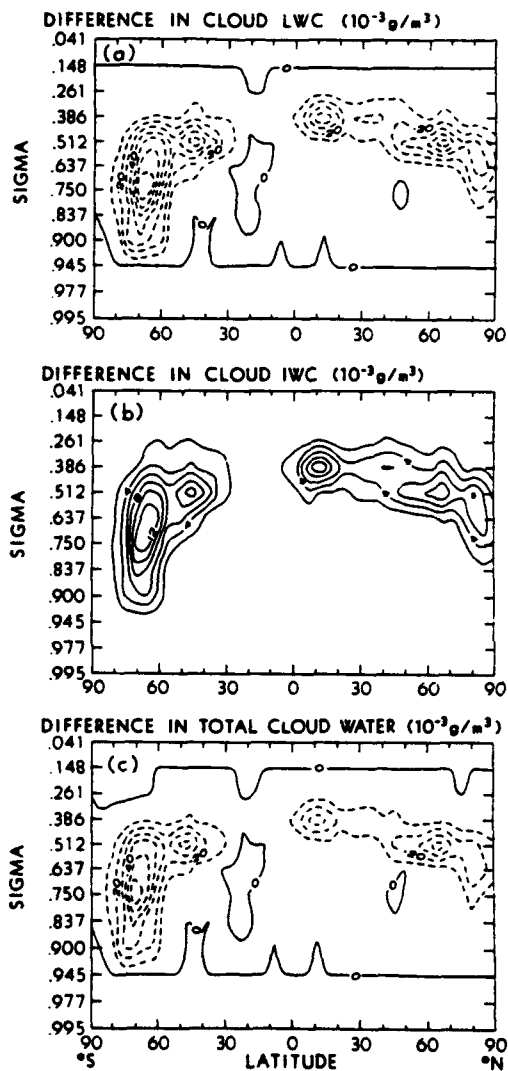


Fig. 10. Zonally averaged differences in (a) cloud LWC, (b) cloud IWC, and (c) total cloud water. The differences are obtained by subtracting the results without ice phase from those with ice phase in the case of a small autoconversion rate. The contour intervals for cloud IWC and cloud LWC and total cloud water are $2 \times 10^{-3} g/m^3$ and $10^{-2} g/m^3$, respectively.

Fig. 9a. Due to the smaller value of the autoconversion rate, the differences in cloud LWC are about five times larger in Fig. 10a than they are in Fig. 9a. The large differences in cloud LWC indicate that a strong Bergeron-Findeisen process takes place when there is more cloud LWC. However, the values of cloud IWC in Fig. 10b are close to those in Fig. 4, even though Bergeron-Findeisen's process is much stronger in the former than in the latter. This indicates that the downward ice flux is larger in the former than in the latter.

Fig. 10c shows the differences in total cloud water content for the smaller c_0 . The total cloud water content decreases in the region where ice clouds are present. The reduction of the total cloud water content is mainly controlled either by autoconversion that converts cloud LWC into precipitation or by gravitational settling that removes ice crystals from the cloud layer. The decrease of total cloud water content when the ice phase processes are included indicates that gravitational settling is an efficient mechanism for reducing the cloud IWC.

6. Conclusions

A time-dependent, three-dimensional, large-scale cloud-moisture model has been developed for the prediction of temperature, cloud cover, cloud LWC, cloud IWC, and precipitation. The wind fields are prescribed using the results from a GCM. The detailed cloud dynamic processes such as top-down turbulence and entrainment are not considered in this large-scale cloud study. Partial cloudiness is allowed to form when the large-scale relative humidity is less than 100%. The cloud microphysical processes simulated in the model include both liquid and ice phases, which are physically included for the first time in a large-scale cloud model to simulate cirrus clouds.

A 96-h model simulation, with the initial conditions taken at 1200 GMT on 1 July 1979 has been carried out to assess the performance of the large-scale cloud model. The comparisons between the model simulation and the satellite observations indicate the large-scale cloud model is capable of realistically simulating zonal means and geographical distributions of cloud fields, including cloud cover, OLR and net solar flux at TOA.

and cloud LWC. Differences in the zonal mean total cloud cover between the simulation and the 3DNEPH data are generally within 10%. Generally, the simulated zonal mean OLRs are within 10 W/m^2 of the ERB results. The zonal mean values of simulated cloud LWP compare quite well with the SMMR observations, with differences being less than 50 g/m^2 , which is the uncertainty of the SMMR data. However, the model underestimates cloud cover and cloud LWC and overestimates the OLR in the tropics, where clouds are predominantly convective types. Convective clouds were not simulated in this model. In the geographical distributions of cloud fields, the large-scale cloud model has simulated the large cloud bands in the ITCZ, monsoon areas, Southern Pacific Convergence Zone, and the mid-latitude storm tracks, although the ITCZ cloud band is less pronounced in the simulation. At the subtropical highs, areas of small cloudiness over southern and northern Africa, and North and South America are clearly identified in both of the observations and the model simulation. The magnitude of the cloud IWC in the simulation is about 0.01 g/m^3 , which is consistent with the aircraft measurements in cirrus clouds, as well as with other model results. The simulated cloud IWC appears to depend more on temperature than on vertical velocity, which is critical to the condensational process.

The model-simulated cloud fields are strongly linked to large-scale circulations. Inspecting the model-predicted cloud fields, such as cloud cover, OLR, and cloud LWC, we find that these cloud properties are closely related to one another. Large amounts of cloud cover coincide with abundant cloud LWC, which generates large precipitation rates by virtue of the autoconversion process simulated in the model. In summary, the atmospheric moisture and cloud fields are linked together by the cloud microphysical processes simulated in the cloud model. More importantly, the moisture, cloud fields and earth's radiation

budget are physically related to large-scale thermal and dynamical structures, such as temperature and vertical velocity.

Sensitivity studies have been performed to examine the effects of radiative heating fields and ice-phase cloud microphysics on large-scale cloud formation. The inclusion of radiative processes in the cloud formation model significantly decreases the cloud temperature, with the strongest cooling occurring at the middle cloud top. However, there may be weak heating located in a low cloud if cloud cover is sufficiently large to produce a strong downward flux. The decrease of temperature by radiative cooling increases the atmospheric relative humidity and condensation in clouds. As a result, cloud cover and total cloud water, including cloud LWC and IWC, increase due to the inclusion of radiative processes.

The inclusion of ice-phase processes has a greater effect on the cloud LWC and IWC than on the temperature and cloud cover fields. If the cloud LWC is large enough to undertake an effective Bergeron-Findeisen process, the total cloud water content decreases, with large decreases located at the regions where the presence of ice clouds is most pronounced. The reduction of the total cloud water content is mainly controlled either by autoconversion, which converts cloud LWC into precipitation, or by gravitational settling, which removes ice crystals from the cloud layer. The decrease of total cloud water content when the ice-phase processes are included indicates that gravitational settling is an efficient mechanism for reducing the cloud IWC.

7. Acknowledgments

The research work contained in this paper has been supported by the Air Force Office of Scientific Research Grant AFOSR-91-0039. We thank Professor H. Sundqvist for helpful comments on the paper.

REFERENCES

- Beard, K. V. and Pruppacher, H. R. 1969. A determination of the terminal velocity and drag of small water drops by means of a wind tunnel. *J. Atmos. Sci.* 26, 1066-1072.
- Hansen, J., Russell, G., Rind, D., Stone, P., Lacis, A., Lebedeff, S., Ruedy, R. and Travis, L. 1983. Efficient three-dimensional global models for climate studies: Models I and II. *Mon. Wea. Rev.* 111, 609-662.

- Henderson-Sellers, A. 1986. Layered cloud amounts for January and July, 1979 from 3-D Nephanalysis. *J. Clim. Appl. Meteor.* 25, 118-132.
- Heymsfield, A. J. 1972. Ice crystal terminal velocities. *J. Atmos. Sci.* 29, 1348-1357.
- Heymsfield, A. J. 1977. Precipitation development in stratiform ice clouds: A microphysical and dynamical study. *J. Atmos. Sci.* 34, 367-381.
- Heymsfield, A. J. and Platt, C. M. R. 1984. A parameterization of the particle size spectrum of ice clouds in terms of the ambient temperature and the ice water content. *J. Atmos. Sci.* 41, 846-856.
- Heymsfield, A. J. and Donner, L. J. 1990. A scheme for parameterizing ice-cloud water content in general circulation models. *J. Atmos. Sci.* 47, 1865-1877.
- Hughes, N. A. 1984. Global cloud climatologies. A historical review. *J. Clim. Appl. Meteor.* 23, 724-751.
- Kessler, E. 1969. On the distribution and continuity of water substance in atmospheric circulations. *Meteor. Monogr.* no. 10, American Meteorological Society, Boston, 84 pp.
- Koenig, L. R. 1971. Numerical modeling of ice deposition. *J. Atmos. Sci.* 28, 226-237.
- Koenig, L. R. and Murray, F. 1976. Ice-bearing cumulus cloud evolution: Numerical simulation and general comparison against observations. *J. Appl. Meteor.* 15, 747-762.
- Koenig, G., Liou, K. N. and Griffin, M. 1987. An investigation of cloud radiation interactions using three-dimensional nephanalysis and earth radiation budget data bases. *J. Geophys. Res.* 92, 5540-5554.
- Kyle, H. L., Hucek, R. R., Groveman, B. and Frey, R. 1990. *Nimbus 7 ERB narrow field of view: earth radiation budget project. User's guide.* Goddard Space Flight Center, Greenbelt, MD.
- Liou, K. N. 1986. Influence of cirrus clouds on weather and climate processes: A global perspective. *Mon. Wea. Rev.* 114, 1167-1199.
- Liou, K. N. and Wittman, G. D. 1979. Parameterization of the radiative properties of clouds. *J. Atmos. Sci.* 36, 1261-1273.
- Liou, K. N. and Ou, S. C. 1981. Parameterization of infrared radiative transfer in cloudy atmospheres. *J. Atmos. Sci.* 38, 2707-2716.
- Liou, K. N. and Ou, S. C. 1983. Theory of equilibrium temperatures in radiative-turbulent atmospheres. *J. Atmos. Sci.* 40, 214-229.
- Liou, K. N. and Zheng, Q. 1984. A numerical experiment on the interactions of radiation, clouds and dynamic processes in a general circulation model. *J. Atmos. Sci.* 41, 1513-1535.
- London, J. 1957. A study of the atmospheric heat balance. AFCRC-TR-57-287, College of Engineering, New York University, N.Y.
- Mason, B. J. 1971. *The Physics of Clouds.* 2nd Edition, Clarendon Press, 671 pp.
- Mitchell, J. F. B., Senior, C. A. and Ingram, W. J. 1989. CO₂ and climate: A missing feedback? *Nature* 341, 132-134.
- Ou, S. C. and Liou, K. N. 1983. Parameterization of carbon dioxide 15 μm absorption and emission. *J. Geophys. Res.* 88, 5203-5207.
- Ou, S. C. and Liou, K. N. 1988. Development of radiation and cloud parameterization programs for AFGL global models. Scientific Report, Air Force Geophysics Laboratory, AFGL-TR-88-0018, 88 pp.
- Prabhakara, C. and Short, D. A. 1984. Nimbus-7 SMMR derived seasonal variations in the water vapor, liquid water and surface winds over the global oceans. *NASA Technical Memorandum 86080*, Goddard Space Flight Center, Greenbelt, Maryland, U.S.A.
- Prabhakara, C., Wang, I., Chang, A. T. C. and Gloersen, P. 1983. A statistical examination of Nimbus 7 SMMR data and remote sensing of sea surface temperature, liquid water content in the atmosphere and surface wind speed. *J. Clim. Appl. Meteor.* 22, 2033-2037.
- Ramanathan, V., Pitcher, E. J., Malone, R. C. and Blackmon, M. L. 1983. The response of a spectral general circulation model to refinements in radiative processes. *J. Atmos. Sci.* 40, 605-630.
- Roeckner, E. 1988. Cloud-radiation feedbacks in a climate model. *Atmos. Res.* 21, 293-303.
- Slingo, J. M. 1987. The development and verification of a cloud prediction scheme for the ECMWF model. *Quart. J. Roy. Meteor. Soc.* 113, 899-927.
- Slingo, A. and Slingo, J. M. 1988. The response of a general circulation model to cloud longwave radiative forcing. I: Introduction and initial experiments. *Quart. J. Roy. Meteor. Soc.* 114, 1027-1062.
- Smagorinsky, J. 1960. On the dynamical prediction of large-scale condensation by numerical methods. *Monograph no. 5*, Amer. Geophys. Union, 71-78.
- Smith, R. N. B. 1990. A scheme for predicting layer clouds and their water content in a general circulation model. *Quart. J. Roy. Meteor. Soc.* 116, 435-460.
- Starr, D. C. and Cox, S. K. 1985. Cirrus clouds. Part I: A cirrus cloud model. *J. Atmos. Sci.* 42, 2663-2681.
- Stephens, G. L. 1978. Radiative properties of extended water clouds. *J. Atmos. Sci.* 35, 2111-2132.
- Sundqvist, H. 1978. A parameterization scheme for non-convective condensation including prediction of cloud water content. *Quart. J. Roy. Meteor. Soc.* 104, 677-690.
- Sundqvist, H. 1981. Prediction of stratiform clouds: Results from a 5-day forecast with a global model. *Tellus* 33, 242-253.
- Sundqvist, H. 1988. Parameterization of condensation and associated clouds in models for weather prediction and general circulation simulation. In: *Physically based modelling and simulation of climate and climatic change.* (ed. M. E. Schlesinger). Reidel, Dordrecht, Part 1, 433-461.
- Washington, W. M. and Williamson, D. L. 1977. A description of the NCAR global circulation models. In: *Methods in computational physics, vol. 17. General circulation models of the atmosphere* (ed. J. Chang), pp. 111-172, Academic Press, New York.
- Washington, W. M. and Mechl, G. A. 1984. Seasonal

- cycle experiment on the climate sensitivity due to a doubling of CO₂ with an atmospheric general circulation model coupled to a simple mixed-layer ocean model. *J. Geophys. Res.* 89, 9475-9503.
- Wetherald, R. T. and Manabe, S. 1988. Cloud feedback processes in a general circulation model. *J. Atmos. Sci.* 45, 1397-1415.
- Xu, K. M. and Krueger, S. K. 1991. Evaluation of cloudiness parameterizations using a cumulus ensemble model. *Mon. Wea. Rev.* 119, 342-367.
- Yang, G. H., Mitchell, K., Norquist, D. and Yee, S. 1989. *Diagnostics for and evaluations of new parameterization schemes for global NWP models.* GL-TR-89-0158. Environmental Research Papers Number 1032, Geophysics Laboratory, Atmospheric Sciences Division, Hanscom AF Base, MA 01731.

Reprinted from JOURNAL OF THE ATMOSPHERIC SCIENCES, Vol. 50, No. 13, 1 July 1993
American Meteorological Society

Parameterization of the Radiative Properties of Cirrus Clouds

QIANG FU AND K. N. LIOU

Parameterization of the Radiative Properties of Cirrus Clouds

QIANG FU AND K. N. LIOU

Department of Meteorology/CARSS, University of Utah, Salt Lake City, Utah

(Manuscript received 6 July 1992, in final form 7 October 1992)

ABSTRACT

A new approach for parameterization of the broadband solar and infrared radiative properties of ice clouds has been developed. This parameterization scheme integrates in a coherent manner the δ -four-stream approximation for radiative transfer, the correlated k -distribution method for nongray gaseous absorption, and the scattering and absorption properties of hexagonal ice crystals. A mean effective size is used, representing an area-weighted mean crystal width, to account for the ice crystal size distribution with respect to radiative calculations. Based on physical principles, the basic single-scattering properties of ice crystals, including the extinction coefficient divided by ice water content, single-scattering albedo, and expansion coefficients of the phase function, can be parameterized using third-degree polynomials in terms of the mean effective size. In the development of this parameterization the results computed from a light scattering program that includes a geometric ray-tracing program for size parameters larger than 30 and the exact spheroid solution for size parameters less than 30 are used. The computations are carried out for 11 observed ice crystal size distributions and cover the entire solar and thermal infrared spectra. Parameterization of the single-scattering properties is shown to provide an accuracy within about 1%. Comparisons have been carried out between results computed from the model and those obtained during the 1986 cirrus FIRE IFO. It is shown that the model results can be used to reasonably interpret the observed IR emissivities and solar albedo involving cirrus clouds. The newly developed scheme has been employed to investigate the radiative effects of ice crystal size distributions. For a given ice water path, cirrus clouds with smaller mean effective sizes reflect more solar radiation, trap more infrared radiation, and produce stronger cloud-top cooling and cloud-base heating. The latter effect would enhance the in-cloud heating rate gradients. Further, the effects of ice crystal size distribution in the context of IR greenhouse versus solar albedo effects involving cirrus clouds are presented with the aid of the upward flux at the top of the atmosphere. In most cirrus cases, the IR greenhouse effect outweighs the solar albedo effect. One exception occurs when a significant number of small ice crystals are present. The present scheme for radiative transfer in the atmosphere involving cirrus clouds is well suited for incorporation in numerical models to study the climatic effects of cirrus clouds, as well as to investigate interactions and feedbacks between cloud microphysics and radiation.

1. Introduction

Cirrus clouds are globally distributed, being present at all latitudes and without respect to land or sea or season of the year. They regularly cover about 20%–30% of the globe and strongly influence weather and climate processes through their effects on the radiation budget of the earth and the atmosphere (Liou 1986). The importance of cirrus clouds in weather and climate research can be recognized by the intensive field observations that have been conducted as a major component of the First ISCCP Regional Experiment in October–November 1986 (Starr 1987) and more recently in November–December 1991.

Cirrus clouds possess a number of unique features. In addition to being global and located high in the troposphere and extending to the lower stratosphere on some occasions, they contain almost exclusively

nonspherical ice crystals of various shapes, such as bullet rosettes, plates, and columns. There are significant computational and observational difficulties in determining the radiative properties of cirrus clouds. A reliable and efficient determination of the radiative properties of cirrus clouds requires the fundamental scattering and absorption data involving nonspherical ice crystals. In addition, appropriate incorporation of gaseous absorption in scattering cloudy atmospheres and an efficient radiative transfer methodology are also required.

Although parameterization of the broadband radiative properties for cirrus clouds has been presented by Liou and Wittman (1979) in terms of ice water content, such parameterization used the scattering and absorption properties of circular cylinders without accounting for the effects of the hexagonal structure of ice crystals. Moreover, the effects of ice crystal size distribution were not included in the parameterization. Using area-equivalent or volume-equivalent ice spheres to approximate hexagonal ice crystals for scattering and absorption properties has been shown to be inadequate,

Corresponding author address: Professor K. N. Liou, Department of Meteorology, University of Utah, 809 William C. Browning Building, Salt Lake City, UT 84112.

and frequently misleading. This is evident in interpreting the scattering and polarization patterns from ice clouds (Takano and Liou 1989) and the observed radiative properties of cirrus clouds, in particular, the cloud albedo (Stackhouse and Stephens 1991).

In this paper, we wish to develop a new approach for the parameterization of the broadband solar and infrared radiative properties of ice crystal clouds. Three major components are integrated in this parameterization, including the scattering and absorption properties of hexagonal ice crystals, the δ -four-stream approximation for radiative transfer, and the correlated k -distribution method for nongray gaseous absorption. Compared with more sophisticated models and aircraft observations, the present parameterization has been shown to be accurate and efficient for flux and heating rate calculations. In section 2, we present parameterization of the single-scattering properties of ice crystals. The manner in which the radiative flux transfer is parameterized using the δ -four-stream approximation and the correlated k -distribution is discussed in section 3. Section 4 presents some comparisons between theoretical results and observed data involving cloud emissivity and albedo. In section 5, we present the effect of ice crystal size distribution on cloud heating rates and on the question of cloud radiative forcing. Summary and conclusions are given in section 6.

2. Parameterization of the single-scattering properties of ice crystals

a. Physical bases

The calculations of the single-scattering properties, including the phase function, single-scattering albedo, and extinction coefficient, require a light scattering program and the detailed particle size distribution. The calculations are usually time consuming. If radiation calculations are to interact with an evolving cloud where particle size distribution varies as a function of time and/or space, the computer time needed for examining just this aspect of the radiation program would be formidable, even with a supercomputer. Thus, there is a practical need to simplify the computational procedure for the calculation of the single-scattering properties of cloud particles. Since spheres scatter an amount of light proportionate to their cross-section area, a mean effective radius, which is defined as the mean radius that is weighted by the cross-section area of spheres, has been used in conjunction with radiation calculations (Hansen and Travis 1974). Higher-order definition, such as dispersion of the droplet size, may be required in order to more accurately represent the droplet size distribution.

Ice crystals are nonspherical and ice crystal size distributions are usually expressed in terms of the maximum dimension (or length). Representation of the size distribution for ice crystals is much more involved than that for water droplets. To the extent that scattering of

light is proportional to the cross-section area of nonspherical particles, we may use a mean effective size analogous to the mean effective radius defined for spherical water droplets as follows:

$$D_e = \frac{\int_{L_{\min}}^{L_{\max}} D \cdot DLn(L)dL}{\int_{L_{\min}}^{L_{\max}} DLn(L)dL}, \quad (2.1)$$

where D is the width of an ice crystal, $n(L)$ denotes the ice crystal size distribution, and L_{\min} and L_{\max} are the minimum and maximum lengths of ice crystals, respectively. A similar definition for circular cylinders has also been proposed by Platt and Harshvardhan (1988). Based on aircraft observations by Ono (1969) and Auer and Veal (1970), the width may be related to the length L . It follows that the mean effective width (or size) can be defined solely in terms of ice crystal size distribution. The geometric cross section area for oriented hexagonal ice crystals generally deviates from DL [see Eq. (2.4) for the condition of random orientation]. To the extent that D is related to L , the definition of D_e in Eq. (2.1), which is an approach to represent ice crystal size distribution, should be applicable to ice crystals with hexagonal structure. The numerator in Eq. (2.1) is related to the ice water content (IWC) in the form

$$\text{IWC} = \frac{3\sqrt{3}}{8} \rho_i \int_{L_{\min}}^{L_{\max}} D \cdot DLn(L)dL, \quad (2.2)$$

where the volume of a hexagonal ice crystal, $3\sqrt{3}D^2L/8$, is used and ρ_i is the density of ice. We shall confine our study to the use of the mean effective size to represent ice crystal size distribution in the single-scattering calculation for ice crystals.

The extinction coefficient is defined by

$$\beta = \int_{L_{\min}}^{L_{\max}} \sigma(D, L)n(L)dL, \quad (2.3)$$

where σ is the extinction cross section for a single crystal. In the limits of geometric optics and using hexagonal ice crystals that are randomly oriented in space, the extinction cross section may be expressed by (Takano and Liou 1989)

$$\sigma = \frac{3}{2} D \left(\frac{\sqrt{3}}{4} D + L \right). \quad (2.4)$$

Substituting Eq. (2.4) into Eq. (2.3) and using the definitions of D_e and IWC, we have

$$\beta = \text{IWC} \left(\frac{1}{\rho_i} \int_{L_{\min}}^{L_{\max}} D^2 n(L)dL / \int_{L_{\min}}^{L_{\max}} D^2 Ln(L)dL + \frac{4}{\sqrt{3}\rho_i} \frac{1}{D_e} \right). \quad (2.5a)$$

The first term on the right cannot be defined in terms

of D_e directly. Since $D < L$, however, this term should be much smaller than the second term, which also involves a factor $4/\sqrt{3}$. To the extent that D is related to L , the first term may be approximated by $a + b'/D_e$, where $b' \ll 4/\sqrt{3}\rho_i$ and a is a certain constant. Using this argument, we obtain the following relationship:

$$\beta \approx \text{IWC}(a + b/D_e), \quad (2.5b)$$

where $b = b' + 4/\sqrt{3}\rho_i$. Using the observed ice crystal size distributions described below, we also show that β/IWC and $1/D_e$ are linearly related in the solar spectral region. Based on the preceding analysis, it is clear that the extinction coefficient is a function of both IWC and mean effective size.

Because cloud absorption is critically dependent on the variation of the single-scattering albedo, it must be accurately parameterized. For a given ice crystal size distribution, the single-scattering albedo, $\tilde{\omega}$, is defined by

$$1 - \tilde{\omega} = \int_{L_{\min}}^{L_{\max}} \sigma_a n(L) dL / \int_{L_{\min}}^{L_{\max}} \sigma n(L) dL, \quad (2.6)$$

where σ_a denotes the absorption cross section for a single crystal. When absorption is small, σ_a is approximately equal to the product of the imaginary part of the refractive index of ice, m_i , and the particle volume; namely,

$$\sigma_a = \frac{3\sqrt{3}\pi m_i(\lambda)}{2\lambda} D^2 L, \quad (2.7)$$

where λ is the wavelength. Using the extinction and absorption cross sections defined in Eqs. (2.4) and (2.7) and noting that D is related to L , based on observations, we obtain

$$1 - \tilde{\omega} \approx c + dD_e, \quad (2.8)$$

where c and d are certain coefficients.

In the preceding discussion, we have used the geometric optics limit to derive the expressions for the extinction coefficient and single-scattering albedo. In view of the observed ice crystal sizes in cirrus clouds (~ 20 – $2000 \mu\text{m}$), the simple linear relationships denoted in Eqs. (2.5b) and (2.8) should be valid for solar wavelengths (0.2 – $4 \mu\text{m}$). For thermal infrared wavelengths (e.g., $10 \mu\text{m}$), the geometric optics approximation may not be appropriate for small ice crystals. We note from aircraft observations, however, that there is a good linear relationship between the extinction coefficient in the infrared spectrum and the extinction coefficient derived based upon the large-particle approximation (Foot 1988).

b. A generalized parameterization

The linear relationship between β/IWC and $1/D_e$ shown in Eq. (2.5b) is derived based on the geometric

optics approximation and the assumption that ice crystals are randomly oriented in space. The linear relationship between $\tilde{\omega}$ and D_e shown in Eq. (2.8) is based on the assumption that ice crystal absorption is small and that ice crystals are randomly oriented. For general cases, we would expect that higher-order expansions may be needed to define more precisely the single-scattering properties of ice crystals in terms of the mean effective size. Thus, we postulate that

$$\beta = \text{IWC} \sum_{n=0}^N a_n / D_e^n, \quad (2.9)$$

$$1 - \tilde{\omega} = \sum_{n=0}^N b_n D_e^n, \quad (2.10)$$

where a_n and b_n are certain coefficients, which must be determined from numerical fitting, and N is the total number of terms required to achieve a prescribed accuracy. When $N = 1$, Eqs. (2.9) and (2.10) are exactly the same as Eqs. (2.5b) and (2.8). When $N = 2$, the term $1/D_e^2$ is proportional to the variance of ice crystal size distribution. Based on numerical experimentation described in subsection c, we find $N = 2$ is sufficient for the extinction coefficient expression to achieve an accuracy within 1%. For the single-scattering albedo, we find that $N = 3$ is required.

For nonspherical particles randomly oriented in space, the phase function is a function of the scattering angle, θ . The phase function is usually expanded in a series of Legendre polynomials P_l in radiative transfer calculations in the form

$$P(\cos\theta) = \sum_{l=0}^M \tilde{\omega}_l P_l(\cos\theta), \quad (2.11)$$

where we set $\tilde{\omega}_0 = 1$. Since the phase function is dependent on ice crystal size distribution, the expansion coefficients must also be related to ice crystal size distribution, which is represented by the mean effective size in the present study. In the case of hexagonal ice crystals, in addition to the diffraction, scattered energy is also produced by the δ -function transmission through parallel planes at $\theta = 0$ (Takano and Liou 1989). Using the similarity principle for radiative transfer, the expansion coefficients in the context of the four-stream approximation can be expressed by

$$\tilde{\omega}_l = (1 - f_\delta) \tilde{\omega}_l^* + f_\delta(2l + 1), \quad l = 1, 2, 3, 4, \quad (2.12)$$

where $\tilde{\omega}_l^*$ represents the expansion coefficients for the phase function in which the forward δ -function peak has been removed, and f_δ is the contribution from the forward δ -function peak. In our notation, $\tilde{\omega}_1 = 3g$, where g is the asymmetry factor. The δ -function peak contribution has been evaluated by Takano and Liou and is a function of ice crystal size. The f_δ value increases with increasing L/D value due to a greater probability for plane-parallel transmission. We may

express $\bar{\omega}_l^*$ and f_s in terms of the mean effective size as follows:

$$\bar{\omega}_l^* = \sum_{n=0}^N c_{n,l} D_c^n, \quad (2.13a)$$

$$f_s = \sum_{n=0}^N d_n D_c^n, \quad (2.13b)$$

where $c_{n,l}$ and d_n are certain coefficients. Based on numerical experimentation described in subsection *c*, we find $N = 3$ is sufficient to achieve an accuracy within 1%.

In the thermal infrared wavelengths, halo and δ -transmission peak features in the phase function are largely suppressed due to strong absorption. For this reason and to a good approximation, we may use the asymmetry factor to represent the phase function via the Henyey-Greenstein function in the form

$$\bar{\omega}_l = (2l + 1)g^l. \quad (2.14)$$

The asymmetry factor may also be expressed in terms of the effective mean size as follows:

$$g(\text{IR}) = \sum_{n=0}^N c'_n D_c^n, \quad (2.15)$$

where c'_n again is a certain coefficient and $N = 3$ is sufficient in the expansion.

c. Determination of the coefficients in the parameterization

The coefficients in Eqs. (2.9), (2.10), (2.13), and (2.15) are determined from numerical fitting to the data computed from "exact" light scattering and absorption programs that include the following. For size parameters larger than about 30, we use the results computed from a geometric ray-tracing program for hexagonal ice crystals developed by Takano and Liou (1989). Note that the parameterization coefficients may be updated if the results for other types of ice crystals, such as bullet rosettes and hollow columns, are available. For size parameters less than about 30, the laws of geometric optics are generally not applicable. Since the exact solution for hexagonal ice crystals based on either the wave equation approach or other integral methods for size parameters on the order of 20–30 has not been developed, we use the results computed from a light scattering program for spheroids developed by Asano and Sato (1980). We have tested and modified this program (Takano et al. 1992) and found that it can be applied to size parameters less than about 30. Naturally occurring ice crystals will have a hexagonal structure that cannot be approximated by spheroids. However, small size parameters are usually associated with infrared wavelengths, where ice is highly absorbing. It is likely that the detailed shape factor may

not be critical in scattering and absorption calculations. Further inquiry into this problem appears necessary.

In the present "exact" computations, 11 ice crystal size distributions from in situ aircraft observations were employed. Table 1 shows the number densities, IWCs, and mean effective sizes for these 11 size distributions. The first two types are for the cirrostratus (Cs) and cirrus uncinus presented by Heymsfield (1975), while the next two types are modified distributions given by Heymsfield and Platt (1984) corresponding to warm and cold cirrus clouds. The size distributions of cirrus clouds at temperatures of -20° , -40° , and -60°C were obtained from the parameterization results presented by Heymsfield and Platt (1984). Other cirrus types, Ci (22 October, 25 October, 1 November, and 2 November), were the ice crystal size distributions derived from the 1986 FIRE cirrus experiments (A. Heymsfield, personal communication). The 11 size distributions cover a reasonable range of cloud microphysical properties in terms of IWC (6.6×10^{-4} – 0.11 g m^{-3}) and mean effective size (23.9–123.6 μm) as shown in Table 1. For scattering and absorption calculations, these size distributions have been discretized in five regions. The aspect ratios, L/D , used are 20/20, 50/40, 120/60, 300/100, and 750/160 (in units of $\mu\text{m}/\mu\text{m}$), roughly corresponding to the observations reported by Ono (1969) and Auer and Veal (1970).

In the single-scattering calculations, the refractive indices for ice, compiled by Warren (1984), were used. In order to resolve the variation in the refractive index of ice and account for the gaseous absorption, 6 and 12 bands were selected for solar and thermal IR regions, respectively. The spectral division is shown in Table 2, where the index for the spectral band ($i = 1, 2, \dots, 18$) is defined. The complex indices of refraction at each wavelength are averaged values over the spectral band, weighted by the solar irradiance (Thekaekara 1973) in solar spectrum and by the Planck function ($T = -40^\circ\text{C}$) in thermal IR spectrum. This temperature is a typical value for cirrus clouds. The single-scattering calculations were carried out at the central

TABLE 1. Characteristics of the 11 ice crystal size distributions employed in the present study.

Particle size distribution	Number of particles (cm^{-3})	Ice water content (g m^{-3})	Mean effective size (μm)
Cs	0.187	4.765×10^{-3}	41.5
Ci Uncinus	0.213	1.116×10^{-1}	123.6
Ci (cold)	0.176	1.110×10^{-3}	23.9
Ci (warm)	0.442	9.240×10^{-3}	47.6
Ci ($T = -20^\circ\text{C}$)	0.247	8.613×10^{-3}	57.9
Ci ($T = -40^\circ\text{C}$)	0.187	9.177×10^{-3}	64.1
Ci ($T = -60^\circ\text{C}$)	0.065	6.598×10^{-4}	30.4
Ci (22 Oct)	0.052	1.609×10^{-2}	104.1
Ci (25 Oct)	0.072	2.923×10^{-2}	110.4
Ci (1 Nov)	0.032	4.968×10^{-3}	75.1
Ci (2 Nov)	0.038	1.406×10^{-2}	93.0

TABLE 2. Spectral division used in the parameterization.

Solar spectrum			Infrared spectrum		
Band <i>i</i>	Central λ (μm)	Band limits (μm)	Band <i>i</i>	Central λ (μm)	Band limits (cm^{-1})
1	0.55	0.2–0.7	7	4.9	2200–1900
2	1.0	0.7–1.3	8	5.6	1900–1700
3	1.6	1.3–1.9	9	6.5	1700–1400
4	2.2	1.9–2.5	10	7.6	1400–1250
5	3.0	2.5–3.5	11	8.5	1250–1100
6	3.7	3.5–4.0	12	9.6	1100–980
			13	11.3	980–800
			14	13.7	800–670
			15	16.6	670–540
			16	21.5	540–400
			17	30.0	400–280
			18	70.0	280–1

wavelength for each spectral band. The coefficients in Eqs. (2.9), (2.10), (2.13), and (2.15) determined by numerical fitting using the "exact" results are listed in Tables 3–5. In the solar spectrum where the law of geometric optics is valid, the extinction coefficients β for a given size distribution are the same regardless of the wavelength, as shown in Table 3. The optical depth $\tau = \beta\Delta z$ can be obtained if the cloud thickness Δz is given. Figures 1–2 show the fitting for β/IWC , $\tilde{\omega}$, and g in the spectral intervals 1.9–2.5 μm and 800–980 cm^{-1} , respectively. For the solar spectrum, we use band number four (1.9–2.5 μm) as an example, because the single-scattering properties in this band significantly depend on size distribution. The linear relationship between β/IWC and $1/D_e$ postulated in Eq. (2.5b) is clearly shown in Fig. 1a. This linear relationship is valid for all other solar bands, because the extinction cross sections for solar bands in the limit of the geometric optics approach are the same, as pointed out previously. The nonlinearity between $\tilde{\omega}$ and D_e becomes important for small $\tilde{\omega}$. This is because the linear relationship developed in Eq. (2.8) is based on the weak absorption assumption. The band 800–980 cm^{-1} is located in the atmospheric window, where the greenhouse effect of clouds is most pronounced. It can be seen that very good fits for single-scattering properties in both solar and infrared spectra are obtained. The relative errors are less than $\sim 1\%$. Other spectral bands also show similar accuracies.

It is known that the minimum ice crystal length that the present optical probe can measure is about 20 μm . To investigate the potential effects of small ice crystals that may exist in cirrus clouds on parameterizations of the single-scattering properties, we used the 11 observed ice crystal size distributions and extrapolated these distributions from 20 to 10 μm in the logarithmic scale. The resulting mean effective sizes range from 18.9 to 122.7 μm . Using these sizes, the numerical fitting coefficients vary only slightly and do not affect the

accuracy of the preceding parameterized single-scattering properties. In the present study, ice crystals are assumed to be randomly oriented in space. In cases when cirrus clouds contain horizontally oriented ice crystals, parameterizations would require modifications. The extinction coefficient, single-scattering albedo, and phase function would depend on the incident direction. The radiative transfer scheme would also require adjustments to account for anisotropic properties. Since fluxes are involved in the parameterization, we anticipate that the modifications should not significantly affect the results and conclusions derived from this study. At any rate, this is an area requiring further research efforts.

3. Parameterization of radiative flux transfer

a. Radiative transfer scheme

We follow the δ -four-stream model developed by Liou et al. (1988) for the calculations of solar radiative flux transfer in a single homogeneous layer. The solution, like various two-stream methods, is in analytic form so that the computational effort involved is minimal. As demonstrated in that paper, results from the δ -four-stream approximation can yield relative accuracies within $\sim 5\%$.

To obtain a single treatment of solar and infrared radiation, we extend the δ -four-stream approach to the transfer of infrared radiation, in which the optical depth dependence of the Planck function must be known. The Planck function can be approximately expressed in terms of the optical depth in the form

$$B(\tau) = B_0 \exp(\tau/\tau_1 \ln B_1/B_0), \quad (3.1)$$

where τ_1 is the optical depth of a layer, and B_0 and B_1 are the Planck functions corresponding to the temperature at the top and bottom of this layer, respectively. This exponential approximation for the Planck func-

TABLE 3. Values of empirical coefficients in Eq. (2.9) for the parameterization of the extinction coefficient β (m^{-1}). Note that the coefficients are determined by using an ice density ρ_i of 0.9167 g cm^{-3} . For other ice densities ρ_i' , they should be adjusted by a factor ρ_i/ρ_i' . (The units for D_e and IWC are in μm and g m^{-3} , respectively.)

Band <i>i</i>	a_0	a_1	a_2
1–6	-6.656×10^{-3}	3.686	0.0
7	-7.770×10^{-3}	3.734	11.85
8	-8.088×10^{-3}	3.717	17.17
9	-8.441×10^{-3}	3.715	19.48
10	-9.061×10^{-3}	3.741	26.48
11	-9.609×10^{-3}	3.768	34.11
12	-1.153×10^{-2}	4.109	17.32
13	-8.294×10^{-3}	3.925	1.315
14	-1.026×10^{-2}	4.105	16.36
15	-1.151×10^{-2}	4.182	31.13
16	-1.704×10^{-2}	4.830	16.27
17	-1.741×10^{-2}	5.541	-58.42
18	-7.752×10^{-3}	4.624	-42.01

TABLE 4. Values of empirical coefficients in Eq. (2.10) for the parameterization of the single-scattering albedo $\tilde{\omega}$.
(The units for D_e are in μm .)

Band i	b_0	b_1	b_2	b_3
1	$.10998 \times 10^{-5}$	$-.26101 \times 10^{-7}$	$.10896 \times 10^{-8}$	$-.47387 \times 10^{-11}$
2	$.20208 \times 10^{-4}$	$.96483 \times 10^{-5}$	$.83009 \times 10^{-7}$	$-.32217 \times 10^{-9}$
3	$.13590 \times 10^{-3}$	$.73453 \times 10^{-3}$	$.28281 \times 10^{-5}$	$-.18272 \times 10^{-7}$
4	$-.16598 \times 10^{-2}$	$.20933 \times 10^{-2}$	$-.13977 \times 10^{-3}$	$-.18703 \times 10^{-7}$
5	.46180	$.24471 \times 10^{-3}$	$-.27839 \times 10^{-5}$	$.10379 \times 10^{-7}$
6	$.42362 \times 10^{-1}$	$.86425 \times 10^{-2}$	$-.75519 \times 10^{-4}$	$.24056 \times 10^{-6}$
7	.19960	$.37800 \times 10^{-2}$	$-.14910 \times 10^{-4}$.0
8	.30140	$.26390 \times 10^{-2}$	$-.11160 \times 10^{-4}$.0
9	.39080	$.12720 \times 10^{-2}$	$-.55640 \times 10^{-5}$.0
10	.31050	$.26030 \times 10^{-2}$	$-.11390 \times 10^{-4}$.0
11	.20370	$.42470 \times 10^{-2}$	$-.18100 \times 10^{-4}$.0
12	.23070	$.38300 \times 10^{-2}$	$-.16160 \times 10^{-4}$.0
13	.56310	$-.14340 \times 10^{-2}$	$.62980 \times 10^{-5}$.0
14	.52070	$-.97780 \times 10^{-3}$	$.37250 \times 10^{-5}$.0
15	.32540	$.34340 \times 10^{-2}$	$-.30810 \times 10^{-4}$	$.91430 \times 10^{-7}$
16	.10280	$.50190 \times 10^{-2}$	$-.20240 \times 10^{-4}$.0
17	.39640	$-.31550 \times 10^{-2}$	$.64170 \times 10^{-4}$	$-.29790 \times 10^{-6}$
18	.80790	$-.70040 \times 10^{-2}$	$.52090 \times 10^{-4}$	$-.14250 \times 10^{-6}$

TABLE 5a. Values of empirical coefficients in Eq. (2.13) for parameterization of the expansion coefficients for the phase function in the solar wavelengths. (The units for D_e are in μm .)

Band i	l	$c_{0,l}$	$c_{1,l}$	$c_{2,l}$	$c_{3,l}$
1	1	$.22110 \times 10^1$	$-.10398 \times 10^{-2}$	$.65199 \times 10^{-4}$	$-.34498 \times 10^{-6}$
	2	$.32201 \times 10^1$	$.94227 \times 10^{-3}$	$.80947 \times 10^{-4}$	$-.47428 \times 10^{-6}$
	3	$.41610 \times 10^1$	$.74396 \times 10^{-3}$	$.82690 \times 10^{-4}$	$-.45251 \times 10^{-6}$
	4	$.51379 \times 10^1$	$.51545 \times 10^{-2}$	$.11881 \times 10^{-4}$	$-.15556 \times 10^{-6}$
2	1	$.22151 \times 10^1$	$-.77982 \times 10^{-3}$	$.63750 \times 10^{-4}$	$-.34466 \times 10^{-6}$
	2	$.31727 \times 10^1$	$.15597 \times 10^{-2}$	$.82021 \times 10^{-4}$	$-.49665 \times 10^{-6}$
	3	$.40672 \times 10^1$	$.25800 \times 10^{-2}$	$.71550 \times 10^{-4}$	$-.43051 \times 10^{-6}$
	4	$.49882 \times 10^1$	$.86489 \times 10^{-2}$	$-.18318 \times 10^{-4}$	$-.59275 \times 10^{-7}$
3	1	$.22376 \times 10^1$	$.10293 \times 10^{-2}$	$.50842 \times 10^{-4}$	$-.30135 \times 10^{-6}$
	2	$.31549 \times 10^1$	$.47115 \times 10^{-2}$	$.70684 \times 10^{-4}$	$-.47622 \times 10^{-6}$
	3	$.39917 \times 10^1$	$.82830 \times 10^{-2}$	$.53927 \times 10^{-4}$	$-.41778 \times 10^{-6}$
	4	$.48496 \times 10^1$	$.15998 \times 10^{-1}$	$-.39320 \times 10^{-4}$	$-.43862 \times 10^{-7}$
4	1	$.23012 \times 10^1$	$.33854 \times 10^{-2}$	$.23528 \times 10^{-4}$	$-.20068 \times 10^{-6}$
	2	$.31730 \times 10^1$	$.93439 \times 10^{-2}$	$.36367 \times 10^{-4}$	$-.38390 \times 10^{-6}$
	3	$.39298 \times 10^1$	$.16424 \times 10^{-1}$	$.10502 \times 10^{-4}$	$-.35086 \times 10^{-6}$
	4	$.47226 \times 10^1$	$.25872 \times 10^{-1}$	$-.77542 \times 10^{-4}$	$-.21999 \times 10^{-7}$
5	1	$.27975 \times 10^1$	$.29741 \times 10^{-2}$	$-.32344 \times 10^{-4}$	$.11636 \times 10^{-6}$
	2	$.43532 \times 10^1$	$.11234 \times 10^{-1}$	$-.12081 \times 10^{-3}$	$.43435 \times 10^{-6}$
	3	$.56835 \times 10^1$	$.24681 \times 10^{-1}$	$-.26480 \times 10^{-3}$	$.95314 \times 10^{-6}$
	4	$.68271 \times 10^1$	$.42788 \times 10^{-1}$	$-.45615 \times 10^{-3}$	$.16368 \times 10^{-5}$
6	1	$.19655 \times 10^1$	$.20094 \times 10^{-1}$	$-.17067 \times 10^{-3}$	$.50806 \times 10^{-6}$
	2	$.28803 \times 10^1$	$.36091 \times 10^{-1}$	$-.28365 \times 10^{-3}$	$.79656 \times 10^{-6}$
	3	$.34613 \times 10^1$	$.58525 \times 10^{-1}$	$-.46455 \times 10^{-3}$	$.13444 \times 10^{-5}$
	4	$.39568 \times 10^1$	$.81480 \times 10^{-1}$	$-.64777 \times 10^{-3}$	$.19022 \times 10^{-5}$
		d_0	d_1	d_2	d_3
1		.12495	$-.43582 \times 10^{-3}$	$.14092 \times 10^{-4}$	$-.69565 \times 10^{-7}$
2		.12363	$-.44419 \times 10^{-3}$	$.14038 \times 10^{-4}$	$-.68851 \times 10^{-7}$
3		.12117	$-.48474 \times 10^{-3}$	$.12495 \times 10^{-4}$	$-.62411 \times 10^{-7}$
4		.11581	$-.55031 \times 10^{-3}$	$.98776 \times 10^{-5}$	$-.50193 \times 10^{-7}$
5		$-.15968 \times 10^{-3}$	$.10115 \times 10^{-6}$	$-.12472 \times 10^{-4}$	$.48667 \times 10^{-9}$
6		.13830	$-.18921 \times 10^{-2}$	$.12030 \times 10^{-4}$	$-.31698 \times 10^{-7}$

TABLE 5b. Values of empirical coefficients in Eq. (2.15) for parameterization of the asymmetry factor in the infrared wavelengths. (The units for D_e are in μm .)

Band i	c_0	c_1	c_2	c_3
7	.79550	2.524×10^{-3}	-1.022×10^{-3}	0.0
8	.86010	1.599×10^{-3}	-6.465×10^{-6}	0.0
9	.89150	1.060×10^{-3}	-4.171×10^{-6}	0.0
10	.87650	1.198×10^{-3}	-4.485×10^{-6}	0.0
11	.88150	9.858×10^{-4}	-3.116×10^{-6}	0.0
12	.91670	5.499×10^{-4}	-1.507×10^{-6}	0.0
13	.90920	9.295×10^{-4}	-3.877×10^{-6}	0.0
14	.84540	1.429×10^{-3}	-5.859×10^{-6}	0.0
15	.76780	2.571×10^{-3}	-1.041×10^{-5}	0.0
16	.72900	2.132×10^{-3}	-5.584×10^{-6}	0.0
17	.70240	4.581×10^{-3}	-3.054×10^{-5}	6.684×10^{-8}
18	.22920	1.724×10^{-2}	-1.573×10^{-4}	4.995×10^{-7}

tion in optical depth has an accuracy similar to the linear approximation for the Planck function developed by Wiscombe (1976). Since the direct solar radiation source has an exponential function form in terms of optical depth, the formulation of the δ -four-stream approximation for infrared wavelengths is the same as that for solar wavelengths. For this reason, the computer program is simplified and the computational speed is enhanced.

In the limit of pure molecular absorption at infrared wavelengths, τ_1 may approach zero for some bands. The major advantage of using Eq. (3.1) is that the solution of the transfer equation is numerically stable when $\tau_1 \rightarrow 0$. If the linear approximation in τ is used, the roundoff error may lead to an unstable solution when τ_1 is very small. We note that the higher-order polynomial approximation in τ for the Planck function can also lead to an unstable solution. As in the case of solar wavelengths, we perform relative accuracy checks for infrared wavelengths with respect to "exact" results computed from the adding method for radiative transfer (Liou 1992). Numerical results reveal that the errors in the δ -four-stream scheme in computing IR cloud emissivity are typically less than 1%. Systematic equations for this scheme that are required in numerical calculations are given in the Appendix.

For applications of the δ -four-stream scheme to nonhomogeneous atmospheres, the atmosphere is divided into N homogeneous layers with respect to the single-scattering albedo and phase function. The $4 \times N$ unknown coefficients in the analytic solution for the transfer equation are determined following the procedure described in Liou (1975). A numerically stable program has been developed to solve the system of linear equations by utilizing the property that the coefficient matrix is a sparse matrix. While this method is similar to the Gaussian elimination method with back substitution, it is carefully optimized so as to minimize the mathematical operations. We perform partial pivoting (interchanging rows only) to guarantee that a

solution always exists. In order to avoid a fatal overflow problem, we follow the scaling technique developed by Stamnes and Conklin (1984) so that numerical solutions can be carried out for large optical depths. Numerical problems that may occur when the single-scattering albedo $\tilde{\omega} = 0$ or 1 are also resolved in the present

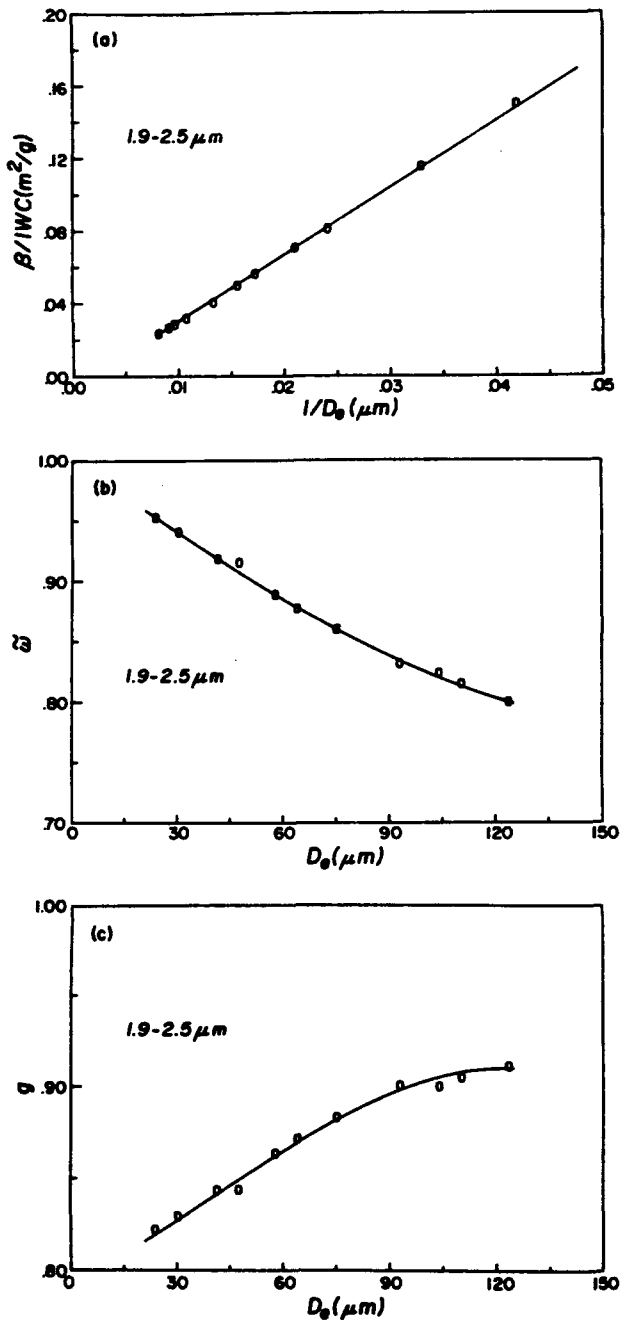


FIG. 1. (a) Extinction coefficient/IWC, (b) single-scattering albedo, and (c) asymmetry factor as functions of the mean effective size for the spectral interval 1.9–2.5 μm . The "O" points represent exact results from the light scattering program, and the curves are from the parameterizations.

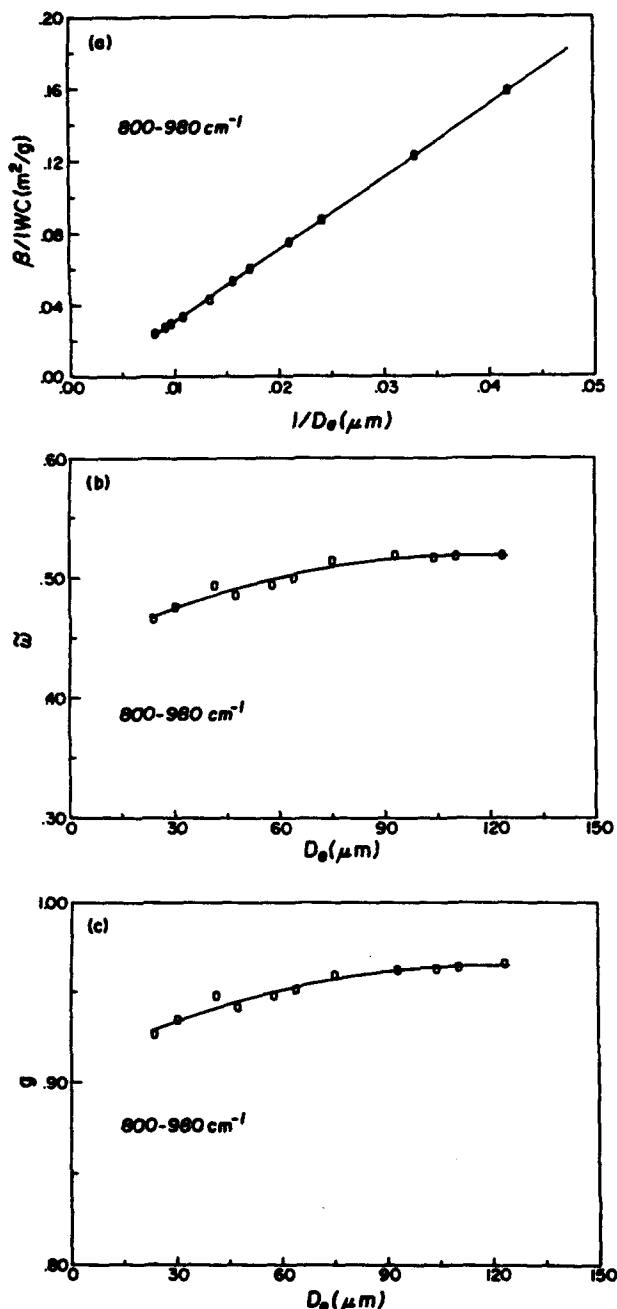


FIG. 2. Same as in Fig. 1 except for the spectral interval 800-980 cm^{-1} .

program. Using results from the adding method as a reference, errors in the δ -four-stream scheme for the nonhomogeneous multilayer cases remain within $\sim 5\%$. Transfer of infrared radiation has not been treated satisfactorily by the two-stream techniques, because they do not produce reliable results in the limit of no scattering. This problem is circumvented in the present algorithm by using the "double Gauss" quad-

rate (Sykes 1951), which produces a correct relation between the flux and intensity from an isotropic source.

Using the δ -four-stream scheme along with the parameterized single-scattering properties reported in section 2, we calculate the solar reflectance and transmittance properties for typical ice clouds with different thicknesses and solar zenith angles. These properties are defined by $r = \sum_i r_i w_i$ and $t = \sum_i t_i w_i$ where r_i and t_i denote the reflectance and transmittance (direct plus diffuse) for an individual band, and w_i is the fraction of solar flux in the band. The relative errors are examined with respect to the "exact" results computed from the adding method using the "exact" phase function. Using Ci (1 November) as an example, Figs. 3a and 3b show the "exact" reflectance and transmittance, respectively, and Figs. 3c and 3d show the corresponding percentage errors in the δ -four-stream scheme for reflectance and transmittance. The δ -four-stream results in most cases achieve relative accuracies within $\sim 5\%$. The errors shown in Figs. 3c and 3d contain not only errors due to the δ -four-stream approximation, but also errors produced by the parameterized single-scattering properties for ice clouds. Generally, errors produced by the latter effect are much smaller ($< 1\%$).

b. Parameterizations of nongray gaseous absorption

In each band shown in Table 2, the scattering properties, solar irradiance, and Planck functions may be treated as constant. In the solar spectrum, absorption due to H_2O (2500-14 500 cm^{-1}), O_3 (in the ultraviolet and visible), CO_2 (2850-5250 cm^{-1}), and O_2 (A , B , and γ bands) is accounted for in the parameterization. In the infrared spectrum, we include the major absorption bands of H_2O (0-2200 cm^{-1}), CO_2 (540-800 cm^{-1}), O_3 (980-1100 cm^{-1}), CH_4 (1100-1400 cm^{-1}), and N_2O (1100-1400 cm^{-1}). The continuum absorption of H_2O is incorporated in the spectral region 280-1250 cm^{-1} .

Nongray gaseous absorption is incorporated into the δ -four-stream scheme based on the correlated k -distribution method developed by Fu and Liou (1992). In this method, the cumulative probability, g , of the absorption coefficient, k , in a spectral interval $\Delta\nu$ is used to replace frequency, ν , as an independent variable. This leads to an immense numerical simplification, in which about 10 000 frequency intervals can be replaced by a few g intervals. With the required accuracy of $\sim 1\%$, we find that the minimum number of quadrature points in the g space ranges from one to about ten for different absorbing gases in different spectral regions. In order to treat overlapping of CO_2 and H_2O absorption, the correlated k distribution has been formulated for a single gas mixture to economize the computational time. Using a minimum number of g intervals to represent the gaseous absorption and to treat overlap within each spectral interval, 121 spectral calculations are required for each vertical profile.

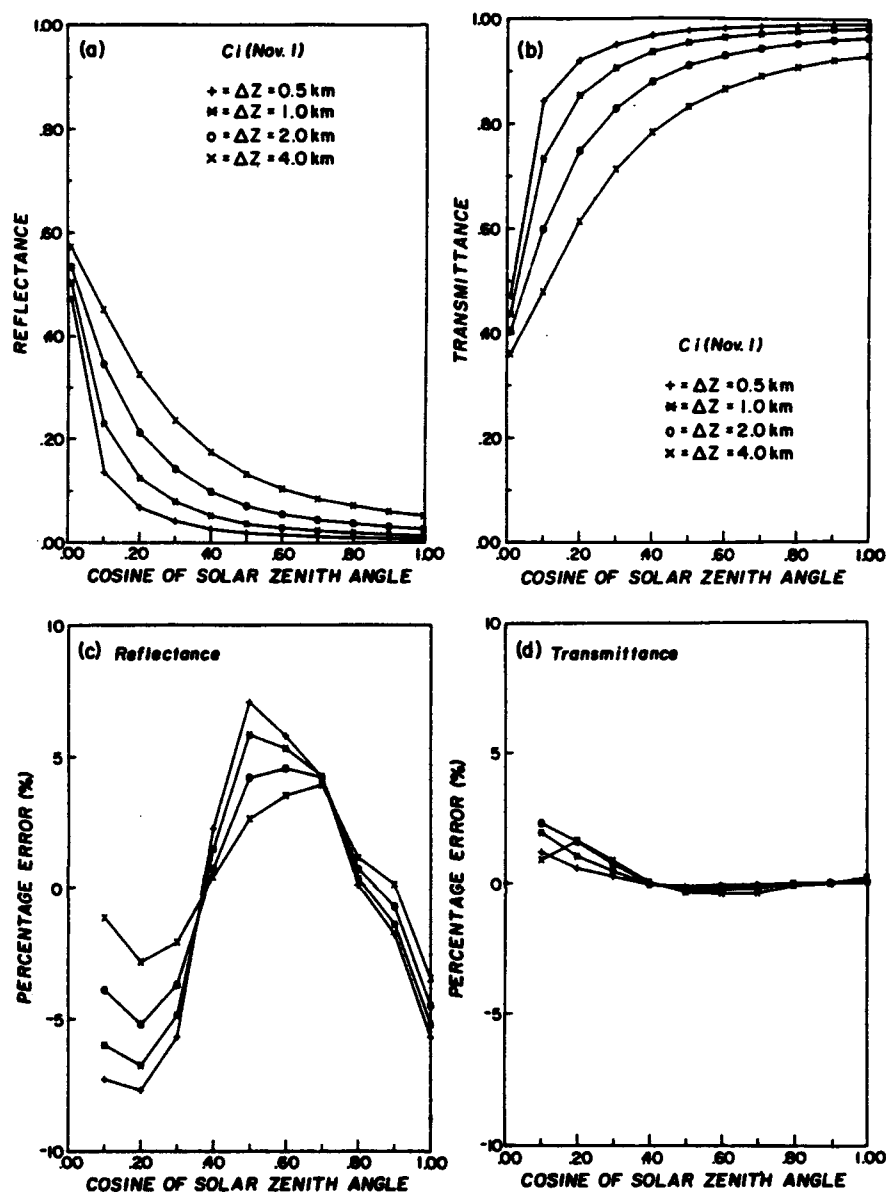


FIG. 3. (a) Solar reflectance and (b) solar transmittance calculated by the adding method using "exact" phase function for Ci (1 Nov). The corresponding percentage errors in solar reflectance and transmittance produced by the δ -four-stream scheme with parameterizations of the single-scattering properties are displayed in (c) and (d).

In the correlated k -distribution method, the vertical nonhomogeneity of the atmosphere is accounted for by assuming a simple correlation of k distribution at different temperatures and pressures. The accuracy of the δ -four-stream scheme coupled with the parameterization program for nongray gaseous absorption has been examined with respect to results computed from a line-by-line program. Shown in Fig. 4a is a comparison of IR cooling rates using the midlatitude summer profile when all the constituents are included in the calculations. A maximum heating rate difference of 0.08 K day^{-1} occurs in the troposphere. The errors in

the calculated flux are within 0.3%. Figure 4b shows a comparison of solar heating rates due to water vapor for different solar zenith angles. The errors in heating rates are less than 0.05 K day^{-1} . The errors in total atmospheric absorption and downward surface fluxes are generally less than 0.5%.

c. Molecular scattering

The average extinction coefficient due to molecular scattering for a given band may be expressed as (Slingo and Schrecker 1982)

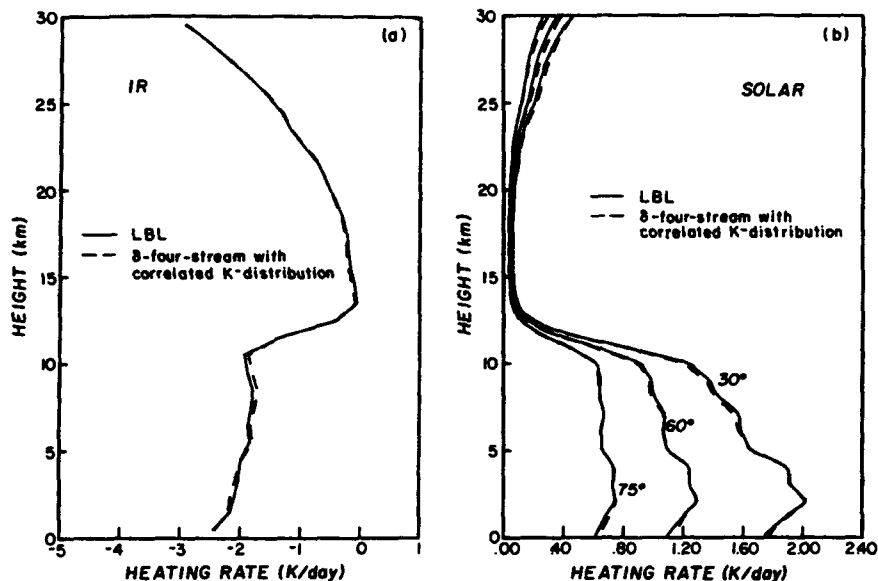


FIG. 4. Comparisons between the present model and line-by-line calculations for (a) infrared cooling rates due to H_2O (with continuum) + CO_2 + O_3 + CH_4 + N_2O in the spectral region 1–2200 cm^{-1} , and (b) solar heating rates due to H_2O in the spectral region 2500–14 500 cm^{-1} , in the midlatitude summer atmosphere.

$$\beta = Rp/T, \quad (3.2)$$

where p is pressure (mb), T is temperature (K), and β is in units of inverse meter. The coefficients R for the six bands in the solar spectrum are 9.022×10^{-6} , 5.282×10^{-7} , 5.722×10^{-8} , 1.433×10^{-8} , 4.526×10^{-9} , and 1.529×10^{-9} .

For Rayleigh scattering, the single-scattering albedo is 1. The phase function $P(\cos\theta) = \frac{3}{4}(1 + \cos^2\theta)$, so that the expansion coefficients $\tilde{\omega}_1 = 0$, $\tilde{\omega}_2 = 1/2$, and $\tilde{\omega}_l = 0$, where $l \geq 3$.

d. Single-scattering properties for combined cloud particles and gases

Consider a nonhomogeneous atmosphere that is divided into N homogeneous layers. For the case when both Rayleigh scattering and extinction by cloud particles are mixed with gaseous absorption, the total optical depth for each layer is

$$\Delta\tau(g) = \Delta\tau^R + \Delta\tau^M + \Delta\tau^G(g), \quad (3.3)$$

where $\Delta\tau^R$ and $\Delta\tau^M$ represent the optical depth due to Rayleigh molecules and cloud particles, respectively; $\Delta\tau^G(g)$ is the optical depth contributed by the gaseous absorption for a given g (the cumulative probability), which can be expressed by

$$\Delta\tau^G(g) = k(g, p, T)\rho\Delta z, \quad (3.4)$$

where $k(g, p, T)$ is the equivalent k function (Fu and Liou 1992), ρ is the density of the absorber, and Δz is the geometric thickness of the layer. In this case, $\Delta\tau^M$

$= \Delta\tau_s^M + \Delta\tau_a^M$, where $\Delta\tau_s^M$ and $\Delta\tau_a^M$ are cloud scattering and absorption optical depths, respectively. Thus, the combined single-scattering albedo and the expansion coefficients for the phase function can be obtained by

$$\tilde{\omega}(g) = \frac{\Delta\tau^R + \Delta\tau_s^M}{\Delta\tau^R + \Delta\tau^M + \Delta\tau^G(g)}, \quad (3.5)$$

$$\tilde{\omega}_l = \frac{\Delta\tau_s^M \tilde{\omega}_l^M + \Delta\tau^R \tilde{\omega}_l^R}{\Delta\tau_s^M + \Delta\tau^R}, \quad (3.6)$$

where $\tilde{\omega}_l^M$ and $\tilde{\omega}_l^R$ denote the expansion coefficients for the phase function for cloud particles and Rayleigh molecules, respectively. Since the phase function is independent of gaseous absorption, the combined $\tilde{\omega}_l$ is constant over a given spectral absorption band. Once the single-scattering properties have been defined for a given g for each level, monochromatic radiative transfer calculations may be carried out, and the total flux over each spectral band can be obtained by integrating the flux solution in the g space. As described in section 3b, a number of intervals are used for the quadrature, which are sufficient to confine the integration errors within 1%.

4. Comparisons with observations

Recently, the cirrus intensive field observation (IFO) was conducted in Wisconsin from 13 October to 2 November 1986 as a major component of the First ISCCP Regional Experiment (FIRE) to improve our understanding of cirrus clouds and their influence on weather

and climate processes (Starr 1987). In cirrus IFO, the microphysical measurements were simultaneously obtained along with radiation measurements by using high altitude research aircraft. This allows comparisons to be made between model calculations and in situ observations. In this section we present comparisons of model-derived infrared emissivity and solar albedo with those obtained from the National Center for Atmospheric Research (NCAR) Sabreliner on 28 October 1986.

The Sabreliner was flown near the western shore of Lake Michigan in the vicinity of Green Bay, Wisconsin, in a thin banded cirrus layer, between 1530 and 1630 UTC (0930–1030 local time). The cloud top and base heights were about 11.1 and 8.9 km, respectively. A racetrack pattern was flown at six different levels throughout the cirrus. The mean solar zenith angle during the flight was 61.3° . Since radiative and microphysical characteristics of the cloud sampled on the south side of the racetrack (referred to as cloud 1) are different from those sampled on the north side (referred to as cloud 2), the data from each side were analyzed separately. Furthermore, each side of the racetrack pattern was divided into thinner, mean, and thicker cases to minimize the sampling error. Details of the description of the observations and data analysis procedure have been given by Smith et al. (1990) and Heymsfield et al. (1990).

The effective upward emissivity ϵ^\dagger and downward emissivity ϵ^\ddagger involving a nonblack cloud may be defined as (Paltridge and Platt 1981)

$$\epsilon^\dagger = \frac{F_L^\dagger(z_i) - F_L^\dagger(z_b)}{\sigma \bar{T}^4 - F_L^\dagger(z_b)}, \quad (4.1)$$

and

$$\epsilon^\ddagger = \frac{F_L^\ddagger(z_b) - F_L^\ddagger(z_i)}{\sigma \bar{T}^4 - F_L^\ddagger(z_i)}, \quad (4.2)$$

where F_L^\dagger and F_L^\ddagger are the infrared broadband upward and downward fluxes, z_i and z_b are the cloud top and base heights, and \bar{T} is the mean cloud temperature; $\sigma \bar{T}^4$ is the flux emitted by a blackbody at \bar{T} .

The solar albedo may be defined as (Paltridge and Platt 1981)

$$\alpha = \frac{F_s^\dagger(z_i)(1 - a) - F_s^\dagger(z_b)}{F_s^\dagger(z_i) - F_s^\dagger(z_b)}, \quad (4.3)$$

where

$$a = \frac{[F_s^\dagger(z_i) - F_s^\dagger(z_i)] - [F_s^\dagger(z_b) - F_s^\dagger(z_b)]}{F_s^\dagger(z_i) + F_s^\dagger(z_b)}. \quad (4.4)$$

In these equations, F_s is the solar broadband flux.

Here ϵ^\dagger , ϵ^\ddagger , and α were derived from broadband flux observations by Stackhouse and Stephens (1991) for the 28 October 1986 FIRE case, which are shown in Figs. 5a–c as a function of the ice water path (IWP),

defined as $IWC \cdot \Delta z$. The error bars through these observation points denote the uncertainties of the observation. The theoretical results are displayed in these figures for comparisons. In the calculations, atmospheric temperature and moisture profiles were averaged over the two soundings from Green Bay at 1400 and 1730 UTC. For CO_2 , CH_4 , and N_2O , uniform mixings were assumed throughout the atmosphere with concentrations of 330, 1.6, and 0.28 ppmv, respectively. The ozone profile and the temperature and moisture profiles above sounding were assumed to be those of the *U.S. Standard Atmosphere*. The cloud was positioned between 8.9 and 11.1 km and the IWP was varied by changing the assumed IWC but keeping the cloud position fixed. Ice saturation mixing ratio was assumed in the cloud. In the computations, the mean effective sizes of 25, 50, 75, 100, and 125 μm were used, corresponding to five solid lines for ϵ^\dagger , ϵ^\ddagger , and α in Figs. 5a–c. For solar radiation, the solar zenith angle used was 61.3° and surface albedo was assumed to be 0.072 (Stackhouse and Stephens 1991). Comparing the theoretical results to observed data, we find that the mean effective sizes of these cases lie in the range of ~ 50 – $\sim 100 \mu\text{m}$ for ϵ^\dagger and ϵ^\ddagger , and ~ 50 – $\sim 75 \mu\text{m}$ for α . The mean effective size for ϵ^\dagger and ϵ^\ddagger in each case appears to be consistent in view of the observational uncertainties; however, the mean effective size associated with solar albedo is smaller than that associated with effective emissivity. This difference can be explained by the fact that solar albedo is more sensitive to the size spectra at the cloud top. Based on observations (Heymsfield et al. 1990), ice crystals progressively range from smaller sizes near the cloud top to larger sizes at the base of the cloud. For the same cloud, for example, cloud 1, Fig. 5 shows that D_e increases as IWP increases. This is expected because larger IWC is usually correlated with larger particle size. As given by Eqs. (4.1) and (4.2), the effective emissivities are defined in terms of fluxes that contain components due to scattering of cloud particles and absorption of gases, principally water vapor. For this reason, the computed effective emissivities may exceed 1 when IWP is large, and may deviate from 0 when $IWP \rightarrow 0$. Figure 5d illustrates the plot of solar albedo versus effective downward emissivity for a number of mean effective sizes. The observed data derived from the 28 October 1986 FIRE case are also displayed. In the domain of albedo–emissivity, the effect of ice crystal size distribution is fairly small. Reasonable agreements are shown between the theoretical results and observations.

We also calculate the emissivity of cloud particles alone by using the δ -four-stream scheme with the parameterized single-scattering properties described in section 2. The results are compared with those derived by Smith et al. (1990) for the 28 October 1986 FIRE case in Fig. 6, where each pair of observed points represents the emittance from the top layer of the cloud and the emittance of the entire cloud layer. Smith et

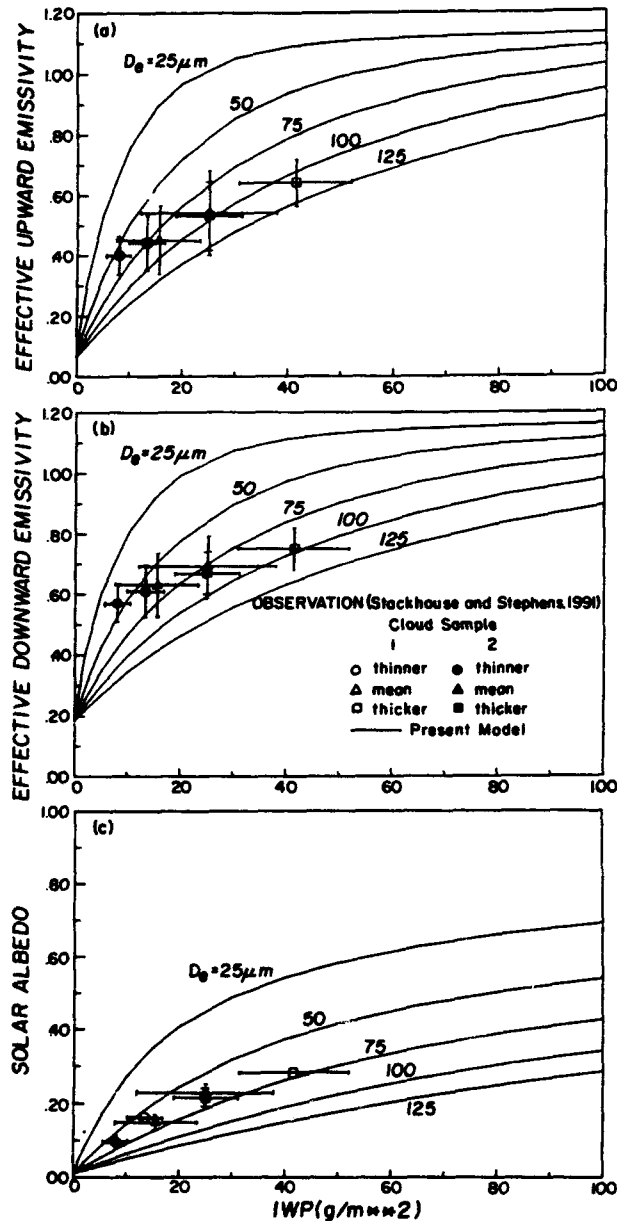


FIG. 5. (a) Effective upward emissivity, (b) effective downward emissivity, and (c) solar albedo as functions of the ice water path. Model results representing the mean effective sizes of 25, 50, 75, 100, and 125 μm are compared with the observed values obtained from the cirrus FIRE IFO.

al. utilized a broadband infrared radiative transfer model (Cox and Griffith 1979) to isolate the emissivity of ice particles by using observed downward infrared fluxes. From this comparison (Fig. 6), we find that the average D_e of the entire cloud layer is in agreement with the value derived from Fig. 5a for each case. Figure 6 also shows that the averaged mean effective size in the upper layer of the cloud is generally smaller than that of the entire cloud layer. From Fig. 6, we note

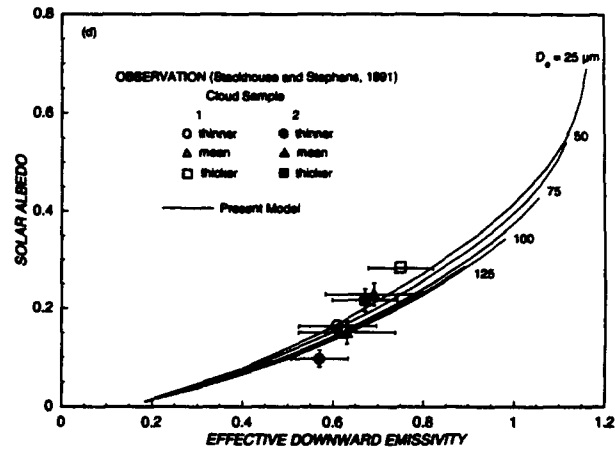


FIG. 5. (Continued) (d) Solar albedo as a function of effective downward emissivity. Model results for the mean effective sizes of 25, 50, 75, 100, and 125 μm are compared with the observed values obtained from the cirrus FIRE IFO.

that the line for the D_e of 25 μm crosses the 50- μm line. This is because a smaller D_e produces larger reflectivity, r . When the optical depth $\tau \rightarrow \infty$, the emissivity $\epsilon = 1 - r$ would be smaller.

From Figs. 5 and 6, the estimated D_e ranges from ~ 50 to ~ 100 μm . Using aspect ratios of 2 for 50 μm and 3 for 100 μm , the effective maximum dimension (L_e) would be from ~ 100 to ~ 300 μm . Wielicki et al. (1990) estimated the median mass weighted maximum dimension (L_m) from Sabreliner observations to be ~ 75 to ~ 400 μm . The averaged L_m is ~ 238 μm . The averaged L_e from the present study is ~ 200 μm . Note that L_m and L_e represent volume and area-weighted mean values. Nevertheless, the computed L_e from the model appears to compare reasonably well with observed data.

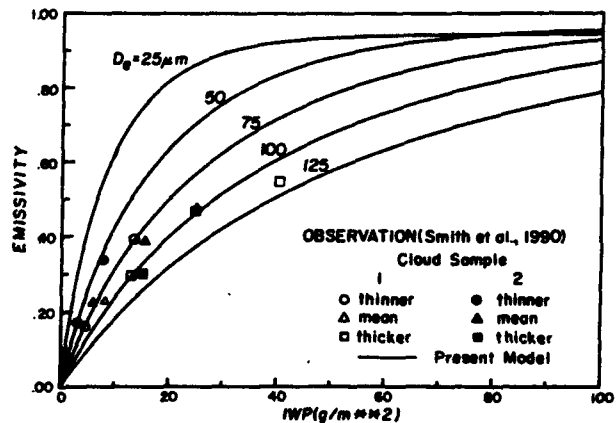


FIG. 6. The emissivity of cloud particles alone as a function of the ice water path. Model results for the mean effective sizes of 25, 50, 75, 100, and 125 μm are compared with the observed values obtained from the cirrus FIRE IFO.

In light of preceding discussion, the observed cloud emissivity and cloud albedo can be reasonably interpreted from the theoretical results, which used the scattering and absorption properties for hexagonal ice crystals (columns and plates). The actual ice crystals that were collected by the optical probe aboard the Sabreliner during the FIRE cirrus experiment were largely bullet rosettes, columns, plates, and compacted spatial particles (occasionally having extensions) (Heymsfield et al. 1990). Although the exact ice crystal shapes were not employed in the scattering and absorption calculations, the theoretical results account for the general hexagonal structure of ice particles and include accurate flux calculations. This perhaps explains some success of the present parameterization scheme in the interpretation of the observed data from aircraft. Past researchers frequently used area-equivalent spheres to interpret the observed radiative properties of cirrus (see, e.g., Stackhouse and Stephens 1991). Since equivalent spheres scatter more light in forward directions and have smaller single-scattering albedo than nonspherical ice crystals, the assumption that ice particles are spheres would lead to an underestimation of the solar albedo of cirrus clouds (Kinne and Liou 1989). Increasing the amount of small spherical ice crystals has not led to a better interpretation of the radiative properties of cirrus clouds. Finally, it should be pointed out that further verification of theoretical results would require narrowing the large experimental uncertainties that are related to radiation and microphysical measurements.

Finally, we examine the relationship for the emissivity of cirrus clouds as a function of the optical depth at $0.55 \mu\text{m}$. Using the present model, a number of emissivities were computed for the 11 observed cirrus cloud types (Table 1) with cloud thicknesses of 0.5, 1, 2, and 4 km. The results are plotted in Fig. 7 as a function of the optical depth. The solid line on the diagram is the least square curve using the function

$$\epsilon = 1 - \exp(-a\tau), \quad (4.5)$$

where τ is the visible optical depth. The fitted coefficient a is 0.79. Using a diffusivity factor of 1.66, the visible optical depth is related to the infrared optical depth (due to absorption) by a factor of 2.1. This result agrees with the observed result reported by Platt et al. (1987), who showed that the ratio of visible extinction to infrared absorption varies from ~ 1.8 to 2.3 for the midlatitude cirrus clouds. Note that the 11 size distributions used in the present study cover a spectrum of ice crystal size spectra that occur in midlatitude cirrus clouds.

5. The radiative effects of ice crystal size distributions

The importance of cirrus clouds on the radiative budget of the earth and the atmosphere has been documented by Liou (1986). Ackerman et al. (1988) have

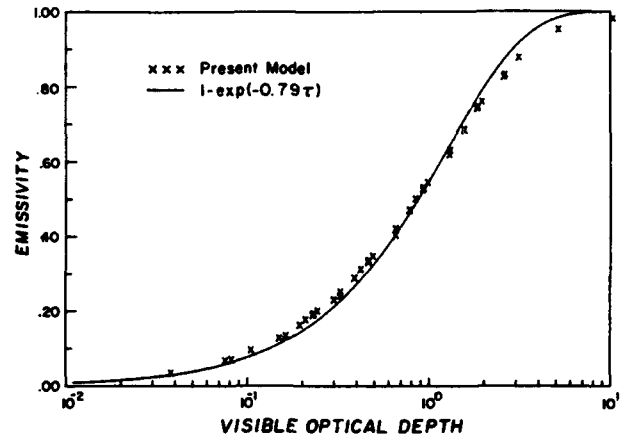


FIG. 7. The emissivity of cirrus clouds as a function of the visible optical depth. The "x" points are obtained from the present model for the 11 cloud types (Table 1) with thicknesses of 0.5, 1, 2, and 4 km. The solid line is from least-square fits.

further carried out an investigation regarding the interaction of infrared and solar radiation with tropical cirrus anvils. They find that the radiative effects of cirrus clouds are very sensitive to the assumed ice water content, the cloud thickness, and the environmental conditions in which the clouds form. Their study, however, was confined to cirrus clouds with a fixed size distribution. In this study, we examine the effects of ice crystal size distributions on the radiative heating and budget using the radiative transfer model developed in the preceding sections. In the present calculations, standard atmospheric temperature, water vapor, and ozone profiles are used. The cirrus cloud layer is inserted in the atmosphere between 9 and 11 km. For water vapor within the cloud layer, the ice saturation mixing ratio is assumed. To compute solar fluxes, a solar constant of 1365 W m^{-2} , a surface albedo of 0.1, a solar zenith angle of 60° , and a 12-h solar day are used. The computations are carried out by using the mean effective sizes, D_e , of 25, 50, 75, 100, and $125 \mu\text{m}$, which cover the range of D_e from observations.

a. Heating rate

The effects of the ice crystal mean effective size on IR, solar, and net (IR + solar) radiative heating rates in the cloud are illustrated in Figs. 8a, 8b, and 8c, respectively. The IWP used is 30 g m^{-2} , which corresponds to an IWC of 0.015 g m^{-3} . In the calculations, the vertical layer thickness is set to be 250 m and the heating rates are layer averages. For the smallest D_e ($25 \mu\text{m}$), IR heating/cooling rates of about 30 K day^{-1} take place close to the bottom and top of the cloud layer. Such large differential heating rates between cloud bottom and top ($\sim 60 \text{ K day}^{-1}$) would have a significant effect on both the entrainment and cloud microphysics (Ackerman et al. 1988). For the largest

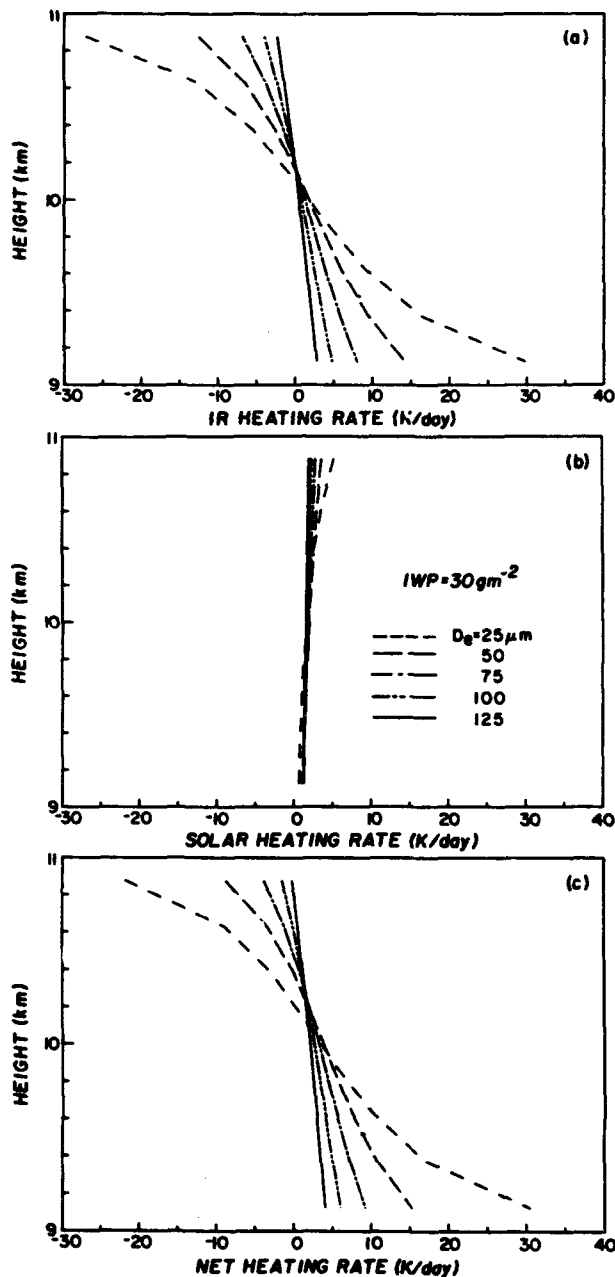


FIG. 8. Heating rates in a cirrus cloud with an ice water content of 0.015 g m^{-3} for five mean effective sizes of 25 (short dash), 50 (long dash), 75 (short-long dash), 100 (double short-long dash), and $125 \mu\text{m}$ (solid). (a) Infrared, (b) solar, and (c) net. For solar radiation, the solar zenith angle is 60° , the surface albedo is 0.1, and a 12-h solar day is used.

D_e of $125 \mu\text{m}$, the IR heating/cooling rates at the cloud bottom and top reduce by as much as a factor of 10. A cloud consisting of smaller D_e emits more IR radiation at the cloud top, resulting in strong cooling. The cloud absorbs, at the same time, more IR radiation emitted from the warmer surface and atmosphere below, resulting in strong heating at the cloud-base region.

If IWC is fixed, a cloud containing smaller D_e would have larger emittance/absorptance because of larger cross-sectional area. The solar heating rate peaks at the cloud top and reaches a value of $\sim 5 \text{ K day}^{-1}$ for D_e of $25 \mu\text{m}$. The net heating rates due to both IR and solar radiation in the cloud are shown in Fig. 8c. It is evident that the cloud heating rate field is largely controlled by IR radiation and that smaller D_e can produce larger radiative heating gradients.

For a given ice crystal size distribution, larger IWC generates a stronger radiative heating gradient, as demonstrated by Ackerman et al. (1988). Based on the preceding discussion on the relation of D_e and heating rates, changes in the heating gradient due to the effects of D_e and IWC are thus in opposite directions. According to observations (e.g., Heymsfield et al. 1990), IWC usually (if not always) increases with increasing ice crystal size. Therefore, the effects of IWC and D_e on heating rates may partially be compensated for if both parameters are interactively included in the calculation.

b. Cloud forcing

The ice crystal size distribution of cirrus clouds has a significant effect on the radiation budget of the earth and the atmosphere. To quantify this effect, we use the cloud radiative forcing concept (e.g., Hartmann et al. 1986) for the flux at the top of the atmosphere (TOA) and define the following:

$$C_{ir,s} = F_{ir,s}^{cl} - F_{ir,s}^{ov},$$

where cl and ov denote clear and overcast conditions, and F_{ir} and F_s are the upward IR and solar fluxes, respectively. The net cloud radiative forcing is

$$C = C_{ir} + C_s.$$

For partly cloudy conditions, if the cloud cover is denoted as η , the cloud radiative forcing is given by ηC .

Figures 9a–c show the results of C_{ir} , C_s , and C as a function of IWP for different mean effective sizes. The IR cloud forcing C_{ir} (Fig. 9a) is always positive, corresponding to the heating of the earth–atmosphere system due to the greenhouse effect of clouds, while the solar cloud forcing C_s (Fig. 9b) is always negative, showing the cooling of the system by the cloud albedo effect. Terms C_{ir} and C_s are strongly dependent on both IWP and D_e . For an IWP of 30 g m^{-2} , C_{ir} decreases from 131 to 54 W m^{-2} as D_e increases from 25 to $125 \mu\text{m}$. The solar cloud forcing counterpart increases from -114 to -24 W m^{-2} . The net cloud forcing (Fig. 9c) shows that cirrus clouds have a net heating effect on the system except for IWP $> 50 \text{ g m}^{-2}$ in the case when $D_e = 25 \mu\text{m}$. These results are similar to those derived from a climate model presented by Stephens et al. (1990).

Usually, small D_e is associated with cold cirrus clouds that have small IWP. We may safely assume that mid-

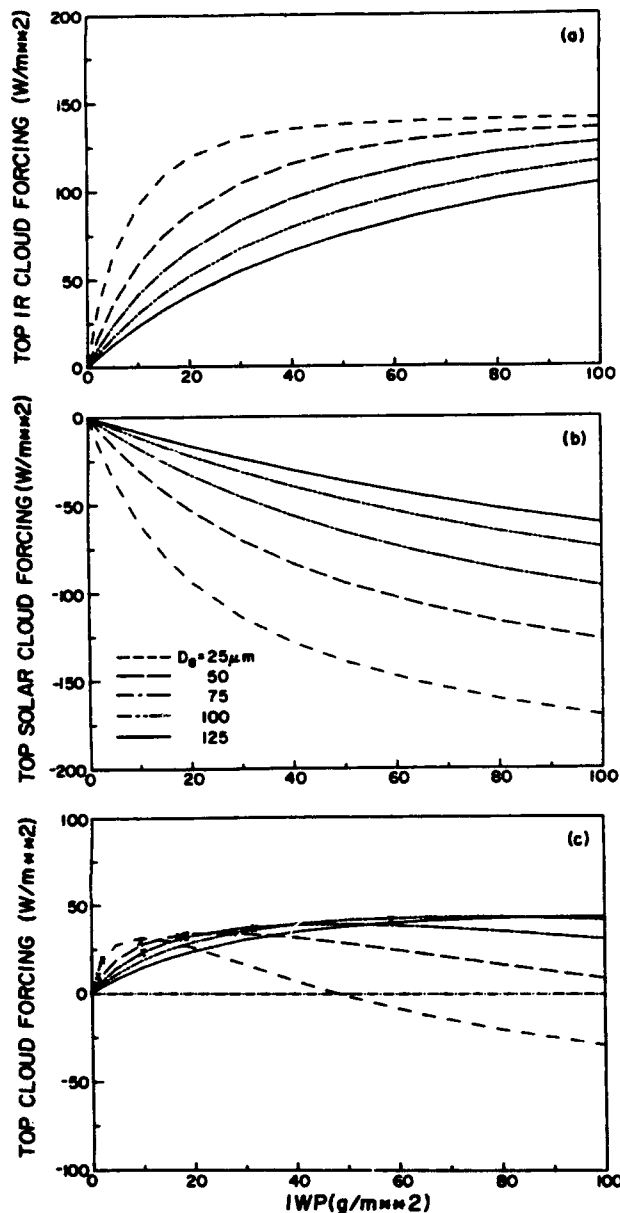


FIG. 9. Cloud radiative forcing at the top of the atmosphere as a function of the ice water path for five mean effective sizes of 25 (short dash), 50 (long dash), 75 (short-long dash), 100 (double short-long dash), and 125 μm (solid). (a) Infrared, (b) solar, and (c) net. For solar radiation, the solar zenith angle is 60° , the surface albedo is 0.1, and a 12-h solar day is used.

latitude cirrus clouds would have positive cloud forcing; that is, the greenhouse effect produced by the presence of these clouds is more pronounced than the albedo effect. The net greenhouse effect is a function of both ice crystal size and IWP. The data points depicted in Fig. 9c are computed from the ten observed ice crystal size distributions (except Ci uncinus, which has a IWP of $\sim 220 \text{ g m}^{-2}$) using a thickness of 2 km. The visible optical depths of these clouds range from about 0.15

to 1.5. Assuming a 20% cloud cover, the cloud forcing values generally range from about 4 to 8 W m^{-2} . When coupled with positive radiative forcings, such as those due to the increase of greenhouse gases, feedbacks produced by the increase or decrease of cirrus parameters could be significant.

Finally, we investigate the cloud radiative forcing at the surface. Figures 10a and 10b show the IR and solar cloud forcing, respectively. In the latter case, the negative cloud forcing values produced by cloud reflection are substantially similar to those presented in Fig. 9b. This is because the atmosphere is largely transparent with respect to solar radiation when clouds are present. For the IR case, the insertion of cirrus clouds produces small effects at the surface ($0\text{--}30 \text{ W m}^{-2}$), because of the strong absorption of the atmosphere between the surface and the cloud in the infrared wavelengths. The cirrus cloud-induced IR heating within the atmosphere and solar cooling at the surface could have a significant impact on the atmospheric circulations and temperature distributions (Ramanathan 1987; Slingo and Slingo 1988).

6. Summary and conclusions

In this paper, a new approach has been devised for the parameterization of radiative transfer in the at-

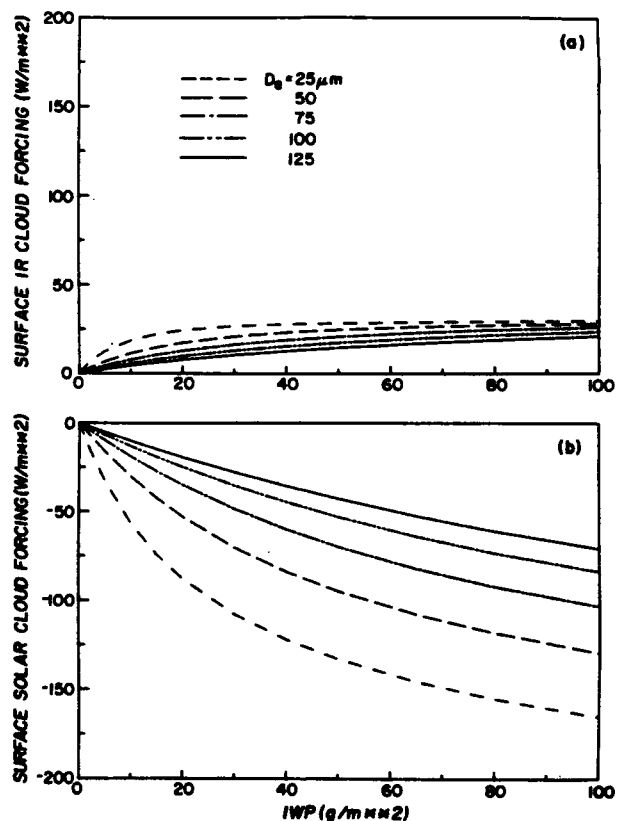


FIG. 10. Same as Fig. 9 except for the cloud radiative forcing at the surface. (a) Infrared and (b) solar.

mosphere involving cirrus clouds. We use a mean effective size, representing ice crystal size distribution, in the development of parameterization for the single-scattering properties of ice crystals. The extinction coefficient, the single-scattering albedo, and the expansion coefficients of the phase function for the 11 observed ice crystal size distributions have been computed from a geometric ray-tracing technique for hexagonal ice crystals (size parameter > 30) and Mie-type solution for spheroids (size parameter < 30). Using these results and basic physical reasonings, we develop simple polynomial relationships between the single-scattering properties and mean effective size that can achieve relative accuracies within $\sim 1\%$.

A δ -four-stream radiative transfer scheme has been developed for flux calculations in both solar and infrared spectra. With respect to the "exact" results computed from the adding method for radiative transfer, this scheme can yield relative accuracies within $\sim 5\%$ for all atmospheric conditions. For nongray gaseous absorptions due to H_2O , CO_2 , O_3 , CH_4 , and N_2O , we use the correlated k -distribution method to obtain a number of equivalent absorption coefficients. A total of 121 spectral calculations for each vertical profile in the entire spectrum is required. Compared with line-by-line calculations for clear midlatitude summer atmosphere, the δ -four-stream scheme coupled with the correlated k -distribution parameterization produces deviations less than 0.1 K day^{-1} in heating rates and within 0.5% in flux calculations. In the limit of no scattering, the δ -four-stream scheme can produce reliable results since the double Gauss quadrature provides a correct relation between the flux and intensity from an isotropic source. The computational time of the scheme is linear with respect to the number of vertical levels.

Comparisons have been carried out between theoretical calculations and aircraft measurements involving cloud emissivity and cloud albedo obtained during the cirrus FIRE IFO. The effect of ice crystal size distribution in terms of the mean effective size is important in the interpretation of the observed data. Further verification of the model results requires the reduction of large experimental uncertainties in both radiation and microphysical measurements.

We further investigate the effects of ice crystal size distributions on the radiative properties of the atmosphere involving cirrus clouds. For a given ice water path, cirrus clouds containing smaller mean effective sizes reflect more solar radiation, trap more thermal infrared, and produce strong cloud-top cooling and cloud-base heating. This pattern would enhance the in-cloud heating rate gradient, which could be significant in terms of cloud microphysical processes. For the observed midlatitude cirrus cases, the IR greenhouse effect outweighs the solar albedo effect. The degree of the greenhouse effect involving cirrus clouds is a function of cloud cover as well as the mean effective size and liquid water path. Assuming the presence within

a sky field of 20% cirrus clouds, a gain of $\sim 4\text{--}8 \text{ W m}^{-2}$ is obtained from the present calculation. With respect to the surface, the presence of cirrus clouds reduces the solar flux available to the surface. In this case, the solar albedo effect dominates the IR greenhouse effect, which is confined largely within the atmosphere.

There are a number of significant new features in the present radiative scheme. First, the ice crystal size distribution consisting of nonspherical particles is effectively accounted for in the parameterization of the single-scattering properties of cirrus clouds. This is especially important in the determination of the solar albedo of cirrus clouds. Second, the IR and solar radiation regions have been treated in a self-consistent fashion using the same parameterization scheme, which is essential to the investigation of the solar albedo versus IR greenhouse effects involving clouds. Third, the present model can efficiently compute the detailed vertical structure of the heating rate profile within clouds, which is critical to the understanding of the effects of radiation on cloud formation. The present parameterization for the radiative transfer in the atmosphere involving cirrus clouds is well suited for incorporation in numerical models to study the climatic effects of cirrus clouds, as well as to investigate interactions and feedbacks between cloud microphysics and radiation.

Acknowledgments. The research work contained herein has been supported by AFOSR Grant 91-0039, NASA Grant NAG5-1050, and NSF Grant 90-24217. We thank Dr. Y. Takano for providing the single-scattering data that are used in the parameterization.

APPENDIX

The δ -Four-Stream Approximation for a Homogeneous Layer

In the following, we present the necessary equations for the flux calculation using the δ -four-stream approximation. The notations used in Liou et al. (1988) are followed. Let the total optical depth of a layer be τ_1 . The upward and downward fluxes at a given optical depth τ ($0 \leq \tau \leq \tau_1$) are given by

$$F^+(\tau) = 2\pi(a_1\mu_1I_1 + a_2\mu_2I_2), \quad (\text{A.1})$$

$$F^-(\tau) = 2\pi(a_1\mu_1I_{-1} + a_2\mu_2I_{-2}) + \mu_0\pi F_\odot e^{-\tau/\mu_0}, \quad (\text{A.2})$$

where the double Gauss quadratures and weights in the four-stream approximation are $\mu_1 = -\mu_{-1} = 0.2113248$, $\mu_2 = -\mu_{-2} = 0.7886752$, and $a_1 = a_{-1} = a_2 = a_{-2} = 0.5$; μ_0 is the cosine of the solar zenith angle; and πF_\odot denotes the direct solar flux at the top of the atmosphere ($\pi F_\odot = 0$ in the thermal infrared). The intensity solutions can be written in the form

$$\begin{bmatrix} I_2 \\ I_1 \\ I_{-1} \\ I_{-2} \end{bmatrix} = \begin{bmatrix} \phi_2^+ e_2 & \phi_1^+ e_1 & \phi_1^- e_3 & \phi_2^- e_4 \\ \Phi_2^+ e_2 & \Phi_1^+ e_1 & \Phi_1^- e_3 & \Phi_2^- e_4 \\ \bar{\phi}_2^- e_2 & \bar{\phi}_1^- e_1 & \bar{\phi}_1^+ e_3 & \bar{\phi}_2^+ e_4 \\ \bar{\Phi}_2^- e_2 & \bar{\Phi}_1^- e_1 & \bar{\Phi}_1^+ e_3 & \bar{\Phi}_2^+ e_4 \end{bmatrix} \begin{bmatrix} G_2 \\ G_1 \\ G_{-1} \\ G_{-2} \end{bmatrix} + \begin{bmatrix} z_2^+ \\ z_1^+ \\ z_1^- \\ z_2^- \end{bmatrix} e^{-k\tau}, \quad (\text{A.3})$$

where $f_0(\text{solar}) = 1/\mu_0$, $f_0(\text{thermal}) = -1/\tau_1 \ln(B_1/B_0)$, B_0 and B_1 are Planck functions evaluated at the top and bottom of the layer, respectively, and the other terms except $G_{\pm 1,2}$ are defined as follows:

$$e_1 = e^{-k_1\tau}, \quad e_2 = e^{-k_2\tau}, \\ e_3 = e^{-k_1(\tau_1-\tau)}, \quad e_4 = e^{-k_2(\tau_1-\tau)},$$

$$z_{\pm 1,2} = \frac{1}{2}(\eta_{1,2} \pm \eta'_{1,2}),$$

$$\phi_{\pm 1,2}^{\pm} = \frac{1}{2} \left(1 \pm \frac{b_{11}^- - A_{1,2} b_{21}^-}{a^-} k_{1,2} \right),$$

$$\Phi_{\pm 1,2}^{\pm} = \frac{1}{2} \left(A_{1,2} \pm \frac{A_{1,2} b_{22}^- - b_{12}^-}{a^-} k_{1,2} \right),$$

where $k_{1,2}$, $A_{1,2}$, $\eta_{1,2}$, $\eta'_{1,2}$, b_{11}^- , b_{21}^- , b_{22}^- , b_{12}^- , and a^- are calculated from the following equations, which are in the order of calculation. The single-scattering albedo is denoted by $\tilde{\omega}$, and $\tilde{\omega}_l$ ($l = 0, 1, 2, 3$) is the expansion coefficient of phase function ($\tilde{\omega}_0 = 1$):

$$b_i(\text{solar}) = \frac{\tilde{\omega}}{4\pi} \pi F_0 \sum_{l=0}^3 \tilde{\omega}_l P_l(\mu_i) P_l(-\mu_0) / \mu_i$$

$$b_i(\text{thermal}) = (1 - \tilde{\omega}) B_0 / \mu_i, \quad i = -2, -1, 1, 2,$$

$$c_{ij} = \frac{\tilde{\omega}}{2} a_j \sum_{l=0}^3 \tilde{\omega}_l P_l(\mu_i) P_l(\mu_j), \quad i, j = -2, -1, 1, 2$$

$$b_{ij} = \begin{cases} c_{ij} / \mu_i, & i \neq j \\ (c_{ij} - 1) / \mu_i, & i = j, \end{cases}$$

$$b_{22}^{\pm} = b_{2,2} \pm b_{2,-2}, \quad b_{21}^{\pm} = b_{2,1} \pm b_{2,-1}$$

$$b_{12}^{\pm} = b_{1,2} \pm b_{1,-2}, \quad b_{11}^{\pm} = b_{1,1} \pm b_{1,-1}$$

$$b_2^{\pm} = b_2 \pm b_{-2}, \quad b_1^{\pm} = b_1 \pm b_{-1},$$

$$a_{22} = b_{22}^+ b_{22}^- + b_{12}^+ b_{21}^-, \quad a_{21} = b_{22}^- b_{21}^+ + b_{21}^- b_{11}^+$$

$$a_{12} = b_{12}^- b_{22}^+ + b_{11}^- b_{12}^+, \quad a_{11} = b_{12}^+ b_{21}^- + b_{11}^+ b_{11}^-$$

$$d_2 = b_{22}^- b_2^- + b_{21}^- b_1^- + b_2^+ f_0$$

$$d_1 = b_{12}^- b_2^- + b_{11}^- b_1^- + b_1^+ f_0,$$

$$a'_{22} = b_{22}^- b_{22}^+ + b_{12}^- b_{21}^+, \quad a'_{21} = b_{22}^+ b_{21}^- + b_{21}^+ b_{11}^-$$

$$a'_{12} = b_{12}^+ b_{22}^- + b_{11}^+ b_{12}^-, \quad a'_{11} = b_{12}^- b_{21}^+ + b_{11}^- b_{11}^+$$

$$d'_2 = b_{22}^+ b_2^+ + b_{21}^+ b_1^+ + b_2^- f_0$$

$$d'_1 = b_{12}^+ b_2^+ + b_{11}^+ b_1^+ + b_1^- f_0,$$

$$b = a_{22} + a_{11}, \quad c = a_{21} a_{12} - a_{11} a_{22}$$

$$a^- = b_{22}^- b_{11}^- - b_{12}^- b_{21}^-,$$

$$k_1 = [(b + \sqrt{b^2 + 4c})/2]^{1/2}$$

$$k_2 = [(b - \sqrt{b^2 + 4c})/2]^{1/2},$$

$$A_{1,2} = (k_{1,2}^2 - a_{22})/a_{21},$$

$$\eta_1 = (d_1 f_0^2 + a_{12} d_2 - a_{22} d_1) / f'$$

$$\eta_2 = (d_2 f_0^2 + a_{21} d_1 - a_{11} d_2) / f'$$

$$\eta'_1 = (d'_1 f_0^2 + a'_{12} d'_2 - a'_{22} d'_1) / f'$$

$$\eta'_2 = (d'_2 f_0^2 + a'_{21} d'_1 - a'_{11} d'_2) / f'$$

$$f' = f_0^4 - b f_0^2 - c.$$

The coefficients G_i ($i = \pm 1, 2$) are to be determined from radiation boundary conditions. Consider a homogeneous cloud layer characterized by an optical depth τ_1 and assume that there is no diffuse radiation from the top and bottom of this layer; then the boundary conditions are

$$\left. \begin{aligned} I_{-1,-2}(\tau = 0) &= 0 \\ I_{1,2}(\tau = \tau_1) &= 0 \end{aligned} \right\}. \quad (\text{A.4})$$

The boundary conditions can be modified to include the nonzero diffuse radiation; G_i can be obtained by an inversion of a four-by-four matrix in Eq. (A.3). We note that the only difference in the four-stream formulation between infrared and solar wavelengths is the definition of f_0 and b_i ($i = \pm 1, 2$).

It is possible to incorporate a δ -function adjustment to account for the forward diffraction peak in the context of the four-stream approximation. We may use the similarity principle for radiative transfer to adjust the optical depth, single-scattering albedo, and expansion coefficients of the phase function in the forms (Liou et al. 1988)

$$\tau' = \tau(1 - f\tilde{\omega})$$

$$\tilde{\omega}' = (1 - f)\tilde{\omega} / (1 - f\tilde{\omega})$$

$$\tilde{\omega}'_l = [\tilde{\omega}_l - f(2l + 1)] / (1 - f), \quad l = 1, 2, 3, \quad (\text{A.5})$$

where the fraction of scattered energy residing in the forward peak, $f = \tilde{\omega}_4/9$.

REFERENCES

- Ackerman, T. P., K.-N. Liou, F. P. J. Valero, and L. Pfister, 1988: Heating rates in tropical anvils. *J. Atmos. Sci.*, **45**, 1606-1623.
 Asano, S., and M. Sato, 1980: Light scattering by randomly oriented spheroidal particles. *Appl. Opt.*, **19**, 962-974.
 Auer, A. H., Jr., and D. L. Veal, 1970: The dimension of ice crystals in natural clouds. *J. Atmos. Sci.*, **27**, 919-926.

- Cox, S. K., and K. T. Griffith, 1979: Estimates of radiative divergence during phase III of the GARP Atlantic tropical experiment. Part I: Methodology. *J. Atmos. Sci.*, **36**, 576-585.
- Foot, J. S., 1988: Some observations of the optical properties of clouds. II: Cirrus. *Quart. J. Roy. Meteor. Soc.*, **114**, 145-164.
- Fu, Q., and K. N. Liou, 1992: On the correlated k -distribution method for radiative transfer in nonhomogeneous atmospheres. *J. Atmos. Sci.*, **49**, 2139-2156.
- Hansen, J. E., and L. D. Travis, 1974: Light scattering in planetary atmospheres. *Space Sci. Rev.*, **16**, 527-610.
- Hartmann, D. L., V. Ramanathan, A. Berroir, and G. E. Hunt, 1986: Earth radiation budget data and climate research. *Rev. Geophys.*, **24**, 439-468.
- Heymsfield, A. J., 1975: Cirrus uncinus generating cells and the evolution of cirriform clouds. *J. Atmos. Sci.*, **32**, 799-808.
- , and C. M. R. Platt, 1984: A parameterization of the particle size spectrum of ice clouds in terms of the ambient temperature and the ice water content. *J. Atmos. Sci.*, **41**, 846-855.
- , K. M. Miller, and J. D. Spinhirne, 1990: The 27-28 October 1986 FIRE IFO cirrus case study: Cloud microstructure. *Mon. Wea. Rev.*, **118**, 2313-2328.
- Kinne, S., and K. N. Liou, 1989: The effects of the nonsphericity and size distribution of ice crystals on the radiative properties of cirrus clouds. *Atmos. Res.*, **24**, 273-284.
- Liou, K. N., 1975: Applications of the discrete-ordinate method for radiative transfer to inhomogeneous aerosol atmospheres. *J. Geophys. Res.*, **80**, 3434-3440.
- , 1986: Influence of cirrus clouds on weather and climate processes: A global perspective. *Mon. Wea. Rev.*, **114**, 1167-1199.
- , 1992: *Radiation and Cloud Processes in the Atmosphere: Theory, Observation, and Modeling*. Oxford University Press, 487 pp.
- , and G. D. Wittman, 1979: Parameterization of the radiative properties of clouds. *J. Atmos. Sci.*, **36**, 1261-1273.
- , Q. Fu, and T. P. Ackerman, 1988: A simple formulation of the δ -four-stream approximation for radiative transfer parameterizations. *J. Atmos. Sci.*, **45**, 1940-1947.
- Ono, A., 1969: The shape and riming properties of ice crystals in natural clouds. *J. Atmos. Sci.*, **26**, 138-147.
- Paltridge, G. W., and C. M. R. Platt, 1981: Aircraft measurements of solar and infrared radiation and the microphysics of cirrus cloud. *Quart. J. Roy. Meteor. Soc.*, **107**, 367-380.
- Platt, C. M. R., and Harshvardhan, 1988: Temperature dependence of cirrus extinction: Implications for climate feedback. *J. Geophys. Res.*, **93**, 11 051-11 058.
- , J. C. Scott, and A. C. Dilley, 1987: Remote sounding of high clouds. Part VI: Optical properties of midlatitude and tropical cirrus. *J. Atmos. Sci.*, **44**, 729-747.
- Ramanathan, V., 1987: The role of earth radiation budget studies in climate and general circulation research. *J. Geophys. Res.*, **92**, 4075-4095.
- Slingo, A., and H. M. Schrecker, 1982: On the shortwave radiative properties of stratiform water clouds. *Quart. J. Roy. Meteor. Soc.*, **108**, 407-426.
- , and J. M. Slingo, 1988: The response of a general circulation model to cloud longwave radiative forcing. I: Introduction and initial experiments. *Quart. J. Roy. Meteor. Soc.*, **114**, 1027-1062.
- Smith, W. L., Jr., P. F. Hein, and S. K. Cox, 1990: The 27-28 October 1986 FIRE IFO cirrus case study: In situ observations of radiation and dynamic properties of a cirrus cloud layer. *Mon. Wea. Rev.*, **118**, 2389-2401.
- Stackhouse, P. W., Jr., and G. L. Stephens, 1991: A theoretical and observational study of the radiative properties of cirrus: Results from FIRE 1986. *J. Atmos. Sci.*, **48**, 2044-2059.
- Stamnes, K., and P. Conklin, 1984: A new multi-layer discrete ordinate approach to radiative transfer in vertically inhomogeneous atmospheres. *J. Quant. Spectrosc. Radiat. Transfer*, **31**, 273-282.
- Starr, D. O., 1987: A cirrus cloud experiment: Intensive field observations planned for FIRE. *Bull. Amer. Meteor. Soc.*, **68**, 119-124.
- Stephens, G. L., S. C. Tsay, P. W. Stackhouse, Jr., and P. J. Flatau, 1990: The relevance of the microphysical and radiative properties of cirrus clouds to climate and climate feedback. *J. Atmos. Sci.*, **47**, 1742-1753.
- Sykes, J. B., 1951: Approximate integration of the equation of transfer. *Mon. Not. R. Astron. Soc.*, **111**, 377-386.
- Takano, Y., and K. N. Liou, 1989: Solar radiative transfer in cirrus clouds. Part I: Single-scattering and optical properties of hexagonal ice crystals. *J. Atmos. Sci.*, **46**, 3-19.
- , —, and P. Minnis, 1992: The effects of small ice crystals on cirrus infrared radiative properties. *J. Atmos. Sci.*, **49**, 1487-1493.
- Thekaekara, M. P., 1973: Solar energy outside the earth's atmosphere. *Sol. Energy*, **14**, 109-127.
- Warren, S. G., 1984: Optical constants of ice from ultraviolet to the microwave. *Appl. Opt.*, **23**, 1206-1225.
- Wielicki, B. A., J. T. Suttles, A. J. Heymsfield, R. M. Welch, J. D. Spinhirne, M.-L. C. Wu, D. O'C. Starr, L. Parker, and R. F. Arduini, 1990: The 27-28 October 1986 FIRE IFO cirrus case study: Comparison of radiative transfer theory with observations by satellite and aircraft. *Mon. Wea. Rev.*, **118**, 2356-2376.
- Wiscombe, W. J., 1976: Extension of the doubling method to inhomogeneous sources. *J. Quant. Spectrosc. Radiat. Transfer*, **16**, 477-489.

Light scattering by nonspherical particles: Remote sensing and climatic implications

K.N. Liou and Y. Takano

Department of Meteorology/CARSS, University of Utah, Salt Lake City, UT 84112, USA

(Received December 8, 1992; revised and accepted April 20, 1993)

ABSTRACT

Calculations of the scattering and absorption properties of ice crystals and aerosols, which are usually nonspherical, require specific methodologies. There is no unique theoretical solution for the scattering by nonspherical particles. Practically, all the numerical solutions for the scattering of nonspherical particles, including the exact wave equation approach, integral equation method, and discrete-dipole approximation, are applicable only to size parameters less than about 20. Thus, these methods are useful for the study of radiation problems involving nonspherical aerosols and small ice crystals in the thermal infrared wavelengths. The geometric optics approximation has been used to evaluate the scattering, absorption and polarization properties of hexagonal ice crystals whose sizes are much larger than the incident wavelength. This approximation is generally valid for hexagonal ice crystals with size parameters larger than about 30.

From existing laboratory data and theoretical results, we illustrate that nonspherical particles absorb less and have a smaller asymmetry factor than the equal-projected area/volume spherical counterparts. In particular, we show that hexagonal ice crystals exhibit numerous halo and arc features that cannot be obtained from spherical particles; and that ice crystals scatter more light in the 60° to 140° scattering angle regions than the spherical counterparts.

Satellite remote sensing of the optical depth and height of cirrus clouds using visible and IR channels must use appropriate phase functions for ice crystals. Use of an equivalent sphere model would lead to a significant overestimation and underestimation of the cirrus optical depth and height, respectively. Interpretation of the measurements for polarization reflected from sunlight involving cirrus clouds cannot be made without an appropriate ice crystal model. Large deviations exist for the polarization patterns between spheres and hexagonal ice crystals. Interpretation of lidar backscattering and depolarization signals must also utilize the scattering characteristics of hexagonal ice crystals.

Equivalent spherical models substantially underestimate the broadband solar albedos of ice crystal clouds because of stronger forward scattering and larger absorption by spherical particles than hexagonal ice crystals. We illustrate that the net cloud radiative forcing at the top of the atmosphere involving most cirrus clouds is positive, implying that the IR greenhouse effect outweighs the solar albedo effect. If the radiative properties of equivalent spheres are used, a significant increase in cloud radiative forcing occurs. Using a one-dimensional cloud and climate model, we further demonstrate that there is sufficient model sensitivity, in terms of temperature increase, to the use of ice crystal models in radiation calculations.

RÉSUMÉ

Les calculs des propriétés de diffusion et d'absorption des cristaux de glace et des aérosols qui en règle générale ne sont pas sphériques requièrent des méthodologies spécifiques. Il n'existe pas de solution théorique unique pour la diffusion par des particules non sphériques. Pratiquement, toutes les solutions numériques pour la diffusion des particules non sphériques, parmi

lesquelles l'équation d'onde exacte, la méthode par intégration et l'approximation à des dipôles discrets, ne sont applicables qu'à des paramètres de dimension inférieurs à 20. Ces méthodes sont donc utiles pour l'étude des problèmes radiatifs relatifs aux aérosols non sphériques et aux petits cristaux de glace dans les longueurs d'onde de l'infrarouge thermique. L'approximation à l'optique géométrique a été employée pour évaluer les propriétés de diffusion, d'absorption et de polarisation des cristaux de glace hexagonaux dont les dimensions sont beaucoup plus élevées que la longueur d'onde incidente. Cette approximation est en général valable pour des cristaux hexagonaux dont les paramètres de dimension sont supérieurs à 30.

D'après des données de laboratoire et des résultats théoriques, on montre que les particules non sphériques absorbent moins et ont un plus petit facteur d'asymétrie que les particules sphériques de surface/volume projeté équivalent. On montre en particulier que les cristaux de glace hexagonaux développent de nombreux phénomènes de halo et d'arc qui ne peuvent pas être obtenus à partir de particules sphériques. On montre également que les cristaux diffusent davantage de lumière vers 60° et 140° que les particules sphériques.

Les mesures par satellite de l'épaisseur optique et de l'altitude des cirrus dans les canaux visibles et infrarouges doivent utiliser les fonctions de phase relatives aux cristaux de glace. L'utilisation d'un modèle d'équivalence à une sphère conduirait à une surestimation appréciable de l'épaisseur optique des cirrus et à une sous-estimation de leur altitude. L'interprétation des mesures de polarisation par les cirrus ne peut pas être faite sans un modèle approprié aux cristaux de glace. On trouve de fortes différences entre les modèles de polarisation par des sphères et des cristaux de glace hexagonaux. L'interprétation des signaux lidar de rétrodiffusion et de dépolarisation doit également utiliser les propriétés diffusantes des cristaux de glace hexagonaux.

Les modèles d'équivalence sphérique sous-estiment fortement les albédos solaires des nuages de glace à cause d'une diffusion avant et d'une absorption plus forte par les particules sphériques que par les cristaux de glace hexagonaux. On montre que le forçage radiatif net à la partie supérieure de l'atmosphère chargée de cirrus est positif, de sorte que l'effet infrarouge de serre dépasse l'effet d'albédo solaire. Si on utilise les propriétés radiatives des sphères équivalentes, on trouve une augmentation significative du forçage radiatif par les nuages. À l'aide d'un modèle de nuage et de climat à une dimension, on démontre en outre que la sensibilité du modèle, en terme d'augmentation de température, permet d'utiliser les modèles relatifs aux cristaux de glace dans les calculs radiatifs.

1. INTRODUCTION

The Earth's atmosphere contains various types of particulates ranging from aerosols, water droplets, and ice crystals, to raindrops and snowflakes. Typical sizes of these particulates are listed in Table 1. Scattering and absorption processes depend both on the incident wavelength and particle size, shape, and orientation. A term referred to as the size parameter, defined as the ratio of the circumference of a particle to the incident wavelength, λ , is commonly used to infer the relative importance of scattering with respect to a specific type of particle. For a spherical particle with a radius a , it is given by $2\pi a/\lambda$. For a nonspherical particle, an appropriate equivalent radius is generally used to define the size parameter.

Also listed in Table 1 are the size parameters using representative wavelengths in the visible, IR and microwave spectra. Aerosols are usually considered to be important in the solar spectrum in view of their size parameters.

TABLE 1

Sizes and size parameters for atmospheric particulates

Type	Size (a)	Size parameters ($2\pi a/\lambda$)		
		λ_v (0.5 μm)	λ_{ir} (10 μm)	λ_m (1 cm)
Aerosol (S*/NS†)	$\leq 1 \mu\text{m}$	1.26×10^1	6.3×10^{-1}	6.3×10^{-4}
Water Droplet (S)	$\sim 10 \mu\text{m}$	1.26×10^2	6.3×10^0	6.3×10^{-3}
Ice Crystal (NS)	$\sim 10^2 \mu\text{m}$	1.26×10^3	5.3×10^1	6.3×10^{-2}
Raindrop (NS)	$\sim 1 \text{ mm}$	1.26×10^4	6.3×10^2	6.3×10^{-1}
Snowflakes (Hailstone) (NS)	$\sim 1 \text{ cm}$	1.26×10^5	6.3×10^3	6.3×10^0

*Spherical; †Nonspherical.

Water droplets and ice crystals are both important in the transfer of solar radiation. Because water clouds are generally opaque in the infrared, the effects of scattering in the thermal IR wavelengths appear to be secondary. Ice clouds, however, are usually semi-transparent and because of the large size parameters for ice particles in the infrared, the scattering processes can play an important role in the transfer of thermal infrared radiation in which the ice's absorption is relatively small.

The shape of aerosols is dependent on their compositions. Solid aerosols are generally irregular. The shape of soluble aerosols (e.g. sulfuric acid) depends on the relative humidity and can be spherical. Because of their sizes, water droplets are usually spherical. Precipitation particles, however, are usually nonspherical. The shape of ice crystals that occur in the atmosphere varies greatly. Laboratory experiments show that the shape and size of an ice crystal is governed by the temperature and supersaturation. In the atmosphere, if the crystal growth involves collision and coalescence, the shapes of ice crystals can be extremely complex. Generally, ice crystals have a basic hexagonal structure. Clearly, a large portion of atmospheric suspensions are nonspherical particles. In view of the size parameters for aerosols and ice crystals and their ubiquitous nature, the scattering processes of these particles play an important role in the radiation budget of the atmosphere as well as in the remote sensing of the atmosphere and the surface.

The Mie theory provides an exact scattering solution for homogeneous isotropic, as well as for concentric nonhomogeneous spheres. However, an exact scattering theory for the solution of nonspherical particles covering all size parameters does not exist in practical terms. Various methodologies and approximations have been developed to solve the scattering and absorption problems involving specific types of nonspherical particles in a limited size parameter region. These methods are reviewed in the second section. In the third section, we present the critical differences in scattering and absorption properties between nonspherical and spherical particles. Implications of these

differences in the interpretation of satellite radiances, polarization measurements from space, and lidar backscattering data are discussed in the fourth section. The fifth section illustrates that the scattering and absorption properties of hexagonal ice crystals are important in the analysis of solar albedo and cloud radiative forcing involving cirrus clouds. Climatic temperature perturbations involving cirrus clouds using hexagonal and spherical models for ice crystals are also performed and assessed using a one-dimensional cloud and climate model. Finally, summary and conclusions are given in the last section.

A REVIEW ON THE METHODOLOGIES USED FOR DETERMINING LIGHT SCATTERING BY NONSPHERICAL PARTICLES

Exact wave equation approach

This approach begins with Maxwell's equations from which the vector equation can be derived. If an appropriate coordinate system can be defined and imposed, we may perform a separation of variables similar to the Mie theory, leading to the solution of the electric and magnetic field vectors of the incident wave in terms of a number of mathematical functions. Subsequently, the scattered electric field at larger distance from the scatterer may be evaluated. Rayleigh (1918) has derived the exact solution for the scattering of a homogeneous dielectric infinite circular cylinder for normal incidence. The case involving arbitrarily oblique incidence has been solved by Wait (1955). Subsequent numerical investigations concerning scattering by infinite circular cylinders have been carried out by van de Hulst (1957), Greenberg et al. (1967), Kerker (1969) and Liou (1972). In particular, Liou (1972) applied the cylindrical solution, for the first time, to model the scattering of light from ice clouds composed of nonspherical ice crystals.

An exact scattering solution for particles with spheroidal shapes has been derived by Asano and Yamamoto (1975). The spheroidal coordinates are obtained by rotating an ellipse about an axis of symmetry and are defined by the angular coordinate, the radial distance, and the azimuthal angle. The parameters can be related to the Cartesian coordinates by an appropriate transformation. If ψ satisfies the scalar wave equation

$$\nabla^2\psi + k^2m^2\psi = 0, \quad (1)$$

where $k (= 2\pi/\lambda)$ is the wave number, λ is the wavelength and m is the index of refraction, then vectors associated with electric and magnetic fields can be expressed in the spheroidal coordinate system such that they satisfy the vector wave equations, which can be derived by replacing ψ with electric and magnetic vectors. The scalar wave equations can then be expressed in terms of scalar spheroidal wave functions.

The two-by-two amplitude matrix that transforms the incident electric vector into the scattered electric vector in the far field may be written in the form

$$\begin{bmatrix} E_i \\ E_r \end{bmatrix} = \frac{\exp(-ikR + ikz)}{ikR} \begin{bmatrix} S_2 & S_3 \\ S_4 & S_1 \end{bmatrix} \begin{bmatrix} E_1^0 \\ E_r^0 \end{bmatrix}. \quad (2)$$

The term z is the vertical direction in the Cartesian coordinates; R is the distance; $i = \sqrt{-1}$; E_i and E_r represent the electric fields parallel (E_i) and perpendicular (r) to a reference plane, commonly denoted as the plane containing the incident and scattered directions (the scattering plane); and the superscript o denotes the incident field. The amplitude functions for spheroids have been derived by Asano and Yamamoto (1975) and are given by

$$S_i(\theta, \phi) = \sum_{m=0}^{\infty} \sum_{n=m}^{\infty} [\alpha_{i,mn} \sigma_{mn}(\theta) + \beta_{i,mn} \chi_{mn}(\theta)] \cos m\phi, \quad (3a)$$

$$S_{i+2}(\theta, \phi) = \sum_{m=0}^{\infty} \sum_{n=m}^{\infty} [\alpha_{i,mn} \chi_{mn}(\theta) + \beta_{i,mn} \sigma_{mn}(\theta)] \sin m\phi, \quad i=1,2, \quad (3b)$$

where θ and ϕ are polar and azimuthal angles with respect to the symmetric axis of the spheroid and

$$\sigma_{mn}(\theta) = \frac{m S_{mn}(\cos \theta)}{\sin \theta}, \quad \chi_{mn}(\theta) = \frac{d}{d\theta} S_{mn}(\cos \theta), \quad (4)$$

with S_{mn} being the spheroidal angular function. The terms α_i and β_i are coefficients that can be determined from the four boundary conditions for the electric and magnetic fields at the surface of a spheroid. They are functions of the orientational angles of the spheroid, incident wavelength, refractive index, and aspect ratio. From the amplitude functions, the scattering phase matrix and the scattering and extinction cross sections can be obtained.

Scattering and absorption computations for randomly oriented spheroids have been carried out by Assano and Sato (1980). For the phase function, the rainbow features produced by spheres are absent in the case of spheroids, which also show smaller backscattering. There are also significant differences in the linear polarization patterns and in scattering phase matrix elements. Note that for spheres, there are only four independent elements, whereas six elements are involved for randomly oriented nonspherical particles. It is not computationally feasible to obtain the scattering and polarization properties of nonspherical particles by replacing them with area- (or volume-) equivalent spheres.

Computations of the amplitude functions involve the evaluation of the coefficients α_i and β_i , which are dependent on the size parameter, $2\pi a/\lambda$, where a is the semi-major axis of the spheroid. For size parameters larger than about 20, the spheroidal angular function becomes computationally unstable. For

this reason, the method has been applied to size parameters less than about 20. An efficient numerical technique must be developed to extend the method to larger size parameters.

Integral equation method

In this approach, a solution is sought for the scattering field in terms of the incident field and the physical characteristics of the scattering object. Consider a scattering volume bounded by a closed smooth surface, S , and let $\vec{E}^i(\vec{r})$ denote the incident electric field at any point, \vec{r} , with respect to an origin inside the scatterer. The scattered electric field may then be determined by

$$\vec{E}^s(\vec{r}) = \vec{\nabla} \times \int_S [\vec{n} \times \vec{E}^t(\vec{r}')] g(k\vec{R}) dS' - \vec{\nabla} \times \vec{\nabla} \times \int_S \frac{1}{i\omega\epsilon_0} [\vec{n} \times \vec{H}^t(\vec{r}')] g(k\vec{R}) dS', \quad (5)$$

where $\vec{n} \times \vec{E}^t$ and $\vec{n} \times \vec{H}^t$ represent the equivalent magnetic and electric surface current densities, respectively; \vec{E}^t and \vec{H}^t are the total electric and magnetic fields external to the scatterer; n is the unit vector normal to the surface; ϵ_0 is the permittivity; $\vec{R} = |\vec{r} - \vec{r}'|$; ω is the circular frequency ($=kc$); and the free space Green's function is defined by

$$g(k\vec{R}) = e^{ik\vec{R}} / (4\pi\vec{R}). \quad (6)$$

The terms in the integrals of Eq. (5) are expanded in terms of the transverse dyadic Green function, which may be expressed by vector spherical harmonics. The total electric field everywhere inside the scatterer can be set to zero so that $-\vec{E}^i(\vec{r}) = \vec{E}^s(\vec{r})$. Equation (5) can then be used to evaluate the total electric field in terms of the incident electric field by expanding all the fields in terms of vector spherical harmonics and by employing their orthogonality properties. The unknown coefficients in the expansion are determined from the boundary conditions at the surface of the scatterer that require the continuity of the tangential components of the electric and magnetic fields.

The preceding integral equation approach was first developed by Waterman (1965) for perfect conductors. Barber and Yeh (1975) modified this method for the calculation of the scattered electric field for spheroids, which is now known as the Extended Boundary Condition Method (EBCM). Iskander et al. (1983) further improved the EBCM in terms of the stability for the numerical procedure. In a series of papers, Mugnai and Wiscombe (1986, 1989) and Wiscombe and Mugnai (1988) applied the EBCM to irregular shapes with smooth surfaces that can be defined by Chebyshev polynomials. The results show that the scattering and absorption properties for irregularly shaped particles differ significantly from those of the spherical counterparts.

In principle, the EBCM may be used to solve the scattering problem involving any irregular, smooth particle of any size. However, in practice, this method has been used for size parameters less than about 20. For size parameters larger than this limit, numerical instability associated with the expanded spherical harmonics occurs. There are also computational difficulties with this method in the case of highly elongated or flattened particles and a significant computational effort is required for concave particles.

Discrete-dipole approximation

The discrete-dipole approximation is a numerical technique for the calculation of scattering and absorption properties of nonspherical particles. The particle is modeled by an array of N -point dipoles at position \vec{r}_i with polarizabilities $\vec{\alpha}_i$. The total electric field at the position of each dipole, $\vec{E}(\vec{r}_i)$, is the sum of the electric field corresponding to an incident wave and the electric field generated from contributions from all other dipoles as follows:

$$\vec{E}(\vec{r}_i) = \vec{E}_{\text{inc},i} + \vec{E}_{\text{self},i}, \quad (7)$$

where

$$\vec{E}_{\text{inc},i} = \vec{E}_0 \exp(i\vec{k} \cdot \vec{r}_i - i\omega t), \quad (8)$$

$$\vec{E}_{\text{self},i} = - \sum_{j \neq i} \vec{A}_{ij} \cdot \vec{P}_j \quad (9)$$

\vec{E}_0 is the amplitude vector of the incident electric field, k is the wave number of the incidence wave, ω is the circular frequency and t is the time. The polarization $\vec{P}_i = \vec{\alpha}_i \cdot \vec{E}(\vec{r}_i)$ and the matrix \vec{A} is a $3N \times 3N$ symmetric complex matrix that is dependent on the particle shape. Thus, the basic equation for the discrete-dipole approximation can be written in the form

$$(\vec{\alpha}_i)^{-1} \vec{P}_i + \sum_{j \neq i} \vec{A}_{ij} \cdot \vec{P}_j = \vec{E}_{\text{inc},i}. \quad (10)$$

Equation (10) can then be used to compute \vec{P} , which requires an inversion of the matrix \vec{A} . To approximate the actual particle, a large number of dipoles ($> 10^3$) is required for particles with dimensions comparable to the wavelength. In this case, efficient numerical techniques must be developed to perform calculations.

The discrete-dipole approximation was first developed by Purcell and Pennypacker (1973) for scattering and absorption calculations involving dielectric grains of cubic shape whose sizes are comparable to or smaller than the wavelength of the incident radiation. Improvements on the numerical techniques for the computations of scattering and absorption properties of rectangular particles have been recently developed by a number of researchers, including Singham and Bohren (1987), Draine (1988), Flatau et al. (1990)

and Goodman et al. (1991). The last authors have extended the scattering calculations to a size parameter of 10 for a cubic particle. Except for cubes, rectangles, and disks, scattering and absorption results for other nonspherical particles have not been presented. While this approximation may work well for small size parameters, innovative numerical approaches are required to apply this method to nonspherical particles with size parameters larger than about 10.

Geometric optics approach

If a particle is much larger than the incident wavelength, the laws of geometric optics may be applied to the scattering of light. In this case, a light beam may be thought of as consisting of a bundle of separate rays that hits the particle. The width of the light beam is much larger than the wavelength and yet small compared with the particle's size. Each ray that hits the particle will undergo reflection and refraction and will pursue its own specific path along a straight line. The rays that emerge from various directions will have different amplitudes and phases. The geometric ray optics approach has been used to identify the positions of various optical phenomena produced by water droplets and ice crystals, such as rainbows and halos (see, e.g., Greenler, 1980; Liou, 1980).

In the geometric optics method, the angles corresponding to incident and refracted rays on a surface are defined by Snell's law: $\sin \theta_i / \sin \theta_r = m$, where m is the index of refraction for the second medium with respect to the first and θ_i and θ_r denote the incident and refracted angles, respectively, with respect to the normal to the surface, for a given ray. The energies that are reflected and refracted from the surface are governed by Fresnel formulas, which are results of continuity requirements for the tangential components of the electric and magnetic vectors at the interface.

Because of the lack of a proper definition of the coordinate system for hexagonal structure, which is typical for ice crystals occurring in the atmosphere, the solution for the scattered electric field by means of the wave equation approach has not been available up to this point. The geometric optics approach has been used to derive the scattering, absorption and polarization properties of hexagonal ice crystals. Consider a hexagonal ice crystal that is arbitrarily oriented with respect to an incident light beam characterized by a specific electric vector. There are eight faces into which light rays may enter. The two components of the electric vectors parallel and perpendicular to the scattering plan can be used in tracing the light rays that undergo reflection and refraction. Electric fields reflected and refracted on a given surface can be computed from Fresnel formulas. The distances between the points of entry and departure, as well as the phase shifts of the electric field due to reflection and refraction, can be evaluated. The electric field vector associated with

all incident rays that undergo external reflection, two refractions, and internal reflections may be obtained by summing the outgoing electric field vectors that have the same direction in space.

Computation of the angular scattering patterns for hexagonal crystals based on the geometric ray-tracing method were first reported by Jacobowitz (1971), assuming infinite long hexagonal columns. A more comprehensive ray-tracing analysis to compute the phase functions for finite hexagonal columns and plates has been undertaken by Wendling et al. (1979) and Coleman and Liou (1981). Cai and Liou (1982) developed a ray-tracing model for arbitrarily oriented hexagonal ice crystals, which takes into account internal absorption and polarization, in which the four-by-four scattering phase matrix can be evaluated. For the first time, diffraction from a hexagonal aperture was also included in the geometric optics method. Along the same line, Takano and Jayaweera (1985), Muinonen et al. (1989), and Rockwitz (1989) also carried out numerical computations for the scattering of oriented hexagonal ice crystals. Takano and Liou (1989) have developed a new geometric ray-tracing program that accounts for the ice crystal size distribution and the possibility of horizontal orientation. Incorporation of the birefringent properties of ice and of the δ -transmission in the 0° scattering angle produced by transmissions through two parallel surfaces are new features that were included in the geometric ray-tracing program. Hexagonal ice crystals have flat surfaces which differ from surfaces involving spheres, circular cylinders and spheroids. Based on the calculations of Takano and Liou (1989) and Takano et al. (1992), it is estimated that the geometric optics approximation is generally valid for hexagonal ice crystals with size parameters larger than about 30.

CRITICAL DIFFERENCES BETWEEN SCATTERING AND ABSORPTION PROPERTIES OF NONSPHERICAL AND SPHERICAL PARTICLES

We shall investigate the differences between the scattering and absorption properties of nonspherical and spherical particles based on results from laboratory measurements as well as theoretical calculations. First, consider the aerosols. Aerosols are important for their influence on solar radiation. The scattering characteristics of aerosols can be measured in the laboratory using the direct method involving ensembles of particles at solar (in particular, visible) wavelengths or the analog experiments that perform similar investigations on individual particles at microwave wavelengths. Interactions of a particle with electromagnetic radiation depend explicitly on the particle size parameter. For this reason, interactions of a particle at solar (visible) wavelengths can be simulated by those in the microwave domain with an appropriately scaled particle. In the analog experiment, the refractive indices of the experimental material at microwave wavelengths must match those of the solar counterpart. Because the analog experiments involve physically large par-

ticles, they can be performed in a much more controlled environment such that shapes, sizes and orientations can be specified in the experiment.

Holland and Gagne (1970) carried out an experiment to measure the scattering phase function for flat plates at a visible wavelength. They found that particles of irregular shape scatter considerably more energy into the side-scatter region than equivalent assemblies of spheres. Using the analogy experiment, Zerull and Giese (1974) and Zerull (1976) and Zerull et al. (1977) measured the scattering patterns for cubes, convex and concave particles with size parameters less than about 20. Recently, Hage et al. (1991) compared theoretical calculations and experiments from a microwave analog experiment including a porous cube.

Figure 1 shows the measured phase function for scattering by an ensemble of randomly oriented convex and concave particles with size parameters between 5.9 and 17.8 and a refractive index of $1.5 + 0.005i$ determined from the analog experiment (Zerull, 1976). Also shown are the phase functions predicted by the Mie theory for equal volume and equal area spheres and that derived by the semi-empirical theory developed by Pollack and Cuzzi (1980). The scattering pattern for nonspherical particles deviate significantly from that for equivalent spheres. Nonspherical particles scatter much more light in the directions between the 60° and 140° scattering angles.

Measurements of scattering and polarization patterns for ice crystals have been carried out in cold chambers where various shapes and sizes may be generated (Dugin and Mirumyants, 1976; Nikiforova et al., 1977; Sassen and

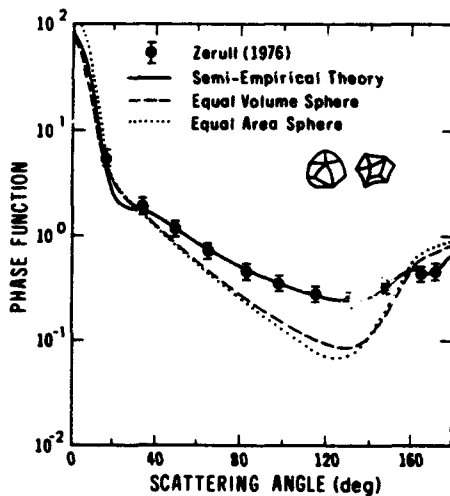


Fig. 1. Comparison of the measured phase function for scattering by an ensemble of convex and concave particles with size parameters ranging from 5.9 to 17.8 determined from a microwave analog experiment (Zerull, 1976) with the results from Mie theory for equal volume and equal area spheres and the semi-empirical theory developed by Pollack and Cuzzi (1980).

Liou, 1979; Volkovitsky et al., 1980). Dugin and Mirumyants measured the scattering phase matrix elements for laboratory clouds containing 20–100 μm plates at the 0.57 μm wavelength. The ice crystals generated in the cold chamber were smaller than those occurring in cirrus clouds. Takano and Liou (1989) compared the theoretical polarization results computed from a geometric ray-tracing program with experimental data. The theoretical results for columns and plates can be used to interpret the measured data.

Figure 2 shows the scattering phase function measured at a wavelength of 0.6328 μm for laboratory clouds containing columns (Volkovitsky et al., 1980). The distinctive features of 22° and 46° halos are produced in the laboratory data. Theoretical ray-tracing results using the ice crystal size distribution for cirrostratus and results from Mie calculations for ice spheres are also shown for comparison. There are general agreements between laboratory scattering data and theoretical ray-tracing results. It is not possible to carry out a precise comparison because the exact sizes for columns were not available, and because the laboratory data lacked values within 10° of forward and backscattering directions due to the limitations of nephelometer measurements. The maximum at about 140° scattering angle for ice spheres is the rainbow feature produced by spherical particles. In comparisons between the phase function patterns for hexagonal columns and ice spheres, significant

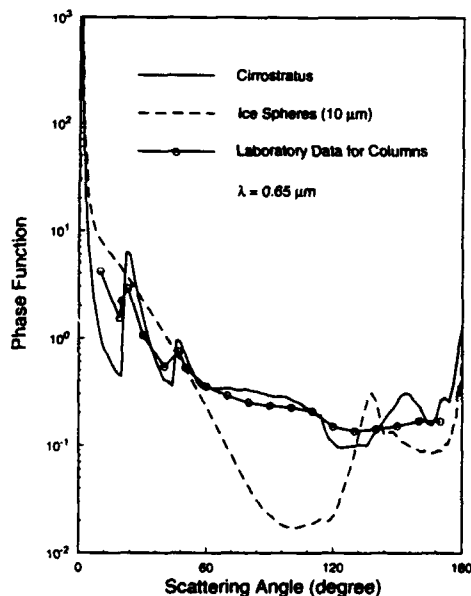


Fig. 2. Comparison of the measured phase function for scattering by columns generated in the cold chamber using the 0.6328 μm wavelength (Volkovitsky et al., 1980) with the theoretical results for randomly oriented ice columns and ice spheres.

differences are present. Hexagonal ice crystals scatter much more light in the side scattering directions from about 60 to 160° scattering angles, except in the vicinity of the rainbow angle. Compared to spheres, hexagonal ice crystals also scatter less in the forward directions.

Finally, we investigate the differences between the single-scattering albedo and asymmetry factor for various sizes of hexagonal ice crystals and area equivalent ice spheres using 0.55 and 2.2 μm (Table 2). Absorption is practically negligible at 0.55 μm . Area equivalent spheres would give approximately the same extinction cross section. For both wavelengths, hexagonal ice crystals have a smaller asymmetry factor than the spherical counterparts. At the 2.2 μm wavelength, hexagonal ice crystals absorb less than the spherical particles. Consider volume equivalent spheres, which would give approximately the same absorption cross section, σ_a , as compared with nonspherical particles. Because of smaller cross sections, volume equivalent spheres would have a smaller scattering cross section, σ_s , resulting in a larger co-single-scattering albedo, $(1 - \tilde{\omega}) = \sigma_a / (\sigma_a + \sigma_s)$. This implies that volume equivalent spheres would absorb more than nonspherical particles in the context of radiative transfer calculations in which one of the fundamental parameters is the single-scattering albedo.

In summary, we conclude that nonspherical particles absorb less and have a smaller asymmetry factor than their equal-area or equal-volume spherical counterparts. These important features are characteristic not only for ice crystals, but also for nonspherical aerosols. The influence of the shape of tropospheric aerosols on the solar albedo has been investigated by Pollack and Cuzzi (1980) who show that sizable differences in global albedo occur between cases involving nonspherical aerosols and their equivalent spherical counterparts. Little research has been carried out regarding the influence of aerosol shape on the active and passive remote sensing of aerosol concentra-

TABLE 2

Single-scattering albedo, $\tilde{\omega}$, and asymmetry factor, g , for hexagonal ice crystal and area* equivalent ice spheres at $\lambda = 0.55$ and 2.2 μm

L/2a ($\mu\text{m}/\mu\text{m}$)	λ (μm)	$1 - \tilde{\omega}$		g	
		Hexagon	Sphere	Hexagon	Sphere
20/20	0.55	0	0	0.7704	0.8759
	2.2	4.085×10^{-2}	4.944×10^{-2}	0.8185	0.8729
120/60	0.55	0	0	0.8155	0.8871
	2.2	1.246×10^{-1}	1.539×10^{-1}	0.8829	0.9174
750/160	0.55	0	0	0.8592	0.8908
	2.2	2.503×10^{-1}	3.583×10^{-1}	0.9380	0.9566

*Give approximately the same extinction cross section.

tions and particle sizes. In the following, we shall confine our discussion to the implications of the nonsphericity of ice crystals on remote sensing and climate modeling.

REMOTE SENSING IMPLICATIONS

A number of examples are given to illustrate the importance of the scattering and absorption properties of ice crystals in the interpretation of satellite radiance observation, polarization measurements from space and lidar back-scattering data.

Satellite remote sensing

Visible and IR two-channel technique

Minnis et al. (1992) developed a retrieval algorithm for the inference of the optical depth and height of cirrus clouds using the two-channel technique. The retrieval algorithm includes the following. First, the observed visible reflectance is interpreted with a parameterization of radiative transfer calculations using the scattering characteristics of two specific cloud particle size distributions; a water droplet distribution having an effective radius of $10\ \mu\text{m}$ and an effective variance of 0.05 and an ice crystal size distribution for cirrostratus. The water droplet model distribution, a model used by the ISCCP, was used to compute the Mie-scattering phase function. The phase function for the cirrostratus model was computed from a geometric ray-tracing program developed by Takano and Liou (1989). An optical depth is determined with the radiative transfer parameterization from a given reflectance observation using one of the two models. This parameterization accounts for the surface reflection, Rayleigh scattering and ozone absorption. The visible optical depth is then used to compute the IR emissivity of cirrus clouds, based on a parameterization involving the two. The IR emissivity is subsequently used along with the observed IR radiance to obtain a better estimate of the true radiating temperature of the cloud. This temperature is then converted to cloud height using the nearest available sounding.

Figure 3 shows the effects of nonsphericity on the retrieval of cloud height using GOES visible ($0.65\ \mu\text{m}$) and IR ($11.2\ \mu\text{m}$) data during the FIRE II experiments in southeastern Kansas between November 13 and December 7, 1992 (Minnis et al., 1992). For comparison purposes, the cloud-center heights determined from the NASA Langley lidar are displayed. As shown in this figure, the hexagonal ice crystal model produces cloud center heights which are within 0.2 km of the lidar derived values. The ice sphere model yields underestimates of the cloud heights.

The preceding example illustrates the importance of using the phase function of hexagonal ice crystals in the interpretation of satellite reflectance mea-

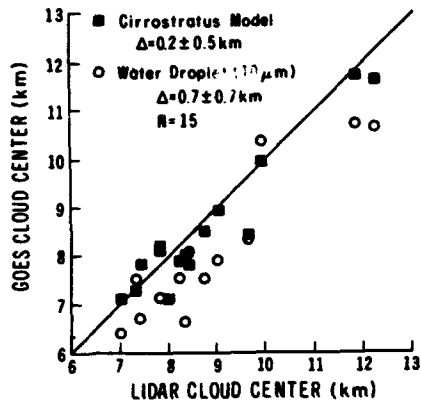


Fig. 3. Comparison of the cloud center height derived from GOES satellite visible and IR radiance measurements and from surface lidar (Minnis et al., 1992, see text for further explanation).

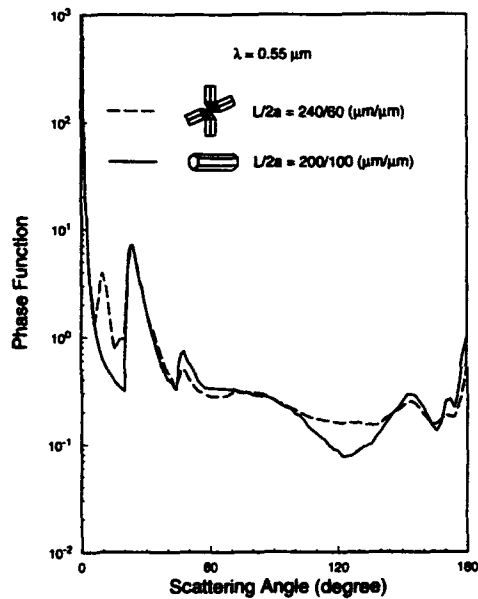


Fig. 4. Comparison of the phase functions for randomly oriented columns and bullet rosettes with the same cross section area.

measurements. We notice from Fig. 2 that significant differences in phase functions for ice spheres and hexagonal columns are evident in the region from 60 to 150° scattering angles. Based on cloud physics observations (Heymsfield and Knollenberg, 1972), a substantial portion of ice crystals are bullet rosettes. We have carried out a geometric ray-tracing program using a Monte Carlo method to compute the phase function for randomly oriented bullet

rosettes. Figure 4 shows a comparison of the phase functions for columns and bullet rosettes whose averaged projected areas are the same. In the case of bullet rosettes, an additional maximum is shown at about the 10° scattering angle that is produced by two refractions involving prism and pyramidal planes. In addition, bullet rosettes scatter more light in the scattering angle region from about 100° to 140° . The phase function for bullet rosettes may be of use in the interpretation of bidirectional reflectance.

Ice crystals in thin cirrus clouds could be horizontally oriented. The fact that numerous arcs and halos are visible demonstrates that horizontal orientation must exist for some cirrus clouds. Figure 5 shows the bidirectional reflectances for randomly oriented (3-D) and horizontally oriented (2-D) columns using the cirrostratus size distribution in the plane defined by the emergent (θ) and relative azimuthal ($\phi - \phi_0$) angles. Two optical depths, τ , of 1 and 4 are used and the cosine of the solar zenith angle is 0.5. In the 3-D case, the maximum at $\theta = 60^\circ$ in the plane of $\phi - \phi_0 = 180^\circ$ is associated with the glory-like feature in the 180° backscattering direction. Large values are also shown around the limb direction ($\theta > 70^\circ$ in the planes of $0^\circ \leq \phi - \phi_0 \leq 45^\circ$). Minimum values occur in the vicinity of the zenith direction ($\theta = 0^\circ$) for both $\tau = 1$ and 4. For $\tau = 4$ the reflectance pattern is more isotropic than that for $\tau = 1$. A maximum occurs in the 2-D case at about $\theta = 60^\circ$ in the plane of $\phi - \phi_0 = 180^\circ$, corresponding to the sub-anthelion feature produced by one internal reflection (the scattering angle is about 180°). Also, a maximum is located at about $\theta = 60^\circ$ in the plane of $\phi - \phi_0 = 0^\circ$, resulting from the subsun features produced by external reflections (the scattering angle is about 60°). This feature does not exist in the 3-D case. The bidirectional reflectances for 2-D columns are more anisotropic than those for 3-D columns with larger values in the vicinity of subanthelion and subsun positions and smaller values in other directions.

IR brightness temperature difference

Figure 6 shows a scatter diagram of the brightness temperature difference between several IR wavelengths, consisting of several hundred points collected for about four hours under cirrus cloud conditions obtained by the HIS instrument aboard the NASA ER-2 during FIRE I (Ackerman et al., 1990). The envelopes are results determined from a theoretical radiative transfer program corresponding to a large set of data points computed by varying the cloud thickness, size distribution and surface temperature (Takano et al., 1992). The solid curve corresponds to the theoretical results for a nonspherical model involving spheroid/hexagonal particles. If the size parameters are greater than 30, the scattering and absorption properties for hexagonal ice crystals are used. If the size parameters are less than 30, those for spheroids with axial ratios of 3 and 5 are employed. The dashed curve corresponds to results involving area-equivalent spheres. The solid envelope covers the ob-

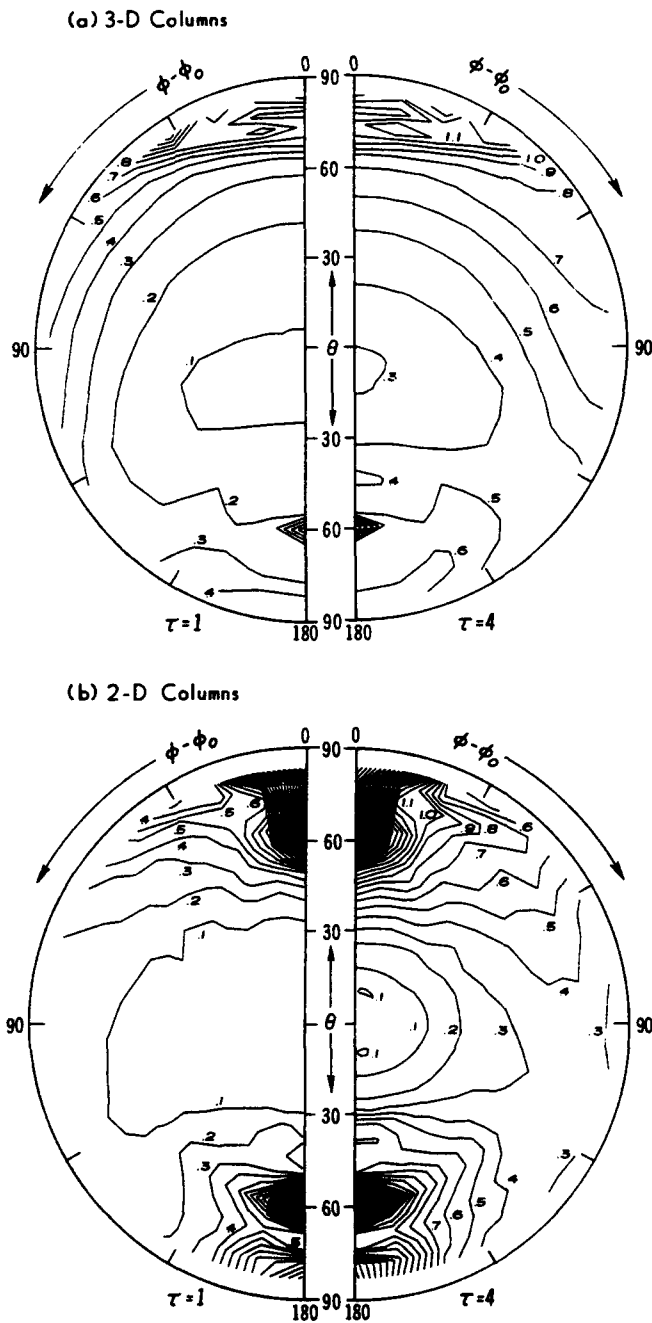


Fig. 5. Bidirectional reflectances for randomly oriented (3-D) and horizontally oriented (2-D) columns in the plane defined by the emergent zenith angle (θ) and relative azimuthal angle ($\phi - \phi_0$) between the position of the sun and satellite. The cosine of the solar zenith angle used in the calculations is 0.5. Results for two optical depths are shown.

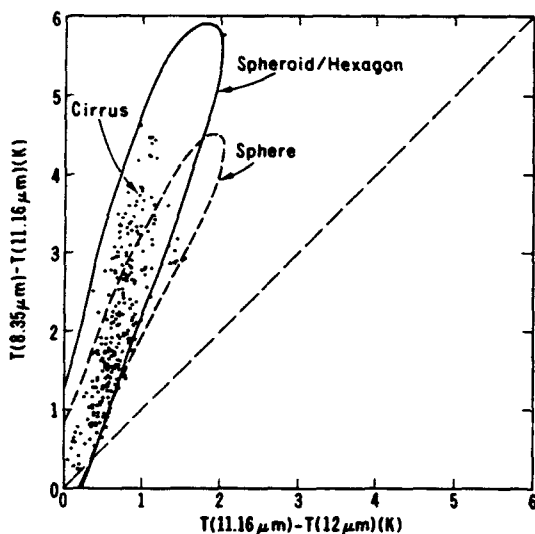


Fig. 6. A scatter diagram of the brightness temperature differences between 11.16 and 12 μm and between 8.35 and 11.16 μm collected by the HIS instrument aboard the NASA ER-2 during FIRE I cirrus IFO (Ackerman et al., 1990). The envelopes are theoretical results computed from a radiative transfer program using an ice crystal model and an ice sphere model. These envelopes correspond to a large set of data points by varying the cloud thickness, size distribution and surface temperature (Takano et al., 1992).

served data for cirrus, whereas the dashed envelope corresponding to equivalent spheres significantly deviates from the observed data. The differences in the single-scattering properties between the 11.16 and 12 μm wavelengths do not significantly depend on the particle shape due to the large absorption property of ice. However, at the 8.35 μm wavelength, equivalent spheres have a smaller single-scattering albedo and, hence, absorb more radiation. Consequently, the brightness temperature for this wavelength is less than that for nonspherical results. The preceding demonstration shows that a better interpretation for the brightness temperature of cirrus clouds can be made by using appropriate nonspherical models.

Polarization and backscattering depolarization measurements

Polarization

Polarization of the reflected sunlight from clouds and aerosols contains information of particle characteristics. In the following, a specific example is given to demonstrate the importance of using a nonspherical particle model to interpret the polarization measurements. Figure 7 shows the linear polarization pattern on the solar principal plane as a function of phase angle (180° -scattering angle) measured from a cirrus cloud with a thickness of 5 km using

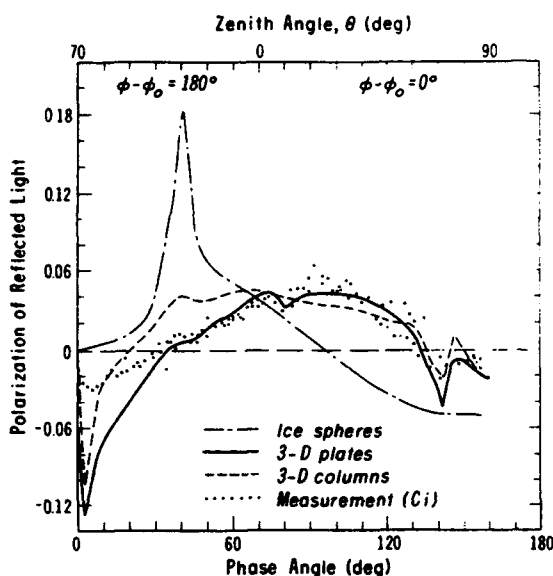


Fig. 7. Linear polarization as a function of phase angle (180° - scattering angle) measured from a cirrus cloud with a thickness of 5 km using the $2.2 \mu\text{m}$ wavelength (Coffeen, 1979). A number of theoretical results are displayed in the diagram for comparisons, including randomly oriented columns and plates and area equivalent spheres.

a wavelength of $2.22 \mu\text{m}$ (Coffeen, 1979). Polarization values are generally less than 6% and are positive from 30 to 130° phase angles. A number of theoretical results are also displayed for comparison, including randomly oriented columns and plates and area equivalent spheres.

The computed polarization pattern used an optical depth of 64 and a solar zenith angle of 70° in order to match the observations (Takano and Liou, 1989). For plates and columns, the negative values around the 140° and 160° phase angles result from the 46° and 22° halos, respectively. Results from the spherical model deviate significantly from the observations. Spheres produce maximum polarization at the rainbow angle. This feature does not exist in the observed pattern. The computed polarization for ice plates fits the observed values quite well. It appears that the cloud particles near the cloud top must be randomly oriented plate-like crystals. There are deviations between the computed and observed polarization around the 0° phase angle (backscattering) because scattered light is partially blocked by the aircraft and because the cloud may contain irregular ice crystals, which would reduce polarization in the backscattering directions. Finally, it should be noted that the observed polarization patterns can be used to differentiate between ice and water clouds.

Lidar backscattering depolarization measurements

The depolarization technique has been developed from lidar backscattering returns for the purpose of differentiating between ice and water clouds in the past 20 years. The technique is based on the fundamental scattering properties of ice crystals and water droplets. For spherical water droplets, the incident polarized light beam will retain the polarization state at the backscattering direction if multiple scattering can be neglected. The cross polarized component, called depolarization, of the incident polarized light occurs for nonspherical particles. For ice crystals in the geometric optics region, depolarization is produced by internal reflections and refractions (Liou and Lahore, 1974). A parameter referred to as the depolarization ratio, defined as the ratio of the cross polarized returned power to the return power of the original polarization state, has been used to differentiate between ice and water clouds as well as the physical characteristics of ice crystal clouds.

Figure 8 shows the linear depolarization ratio for various types of ice crystals and water droplets derived from laboratory and field studies (Sassen, 1976). For water droplets, this ratio is close to zero as is predicted from the theory. For pure ice crystals, the depolarization ratio is on the order of 50 to 70%. Large plate and column crystals tend to orient in the direction parallel to the ground. In the case of horizontally oriented plate crystals, the depolarization ratio would be zero because of the symmetry of the two parallel crystal surfaces. Figure 9 illustrates the backscattering coefficient and depolarization ratio as functions of altitude and scan angle (Platt et al., 1978). At the backscattering direction (zenith angle of 0.0°), the depolarization ratio is close to zero. This ratio increases significantly as the lidar scans a few degrees off the

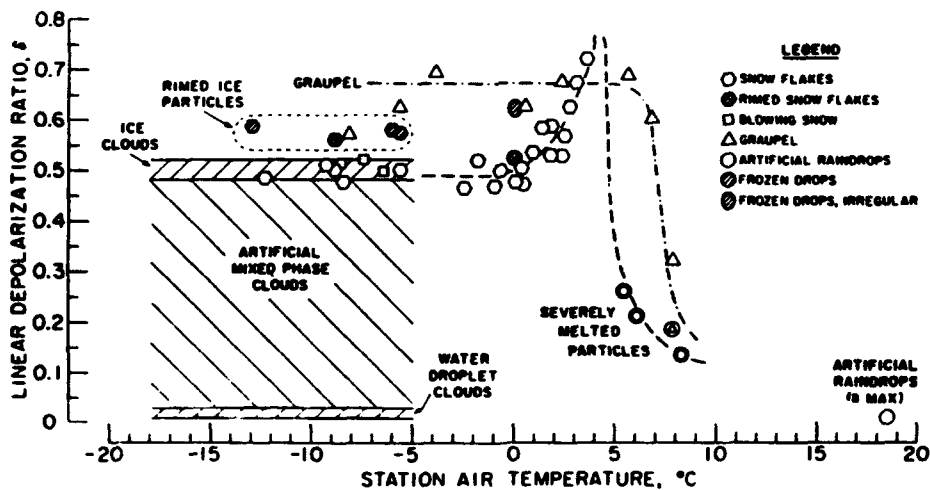


Fig. 8. Depolarization ratio for various types of ice crystals and water droplets derived from laboratory and field studies using the CW laser and lidar approach (Sassen, 1976).

vertical, revealing that the ice clouds, occurring in the temperature range of -9 to -13.4°C , must contain horizontally oriented plate crystals. The two preceding examples demonstrate the importance of the scattering characteristics of ice crystals in terms of shape and orientation in the interpretation of the lidar backscattering returns.

The scattering properties of hexagonal columns and plates have been comprehensively computed by Takano and Liou (1989) based on the principle of geometric ray tracing. An example of the scattering phase function for randomly oriented bullet rosettes has also been shown in Fig. 4. The shape of ice crystals is primarily controlled by temperature and supersaturation. Hollow columns occur when excess vapor density over ice is greater than about 0.04 g/m^3 but less than 0.1 g/m^3 (Fletcher, 1962). Figure 10 shows the phase functions for randomly oriented hollow and solid columns with a length of $200\text{ }\mu\text{m}$ and a width of $80\text{ }\mu\text{m}$ for the $0.55\text{ }\mu\text{m}$ wavelength. The depth of the hollow structure is $50\text{ }\mu\text{m}$ on both ends. Significant differences are evident in the backward (140° – 180°) and forward (10° – 20°) directions. Also, the 46° halo disappears in the case of hollow columns because of the lack of two refractions through the 90° angle. The backscattering for the present hollow

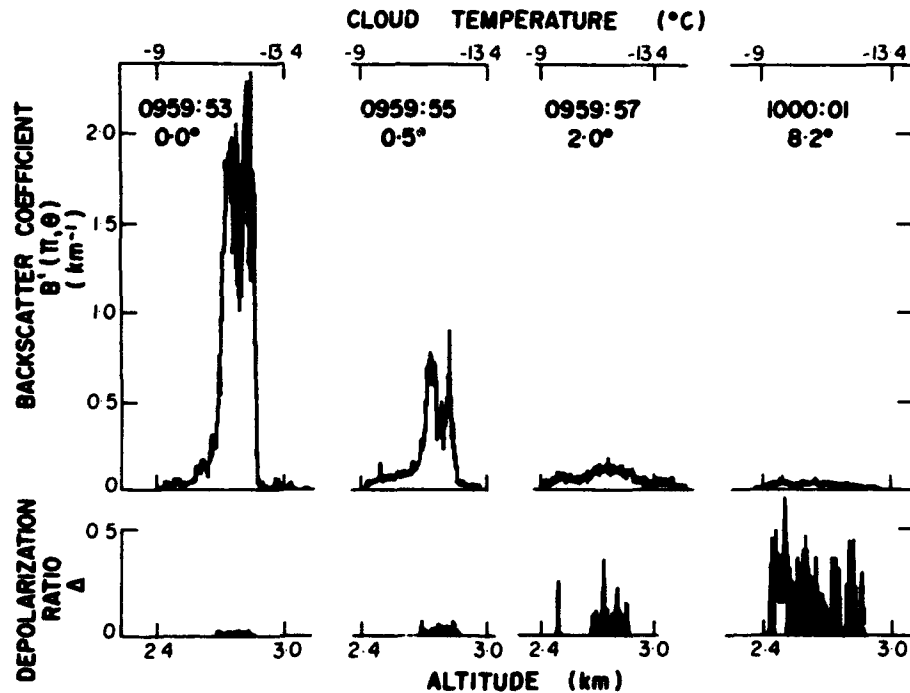


Fig. 9. Cloud backscattering coefficients and depolarization ratios derived from a lidar experiment for a number of vertical scans (Platt et al., 1978).

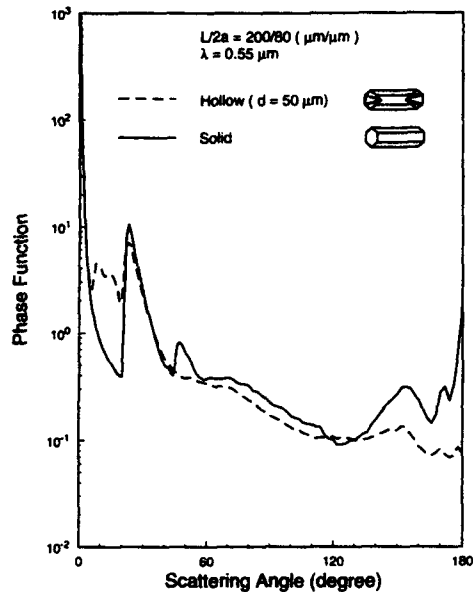


Fig. 10. The phase functions for randomly oriented hollow and solid columns with a length of $200 \mu\text{m}$ and a width of $80 \mu\text{m}$ for the $0.55 \mu\text{m}$ wavelength. The depth of the hollow structure used in the geometric ray-tracing calculation is $50 \mu\text{m}$ on both ends.

columns is a factor of 20 smaller than that for solid columns. This large difference undoubtedly would have a significant effect in the interpretation of lidar backscattering returns in cases when clouds contain hollow ice crystals.

As discussed previously, the shapes of ice crystals that occur in cirrus clouds are dependent on temperature and supersaturation. Interpretation of active and passive remote sensing measurements for the inference of the composition and thickness of cirrus clouds must utilize the scattering and absorption properties of appropriate ice crystal models. Concurrent cloud microphysics observations would assist in the development of remote sensing techniques.

CLIMATIC IMPACT OF CIRRUS CLOUDS

We have pointed out in the discussion of the retrieval of cloud optical depth and cloud height using visible and IR radiances that the bidirectional reflectance from clouds consisting of nonspherical ice crystals is much brighter than the spherical counterparts. The reason is that spherical particles have a larger asymmetry factor and, hence, more light is scattered in the forward directions resulting in weaker backscattering. It is expected that for a given optical depth, clouds composed of nonspherical particles would have larger solar albedos, i.e., larger reflected flux at the cloud top, than spherical particles.

Broadband flux observations from aircraft involving cirrus clouds have been carried out during the FIRE experiment in Wisconsin, October–November, 1986. Results for solar albedo were analyzed by Stackhouse and Stephens (1991) for the October 28 case (Fig. 11). The extensions of the vertical and horizontal lines through the data points denote the uncertainties of measurements. The dashed lines show the theoretical results as functions of the ice water path (IWP) using the observed size distributions converted into equivalent spheres. These results are much smaller than the observed values. The solid lines represent theoretical results using the scattering and absorption properties of hexagonal ice crystals in a radiative transfer parameterization program involving the δ -four-stream method for radiative transfer and the correlated k-distribution for gaseous absorption. The solar albedo values are functions of both IWP (g/m^2) and the mean effective size, defined as the ice crystal width weighted by the cross sectional area of ice particles as follows:

$$D_e = \frac{\int_{L_{\min}}^{L_{\max}} D^2 L n(L) dL}{\int_{L_{\min}}^{L_{\max}} D L n(L) dL}, \quad (11)$$

where D is the width; L the length of an ice crystal; $n(L)$ denotes the ice crystal size distribution; and L_{\min} and L_{\max} are the minimum and maximum lengths of ice crystals, respectively. The mean size of ice crystals determined from theoretical computations ranges from 50 to 75 μm , in agreement with the observed ice crystal size. It is clear that the spherical assumption is unable to reliably interpret the observed solar albedo values involving cirrus clouds.

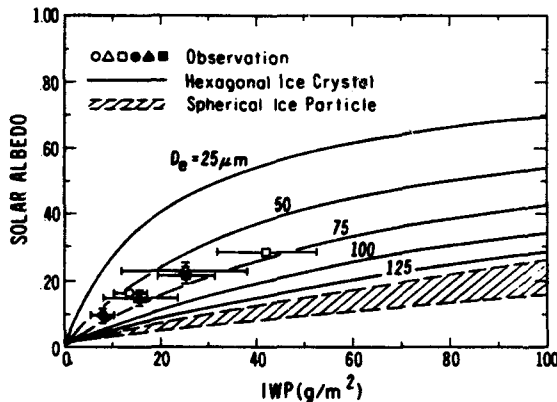


Fig. 11. Solar albedo as a function of ice water path (IWP) determined from broadband flux observations from aircraft involving cirrus clouds during FIRE I cirrus IFO (Stackhouse and Stephens, 1991). The extensions of the vertical and horizontal lines through the data points denote the uncertainties of measurements. The dashed lines show the theoretical results using the observed size distribution converted into equivalent spheres. The solid lines represent theoretical results using the scattering and absorption properties of hexagonal ice crystals in terms of mean effective size, D_e (see text for further explanation).

To quantify the effects of nonspherical particles on the radiation budget of the earth and the atmosphere, we use the cloud radiative forcing concept for the flux at the top of the atmosphere. This forcing is defined as the difference of the clear sky and overcast net fluxes in the form

$$C = C_{ir} + C_s, \quad (12)$$

where

$$C_{ir,s} = F_{ir,s}^{cl} - F_{ir,s}^{ov}, \quad (13)$$

and F^{cl} and F^{ov} denote the flux at the top of the atmosphere for clear and overcast conditions, respectively; the subscript *ir* denotes the broadband IR, and *s* the broadband solar components. If C is positive, the IR greenhouse effect outweighs the solar albedo effect and there will be a net gain of energy within the atmosphere. However, if C is negative, the reverse is true. In the calculations, a mean effective size of about $42 \mu\text{m}$ corresponding to the ice crystal size distribution for C_s was used, along with a cloud base of 9 km, a cosine of the solar zenith angle of 0.5, a solar duration of 12 hours, and a surface albedo of 0.1. The cloud cover employed in this illustration is 100%. Figure 12 shows the cloud radiative forcing, which is expressed in terms of IWP as well as optical depth. In this figure and in Fig. 13, IWP is the independent variable, while the optical depth is calculated by using the extinction coefficient for hexagonal ice crystals. We use the same optical depth for equivalent ice spheres to investigate the effects of the single-scattering albedo and phase function on the cloud radiative forcing and climatic temperature per-

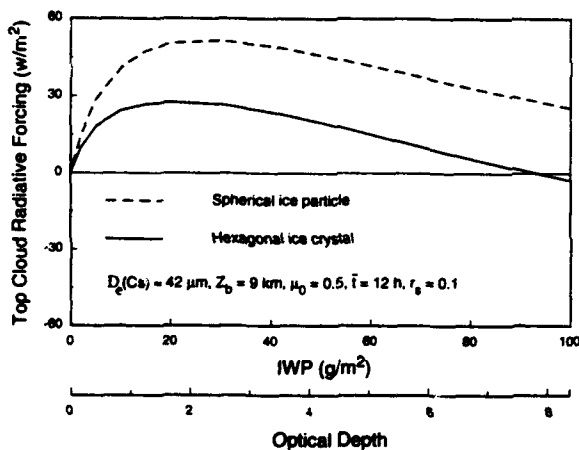


Fig. 12. Cloud radiative forcing at the top of the atmosphere expressed in terms of ice water path (IWP) as well as optical depth. The cloud cover used in the calculation is 100% and other relevant parameters are displayed in the figure. Solid and dashed curves are results using hexagonal ice crystal and ice sphere models.

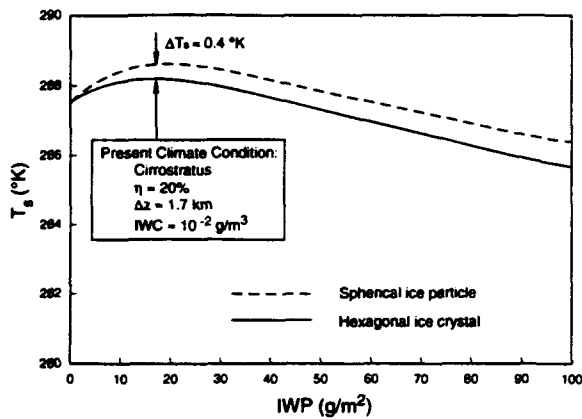


Fig. 13. Surface temperatures determined from a one-dimensional cloud and climate model developed by Liou and Ou (1989). The condition for the present climate is depicted in the diagram. Solid and dashed curves are for results using hexagonal ice crystal and ice sphere models. Feedbacks between temperature and ice water path and ice crystal size are not accounted for in the present model calculations.

turbation. Results involving hexagonal ice crystals show positive radiative forcing, revealing that the greenhouse effect outweighs the solar albedo effect for a realistic range of optical depths for cirrus clouds. This positive forcing is in part produced by the position of cirrus clouds and their downward emission. Using the spherical particle assumption, the cloud radiative forcing values increase substantially. This large increase is a result of the smaller solar albedo values in the case of spherical particles, as shown in Fig. 11. For partly cloudy conditions, cloud radiative forcing can be obtained by multiplying the present results by the fraction of cloud cover.

Finally, we investigate the potential effect of particle nonsphericity in light scattering on the climatic temperature perturbation. Using a onedimensional cloud-climate model developed by Liou and Ou (1989), perturbation calculations were performed by varying the IWP using a Cs cloud model. Cloud positions and covers for high, middle and low cloud types are prescribed. In the perturbation runs, only the IWP of high clouds is varied; all other components remain unchanged. The model simulations use the radiative properties of cirrus clouds involving hexagonal ice crystals and area-equivalent spherical ice particles that are computed from a radiative transfer parameterization program in terms of IWP and Cs size distribution. In the model, the present climate condition, with a surface temperature of 288 K, corresponds to an IWP of about 20 g/m^2 , and a cirrus cloud cover of about 20%. Perturbations were carried out by varying the IWP. Figure 13 shows that the surface temperature decreases as the IWP increases. The reason is that the increase in IR emissivity is very small and a significant increase in solar albedo occurs,

resulting in the domination of the solar albedo effect. Using the spherical model, we showed that the cloud radiative forcing increases by about a factor of two because of the reduction of solar albedo. For this reason, larger surface temperatures are produced relative to the case involving the hexagonal ice crystal model. At the present climate condition, the increase amounts to about 0.4 K, which is substantial. In these perturbation exercises, the feedbacks between temperature and particle size and IWP have not been considered. The prime objective of this illustration is to show that using the radiative properties of cirrus clouds for spherical and nonspherical models, sufficient sensitivity in climatic temperature perturbations can be produced.

SUMMARY AND CONCLUSIONS

A large portion of atmospheric suspensions, in particular, aerosols and ice crystals, are nonspherical particles. We have reviewed a number of methodologies for the calculation of the scattering and absorption properties of nonspherical particles with various shapes. Practically, all of the numerical solutions for the scattering of nonspherical particles, including the exact wave equation solution, integral equation method, and discrete-dipole approximation are applicable to size parameters less than about 20. Thus, these methods are useful for the study of radiation problems involving nonspherical aerosols. For hexagonal ice crystals whose sizes are much larger than the incident wavelength, the geometric optics approximation has been used to evaluate the scattering, absorption and polarization properties of these types of particles. This approximation is valid for ice crystal size parameters larger than about 30. From existing laboratory data and theoretical results, we illustrate that nonspherical particles absorb less and have a smaller asymmetry factor than the equal-area or equal-volume spherical counterparts. In particular, we show that hexagonal ice crystals scatter more light in the region from the 60° to 140° scattering angles than the spherical counterparts. It is apparent that exact and approximate scattering solutions for nonspherical particles with size parameters between 10 and 30 are lacking. Extensive research is required.

Implications of the scattering and absorption properties of nonspherical particles are discussed with respect to remote sensing and clouds and climate. We show that determination of the optical depth and height of cirrus clouds using visible and IR channels must use appropriate phase functions for ice crystals. Use of an equivalent sphere model would lead to a significant overestimate and underestimate of the cloud optical depth and height, respectively. The horizontal orientation property of ice crystals within some cirrus clouds and the scattering characteristics of bullet rosettes could be important in the interpretation of bidirectional reflectance measurements. With respect to polarization measurements for ice clouds, interpretations can not be made by spherical models, which produce a large polarization at the rainbow angle

that does not exist for hexagonal ice crystals. Polarization data from reflected sunlight can be used to differentiate between ice and water clouds. With respect to lidar backscattering, ice crystals generate significant depolarization in the returned power, which is dependent on the shape and orientation of ice crystals. It is not possible to interpret the backscattering patterns using spherical models. Moreover, we show that hollow structure in the columns reduces significantly the backscattering energy and can be important in the interpretation of lidar returns from ice clouds.

Interpretation of broadband solar albedo for cirrus clouds must use the scattering and absorption properties of hexagonal ice crystals. The equivalent spherical assumption substantially underestimates the solar albedo values, because of stronger forward scattering and larger absorption by spherical particles. For most cirrus clouds, the net cloud radiative forcing is positive, implying that the greenhouse effect outweighs the solar albedo effect. If the radiative properties of equivalent spheres were used, the cloud radiative forcing value increases; a result produced by smaller solar albedos. Using a one-dimensional cloud and climate model, temperature perturbations, generated by varying the IWP of cirrus clouds, are computed by incorporating the radiative properties of hexagonal ice crystals and spheres. The spherical model has a larger temperature increase (by about 0.4 K) than the hexagonal ice crystal model. In light of the one-dimensional results presented herein, it appears important to use the scattering and absorption properties of appropriate non-spherical ice crystal/aerosol models in radiation calculations in conjunction with climate modeling and climate sensitivity analysis.

ACKNOWLEDGEMENTS

Research contained in this paper has been supported by the National Science Foundation grant ATM90-24217, NASA grants NAG5-1050 and NAG1-1048, and the Air Force Office of Scientific Research grant AFOSR91-0039. We thank Steve Ou and Qiang Fu for providing a number of illustrations presented in the paper.

REFERENCES

- Ackerman, S.A., Smith, W.L., Spinhirne, J.D. and Revercomb, H.E., 1990: The 27-28 October 1986 FIRE IFO cirrus case study: Spectral properties of cirrus clouds in the 8-12 μm window. *Mon. Weather Rev.*, 118: 2377-2388.
- Asano, S. and Sato, M., 1980. Light Scattering by randomly oriented spheroidal particles. *Appl. Opt.*, 19: 962-974.
- Asano, S. and Yamamoto, G., 1975. Light scattering by a spheroidal particle. *Appl. Opt.*, 14: 29-49.

- Barber, P. and Yeh, C., 1975. Scattering of electromagnetic waves by arbitrarily shaped dielectric bodies. *Appl. Opt.*, 14: 2864-2872.
- Cai, Q. and Liou, K.N., 1982. Polarized light scattering by hexagonal ice crystals: Theory. *Appl. Opt.*, 21: 3569-3580.
- Coffeen, D.L., 1979. Polarization and scattering characteristics in the atmosphere of Earth, Venus, and Jupiter. *J. Opt. Soc. Am.*, 69: 1051-1064.
- Coleman, R.F. and Liou, K.N., 1981. Light scattering by hexagonal ice crystals. *J. Atmos. Sci.*, 38: 1260-1271.
- Draine, B.T., 1988. The discrete-dipole approximation and its application to interstellar graphite grains. *Astrophys. J.*, 333: 848-872.
- Dugin, V.P. and Mirumyants, S.O., 1976. The light scattering matrices of artificial crystalline clouds. *Izv. Acad. Sci. USSR Atmos. Ocean. Phys.*, 12: 988-991.
- Flatau, P.J., Stephens, G.L. and Draine, B.T., 1990. Light scattering by rectangular solids in the discrete-dipole approximation: a new algorithm exploiting the Block-Toeplitz structure. *J. Opt. Soc. Am. A.*, 4: 593-600.
- Fletcher, N.H., 1962. *The Physics of Rain Clouds*. Cambridge University Press, Cambridge, 340 pp.
- Goodman, J.J., Draine, B.T. and Flatau, P.J., 1991. Application of fast-Fourier-transform techniques to the discrete-dipole approximation. *Opt. Lett.*, 16: 1198-1200.
- Greenberg, J.M., Lind, A.C., Wang, R.T. and Libelo, L.F., 1967. Scattering by nonspherical system. In: R.L. Rowell and F.S. Stein (Editors), *Electromagnetic Scattering*, Gordon and Breach, New York, pp. 3-54.
- Greenler, R., 1980. *Rainbows, Halos, and Glories*. Cambridge University Press, Cambridge, 195 pp.
- Hage, J.I., Greenberg, J.M. and Wang, R.T., 1991. Scattering from arbitrarily shaped particles: theory and experiment. *Appl. Opt.*, 30: 1141-1152.
- Heymsfield, A.J. and Knollenberg, R.G., 1972. Properties of cirrus generating cells. *J. Atmos. Sci.*, 29: 1358-1366.
- Holland, A.C. and Gagne, G., 1970. The scattering of polarized light by polydisperse systems of irregular particles. *Appl. Opt.*, 9: 1113-1121.
- Iskander, M.F., Lakhtakia, A. and Durney, C., 1983. A new procedure for improving the solution stability and extending the frequency range of the EBCM. *IEEE Trans. Antennas and Propagat.*, AP-31: 317-324.
- Jacobowitz, H., 1971. A method for computing transfer of solar radiation through clouds of hexagonal ice crystals. *J. Quant. Spectrosc. Radiat. Transfer*, 11: 691-695.
- Kerker, M., 1969. *The Scattering of Light and Other Electromagnetic Radiation*. Academic Press, New York, 666 pp.
- Liou, K.N., 1972. Light scattering by ice clouds in the visible and infrared: a theoretical study. *J. Atmos. Sci.*, 29: 524-536.
- Liou, K.N., 1980. *An Introduction to Atmospheric Radiation*. Academic Press, New York, 392 pp.
- Liou, K.N. and Lahore, H., 1974. Laser sensing of cloud composition: A backscatter depolarization technique. *J. Appl. Meteor.*, 13: 257-263.
- Liou, K.N. and Ou, S.C., 1989. The role of cloud microphysical processes in climate: An assessment from a one-dimensional perspective. *J. Geophys. Res.*, 94: 8599-8607.
- Lord Rayleigh, 1918. The dispersal of light by a dielectric cylinder. *Phil. Mag.*, 36: 365-376.
- Minnis, P., Young, D., Heck, P., Liou, K.N. and Takano, Y., 1992. Satellite analyses of cirrus cloud properties during the FIRE phase-II cirrus intensive field observations over Kansas. 11th Int. Conf. Clouds and Precipitation, Montreal, Canada, August 17-21, pp. 480-483.
- Mugnai, A. and Wiscombe, W.J., 1986. Scattering from nonspherical Chebyshev particles. 1:

- Cross sections, single-scattering albedo, asymmetry factor, and backscattered fraction. *Appl. Opt.*, 25: 1235-1244.
- Mugnai, A. and Wiscombe, W.J., 1989. Scattering from nonspherical Chebyshev particles. 3: Variability in angular scattering patterns. *Appl. Opt.*, 28: 3061-3073.
- Muinonen, K., Lumme, K., Peltoniemi, J. and Irvine, W.M., 1989. Light scattering by randomly oriented crystals. *Appl. Opt.*, 28: 3051-3060.
- Nikiforova, N.K., Pavlova, L.N., Petrushin, A.G., Snykov, V.P. and Volkovitsky, O.A., 1977. Aerodynamic and optical properties of ice crystals. *J. Aerosol Sci.*, 8: 243-250.
- Platt, C.M.R., Abshire, N.L. and McNice, G.T., 1978. Some microphysical properties of an ice cloud from lidar observations of horizontally oriented crystals. *J. Appl. Met.*, 17: 1220-1224.
- Pollack, J.B. and Cuzzi, J.N., 1980. Scattering by nonspherical particles of size comparable to a wavelength: a new semi-empirical theory and its application to tropospheric aerosols. *J. Atmos. Sci.*, 37: 868-881.
- Purcell, E.M. and Pennypacker, C.R., 1973. Scattering and absorption of light by nonspherical dielectric grains. *Astrophys. J.*, 186: 705-714.
- Rockwitz, K.D., 1989. Scattering properties of horizontally oriented ice crystal columns in cirrus clouds. Part 1. *Appl. Opt.*, 28: 4103-4110.
- Sassen, K., 1976. Polarization diversity lidar returns from virga and precipitation: Anomalies and the bright band analogy. *J. Appl. Meteorol.*, 15: 292-300.
- Sassen, K. and Liou, K.N., 1979. Scattering of polarized laser light by water droplet, mixed phase, and ice crystal clouds: I. Angular scattering patterns. *J. Atmos. Sci.*, 36: 838-851.
- Singham, S.B. and Bohren, C.F., 1987. Light scattering by an arbitrary particle: a physical reformulation of the coupled dipole method. *Opt. Lett.*, 12: 10-12.
- Stackhouse, P.W. and Stephens, G.L., 1991. A theoretical and observational study of the radiative properties of cirrus: results from FIRE 1986. *J. Atmos. Sci.*, 48: 2044-2059.
- Takano, Y. and Jayaweera, K., 1985. Scattering phase matrix for hexagonal ice crystals computed from ray optics. *Appl. Opt.*, 24: 3254-3263.
- Takano, Y. and Liou, K.N., 1989. Solar radiative transfer in cirrus clouds. Part I: Single-scattering and optical properties of hexagonal ice crystals. *J. Atmos. Sci.*, 46: 3-19.
- Takano, Y., Liou, K.N. and Minnis, P., 1992. The effects of small ice crystals on cirrus infrared radiative properties. *J. Atmos. Sci.*, 49: 1487-1493.
- van de Hulst, H.C., 1957. *Light Scattering by Small Particles*. Wiley, New York, 470 pp.
- Volkovitsky, O.A., Pavlova, L.N. and Petrushin, A.G., 1980. Scattering of light by ice crystals. *Izv. Acad. Sci. USSR. Atmos. Ocean. Phys.*, 198: 90-102.
- Wait, J.R., 1955. Scattering of a plane wave from a circular dielectric cylinder at oblique incidence. *Can. J. Phys.*, 33: 189-195.
- Waterman, P.C., 1965. Matrix formulation of electromagnetic scattering. *Proc. IEEE*, 53: 805-812.
- Wendling, P., Wendling, R. and Weickmann, H.K., 1979. Scattering of solar radiation by hexagonal ice crystals. *Appl. Opt.*, 18: 2663-2671.
- Wiscombe, W.J. and Mugnai, A., 1988. Scattering from nonspherical Chebyshev particles. 2: Means of angular scattering patterns. *Appl. Opt.*, 27: 2405-2421.
- Zerull, R.H., 1976. Scattering measurements of dielectric and absorbing nonspherical particles. *Beitr. Phys. Atmos.*, 49: 168-188.
- Zerull, R.H. and Giese, R.H., 1974. Microwave analogue studies. In: T. Gehrels (Editor), *Planets, Stars, and Nebulae Studied with Photopolarimetry*, University of Arizona Press, 901-914.
- Zerull, R.H., Giese, R.H. and Weiss, K., 1977. Scattering measurements of irregular particles vs. Mic theory. *Opt. Polar.*, 112: 191-199.

**Improvements of an Ice-Phase Microphysics Parameterization for use in
Numerical Simulations of Tropical Convection**

STEVEN K. KRUEGER, QIANG FU, AND K. N. LIOU

Department of Meteorology, University of Utah, Salt Lake City, Utah

HUNG-NENG S. CHIN

Lawrence Livermore National Laboratory, Livermore, California

To Appear in *Journal of Applied Meteorology*, November, 1994

Corresponding author address: Prof. Steven K. Krueger, Department of Meteorology,
University of Utah, Salt Lake City, UT 84112

ABSTRACT

It is important to properly simulate the extent and ice water content of tropical anvil clouds in numerical models that explicitly include cloud formation because of the significant effects that these clouds have on the radiation budget. For this reason, a commonly used bulk ice-phase microphysics parameterization was modified to more realistically simulate some of the microphysical processes that occur in tropical anvil clouds. Cloud ice growth by the Bergeron process and the associated formation of snow were revised. The characteristics of graupel were also modified in accord with a previous study. Numerical simulations of a tropical squall line demonstrate that the amount of cloud ice and the extent of anvil clouds are increased to more realistic values by the first two changes.

1. Introduction

Satellite imagery shows that large portions of the tropics are covered by extensive cirrus anvil clouds (Liou 1986) associated with mesoscale convective systems. Recent GCM simulations show that tropical anvil clouds strongly influence both convection and the large-scale circulation of the atmosphere through their effects on the radiation budget and through the thermodynamical consequences of phase changes within clouds (Randall et al. 1989). The importance of tropical anvil clouds is also evident from the fact that the stratiform (anvil) rain accounts for 32 to 49% of the total rain in the tropics (Gamache and Houze 1983).

More realistic parameterizations of tropical anvil clouds are needed in GCMs (Randall et al. 1989). For studying cloud-radiation interactions and improving GCM cloud parameterizations, cumulus ensemble models (CEMs) are an important tool (Xu 1993). CEMs are cloud-resolving models used for relatively large-domain and long-time simulations. To study cloud-radiation interactions in tropical mesoscale convective systems with a CEM (or other numerical model that includes explicit cloud formation), the cloud properties that strongly affect the radiative fluxes, such as the extent and ice water content of anvil clouds, should be realistically simulated.

In cloud-resolving models used for simulating tropical convection, microphysical processes are most commonly parameterized following the bulk method with the hydrometeors categorized into five types: cloud droplets, raindrops, ice crystals, snow, and hail or graupel (McCumber et al. 1991). For several years, the bulk ice-phase microphysics code developed by Lord et al. (1984) and based on Lin et al. (1983) has been used in the 2D UCLA/University of Utah CEM (UU CEM) (Xu and Krueger 1991; Xu et al. 1992). Lord et al. generally followed Lin et al. except that they modified the density of graupel and the intercept parameter of rain to represent conditions in hurricanes better.

McCumber et al. (1991) compared simulations of tropical convection using the Lin et al., Lord et al., and Rutledge and Hobbs (1984) microphysical parameterization schemes. They compared some features of the simulated convection (the anvil portion of the surface rainfall and the intensity

of the radar bright band) to observations. They found that for the three-ice-class schemes, the optimal mix of bulk ice hydrometeors is cloud ice-snow-graupel.

We have extended McCumber et al.'s study by examining the extent and ice water content of tropical anvil clouds simulated by the UU CEM using the Lord et al. microphysics code. We find that the extent of the anvil clouds is underpredicted and that the cloud ice content is too low compared with observations (Houze and Betts 1981; Ackerman et al. 1988). Lord et al. noted that parameterization of nucleation and subsequent growth processes for cloud water and cloud ice is an extremely difficult task because these processes are highly dependent on temperature, local supersaturation, droplet size and crystal habit. Consequently, it is currently impractical to predict the detailed evolution of the cloud water and cloud ice fields in cloud-resolving models. However, improvements can be made within the framework of Lord et al.'s microphysics parameterization to simulate a more realistic cloud ice distribution in tropical anvil clouds for radiative heating calculations.

In the next two sections, we describe our modifications to Lord et al.'s parameterizations of cloud ice growth by the Bergeron process and snow formation associated with the Bergeron process. In section 4, we document the changes we made to Lord et al.'s graupel parameters based on McCumber et al.'s results. In section 5, we compare the anvil extent, hydrometeor evolution, and hydrometeor profiles in two simulations of a tropical squall: one with Lord et al.'s original microphysics code, and one with our modified version. The results are summarized in section 6.

2. Growth of cloud ice by the Bergeron process

In Lord et al.'s parameterization, cloud ice increases due to nucleation and depositional growth, and decreases due to sublimation, conversion to snow, and accretion by snow and graupel. The interactions among cloud water, cloud ice, and water vapor due to condensation/evaporation, deposition/sublimation, melting of cloud ice ($T \geq 0^\circ \text{C}$), and homogeneous freezing of cloud water ($T \leq -40^\circ \text{C}$) are represented by a "saturation adjustment" scheme and a simple model of the Bergeron process.

A saturation adjustment scheme is based on the assumption that all supersaturated vapor condenses or deposits. Lord et al. introduced a generalized saturation adjustment scheme for cloud water and cloud ice. In their scheme, the saturation mixing ratio is defined as the mass-weighted average of the respective saturation values over liquid water and ice when both cloud water and cloud ice are present. All supersaturated water vapor is partitioned between cloud water and cloud ice as a linear function of temperature between 0° C and 40° C.

The Bergeron process represents the vapor depositional growth of cloud ice or snow at the expense of cloud water in supercooled clouds ($-40^{\circ} \text{C} \leq T \leq 0^{\circ} \text{C}$) which are saturated with respect to water and therefore supersaturated with respect to ice due to the difference in saturation vapor pressures of ice and water. This process cannot be accounted for by a saturation adjustment scheme. The Bergeron process for cloud ice in Lord et al. (I_{dw}) is based on the formulation by Lin et al. (P_{IDW}) which follows that of Hsie et al. (1980) (P_{CNWD}). We will use Lin et al.'s notation henceforth.

The growth rate of cloud ice due to nucleation and the Bergeron process (P_{IDW}) is based on the growth rate of ice crystals with the mass of a natural ice nucleus ($1.05 \times 10^{-15} \text{ g}$) and a number concentration equal to the number of natural ice nuclei. The growth rate of a single crystal, as parameterized by Koenig (1971), is

$$dm_i/dt = a_1 m_i^{a_2},$$

where m_i is the ice crystal mass, and a_1 and a_2 are positive temperature-dependent coefficients tabulated by Koenig, where a_2 ranges from about 0.4 to 0.6. The mass of a natural ice nucleus is much smaller than a typical ice crystal mass. In our modified formulation, instead of the ice nucleus mass, we use the average mass of an ice crystal, which is estimated to be

$$m_i = q_i \rho_a / N_n,$$

where q_i is the mixing ratio of cloud ice, ρ_a is the density of air, and N_n is the number concentration of active natural ice nuclei (Fletcher 1962).

To verify that this modification better represents the Bergeron process, a rising-parcel model was used along with Lord et al.'s saturation adjustment and P_{IDW} in its original and modified forms. The results are compared to those produced by a more realistic approach that explicitly calculates the condensation and evaporation of cloud water, the initiation of cloud ice, and the depositional growth of cloud ice (Rutledge and Hobbs 1983). The parcel is assumed to rise without mixing with its environment. The initial pressure, temperature, and mixing ratio of water vapor are taken to be 559 mb, 270 K, and 2.1 g kg⁻¹, respectively. The parcel moves upward with a speed of 0.02 mb s⁻¹ and at the same time the pressure in the parcel adjusts to the ambient pressure. A 25-s time step was used in model simulations.

Fig. 1 shows the parcel model results for the mixing ratios of water vapor, cloud water, and cloud ice as a function of time using (a) the original Lord et al. formulation, (b) the modified formulation, and (c) the Rutledge and Hobbs formulation. The depositional growth of cloud ice at the expense of cloud water is insignificant when using the original Lord et al. formulation (Fig. 1a). Results computed using the modified ice crystal mass (Fig. 1b) show much better agreement with the results obtained using Rutledge and Hobbs' approach (Fig. 1c). After 350 time steps, the mixing ratio of cloud water becomes zero in Fig. 1b due to the Bergeron process. The slight differences between Figs. 1b and 1c are attributed to the different mechanisms of cloud ice initiation in the two schemes.

3. Snow formation associated with the Bergeron process

The parameterized Bergeron process just described also produces snow from cloud ice via the growth of Bergeron process embryos (P_{SFI}) and from cloud water via the Bergeron process and riming (P_{SFW}). Hsie et al. and Lin et al. expressed P_{SFI} and P_{SFW} as

$$P_{SFI} = q_i / \Delta t_1, \quad (1)$$

and

$$P_{SFW} = N_{ir} (a_1 m_{ir}^{a_2} + \pi \rho_a q_c r^2 U_{ir}),$$

where Δt_1 is the time scale needed for a crystal to grow from radius r_0 to radius r given by

$$\Delta t_1 = \frac{1}{a_1(1-a_2)} \left[m_{ir}^{(1-a_2)} - m_{ir_0}^{(1-a_2)} \right],$$

and q_c is the mixing ratio of cloud water, and m_{ir} and U_{ir} are the mass and terminal velocity of an ice crystal with radius r . The number concentration of ice crystals with radius r is

$$N_{ir} = \frac{q_i \Delta t}{m_{ir} \Delta t_1},$$

where Δt is the time step in the numerical simulation.

Eq. (1) indicates that the time scale Δt_1 determines the rate at which cloud ice is converted to snow. In their expressions for P_{SFI} and P_{SFW} , Lin et al. used a time scale for a crystal to grow from $r_0 = 40 \mu\text{m}$ to $r = 50 \mu\text{m}$, which is somewhat artificially set (Hsie et al.). Based on in situ aircraft observations, the mean effective sizes of ice crystal size distributions in ice clouds range from 24 to 124 μm (Fu and Liou 1993), which correspond to area-equivalent effective radii from 14 to 126 μm . Therefore, it is more realistic to define Δt_1 as the time needed for an ice crystal to

grow from 40 to 100 μm and to determine P_{SFW} based on a 100 μm radius ice crystal. Note that 40 μm is smaller than the median and 100 μm may be also smaller than the upper bound of the observed range of mean effective radii, because very small ice crystals ($< 20 \mu\text{m}$) cannot be observed by present optical probes. The maximum q_i obtained using the new time scale in the parcel model is about three times larger than obtained using the original time scale.

Cloud ice continues to be converted to snow by P_{SFI} in Lord et al.'s formulation even when there is no cloud water. Since Lord et al. assumed that cloud ice does not fall, but snow does, P_{SFI} in this case acts like a crude fall speed parameterization for cloud ice. To validate this approach, it should be compared to a detailed parameterization of ice crystal fall speeds.

4. Graupel characteristics

For tropical cumuli over the oceans, McCumber et al. concluded that it is better to choose the bulk ice hydrometeor mix to be cloud ice-snow-graupel rather than cloud ice-snow-hail. In their numerical simulations of tropical convection, graupel, with a small terminal velocity, produced more realistic dynamic, thermodynamic, and radar characteristics of anvil clouds than did fast-falling hail. In particular, McCumber et al. found that choosing graupel parameters rather than hail parameters for the graupel/hail class of precipitating ice produced more realistic radar bright bands in tropical squall line simulations. Therefore, we now use the intercept parameter n_0 and density ρ for graupel given by Rutledge and Hobbs (1984): $n_{0G} = 4 \times 10^6 \text{ m}^{-4}$ and $\rho_G = 0.4 \times 10^3 \text{ kg m}^{-3}$. Lord et al. used $n_{0G} = 4 \times 10^4 \text{ m}^{-4}$ and $\rho_G = 0.3 \times 10^3 \text{ kg m}^{-3}$. The most significant difference is in the intercept parameter. Rutledge and Hobbs' graupel parameters result in lower mass-weighted fall speeds. Lord et al.'s n_{0G} value is actually more representative of hail. This is evident in McCumber et al.'s reported average terminal velocities for graupel/hail for the three schemes: Lin et al. (hail), 10.2 m s^{-1} ; Lord et al., 7.0 m s^{-1} ; and Rutledge and Hobbs (graupel), 2.5 m s^{-1} .

We use the intercept parameter for rain given by Lin et al., $n_{0R} = 8 \times 10^6 \text{ m}^{-4}$, in place of that used by Lord et al. (which is more appropriate for tropical cyclones), $n_{0R} = 22 \times 10^6 \text{ m}^{-4}$. The snow parameters are unchanged from Lord et al.'s: $n_{0S} = 3 \times 10^6 \text{ m}^{-4}$ and $\rho_S = 0.1 \times 10^3 \text{ kg m}^{-3}$.

The terminal velocity that we use for graupel was determined from measurements reported by Locatelli and Hobbs (1974). Figure 2 shows fall speed vs. diameter curves for five different graupel types based on the velocity-size relationships given by Locatelli and Hobbs. The fallspeed-diameter relation used by Rutledge and Hobbs (1984) is for "lump graupel c". We expect that the average relationship is more suitable for a microphysics parameterization. Using numerical fitting, we obtained an average relationship as follows: $V_G = 1.288D^{0.5}$, where the units for V_G and D are in $m\ s^{-1}$ and mm , respectively. The fall speed vs. diameter curve determined from the above equation is also shown in Fig. 2.

Following Rutledge and Hobbs (1984), the collection efficiencies of snow for cloud ice and of graupel for snow ($T < 0^\circ C$) are both set to 0.1. These values are a better match to the measurements presented by Lin et al. (in their Fig. 4) than the collection efficiencies used by Lin et al. Also, the thresholds for cloud ice and snow aggregation we use are 0.6×10^{-3} and 1.0×10^{-3} , instead of 1.0×10^{-3} and 0.6×10^{-3} as reported by Lin et al. (1983). There is an error in the units of a_1 in Hsie et al. (1980). The units should be $g^{1-a_2}s^{-1}$ in order to agree with Koenig (1971). There are also errors in Eqs. (43) and (47) in Lin et al. (1983). The denominator $3C_D$ should be multiplied by ρ in each.

5. Numerical Simulations and Results

We used the UU CEM to perform two simulations of an idealized tropical squall line to assess the effects of our modifications to the microphysics parameterization. One simulation used Lord et al.'s original microphysics scheme while the other used the modified microphysics scheme described in the previous section. The UU CEM is described in Krueger (1988) and Xu and Krueger (1991). For the two tropical squall line simulations, we used a large horizontal domain in order to include an extensive anvil. The domain is 512 km wide with a horizontal grid size of 1 km. The depth of the domain is about 19 km with a stretched coordinate consisting of 33 layers. Near the surface the vertical grid size is 100 m, while near the model top it is 1 km. The initial thermodynamic state is based on the GATE Phase III mean sounding. The geostrophic (and initial)

horizontal wind profile normal to the squall line is similar to the one used by Xu et al. (1992) in their simulation Q04 and resembles squall line profiles observed during GATE Phase III. We used the same large scale advective cooling and moistening profiles as were used in simulation Q04. Each simulation was for 12 hours. The squall line was initialized by a low-level cool pool (Tao et al. 1991) after one hour. In each simulation, the large-scale forcing was constant for the first 4 hours, decreased to zero during the next 4 hours, and then remained zero for the last 4 hours.

Fig. 3 shows Hovmüller ($x-t$) diagrams of cloud top temperature from the simulations with (a) Lord et al.'s original microphysics scheme and (b) the modified scheme. The temperature is indicated by a linear gray scale: white represents 200 K, while black denotes 300 K. The cloud top temperature is defined here as the temperature at the first level for which the mass of "suspended water" integrated downward from the model top exceeds 0.1 kg m^{-2} . "Suspended water" includes cloud water, cloud ice, and snow. Anvil clouds associated with the squall lines appear bright in Fig. 3. Because snow is included in "suspended water", the differences between the two simulations are less dramatic than they would be if snow was not included. Despite this, the anvil cloud displayed in Fig. 3b (modified scheme) is still significantly more extensive than the one in Fig. 3a (original scheme). The maximum size of the anvil increased from less than 100 km (Fig. 3a) to about 180 km (Fig. 3b) due to the microphysics modifications. The typical anvil size observed during GATE was about 200 km (Houze and Betts 1981).

Hovmüller diagrams of the vertically integrated cloud ice content for the two simulations are shown in Fig. 4. In the black regions enclosed by white, amounts exceed 0.5 kg m^{-2} . Here the differences are dramatic: the modified scheme produces much more cloud ice than the original scheme. Amounts exceeding 0.5 kg m^{-2} are limited to the convective line with the original scheme, but extend about 50 km into the anvil with the modified scheme.

Fig. 5 shows time series of domain total amounts of each hydrometeor species for the two simulations. The cloud water and rain water amounts do not differ significantly between the two. Cloud ice and graupel increase with the modified scheme, while snow decreases. In the original

scheme, "cloud ice" represents small ice crystals, "snow" represents medium to large ice crystals plus aggregates, while "graupel" represents large, fast-falling ice particles. The result is small cloud ice amounts, large snow amounts, and small graupel amounts. In the modified scheme, "cloud ice" represents small to medium-sized ice crystals, "snow" represents large ice crystals, and "graupel" represents small, slow-falling ice particles (graupel and aggregates). The result is larger cloud ice amounts, lower snow amounts, and larger graupel amounts.

Fig. 6 shows time and horizontally averaged mixing ratio profiles for each hydrometeor species for the two simulations. Lord et al.'s hydrometeor profiles in a mesoscale convective region of a tropical cyclone resemble ours using the original code (compare our Fig. 6a to their Fig. 6). The average cloud ice and graupel mixing ratios are larger with the modified scheme, and the average snow mixing ratios less. Comparing our Fig. 6 to McCumber et al.'s Fig. 3 shows that changing the graupel parameters alone has a rather small effect on the average cloud ice mixing ratios compared to the the modifications that we made to increase the anvil's extent and its cloud ice content.

The sum of the graupel and snow profiles in the upper troposphere in the modified case is similar to the snow profile in the original case. This suggests that the lower fall speed of the graupel in the modified scheme allows it to be carried to higher levels in the convective cores, from which it is expelled into the anvil cloud where it descends and grows by accreting snow. The graupel profile in the modified case has a sharp lower boundary where it melts. This produces a more realistic radar bright band than in the original case (McCumber et al. 1991).

The microphysical changes also affect the simulated squall line dynamics. Analyzing these effects in detail is a worthy task for future research, but is beyond the scope of this note. However, we did examine the gust front relative horizontal velocity fields for both simulations averaged over the two hour period from 6 to 8 hours. We found that (1) the rear inflow jet is weaker but more extensive and deeper with the modified compared to the original microphysics, and that (2) the front-to-rear jet is also weaker with the modified compared to the original

microphysics. The second result suggests that the more extensive anvil with the modified microphysics is not due to a stronger front-to-rear jet.

6. Summary

It is important to properly simulate the extent and ice water content of tropical anvil clouds in numerical models that explicitly include cloud formation because of the significant effects that these clouds have on the radiation budget. For this reason, the bulk ice-phase microphysics parameterization developed by Lord et al. (1984) and based on Lin et al. (1983) was modified to more realistically simulate some of the microphysical processes that occur in tropical anvil clouds. Cloud ice growth by the Bergeron process and the associated formation of snow were revised. The characteristics of graupel were also modified in accord with McCumber et al.'s (1991) conclusions. Numerical simulations of a tropical squall line demonstrate that the amount of cloud ice and the extent of anvil clouds are increased to more realistic values by the first two changes.

Acknowledgments. This research has been supported by AFOSR Grant 91-0039, NASA Grant NAG 5-1050, and the ARM program under the auspices of the DOE by the Lawrence Livermore National Laboratory under Contract W-7405-Eng-48. We thank Dr. N. Rao for assistance in preparing this manuscript.

REFERENCES

- Ackerman, T.P., K.N. Liou, F.P.J. Valero, and L. Pfister, 1988: Heating rates in tropical anvils. *J. Atmos. Sci.*, **45**, 1606-1623.
- Fletcher, N.H., 1962: *The Physics of Rain Clouds*. Cambridge University Press. 390 pp.
- Fu, Q., and K.N. Liou, 1993: Parameterization of the radiative properties of cirrus clouds. *J. Atmos. Sci.*, **50**, 2008-2025.

- Gamache, J.F., and R.A. Houze, Jr., 1983: Water budget of a mesoscale convective system in the tropics. *J. Atmos. Sci.*, **40**, 1835-1850.
- Hsie, E.Y., R.D. Farley, and H.D. Orville, 1980: Numerical simulation of ice phase convective cloud seeding. *J. Appl. Meteor.*, **19**, 950-977.
- Houze, R.A., Jr., and A.K. Betts, 1981: Convection in GATE. *Rev. Geophys. Space Phys.*, **16**, 541-576.
- Koenig, L.R., 1971: Numerical modeling of ice deposition. *J. Atmos. Sci.*, **28**, 226-237.
- Krueger, S.K., 1988: Numerical simulation of tropical cumulus clouds and their interaction with the subcloud layer. *J. Atmos. Sci.*, **45**, 2221-2250.
- Lin, Y.L., R.D. Farley, and H.D. Orville, 1983: Bulk parameterization of the snow field in a cloud model. *J. Climate Appl. Meteor.*, **22**, 1065-1092.
- Liou, K.N., 1986: Influence of cirrus clouds on weather and climate processes: A global perspective. *Mon. Wea. Rev.*, **114**, 1167-1199.
- Locatelli, J.D., and P.V. Hobbs, 1974: Fall speeds and masses of solid precipitation particles. *J. Geophys. Res.*, **79**, 2185-2197.
- Lord, S.J., H.E. Willoughby, and J.M. Piotrowicz, 1984: Role of a parameterized ice-phase microphysics in an axisymmetric, nonhydrostatic tropical cyclone model. *J. Atmos. Sci.*, **41**, 2836-2848.
- McCumber, M., W.K. Tao, J. Simpson, R. Penc, and S.T. Soong, 1991: Comparison of ice-phase microphysical parameterization schemes using numerical simulations of convection. *J. Appl. Meteor.*, **30**, 985-1004.
- Randall, D.A., Harshvardhan, D.A. Dazlich, and T.G. Corsetti, 1989: Interactions among radiation, convection, and large-scale dynamics in a general circulation model. *J. Atmos. Sci.*, **46**, 1943-1970.
- Rutledge, S.A., and P.V. Hobbs, 1983: The mesoscale and microscale structure and organization of clouds and precipitation in midlatitude cyclones. Part VIII: A model for 'seeder-feeder' process in warm-frontal rainbands. *J. Atmos. Sci.*, **40**, 1185-1206.

- Rutledge, S.A., and P.V. Hobbs, 1984: The mesoscale and microscale structure and organization of clouds and precipitation in midlatitude cyclones. Part XII: A diagnostic modeling study of precipitation development in narrow cold-frontal rainbands. *J. Atmos. Sci.*, **41**, 2949-2972.
- Tao, W.K., J. Simpson, and S.T. Soong, 1991: Numerical simulation of a subtropical squall line over the Taiwan strait. *Mon. Wea. Rev.*, **119**, 2699-2723.
- Xu, K.-M., 1993: Cumulus ensemble simulation. *The Representation of Cumulus Convection in Numerical Models*, K. A. Emanuel and D. J. Raymond, Eds., Amer. Meteor. Soc., 221-235.
- Xu, K.M., and S.K. Krueger, 1991: Evaluation of cloudiness parameterizations using a cumulus ensemble model. *Mon. Wea. Rev.*, **119**, 342-367.
- Xu, K.M., A. Arakawa, and S.K. Krueger, 1992: The macroscopic behavior of cumulus ensembles simulated by a cumulus ensemble model. *J. Atmos. Sci.*, **49**, 2402-2420.

FIGURE CAPTIONS

Figure 1. Parcel model results for the mixing ratios of water vapor, cloud water, and cloud ice as a function of time using (a) the original Lord et al. (1984) formulation, (b) the modified formulation, and (c) the Rutledge and Hobbs (1983) formulation.

Figure 2. Fall speed vs. diameter for five different graupel types based on the velocity-size relationships given by Locatelli and Hobbs (1974). Using numerical fitting, we obtained an average relationship: $V_G = 1.288D^{0.5}$, where the units for V_G and D are in $m\ s^{-1}$ and mm , respectively. The fall speed vs. diameter curve based on the fitting is also shown.

Figure 3. Hovmüller ($x-t$) diagrams of cloud top temperature (see text for definition) from the simulations with (a) Lord et al.'s original microphysics scheme and (b) the modified scheme. The temperature is indicated by a linear gray scale from 300 K (black) to 200 K (white).

Figure 4. Hovmüller ($x-t$) diagrams of the vertically integrated cloud ice content from the simulations with (a) Lord et al.'s original microphysics scheme and (b) the modified scheme. The ice content is indicated by a linear gray scale from zero (black) to $0.5\ kg\ m^{-2}$ (white). In the black regions enclosed by white, the ice content exceeds $0.5\ kg\ m^{-2}$.

Figure 5. Time series of domain total amounts of each hydrometeor species from the simulations with (a) Lord et al.'s original microphysics scheme and (b) the modified scheme.

Figure 6. Time and horizontally averaged mixing ratio profiles for each hydrometeor species from the simulations with (a) Lord et al.'s original microphysics scheme and (b) the modified scheme.

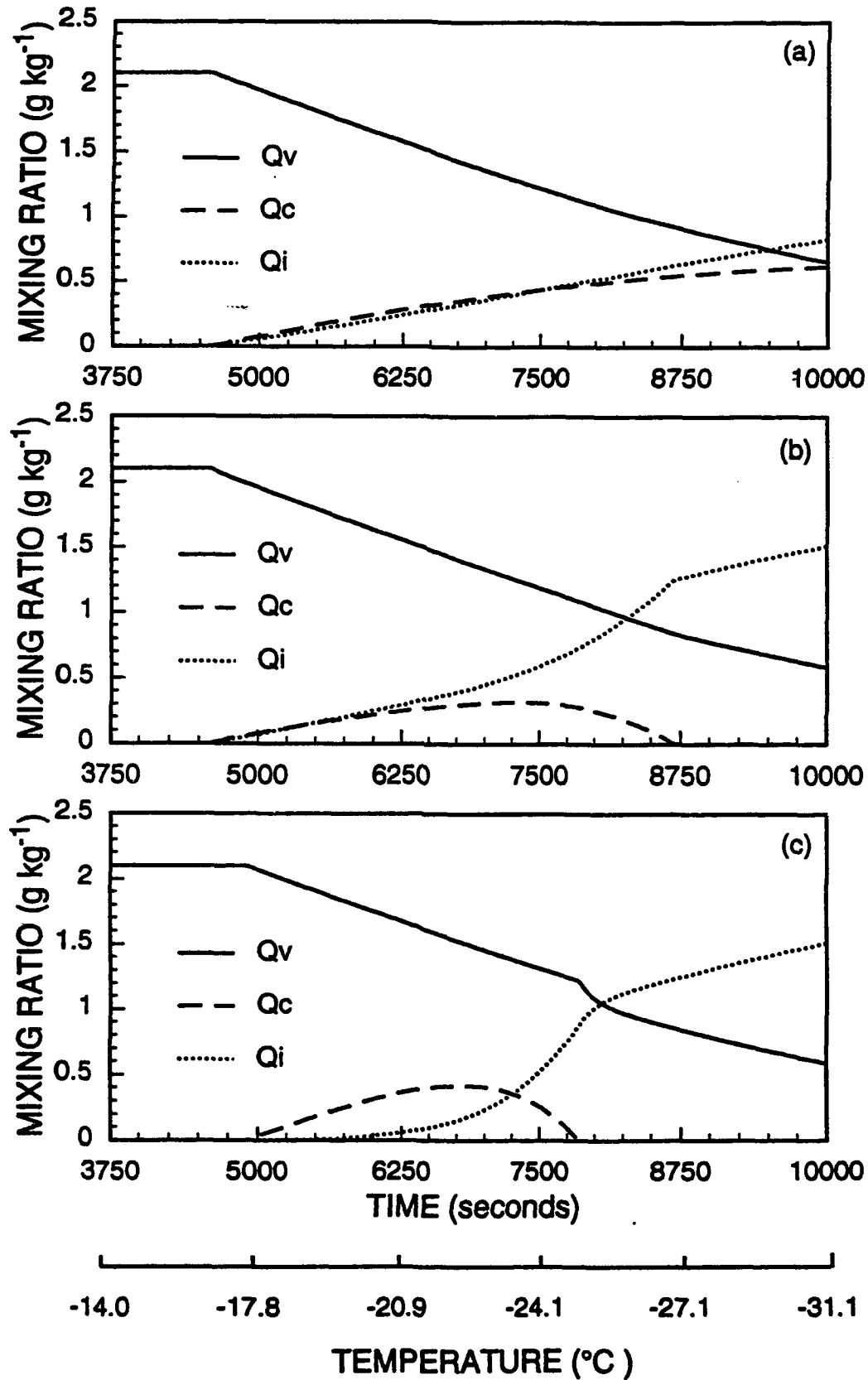


Figure 1. Parcel model results for the mixing ratios of water vapor, cloud water, and cloud ice as a function of time using (a) the original Lord et al. (1984) formulation, (b) the modified formulation, and (c) the Rutledge and Hobbs (1983) formulation.

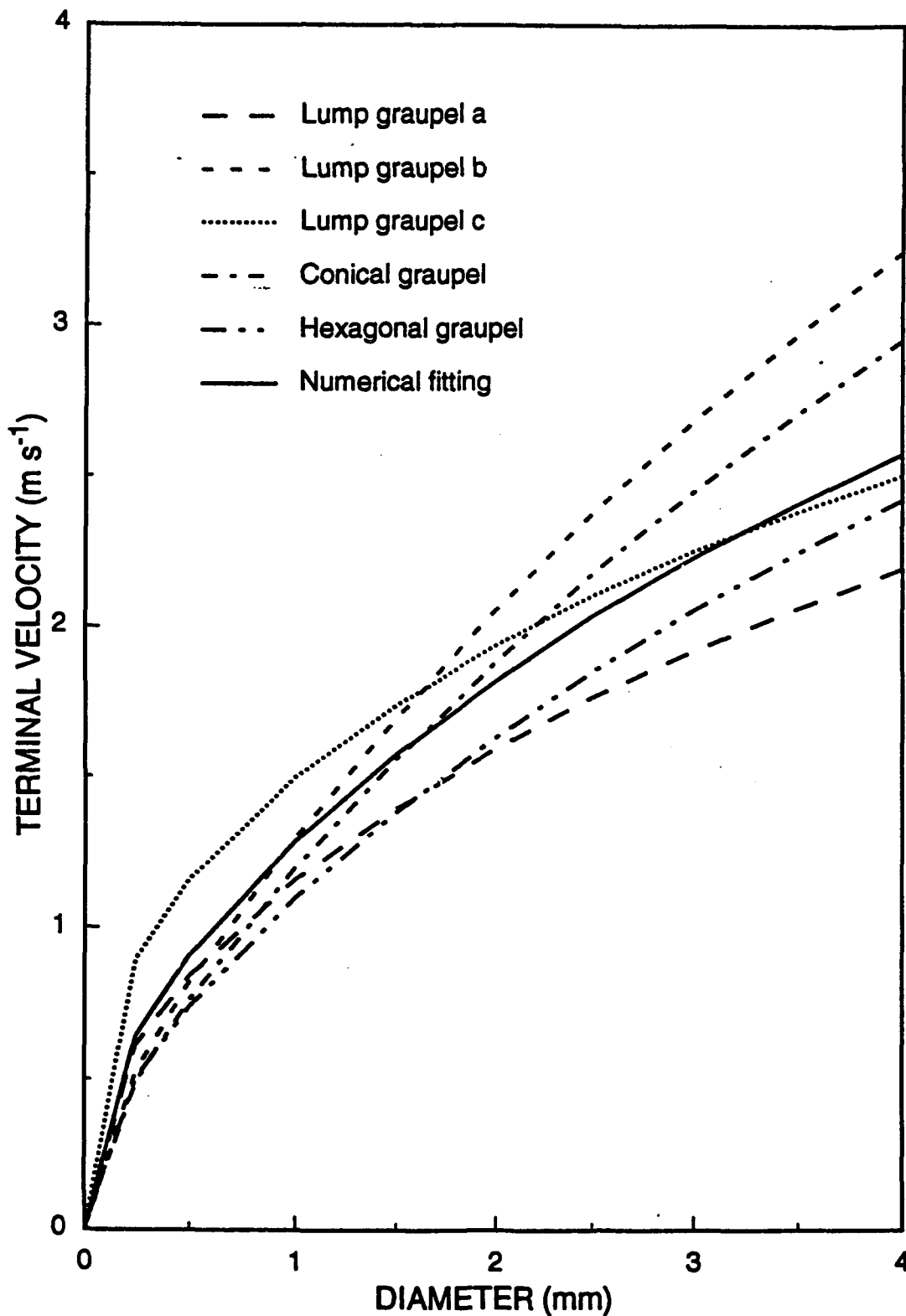


Figure 2. Fall speed vs. diameter for five different graupel types based on the velocity-size relationships given by Locatelli and Hobbs (1974). Using numerical fitting, we obtained an average relationship: $V_G = 1.288D^{0.5}$, where the units for V_G and D are in $m s^{-1}$ and mm , respectively. The fall speed vs. diameter curve based on the fitting is also shown.

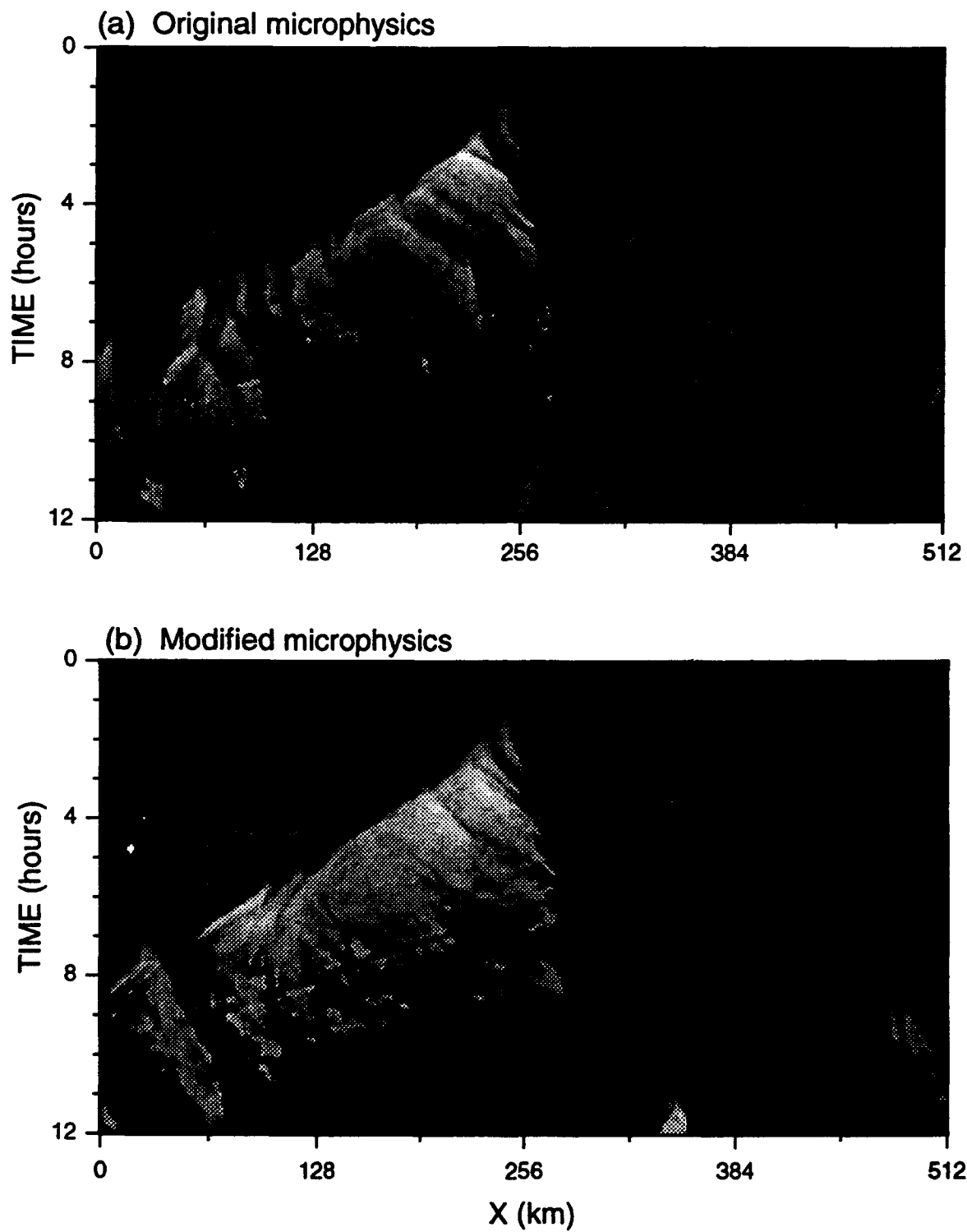


Figure 3. Hovmüller ($x-t$) diagrams of cloud top temperature (see text for definition) from the simulations with (a) Lord et al.'s original microphysics scheme and (b) the modified scheme. The temperature is indicated by a linear gray scale from 300 K (black) to 200 K (white).

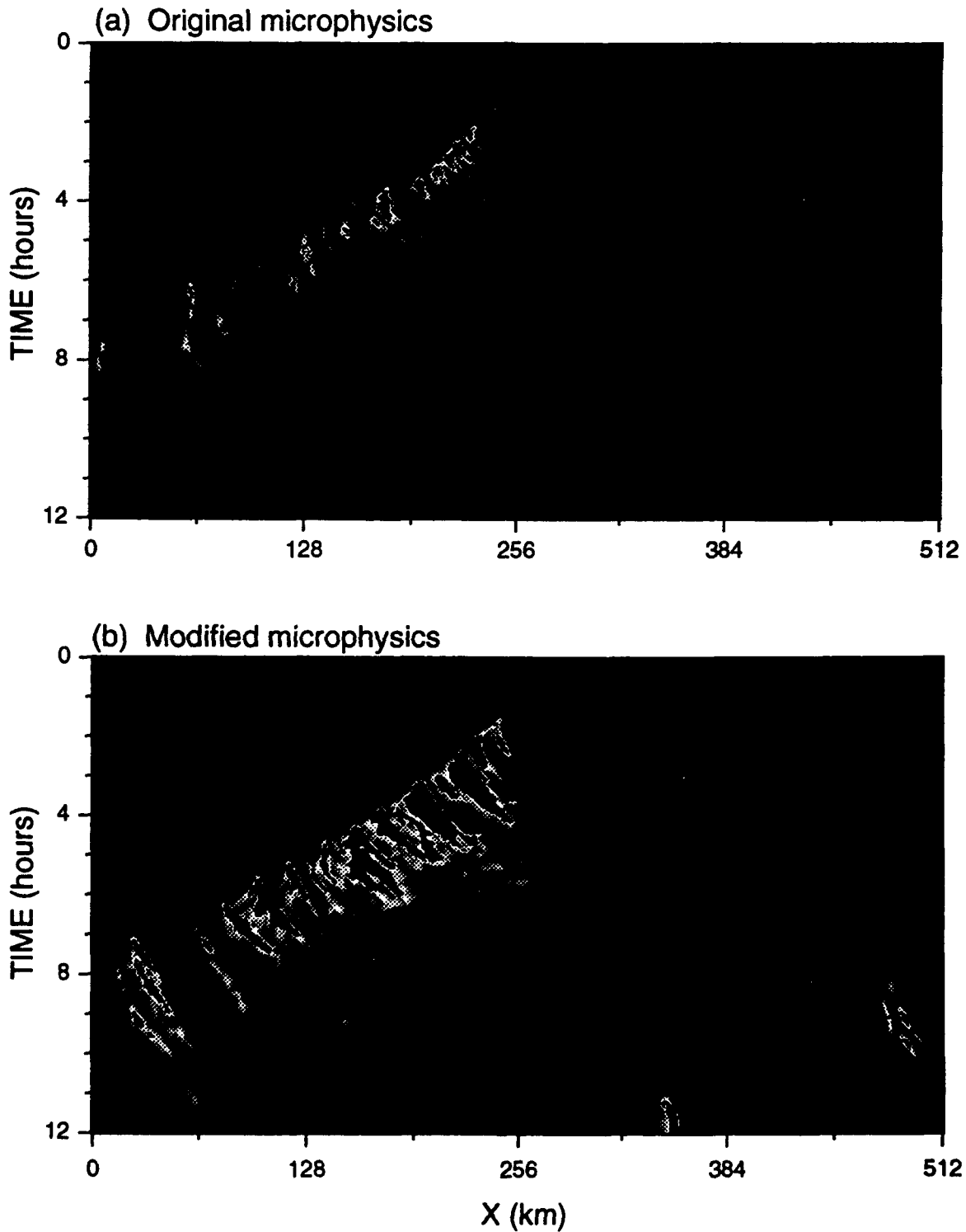


Figure 4. Hovmüller ($x-t$) diagrams of the vertically integrated cloud ice content from the simulations with (a) Lord et al.'s original microphysics scheme and (b) the modified scheme. The ice content is indicated by a linear gray scale from zero (black) to 0.5 kg m^{-2} (white). In the black regions enclosed by white, the ice content exceeds 0.5 kg m^{-2} .

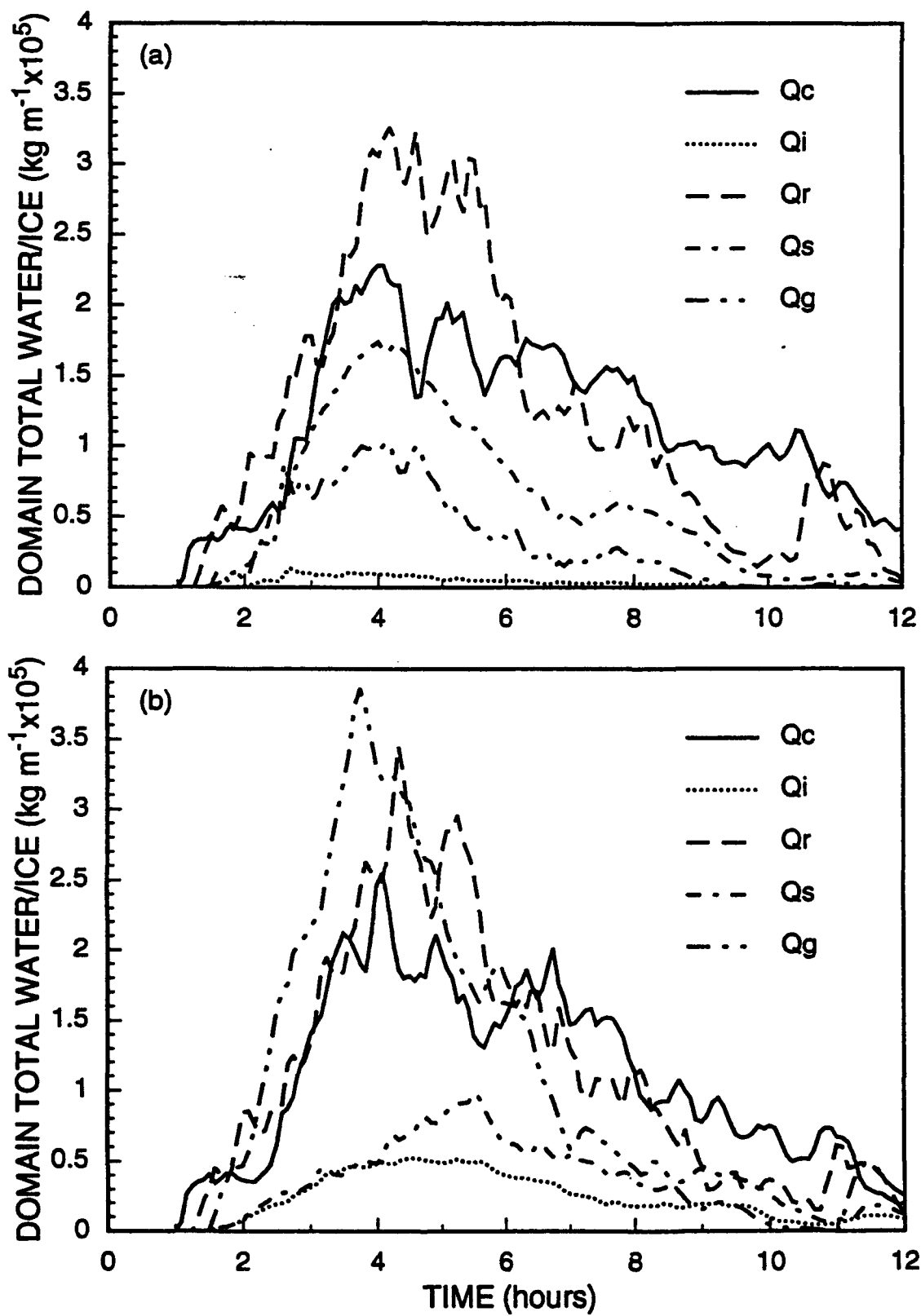


Figure 5. Time series of domain total amounts of each hydrometeor species from the simulations with (a) Lord et al.'s original microphysics scheme and (b) the modified scheme.

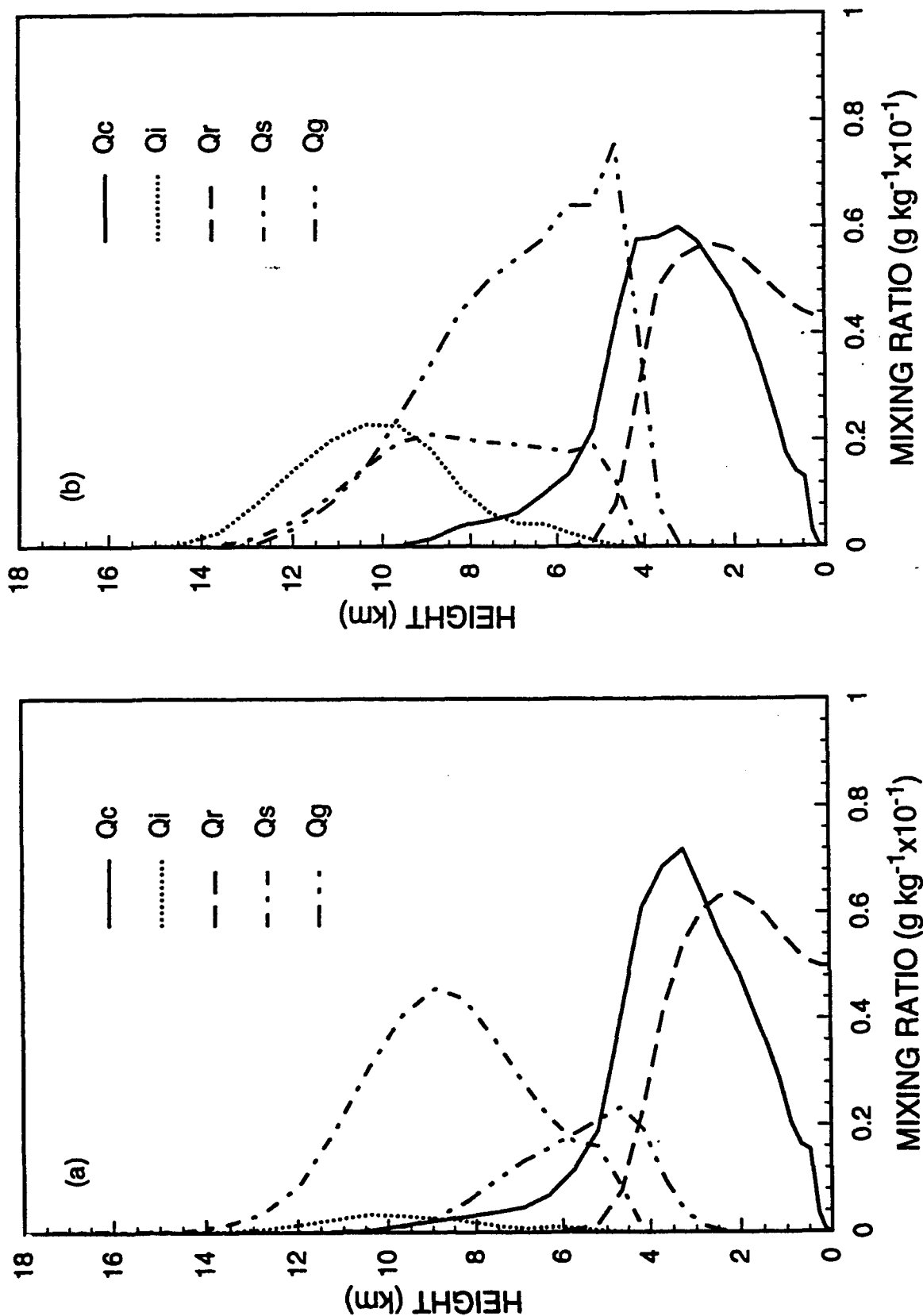


Figure 6. Time and horizontally averaged mixing ratio profiles for each hydrometeor species from the simulations with (a) Lord et al.'s original microphysics scheme and (b) the modified scheme.

INTERACTIONS OF RADIATION AND CONVECTION
IN SIMULATED TROPICAL CLOUD CLUSTERS

Qiang Fu, Steven K. Krueger, and K.N. Liou

Department of Meteorology/CARSS

University of Utah, Salt Lake City, Utah

Submitted to *Journal of the Atmospheric Sciences*

April 1994

Corresponding author address: Dr. Qiang Fu, Department of Meteorology, 819
Wm. C. Browning Bldg., University of Utah, Salt Lake City, UT 84112

ABSTRACT

A two-dimensional cumulus ensemble model is used to study the interactions of radiation and convection in tropical squall cloud clusters. The model includes cloud-scale and mesoscale dynamics, an improved bulk ice microphysics parameterization, and an advanced interactive radiative transfer scheme. The life cycle of a tropical squall line is simulated over a 12-hour period using thermodynamic and kinematic initial conditions as well as large-scale advective forcing typical of a GATE Phase III squall cluster environment. We have focused on the interaction and feedback between longwave (or IR) radiation and cloud processes.

We show that clear-sky IR cooling enhances convection, and hence, surface precipitation. Simulation results reveal an increase of surface precipitation by - 15% (~ 1.7 mm) over a 12-hour period due to this clear-sky cooling. With fully interactive IR radiative heating, direct destabilization of clouds via IR radiative top-cooling and base-warming generates more turbulence and contributes to the longevity and extent of the upper tropospheric stratiform (anvil) clouds associated with deep convection. The greater extent of anvil clouds decreases the outgoing IR flux at the top of the atmosphere by as much as 20 W m^{-2} .

With fully interactive IR radiative heating, the anvil cirrus reduces the IR cooling of the troposphere with respect to the clear-sky values. This cloud IR radiative forcing has a negative feedback on tropical deep convection which we refer to as "anvil cloud IR radiative feedback". This feedback decreases surface precipitation by - 10% (~ 1.3 mm). We also show that IR radiative processes modify the hydrometeor profiles by affecting convection. On changing the cloud particle size distributions prescribed in radiation calculations, we

further demonstrate that the size distributions significantly influence the convective activity through their effects on the cloud IR radiative forcing.

The impact of clear-air IR cooling and cloud radiative forcing on deep convection is further examined by using the cloud-work function, which is a generalized measure of the moist convective instability in the large-scale environment. The clear-air IR cooling tends to increase the cloud-work function, but the cloud IR radiative forcing tends to reduce it, especially for the deepest clouds.

1. Introduction

Cloud systems influence the large-scale circulation of the atmosphere through radiative effects, thermodynamical consequences of phase changes, turbulent and convective transport, and precipitation. Significant uncertainties exist in the representation of clouds and cloud processes in general circulation models (GCMs). Reliable prediction of global climate change will require a comprehensive understanding of and appropriate parameterizations for different kinds of cloud systems. Among them, tropical deep convection is of primary importance (Riehl and Malkus 1958; Simmons 1982). Moreover, the upper tropospheric stratiform (anvil) clouds associated with deep convection require more and specific attention because of their importance in climate studies and because of the infancy of the parameterizations for these clouds (Randall 1989; Randall et al. 1989).

Radiative heating plays an important role in the evolution of tropical deep convection. Based on cloud-scale and mesoscale modeling and observational studies, three mechanisms for the interaction of radiation and convection have been proposed: (1) radiative destabilization of the tropical environment (Dudhia 1989); (2) direct destabilization of the upper-tropospheric stratiform clouds via cloud base-warming and top-cooling (Chen and Cotton 1988; Ackerman et al. 1988; Lilly 1988); (3) production of a secondary circulation by horizontal differential radiative heating between cloudy and clear regions (Gray and Jacobson 1977). The first mechanism is due to the domainwide clear-air radiative cooling above a moist boundary layer, which enhances convection and hence surface precipitation. The second contributes to the longevity of anvil clouds but has little direct effect on precipitation. The third also tends to sustain convection. These mechanisms have been widely used to explain interactions between radiation and convection (Churchill and Houze 1991; Tao et al. 1991, 1993; Miller and Frank 1993; Sui et al. 1994; Chin 1994; Xu and Randall 1994). One aspect of cloud-

radiation interaction that has not been addressed in these studies, however, is the effect on convection of atmospheric IR warming due to clouds.

Clouds are the most important regulator of both solar and IR radiative fields. By reflecting incoming solar radiation back to space, clouds cool the earth-atmosphere system (solar albedo effect). At the same time, by absorbing IR radiation emitted by the underlying atmosphere and surface and reradiating it to space at colder temperatures, clouds warm the earth-atmosphere system (IR greenhouse effect). Because the atmosphere is relatively transparent to solar radiation, cooling of the system due to the solar albedo effect occurs primarily at the surface. The upper-tropospheric stratiform anvil clouds associated with tropical deep convection produce a strong IR greenhouse effect, which is mainly confined within the atmosphere (Ramanathan 1987; Fu and Liou 1993). In the last few years, a term referred to as cloud radiative forcing has been frequently used to denote the effect of clouds on the radiation field. The cloud IR radiative forcing through the atmospheric IR warming effect of anvil clouds could have a significant effect on the evolution of convection.

In this study we use a two-dimensional cumulus ensemble model (CEM) to examine the interactions between radiation and maritime tropical cloud clusters and to determine the effects of cloud-induced IR heating of the troposphere on convection. A CEM is a cloud-resolving numerical model that covers a large area. It can simulate an ensemble of cumulus clouds and its mesoscale organization. In a CEM, the large-scale advective processes are prescribed. Thus, there is no feedback from the CEM to the large-scale dynamics. However, since the cloud radiative forcing depends on the extent and microphysical properties of anvil clouds produced by convection, there will be feedbacks in the CEM among the anvil cirrus, radiation, and convection. This paper focuses on mesoscale convection-radiation interactions and investigates their impact on the parameters related to large-scale motions. For simplicity, we have restricted our attention to

tropical cloud clusters over an ocean with a fixed sea surface temperature. In this circumstance, cloud solar radiative forcing at the surface is absent. We have also confined our study principally to the interaction of IR radiation and cloud processes because the cloud radiative forcing in the atmosphere is dominated by IR radiation (see, e.g., Fu and Liou 1993) and because only IR radiation is present during the nighttime. In addition, the incorporation of the diurnal variation of solar radiation in the model will increase the complexity of the interaction and feedback studies in view of the fact that the large-scale forcing is also a function of time.

To investigate the interactions between radiation and convection in tropical cloud clusters, we perform five simulations that have identical large-scale advective forcing, but include different interactive radiation fields. Each simulation encompasses the life cycle of a cloud cluster. This series of simulations allow us to examine the effects of clear-sky IR radiative heating, the effects of cloud IR radiative forcing, the sensitivity of cloud-radiation interactions to the cloud particle size distribution, and some of the effects of solar radiative heating. Tropical cloud clusters are usually classified as either squall or non-squall clusters. We choose to simulate squall cloud clusters because the associated anvil clouds are more extensive in these clusters, so that cloud radiative effects become more important. Moreover, due to the effects of vertical wind shear on convection, squall clusters are better organized than non-squall clusters, so that their structure is more reproducible from one simulation to another. This makes comparisons between individual simulations meaningful for squall clusters.

This paper is organized as follows. In Section 2, we describe the CEM that includes a bulk microphysics parameterization and an interactive radiation scheme. The design of numerical simulations is described in Section 3. The simulation results are presented in Section 4. In Section 5, we discuss the

physical mechanisms associated with cloud-radiation interactions and feedbacks. Finally, summary and conclusions are given in Section 6.

2. The Model

The CEM that is used for studying the interactions between radiation and convection in tropical cloud clusters should explicitly simulate cloud-scale and mesoscale circulations, parameterize the turbulent fluxes in a general way, and simply specify the large-scale advection (forcing). Ice-phase microphysical processes must be included and the cloud properties that strongly affect the radiative fluxes, such as the extent and ice water content of anvil clouds, should be realistically simulated. The radiative processes also need to be carefully parameterized. Earlier versions of the CEM associated with the present study have been described in detail in Krueger (1988) and Xu and Krueger (1991). The current version includes an improved bulk ice-phase microphysics parameterization and an interactive radiative transfer scheme, which are presented in subsections 2b and 2c following a brief description of the basic features of the CEM.

a. Basic features

The time-dependent and nonhydrostatic CEM is based on the two-dimensional (x-z) anelastic system of equations that includes the Coriolis force. The resulting mesoscale and cloud-scale dynamical equations are coupled with a third-moment turbulence closure. The motivation for using a third-moment turbulence closure is to improve the simulation of turbulent processes in the boundary layer as well as in clouds. Third-moment closure has a distinct advantage over simpler closures because it is more general. The full set of turbulence equations includes 11 prognostic equations for second moments, 24 for third moments, and a diagnostic one for the turbulent length scale.

A CEM is designed to resolve many individual cumulus clouds and simulate their mesoscale organization. Since tropical anvils associated with a mesoscale convective system are about 200 km wide, we use a horizontal domain of 512 km with a grid size of 1 km. The depth of the domain is about 18 km and contains 33 levels. In order to provide adequate vertical resolution in the boundary layer, the vertical grid interval ranges from about 100 m near the surface to about 1000 m near 18 km.

The upper and lower boundaries of the CEM are rigid, while the lateral boundaries use the cyclic boundary condition. The lower boundary in this study is the sea surface which is characterized by its specified temperature and roughness. The surface turbulent fluxes are calculated from flux-profile relationships following Deardorff's (1972) approach.

In the tropics, large-scale vertical advection is the primary modulator of cumulus convection on synoptic time scales (Yanai et al. 1976; Lord 1982). For this reason, the CEM includes prescribed large-scale advective tendencies of potential temperature and water vapor.

b. Microphysics parameterization

The present model utilizes a bulk method to represent the cloud microphysical processes, in which the hydrometeors are categorized into five types: cloud droplets, ice crystals, raindrops, snow, and graupel. Although the parameterized cloud microphysics largely follows Lin et al. (1983) and Lord et al. (1984), we have recently improved the ice-phase parameterizations so that the microphysical processes that occur in tropical cloud clusters can be more realistically simulated (Krueger et al. 1994). Major modifications have been made to the growth of cloud ice by the Bergeron process, the conversion of cloud ice to snow, and the characteristics of graupel. The amount of cloud ice and the extent of anvil cirrus are increased to more realistic values by these changes.

Ice water contents (IWCs) in the upper-tropospheric stratiform clouds are one of the most important cloud properties that determine the atmospheric radiation budget and the heating rate profile within anvils (Ackerman et al. 1988; Fu and Liou 1993). We have used a one-dimensional version of CEM to evaluate the improved microphysics parameterization. We turn off cloud dynamics and turbulence, which leads to a kinematic model in which the air motion pattern is fixed in the simulation. The model inputs are profiles of vertical velocity, temperature, pressure, and water vapor mixing ratio. The initial thermodynamic state is based on the GATE Phase-III mean sounding. The prescribed vertical velocity profile is typical of the air motion pattern in the stratiform region associated with a tropical squall line (Rutledge 1986; Gamache and Houze 1982). The simulation time is 24 hours, and the time step is 10 seconds. The model produces a distribution of IWCs and temperatures that are in equilibrium with the air motion pattern.

Variations in the simulated and observed IWCs as functions of temperature and vertical velocity are shown in Fig. 1. The curves are taken from the parameterization results presented by Heymsfield and Donner (1990) for applications to GCMs. IWCs determined from measurements and model simulations are partitioned into vertical velocity intervals. The small symbols are based on measurements obtained in the tropics presented by these authors. The large symbols are the simulation results based on Lord's original microphysics scheme (Fig. 1a) and the improved microphysics parameterization (Fig. 1b). IWCs computed from Lord's scheme are about one order smaller than the measured values (Fig. 1a). IWCs computed from the present parameterization are much improved and comparable with the measured data, as shown in Fig. 1b.

c. Radiative transfer parameterization

The radiative transfer parameterization scheme for application to a mesoscale cloud model is based on the delta-four-stream approximation (Liou et

al. 1988) in both solar and thermal infrared wavelengths. For IR wavelengths, the Planck function is expressed in terms of the optical depth in an exponential form. By dividing the atmosphere into a number of homogeneous layers with respect to the single-scattering albedo and phase function, and by using the boundary conditions and the internal continuity requirements (Liou 1975), the delta-four-stream scheme can be used to calculate the flux distribution. In the resulting matrix formulation, one third of the elements in the diagonal band of the coefficient matrix are zero. We have developed a numerically stable technique to solve the system of linear equations, which is significantly faster than the standard routines available in the IMSL or LAPACK libraries. The delta-four-stream scheme has an accuracy within ~ 5% for all atmospheric conditions with reference to results computed from the "exact" adding method for radiative transfer.

Six solar and 12 IR bands are used in the radiation code to resolve the variations in the refractive indices of ice and water and to account for the gaseous absorption. The nongray gaseous absorption due to H₂O, CO₂, O₃, CH₄, and N₂O is incorporated in the scattering model by using the correlated k-distribution approach (Fu and Liou 1992). The continuum absorption of H₂O and the overlap between H₂O and CO₂ are carefully treated in the infrared. Using the correlated k-distribution method, 121 spectral calculations are required for each vertical profile. The accuracy of the parameterization for nongray gaseous absorption has been checked with the results computed from a line-by-line program. For all gases the differences in heating rates are less than 0.05 K day⁻¹, while those in fluxes are less than 1 W m⁻².

In conjunction with the radiative transfer scheme, the single-scattering properties, including the extinction coefficient, single-scattering albedo, and phase function expansion coefficients, for each hydrometeor species are efficiently parameterized. For hexagonal ice crystals, the parameterization is

made in terms of the mean effective size and IWC based on "exact" results using 11 observed ice crystal size distributions (Fu and Liou 1993). In the "exact" calculations, the geometric ray-tracing program for hexagonal ice crystals (Takano and Liou 1989) is used for size parameters greater than 30, while the exact scattering program for spheroids is employed for size parameters less than 30. For water clouds, a parameterization for the single-scattering properties is developed based on Mie calculations using the observed water droplet size distributions (Fu 1991) in terms of cloud liquid water content and mean effective radius. For rain, snow, and graupel, which are assumed to be spherical particles, truncated constant-slope gamma distributions (Manton and Cotton 1977) are used in Mie calculations. The single-scattering properties of rain, snow, and graupel depend only on their water contents.

To reduce the computational time, the radiation code has been vectorized by placing the loop over the atmospheric columns as the most inner loop. In this manner, radiation calculations can be performed for many model columns simultaneously. For example, on a CRAY Y-MP8/864, the vectorized radiation code is called once for every 64 columns for maximum vectorization efficiency. After vectorizing the code, the computer time for radiation calculations using a CRAY Y-MP8/864 has been reduced by a factor of about 10.

The model top for the radiation calculations is set at 60 km and two additional levels at 21 and 60 km are added above the CEM model top of 18 km. Temperature, water vapor, and ozone profiles at 21 km are assumed to be the same as those of the standard tropical atmosphere. The mixing ratios of H₂O and O₃ at 60 km are determined by equating the path lengths between 21 and 60 km and those obtained from the detailed tropical atmospheric profile. The temperature at 60 km is set at 240 K, which is the average temperature between 21 and 60 km. The differences in heating rates below 18 km between the values obtained from the

detailed profile above the cloud model domain and those computed from only two levels are within 0.02 K day^{-1} .

The average IR heating rate for the lowest model layer is extremely sensitive to the surface air temperature and water vapor mixing ratio. Based on numerical experiments, these values must be obtained from the surface layer similarity profiles at a height z (in meters), which can be expressed as

$$z = 0.2766 + 0.2324 \ln|L|, \quad (2.1)$$

where L is the Monin-Obukhov length (in meters).

The potential temperature and water vapor at any height z within the surface layer can be obtained from their values at the surface and at $z = z_m$, the first CEM level height above the surface. Using the flux profile relationships (Deardorff 1972), we have

$$\theta(z) = \theta_s - (\theta_s - \theta_m) C(z_m)/C(z), \quad (2.2)$$

and

$$q_v(z) = q_{vs} - (q_{vs} - q_{vm}) C(z_m)/C(z), \quad (2.3)$$

where θ_s is the potential temperature corresponding to the sea surface temperature, q_{vs} is the saturation mixing ratio at this temperature, and θ_m and q_{vm} are the CEM potential temperature and mixing ratio values at $z = z_m$. The similarity function for the unstable surface layer is

$$C^{-1}(z) = \frac{0.74}{\kappa} \left[\ln \left(\frac{z}{z_0} \right) - 2 \ln \left(\frac{1+y}{2} \right) \right], \quad (2.4)$$

where $y = (1 - 9\zeta)^{1/2}$, $\zeta = z/L$, κ is the von Karman constant (0.35), and z_0 is the roughness length. Based on GATE data, typical values for z_0 and L are $2 \times 10^{-4} \text{ m}$ and -5 m , respectively.

3. Design of the Numerical Experiment

We have designed five numerical simulations to examine the interactions of longwave radiation and cloud processes. In simulation R1, radiative heating is not included in the thermodynamic equation. We may, however, compute the radiation field diagnostically from the model fields. Simulation R2 includes only the clear-sky IR radiative heating. By comparing results from R2 and R1, radiative destabilization of the tropical environment due to the domainwide clear-air radiative cooling can be studied. In simulation R3, fully interactive IR radiative heating is included. Since the bulk microphysics parameterization does not provide information on cloud particle size distributions, we must prescribe the mean effective size for ice particles (D_e) and the mean effective radius of cloud droplets (r_e) which are required in the radiation code. In simulation R3, we set $D_e = 25 \mu\text{m}$ and $r_e = 5 \mu\text{m}$; values within the range of the observed data (Fu and Liou 1993; Knollenberg et al. 1993; Fu 1991). Comparing results from R3 and R2, the effect of cloud radiative forcing on convection and on the longevity and extent of anvil clouds via cloud base-warming and top-cooling can be investigated. R4 is identical to R3 except that the prescribed mean effective particle sizes are larger. As shown by Fu and Liou (1993), the cloud radiative forcing is very sensitive to the cloud particle size distribution. In simulation R4, we set $D_e = 125 \mu\text{m}$ and $r_e = 12 \mu\text{m}$; values also within the range of the observed data. This experiment is designed to study the sensitivity of cloud particle size distribution to cloud-radiation interactions which has not been explored previously. The final simulation R5 includes fully interactive net (IR + solar) radiative heating. The prescribed D_e and r_e in the radiation calculations are the same as those in R4. For solar radiation, the cosine of the solar zenith angle is set as 0.5 and the solar constant is 1365 W m^{-2} , representing the average day-time condition. The five numerical experiments are summarized and listed in Table 1.

The initial thermodynamic state for all simulations is based on the GATE

Table 1. Summary of the numerical simulations.

R1:	Without radiation
R2:	With clear-sky IR radiation
R3:	With fully interactive IR radiation: $D_0 = 25 \mu\text{m}$, $r_0 = 5 \mu\text{m}$
R4:	With fully interactive IR radiation: $D_0 = 125 \mu\text{m}$, $r_0 = 12 \mu\text{m}$
R5:	With fully interactive net (IR + solar) radiation: $D_0 = 125 \mu\text{m}$, $r_0 = 12 \mu\text{m}$; $\mu_0 = 0.5$, $S = 1365 \text{ W m}^{-2}$.

Phase III mean sounding (Fig. 2a). The geostrophic (and initial) horizontal wind profile normal to the squall line (Fig. 2b) is obtained from a 6-hour average from 4.75 to 5 days of the Q04 simulation presented by Xu et al. (1992). This profile resembles the 11 September 1974 squall line environment observed during GATE Phase III (Sui and Yanai 1986). The wind profile favors the formation of a long lasting squall line system. The large-scale advective cooling and moistening profiles (Fig. 2c) are the same as those used in the Q04 simulation. The large-scale advective forcing is typical of the GATE Phase III disturbed periods. The initial thermodynamic state, the initial wind field, and the imposed large-scale advective forcing are horizontally uniform. The simulation time is 12 hours with a time step of 10 seconds. The large-scale forcing is applied constantly for the first 4 hours and decreases to zero during the next 4 hours according to a cosine function which has a period of 8 hours. For the last 4 hours, the large-scale forcing remains zero. The sea surface temperature is fixed at 299.9 K and the Coriolis parameter for 15°N is used.

The convection is initiated by a low-level cool pool (Tao et al. 1991) that is gradually introduced over 10 minutes after the first 60 minutes of integration. Following Tao et al., the cool pool is 45 km wide and 3 km deep (from the surface to the dry layer near 700 mb) which is vertically but not horizontally uniform. The dependence on horizontal location, x , can be expressed as follows:

$$\left(\frac{\partial\theta}{\partial t}\right)_{cp} = \begin{cases} \left(\frac{\partial\theta}{\partial t}\right)_{cpmax} \ln\eta(x)/\ln 0.25, & \text{for } x_1 \leq x \leq x_2 \\ 0 & \text{otherwise} \end{cases} \quad (3.1)$$

where

$$\eta(x) = \frac{0.75}{x_2 - x_1} (x - x_1) + 0.25. \quad (3.2)$$

In these equations, θ is the potential temperature; x_1 is the location where $(\partial\theta/\partial t)_{cp} = (\partial\theta/\partial t)_{cpmax}$; x_2 is the location where $(\partial\theta/\partial t)_{cp} = 0$; and $(\partial\theta/\partial t)_{cpmax} = 0.00875 \text{ K s}^{-1}$. The maximum cooling rate is at $x = x_1$ since the squall line system propagates toward smaller x with the wind profile imposed.

The radiative fields are calculated every minute, i.e. every 6 dynamical time steps during which interval the radiative heating rates remain constant. Because the propagation speed of the squall line is -12 m s^{-1} (Fu et al. 1994), the system moves about 720 m per minute, which is less than the horizontal grid size of 1000 m. Thus, during one minute, the cloud system will largely remain in the same grid points. The radiation calculations use the thermodynamic and bulk hydrometeor fields provided from the CEM. The ozone profile is taken from the standard tropical atmosphere. For CO_2 , CH_4 , and N_2O , uniform mixing ratios are assumed throughout the atmosphere with concentrations of 330, 1.6, and 0.28 ppmv, respectively.

In strong convective regions, atmospheric temperatures and humidities are directly affected by the presence of convection. In simulation R2, the clear-sky radiative heating rates are computed from thermodynamic profiles in the squall line environment at $x = 324 \text{ km}$. The evolution of these profiles is largely determined by the large-scale advective forcing and the subsiding motion in the environment due to convection. These processes tend to balance, so the

thermodynamic profiles in the environment differ only slightly from the initial ones.

As mentioned in the introduction, Gray and Jacobson (1977) proposed the secondary circulation generated by horizontal differential radiative heating between cloudy and clear regions which can assist in sustaining convection. However, the studies by Miller and Frank (1993) and Xu and Randall (1994) suggested that this cloud-induced secondary circulation plays a relatively minor role in modulating tropical convection. A recent study by Wong and Stephens (1994) concluded that the strength of this circulation is a function of both the vertical wind shear profile and the low level stability of the environment. They found that the cloud-induced secondary circulation is strongest when the vertical wind shear is weak. As the wind shear increases, the secondary circulation weakens. Thus, it is expected that the Gray-Jacobson mechanism is insignificant in our simulations because of the presence of a strong vertical wind shear profile.

4. Results from the Numerical Simulations

The structure of the simulated squall cloud cluster's hydrometeor fields is first examined. Figure 3 shows snapshots of the total hydrometeor mixing ratio, including cloud water, ice, rain, snow, and graupel, based on the R3 simulation at three different times. The logarithm of the mixing ratio is denoted by a linear gray scale: black represents mixing ratios larger than 10^{-2} and white represents mixing ratios smaller than 10^{-6} . Contours for values of 10^{-6} and 10^{-4} are shown in the figure. At the earlier time (Fig. 3a), the cloud cluster consists of isolated precipitating convective towers. In the mature stage (Fig. 3b), the anvil cloud associated with the mesoscale convective system has a horizontal scale of ~ 180 km, which extends from the front to the back of the system. The system moves westward (from right to left) at an average speed

of 12 m s^{-1} and consists of significant precipitation that covers a region of $\sim 140 \text{ km}$. The deep cumulonimbi continually propagate into the ambient air ahead where new growth occurs, while older towers successively join the main anvil mass (Zipser 1977). In the dissipating stage (Fig. 3c), little precipitation remains and the upper tropospheric stratiform clouds are thinning and breaking up (Houze 1982). The typical life cycle and structure of a cloud cluster (e.g., Leary and Houze 1979) can be seen in Fig. 3. In the following, we discuss the cloud-radiation interactions based on numerical simulations, beginning with the cloud top temperature, which can be directly related to infrared satellite imagery.

a. Cloud top temperature

Figures 4a (from R1 with no radiative heating), 4b (from R2 with only clear-sky IR radiative heating), and 4c (from R3 with fully interactive IR radiative heating) show the time evolution of the cloud top temperature, indicated by a linear gray scale: white for 200 K and black for 300 K. The cloud top temperature is defined here as the temperature at the first level to which the "suspended water" path from the model top exceeds 0.1 kg m^{-2} . "Suspended water" includes cloud water, cloud ice, and snow. Cirrus anvils associated with the squall line appear light gray. Several significant features are shown in Fig. 4. First, the cloud top temperature in Fig. 4b is generally lower than that in Fig. 4a, which indicates that clear-sky IR radiation enhances convection. Second, the anvil clouds with interactive IR radiation (Fig. 4c) appear to last longer. Third, by comparing Fig. 4c and Fig. 4b, convective activity appears to dissipate faster due to cloud radiative forcing. To examine these features, we show the time-height cross-sections of the domain averages of the radiative heating rates in Fig. 5. The contour interval is 0.5 K day^{-1} with positive values shaded. Figure 5a and 5b contain the radiative heating rates for R2 and R3, respectively. In Fig. 5c, the cloud radiative forcing is obtained by taking the differences between Fig. 5b and Fig. 5a.

Basically, the differences between R2 and R1 simulations are caused by clear-sky radiative heating rates (Fig. 5a), while those between R3 and R2 are due to the cloud radiative forcing (Fig. 5c). Consistent with the results presented by Dudhia (1989), clear-air radiative cooling (Fig. 5a) enhances convection, as shown in Fig. 4. The cloud radiative forcing pattern between ~ 10.5 km and ~ 13.5 km displayed in Fig. 5c is due to radiative cloud base-warming and top-cooling, which contributes to the longevity of anvil clouds through direct radiative destabilization. Before ~ 4 hours, strong cooling at cloud tops (Fig. 5c) can also enhance shallow convection. After that time, the cloud radiative forcing tends to warm the whole troposphere due to the presence of extensive sheets of anvil clouds. We hypothesize that the atmospheric IR warming effect of clouds has a negative feedback on deep convection. The physical basis of this hypothesis will be examined in Section 5.

b. Surface precipitation

The surface precipitation can be used as a proxy for deep convection (Gray and Jacobson 1977; Xu et al. 1992). Fig. 6 presents the time series of domain total surface precipitation. The results from R1 are denoted by the solid line, R2 by the dashed line, and R3 by the dotted line. The difference between R2 and R1 is due to clear-sky IR radiation. It is evident that the domainwide clear-air radiative cooling in the troposphere increases surface precipitation. This increase is $\sim 15\%$ (i.e., ~ 1.7 mm) over the 12-hour simulation. The difference between R3 and R2 is due to the cloud IR radiative forcing, which decreases surface precipitation. This is especially evident after ~ 6.5 hours. The response of surface precipitation to cloud radiative warming appears to exhibit a time lag. In the present simulations, there is $\sim 10\%$ (i.e., ~ 1.3 mm) decrease of surface precipitation due to cloud IR radiative forcing. The domain total precipitation from R3 is slightly larger than R2's before ~ 4.5 hours (Fig. 6) due to the direct radiative destabilization of cloud layers. Based on these

results we conclude that the clear-air IR radiative cooling enhances convection, while the cloud IR radiative forcing suppresses convection.

c. Convective heating and convective drying

The goal of cumulus parameterization is to determine the convective heating ($Q_1 - Q_R$) and convective drying Q_2 profiles, where Q_R is the radiative heating rate, and Q_1 and Q_2 are the apparent heat source and the apparent moisture sink of a large-scale system (Yanai et al. 1973). ($Q_1 - Q_R$) and Q_2 are directly related to the contributions of convective effects, which can be explicitly calculated by the CEM.

The convective heating and drying profiles in R1 represent the response of the cumulus ensemble to the advective forcing alone, which is prescribed and assumed to be the same for all simulations. The convective heating and drying profiles in R2 and R3 represent the response not only to the advective forcing but also to the radiative processes. Figures 7a-7d present the time- and domain-averaged profiles of ($Q_1 - Q_R$), Q_R , Q_1 , and Q_2 , respectively. By comparing these profiles for R2 and R1 shown in Figs. 7a and 7d, we find that ($Q_1 - Q_R$) and Q_2 significantly increase in response to clear-sky IR radiative cooling (see Q_R for R2 in Fig. 7b). However, the cloud radiative forcing, i.e., the difference between Q_R for R3 and R2 (Fig. 7b), tends to warm, and has the opposite effect throughout the low and middle troposphere. By comparing the results from R3 and R2, as shown in Figs 7a and 7d, it is seen that the cloud IR radiative forcing tends to suppress convective activity. In the upper troposphere, however, this forcing produces a slight increase in convective activity because convective overturning develops within the large stratiform anvil clouds. This is associated with the direct radiative destabilization. In Fig. 7b we find that cloud radiative forcing tends to cool the cloud top relative to cloud base.

Figure 8 shows the time- and domain-averaged profiles of (a) temperature and (b) water vapor mixing ratio deviations with respect to initial conditions.

The thermodynamic changes result from the combined effects of large-scale cooling, radiative heating, and convective heating. The apparent heating (Fig. 7c) is the combined result of radiative and convective heating. Both clear-sky IR radiation and cloud radiative forcing play an important role in the thermodynamic changes because the large-scale cooling and apparent heating, despite their relatively large magnitudes, tend to balance. The water vapor mixing ratio changes are caused by large-scale moistening and apparent drying (convective drying). Radiation affects the water vapor profile through convection. It is significant above ~ 2 km. Below ~ 7 km, the clear-sky IR cooling tends to dry the atmosphere. The opposite is true for cloud radiative forcing. Above ~ 7 km, the cloud radiative forcing dries the atmosphere because of direct radiative destabilization. From the results presented in Fig. 8, it is clear that the radiative heating rate and its effect on convective heating and drying must be reliably accounted for in climate modeling studies.

d. Cloud characteristics and outgoing IR flux

One of the most important quantities for climate studies is the outgoing IR flux at the top of the atmosphere. This flux is strongly modulated by the cloud amount, cloud top height, and hydrometeor water content. We shall first investigate the impact of cloud-radiation interactions on cloud fields.

Figure 9a illustrates time- and domain-averaged cloud amount profiles. The definition of cloud amount in a GCM grid box (1 km wide) follows Xu and Krueger (1991). The maximum cloud amounts occur at ~ 12 km for all three cases. They are 0.40, 0.43, and 0.52 for R1, R2, and R3, respectively. The clear-sky IR cooling tends to increase the cloud amount throughout the atmosphere. The most interesting feature of Fig. 9a is that the cloud IR radiative forcing increases the anvil cloud amount significantly ($\sim 21\%$). This is due to the direct radiative destabilization via cloud base-warming and top-cooling, which increases cloud longevity. Lilly (1988) proposed that the in-cloud radiative

destabilization generates buoyant turbulence in anvil clouds and contributes to their longevity. Figure 9b shows the time- and domain-averaged profiles of turbulent kinetic energy (TKE). Compared with results from R1 and R2, the dotted line from R3 (with fully interactive IR radiation) is generally larger, especially at ~ 11.5 km. The preceding results are consistent with Lilly's theory. The significant increase of TKE at ~ 2 km for R3 is also due to the direct radiative destabilization. It is clear from Figs. 9a that cloud-radiation interactions significantly modulate the cloud fields, especially the upper tropospheric stratiform clouds.

The effects of radiation on the hydrometeor fields are also significant. Figures 10a and 10b show the time and domain average of mixing ratio profiles for cloud water plus cloud ice, and snow plus graupel plus rain, respectively. Clear-air IR cooling leads to changes in the cloud and precipitating hydrometeor profiles. It is interesting to note that the cloud radiative forcing reduces the mixing ratio of precipitating particles throughout the atmosphere. However, it does not have a significant impact on the cloud mixing ratio profiles. By comparing the results presented in Fig. 10a and Fig. 9a, it is evident that the anvil cloud amount is not necessarily related to cloud ice water mixing ratio (or content).

To examine the impact of convective-radiative interactions on the outgoing IR flux at the top of the atmosphere, we calculate this flux using the radiation code and the cloud thermodynamic and bulk hydrometeor fields generated from R1, R2, and R3. This flux is referred to here as the diagnostic flux. The time- and domain-averaged outgoing IR fluxes are 225.8 , 221.9 , and 216.9 W m^{-2} for R1, R2, and R3, respectively. The clear-sky IR cooling decreases the outgoing IR flux by -3.9 W m^{-2} , while the cloud radiative forcing further decreases this flux by -5.0 W m^{-2} . Convection-radiation interactions modulate the outgoing IR flux at the top of the atmosphere mainly through their effect on the extent of anvil

clouds (Fig. 9a). The time series of domain-averaged outgoing fluxes at the top of the atmosphere are shown in Fig. 11. The difference between R1 and R3 is as large as 20 W m^{-2} ; a result of the longevity of anvil clouds associated with the direct radiative destabilization.

e. Effects of cloud particle size distribution and solar radiation

In light of the preceding discussion, it is clear that the cloud IR radiative forcing stabilizes convection significantly. It has been noted that the cloud IR radiative forcing is very sensitive to the cloud particle size distribution (e.g., Fig. 9a of Fu and Liou 1993). Consequently, the evolution of tropical mesoscale systems and tropical rainfall will depend on the cloud particle size distribution through convection-radiation interactions. Note that in the cloud microphysics parameterization, only ice/liquid water contents are involved. Runs R3 and R4 both include fully interactive IR radiation but use different mean effective sizes and effective radii for ice and water cloud particles in the radiation calculations. Figure 12 shows the domain total surface precipitation as a function of time for R3 (solid line) and R4 (dashed line). Because clouds containing larger mean effective sizes absorb less longwave radiation, the atmospheric radiative warming effect of such clouds is reduced, leading to stronger convection and more surface precipitation. On the other hand, the direct destabilization of cloud layers is weaker in R4, leading to a slight decrease in surface precipitation before 4.5 hours. The present study suggests that cloud particle size distributions should be realistically specified in or predicted by cloud models.

The effect of solar heating in the atmosphere on surface precipitation is shown in Fig. 13. In this case, atmospheric solar heating decreases surface precipitation because the domainwide clear-air solar warming in the troposphere suppresses convection. The solar heating also reduces the cloud direct

destabilization effects produced by IR radiation flux exchanges because the solar heating rate peaks at the cloud top (Ackerman et al. 1988).

5. Mechanisms for Convection-Radiation Interactions

In the present study, the life cycle of a tropical squall cloud cluster has been simulated. We have investigated interactions between radiation and convection in the simulated cloud cluster. The results suggest that radiation has a significant impact on the macroscopic behavior of cumulus ensembles.

As summarized in the introduction, previous explanations for mesoscale cloud-radiation interactions can be grouped into three basic categories: destabilization of the environment due to clear-air radiative cooling, direct destabilization of anvil clouds via cloud base-warming and top-cooling, and production of a secondary circulation by horizontal differential radiative heating between cloudy and clear regions. All of these mechanisms tend to enhance convection. The first two are significant in our simulations, but the third is less important as discussed in Section 3. The mechanism associated with the suppression of convection due to the atmospheric IR warming effect of clouds, however, has not been previously investigated. Our results reveal that this mechanism plays a significant role during the mature stage of the cloud cluster during which an upper tropospheric stratiform anvil shield develops and covers an extensive area.

Direct destabilization of anvil clouds via cloud base-warming and top-cooling is confirmed to be important for upper tropospheric stratiform clouds. This mechanism mainly contributes to the longevity of these clouds in line with the findings presented by Dudhia (1989), Churchill and Houze (1991), and Xu and Randall (1994). Our results also reveal that direct destabilization prolongs the lifetime of anvil clouds by generating more turbulence in these clouds in agreement with the theory proposed by Danielson (1982) and Lilly (1988).

The primary effect of clear-air IR cooling is to destabilize the troposphere and enhance deep convection. However, cloud IR radiative forcing tends to stabilize the atmosphere. Destabilization is related to an increase of the vertically-integrated buoyancy of a parcel that rises from the subcloud layer (the layer below cumulus cloud base) to its non-buoyancy level. Destabilization can occur by warming or moistening the subcloud layer where the parcel originates, and by cooling or moistening the atmosphere above cloud base. Over a region with a fixed SST, such as considered in this study, destabilization is due primarily to cooling or moistening of the atmosphere above cloud base. Over such a region, any process which tends to cool the atmosphere is "destabilizing", while the reverse is true for any process that tends to warm the atmosphere. In the following, we examine the destabilizing effects of clear-air radiative cooling and the stabilizing effects of cloud IR radiative forcing on deep convection by using the cloud-work function.

The cloud-work function is a generalized measure of the moist convective instability in the large-scale environment. It is defined as the cumulus cloud subensemble kinetic energy generation (per unit cloud-base mass flux) due to work done by the buoyancy force (Arakawa and Schubert 1974; Lord and Arakawa 1980; Lord 1982; Lord et al. 1982). It is given by

$$A(z_t) = \int_{z_b}^{z_t} \frac{g}{\bar{\theta}(z)} e^{\lambda(z_t)(z-z_b)} \left\{ \theta_{vc} [z, \lambda(z_t)] - \bar{\theta}_v(z) \right\} dz, \quad (5.1)$$

where z_t is the cloud-top height (defined as the non-buoyancy level), z_b is the cloud base height, g is the gravitational acceleration, $\bar{\theta}$ is the environmental potential temperature, θ_{vc} and $\bar{\theta}_v$ are the subensemble and environmental virtual potential temperatures, respectively, and λ is the fractional entrainment rate determined by the cloud-top non-buoyancy condition. In Eq.(5.1), $g(\theta_{vc} - \bar{\theta}_v)/\bar{\theta}$ is the buoyancy force. Therefore, A is an integral measure of the buoyancy force

with the weighting function $e^{\lambda(z-z_b)}$, representing the normalized cloud mass flux. The cloud-work function is a property of the thermodynamic structure of the large-scale environment. An increase in $A(z_t)$ corresponds to destabilization for clouds with cloud tops at $z = z_t$, while a decrease corresponds to stabilization. The cloud-work function may increase or decrease due to large-scale advection, radiation, and surface fluxes. Cumulus convection usually tends to decrease the cloud-work function.

To calculate the destabilization due to large-scale advection and radiation, we calculate dA/dt due to those processes alone. In the computation of the cloud-work function, we use the domain-average temperature and water vapor mixing ratio profiles stored at 5 minute interval from runs R1, R2, and R3. These data are then averaged over 30 minutes to produce "observation" of the environmental profiles. From each of these profiles, the cloud-work function $A(z_t)$ is calculated for clouds with different cloud top heights z_t . The cloud base is fixed at 500 m. The temperature and water vapor mixing ratio profiles modified by the prescribed large-scale advective cooling and moistening and the radiative heating from R1, R2, and R3 simulations in a time interval Δt are then used to compute a new cloud-work function $A'(z_t)$. It follows that the time derivative of the cloud-work function can be written as:

$$\left[\frac{dA}{dt} \right]_{L.S.+Rad} = \frac{A'(z_t) - A(z_t)}{\Delta t}, \quad (5.2)$$

where Δt is set as 30 minutes.

Figure 14 shows the 12-hour-averaged dA/dt for R1, R2, and R3 as a function of cloud top height. The solid line is for results due solely to the prescribed advective cooling and moistening (R1). Because the cloud-work function tends to increase, the large-scale advection tends to destabilize the cloud system and to increase the moist convective instability. Clear-air radiative cooling (R2) significantly increases dA/dt , the rate of increase of moist convective

instability, as shown by the dashed line. However, the cloud radiative forcing, i.e. the atmospheric radiative warming effect of clouds, decreases dA/dt , especially for deep convection. Because there is typically a near-balance (i.e., quasi-equilibrium) between the generation of moist convective instability and its destruction by cumulus clouds (Arakawa and Schubert 1974), we conclude that the differences in destabilization rate produced by radiative forcing result in the differences in the intensity of convection.

Lord (1982) used the Arakawa-Schubert cumulus parameterization (i.e., quasi-equilibrium) to investigate the sensitivity of the time-averaged precipitation rate to the prescribed radiative heating rate profiles during GATE Phase III. Using cooling rate profiles for a clear atmosphere and for an atmosphere with 100% cirrus cover, Lord (1982) found that the time-averaged precipitation rate for the cloudy case was 23% less than the rate for the clear case over an 18-day period. The difference is mainly due to cloud IR forcing because the impact of cloud solar forcing is primarily at the surface. The radiative heating rate profile produced from simulation R3 lies between those of the clear and cloud (100%) profiles. In R3, the surface precipitation decreases by ~ 10% due to cloud radiative forcing consistent with Lord's results.

Figure 15 is a schematic illustration of the interactions between radiation and convection in tropical squall cloud clusters based on simulation results. Cumulus convection is forced by the large-scale advective cooling and moistening. The clear-air IR radiation cools the atmosphere and augments the convective response to the advective forcing. A cumulus ensemble affects its large-scale environment primarily by compensating subsidence (Arakawa and Schubert 1974). The subsidence warms and dries the environment, leading to a negative feedback on convection. The anvil clouds produced by convection reduce the IR radiative cooling, warm the troposphere, and produce a negative feedback on moist convective instability which is referred to as "anvil cloud IR radiative

feedback". At the same time, the IR cloud radiative forcing has a positive feedback on the anvil clouds via cloud-top cooling and cloud-base warming. This feedback destabilizes the anvil clouds, promotes convective overturning with the cloud layer, and increases the longevity of anvil clouds. As a result, the atmospheric IR warming effect of anvil clouds increases, leading to a more negative feedback to moist convective instability. The present study represents the first attempt to examine the IR warming effect of clouds on deep convection using a cumulus ensemble model. We have demonstrated that the stabilization of deep convection is significantly influenced by the cloud warming effect. Since the microphysics, thermodynamics, and dynamics in cloud systems may vary substantially among the population of mesoscale cloud systems (MCSs), the importance of the preceding mechanisms for cloud-radiation interactions may vary for different tropical MCSs. Finally, it should be noted that feedbacks of cumulus convection and radiative processes to large-scale motions, denoted by dashed lines in Fig. 15, are not included in the present CEM. In a GCM, the mesoscale convective-radiative feedbacks are confined to a single column. Thus, in order to include these feedbacks for climate study, it is important to develop appropriate and consistent parameterizations for cumulus clouds, anvils, and radiative transfer processes.

6. Summary and Conclusions

A two-dimensional CEM has been used to investigate the effects of cloud-radiation interactions on a simulated tropical MCS. The model includes a modified ice phase bulk microphysics parameterization and an advanced radiation code. The microphysics parameterization has been used to determine the microphysical tendencies of hydrometeors (cloud ice, cloud water, rain, snow, and graupel). The simulated IWCs in tropical conditions compare reasonably well with aircraft observed values. We have also incorporated in the CEM a state-of-the-

art radiation program which integrates in a coherent manner the delta-four-stream approximation for radiative transfer, the correlated k-distribution method for nongray gaseous absorption, and parameterizations of the single-scattering properties for hydrometeors. The radiation code is fully interactive with microphysics, turbulence, and cloud dynamics.

The life cycle of a tropical squall line has been simulated over a 12-hour period by using thermodynamic and kinematic initial conditions and large-scale forcing typical of a GATE Phase III squall cluster environment. A number of numerical simulations have been designed to examine the mechanisms for cloud-radiation interactions, including runs without incorporating radiative heating, with clear-air IR radiative heating, and with fully interactive IR and net radiative transfer programs. The main results are summarized in the following:

(1). Clear-air radiative cooling enhances convection, and hence, surface precipitation. In the present study, the surface precipitation over a 12-hour period increases by ~ 15% (1.7 mm). The cooling also leads to increases in convective heating ($Q_1 - Q_R$) and convective drying Q_2 and changes the hydrometeor profiles.

(2). Direct destabilization of clouds via cloud top-cooling and base-warming contributes to the longevity of anvil cirrus and to the increase in cloud cover. Because of this increase, the outgoing IR flux at the top of the atmosphere can be reduced by as much as 20 W m^{-2} . Radiative destabilization prolongs cirrus clouds by generating more turbulence.

(3). Cloud IR radiative forcing associated with anvils in the atmosphere acts to suppress the tropical deep convection and decreases surface precipitation. The present study shows a 10% (1.3 mm) decrease associated with this process which we refer to as "anvil cloud IR radiative feedback".

(4). The particle size distributions in clouds play a significant role in cloud-radiation interactions. Clouds containing larger mean effective

sizes/radii would have smaller cloud IR radiative forcing and less effect on suppressing convection. This suggests that cloud particle size distributions should be simulated simultaneously in order to understand more comprehensively interactions among radiative heating, cloud microphysics, and dynamics processes in a cloud model.

The effects of clear-air IR cooling and cloud IR radiative forcing on deep convection are further examined by using the cloud-work function, which is a generalized measure of the moist convective instability in the large-scale environment. Clear-air IR cooling increases the cloud-work function, but the cloud IR radiative forcing tends to reduce it, especially for the deepest clouds. The present study represents the first attempt to examine the impact of cloud IR radiative forcing on deep convection by using a CEM. In particular, we have provided a fundamental understanding of the role of upper tropospheric stratiform clouds associated with deep convection in the interactions between radiation and convection. Such an understanding is essential for the parameterization of these clouds in climate models.

Acknowledgments. The research work contained herein was supported by AFOSR Grant 91-0039 and in part by NASA Grant NAG5-1050 and NSF Grant ATM 90-24217. Numerical computations for this work were performed on the CRAY Y-MP8/864 computer at the National Center For Atmospheric Research. We thank Dr. S. Chin of the Lawrence Livermore Laboratory for useful discussions and Dr. N. Rao for assistance in preparing the diagrams presented in the text.

REFERENCES

- Ackerman, T.P., K.N. Liou, F.P.J. Valero, and L. Pfister, 1988: Heating rates in tropical anvils. J. Atmos. Sci., 45, 1606-1623.
- Arakawa, A., and W.H. Schubert, 1974: Interaction of a cumulus cloud ensemble with the large-scale environment, Part I. J. Atmos. Sci., 31, 674-701.
- Chen, S., and W.R. Cotton, 1988: The sensitivity of a simulated extra tropical mesoscale convective system to longwave radiation and ice-phase micro-physics. J. Atmos. Sci., 45, 3897-3910.
- Chin, H.N.S., 1994: The impact of the ice phase and radiation on a midlatitude squall line. J. Atmos. Sci., in press.
- Churchill, D.D., and R.A. Houze, Jr., 1991: Effects of radiation and turbulence on the diabatic heating and water budget of the stratiform region of a tropical cloud cluster. J. Atmos. Sci., 48, 903-922.
- Danielson, E.F., 1982: A dehydration mechanism for the stratosphere. Geophys. Res. Lett., 9, 605-608.
- Deardorff, J.W., 1972: Parameterization of the planetary boundary layer for use in general circulation models. Mon. Wea. Rev., 100, 93-106.
- Dudhia, J., 1989: Numerical study of convection observed during the winter monsoon experiment using a mesoscale two-dimensional model. J. Atmos. Sci., 46, 3077-3107.
- Fu, Q., 1991: Parameterization of radiative processes in vertically non-homogeneous multiple scattering atmospheres. Ph.D. dissertation, University of Utah, 259 pp.
- Fu, Q., and K.N. Liou, 1992: On the correlated k-distribution method for radiative transfer in nonhomogeneous atmospheres. J. Atmos. Sci., 49, 2139-2156.

- Fu, Q., and K.N. Liou, 1993: Parameterization of the radiative properties of cirrus clouds. J. Atmos. Sci., 50, 2008-2025.
- Fu, Q., K.N. Liou, and S.K. Krueger, 1994: Cloud-radiation interactions in tropical anvils. 6th conference on climate variations, Nashville, 235-239.
- Gamache, J.F., and R.A. Houze, Jr., 1982: Mesoscale air motions associated with a tropical squall line. Mon. Wea. Rev., 110, 118-135.
- Gray, W.M., and R.W. Jacobson, Jr., 1977: Diurnal variation of deep cumulus convection. Mon. Wea. Rev., 105, 1171-1188.
- Heymsfield, A.J., and L.J. Donner, 1990: A scheme for parameterizing ice-cloud water content in general circulation models. J. Atmos. Sci., 47, 1865-1877.
- Houze, R.A., Jr., 1982: Cloud clusters and large-scale vertical motions in the tropics. J. Meteor. Soc. Jap., 60, 396-410.
- Knollenberg, R.G., K. Kelly, and J.C. Wilson, 1993: Measurements of high number densities of ice crystals in the tops of tropical cumulonimbus. J. Geophys. Res., 98, 8639-8664.
- Krueger, S.K., 1988: Numerical simulation of tropical cumulus clouds and their interaction with the subcloud layer. J. Atmos. Sci., 45, 2221-2250.
- Krueger, S.K., Q. Fu, K.N. Liou, and H.-N.S. Chin, 1994: Improvement of an ice-phase microphysics parameterization for use in numerical simulations of tropical convection. J. Appl. Meteor (accepted).
- Leary, C.A., and R.A. Houze, Jr., 1979: The structure and evolution of convection in a tropical cloud cluster. J. Atmos. Sci., 36, 437-457.
- Lilly, D.K., 1988: Cirrus outflow dynamics. J. Atmos. Sci., 45, 1594-1605.
- Lin, Y.L., R.D. Farley, and H.D. Orville, 1983: Bulk parameterization of the snow field in a cloud model. J. Climate Appl. Meteor., 22, 1065-1092.

- Liou, K.N., 1975: Applications of the discrete-ordinate method for radiative transfer to inhomogeneous aerosol atmospheres. J. Geophys. Res., 80, 3434-3440.
- Liou, K.N., Q. Fu, and T.P. Ackerman, 1988: A simple formulation of the delta-four-stream approximation for radiative transfer parameterizations. J. Atmos. Sci., 45, 1940-1947.
- Lord, S.J., and A. Arakawa, 1980: Interaction of a cumulus cloud ensemble with the large-scale environment. Part II. J. Atmos. Sci., 37, 2677-2692.
- Lord, S.J., 1982: Interaction of a cumulus cloud ensemble with the large-scale environment. Part III: Semi-prognostic test of the Arakawa-Schubert cumulus parameterization. J. Atmos. Sci., 39, 88-103.
- Lord, S.J., W.C. Chao, and A. Arakawa, 1982: Interaction of a cumulus cloud ensemble with the large-scale environment. Part IV: The discrete model. J. Atmos. Sci., 39, 104-113.
- Lord, S.J., H.E. Willoughby, and J.M. Piotrowicz, 1984: Role of a parameterized ice-phase microphysics in an axisymmetric, nonhydrostatic tropical cyclone model. J. Atmos. Sci., 41, 2836-2848.
- Manton, M.J., and W.R. Cotton, 1977: Formulation of approximate equations for modeling moist deep convection on the mesoscale. Atmospheric Science Paper No. 266, Dept. of Atmospheric Science, Colorado State University, Fort Collins, CO, 62 pp.
- Miller, R.A. and W.M. Frank, 1993: Radiative Forcing of simulated tropical cloud clusters. Mon. Wea. Rev., 121, 482-498.
- Ramanathan, V., 1987: The role of earth radiation budget studies in climate and general circulation research. J. Geophys. Res., 92, 4075-4095.
- Randall, D.A., 1989: Cloud parameterization for climate modeling: Status and Prospects. Atmos. Res., 23, 345-361.

- Randall, D.A., Harshvardhan, D.A. Dazlich, and T.G. Corsetti, 1989: Interactions among radiation, convection, and large-scale dynamics in a general circulation model. J. Atmos. Sci., 46, 1943-1970.
- Riehl, H., and J.S. Malkus, 1958: On the heat balance in the equatorial trough zone. Geophysica, 6, 503-538.
- Rutledge, S.A., 1986: A diagnostic modeling study of the stratiform region associated with a tropical squall line. J. Atmos. Sci., 43, 1356-1377.
- Simmons, A.J., 1982: The forcing of stationary wave motion by tropical diabatic heating. Q. J. R. Meteorol. Soc., 108, 503-534.
- Sui, C.H., and M. Yanai, 1986: Cumulus ensemble effects on the large-scale vorticity and momentum fields of GATE. Part I: Observational evidence. J. Atmos. Sci., 43, 1618-1642.
- Sui, C.H., K.M. Lau, W.K. Tao, and J. Simpson, 1994: The tropical water and energy cycles in a cumulus ensemble model. Part I: Equilibrium climate. J. Atmos. Sci., 51, 711-728.
- Takano, Y., and K.N. Liou, 1989: Radiative transfer in cirrus clouds. I. Single-scattering and optical properties of hexagonal ice crystals. J. Atmos. Sci., 46, 3-19.
- Tao, W.K., J. Simpson, and S.T. Soong, 1991: Numerical simulation of a subtropical squall line over the Taiwan strait. Mon. Wea. Rev., 119, 2699-2723.
- Tao, W.K., J. Simpson, C.H. Sui, B. Ferrier, S. Lang, J. Scala, M.-D. Chou, and K. Pickering, 1993: Heating, moisture and water budgets of tropical and midlatitude squall lines: Comparisons and sensitivity to longwave radiation. J. Atmos. Sci., 50, 673-690.

- Wong, T., and G.L. Stephens, 1994: A numerical study on the interactions between tropical cloud clusters, radiation, and dynamics. 6th conference on climate variations. Nashville, Preprints 307-312.
- Xu, K.M., and S.K. Krueger, 1991: Evaluation of cloudiness parameterizations using a cumulus ensemble model. Mon. Wea. Rev., 119, 342-367.
- Xu, K.M., A. Arakawa, and S.K. Krueger, 1992: The macroscopic behavior of cumulus ensembles simulated by a cumulus ensemble model. J. Atmos. Sci., 49, 2402-2420.
- Xu, K.M., and D.A. Randall, 1994: Impact of interactive radiative transfer on the macroscopic behavior of explicitly simulated cumulus ensembles. J. Atmos. Sci (submitted).
- Yanai, M., S. Esbensen, and J. Chu, 1973: Determination of average bulk properties of tropical cloud clusters from large-scale heat and moisture budgets. J. Atmos. Sci., 30, 611-627.
- Yanai, M., S. Esbensen, and J.H. Chu, 1976: Response of deep and shallow tropical maritime cumuli to large-scale processes. J. Atmos. Sci., 33, 976-991.
- Zipser, E.J., 1977: Mesoscale and convective-scale downdrafts as distinct components of squall-line structure. Mon. Wea. Rev., 105, 1568-1589.

FIGURE CAPTIONS

- Fig. 1 Ice water content as a function of the temperature and vertical air velocity. The curves are from the parameterization presented by Heymsfield and Donner (1990) for GCMs. The smaller symbols correspond to measured data in tropical conditions taken from the same paper. The bigger symbols are from model simulations by using (a) Lord's original microphysics scheme and (b) the improved microphysics scheme. Crosses: $0 - 2.5 \text{ cm s}^{-1}$; triangles: $2.5 - 10 \text{ cm s}^{-1}$; circles: $10 - 33 \text{ cm s}^{-1}$; squares: $> 33 \text{ cm s}^{-1}$.
- Fig. 2 (a) Initial thermodynamic sounding, (b) initial horizontal wind profile normal to the squall line, and (c) imposed large-scale advective cooling (solid line) and moistening effects (dashed line) for the first 240-minute simulation time.
- Fig. 3 Snapshots (x-z sections) of the total hydrometeor mixing ratio, including cloud water, cloud ice, rain, snow, and graupel at (a) 120, (b) 325, and (c) 645 minutes. The gray scale is linear to the logarithm of mixing ratio: black and white represent mixing ratios larger than 10^{-2} and smaller than 10^{-6} , respectively. Contours for values of 10^{-6} and 10^{-4} are shown in the figure.
- Fig. 4 Hovmöller diagrams (x-t sections) of the cloud top temperature for (a) R1, (b) R2, and (c) R3. The cloud top temperature is shown by a linear gray scale: white represents 200 K; black represents 300 K.
- Fig. 5 Time-height cross-section for the domain averaged radiative heating rates. The contour interval is 0.5 K day^{-1} with positive values shaded. (a) and (b) are for radiative heating rates in the cases of

R2 and R3, respectively. In (c), the cloud radiative forcing is calculated by taking the difference between the two cases.

- Fig. 6 Domain total amount of surface precipitation as a function of time. The solid, dashed, and dotted lines are from runs R1, R2, and R3, respectively.
- Fig. 7 Time- and domain-averaged profiles of (a) convective heating ($Q_1 - Q_R$), (b) radiative heating Q_R , (c) apparent heating Q_1 , and (d) apparent (or convective) drying Q_2 . The solid, dashed, and dotted lines are from runs R1, R2, and R3, respectively.
- Fig. 8 Time and domain average of (a) the temperature deviation, and (b) the water vapor mixing ratio deviation, with respect to initial conditions.
- Fig. 9 Time and domain average of (a) cloud amount and (b) turbulent kinetic energy profiles.
- Fig. 10 Time- and domain-averaged mixing ratio profiles for (a) cloud water plus cloud ice and (b) snow plus graupel plus rain.
- Fig. 11 Time series of the domain-averaged outgoing IR flux at the top of the atmosphere. The fluxes are computed from the radiation code using the thermodynamic and bulk hydrometeor fields simulated from R1 (solid line), R2 (dashed line), and R3 (dotted line).
- Fig. 12 Domain total amount of the surface precipitation as a function of time for the 12-hour simulations. Results using different mean effective sizes in the simulations are denoted by the solid line (R3) and the dashed line (R4), respectively.
- Fig. 13 Domain total amount of the surface precipitation as a function of time. Results with IR and net (IR + solar) radiation in the simulations are denoted by the solid line (R4) and the dashed line (R5), respectively.

Fig. 14 Time and domain average of the time derivative of the cloud-work function due to the large-scale advection and radiation. The ordinate is the cloud-top height in km. The solid, dashed, and dotted lines for R1, R2, and R3, respectively.

Fig. 15 A schematic illustration of mesoscale radiative-convective interactions and feedbacks. The dashed lines are feedbacks that have not been included in the present CEM.

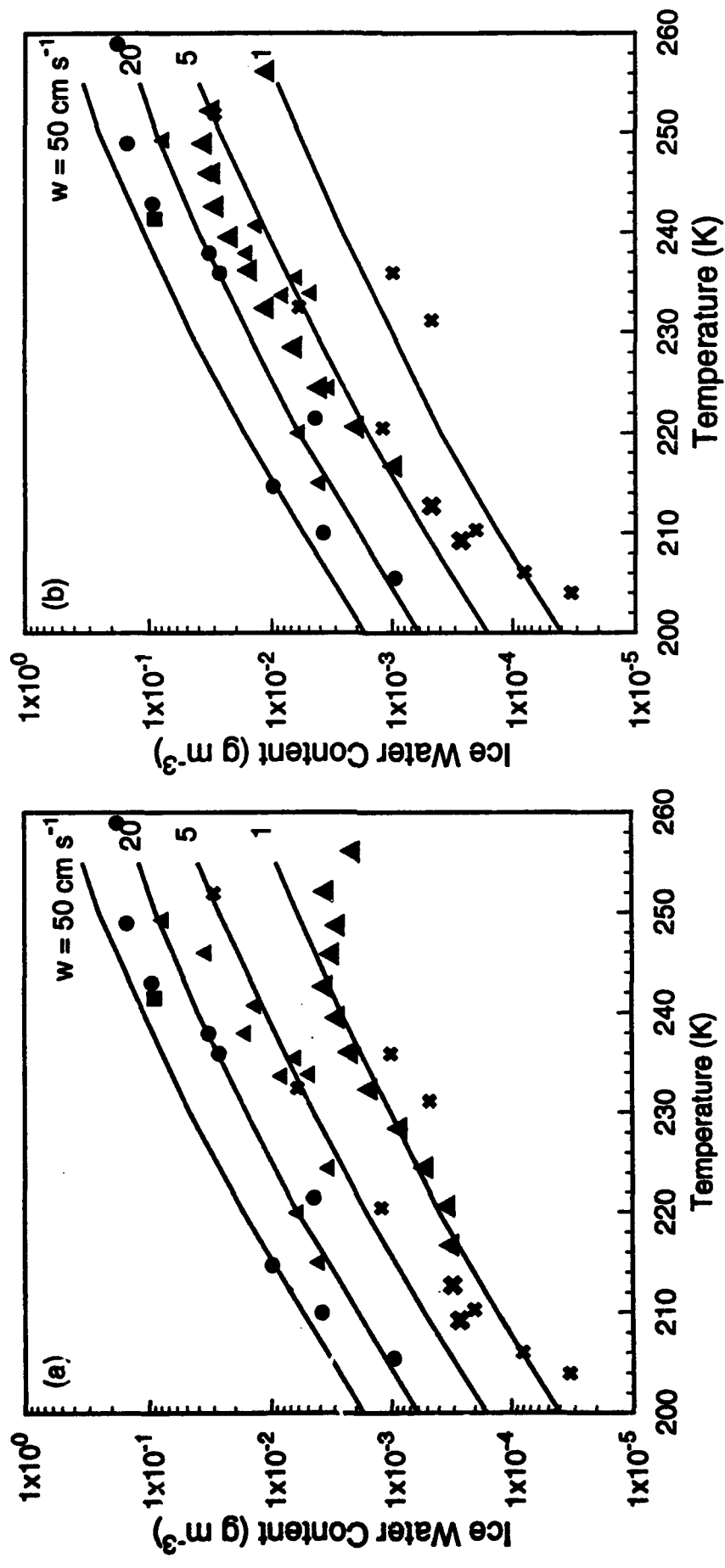


Fig. 1

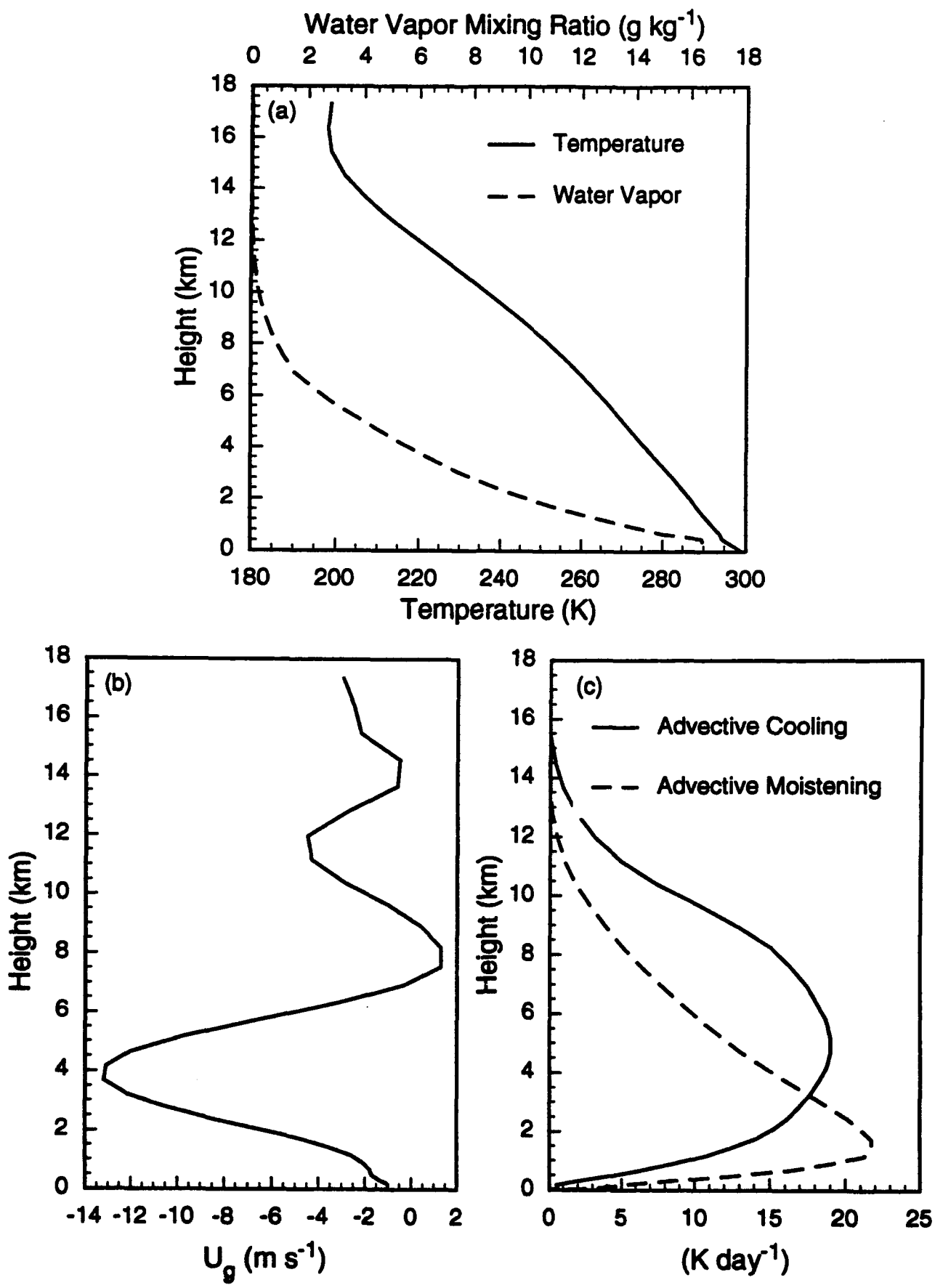


Fig. 2

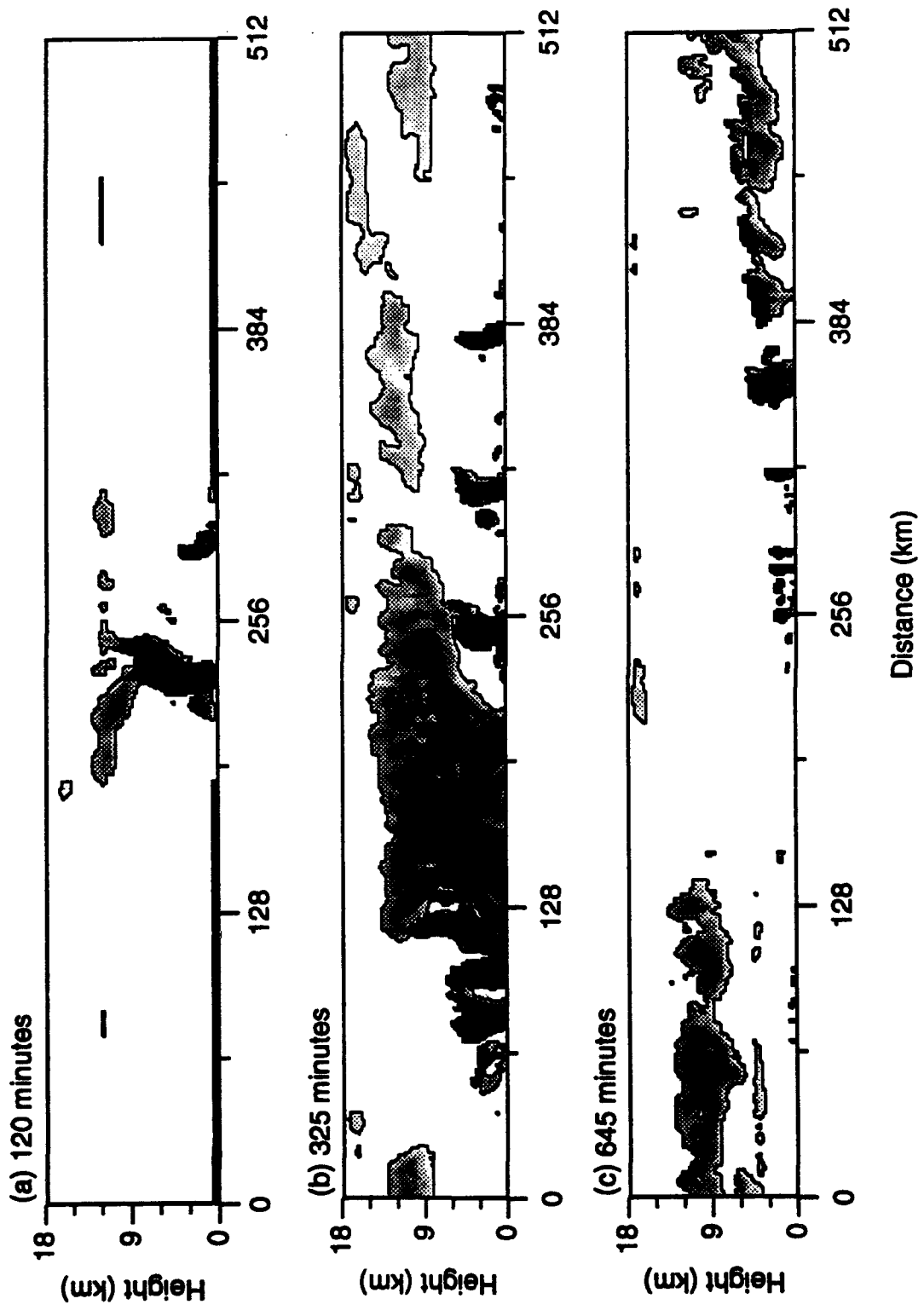


Fig. 3

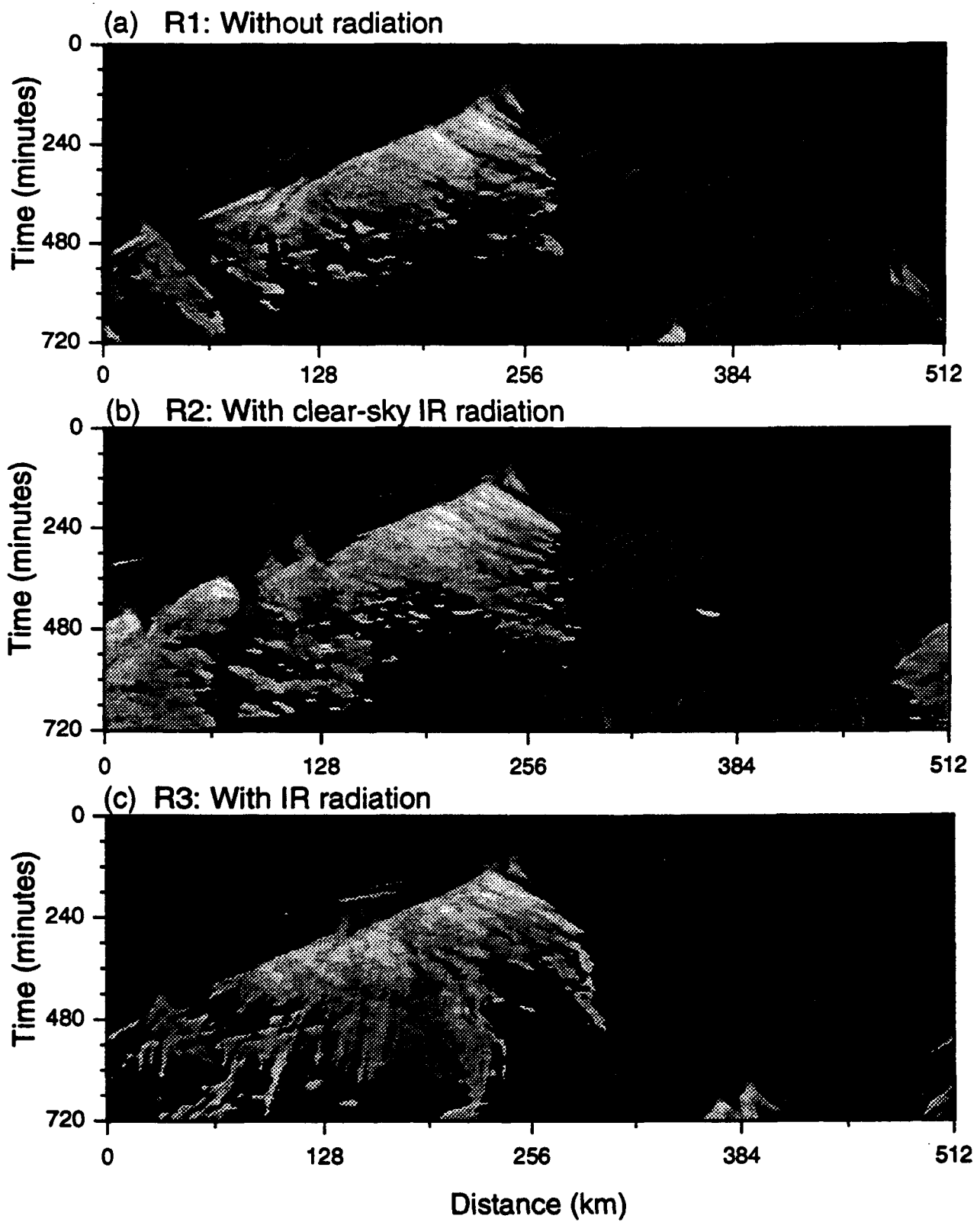


Fig. 4

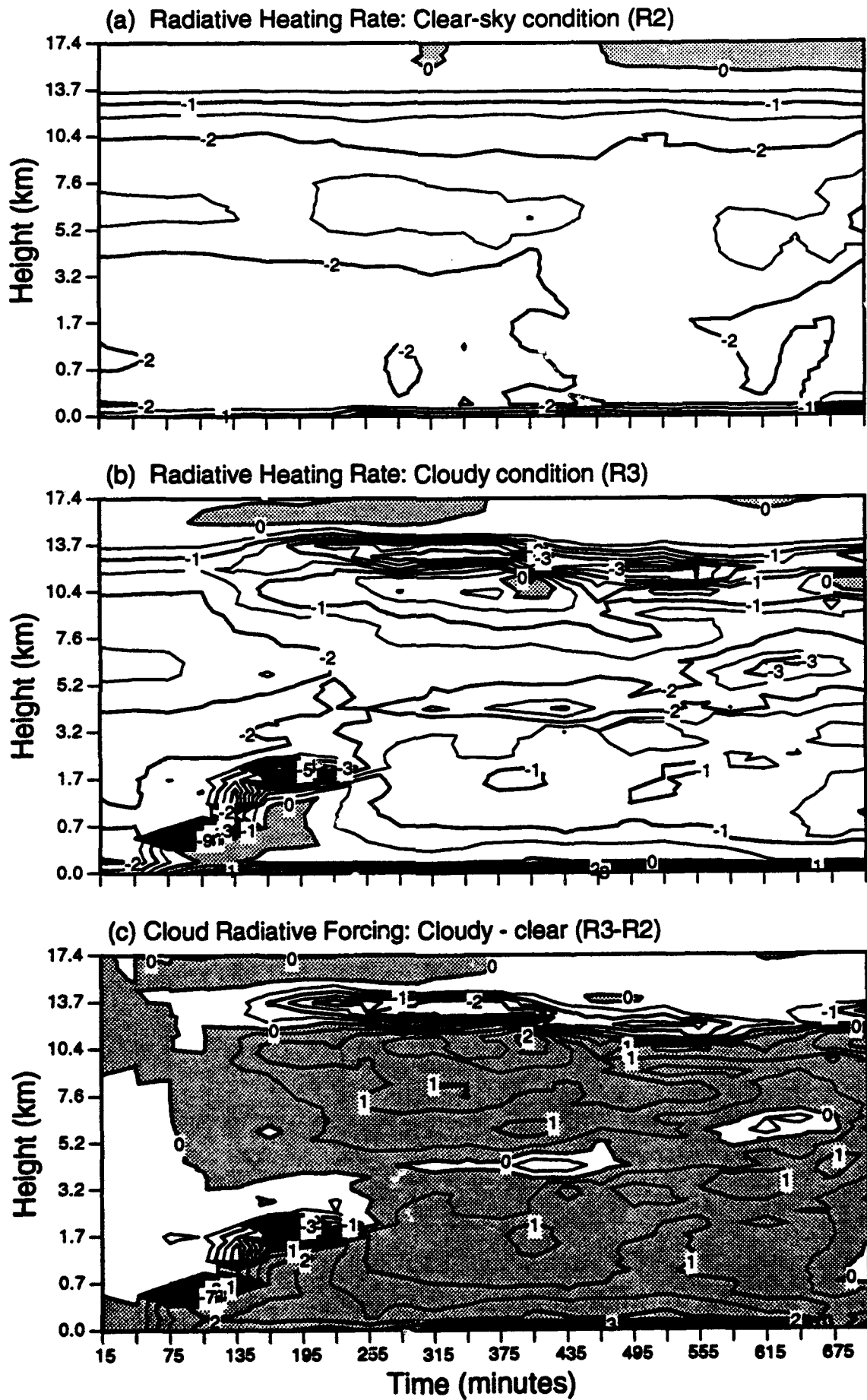


Fig. 5

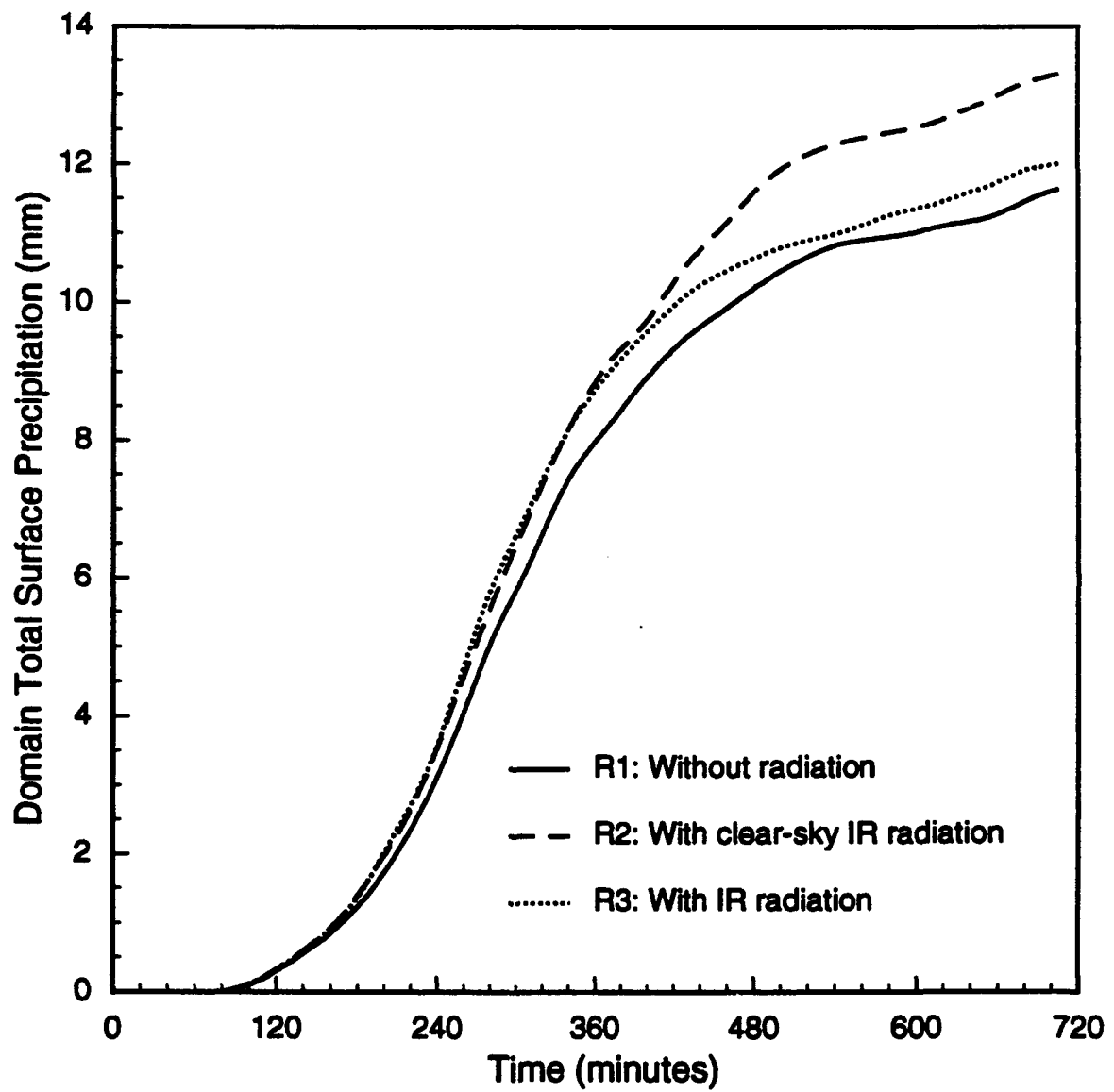


Fig. 6

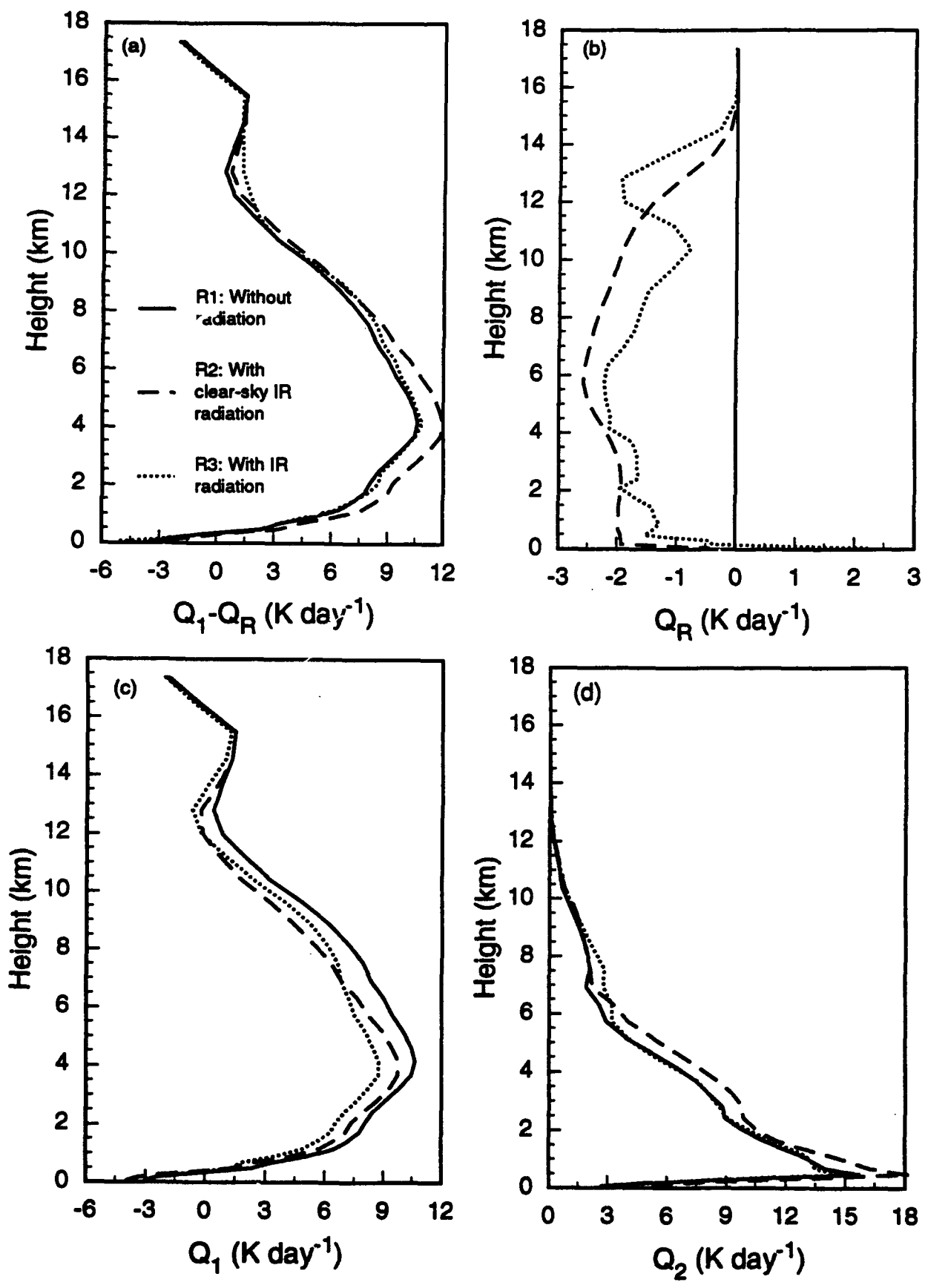


Fig. 7

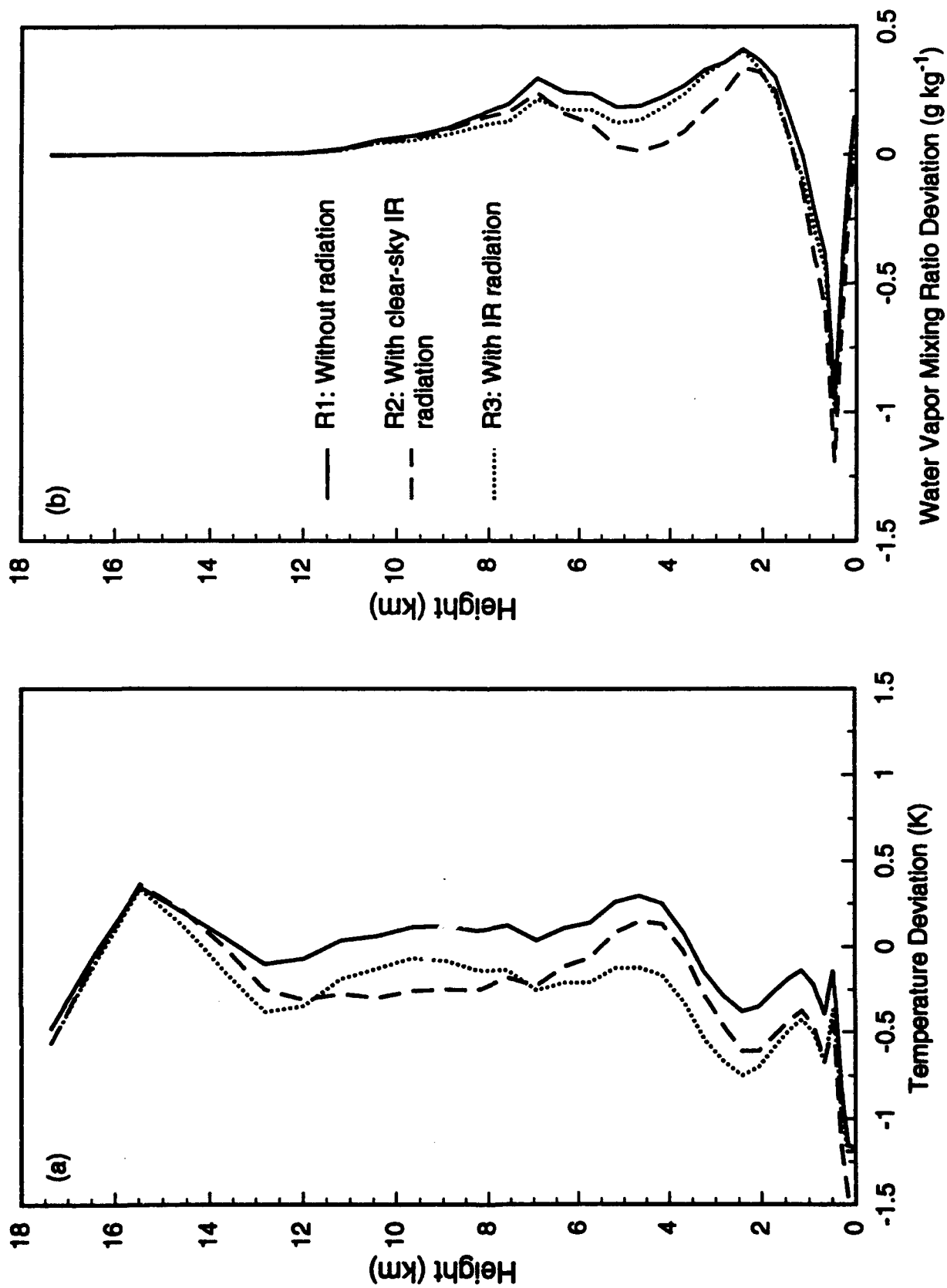
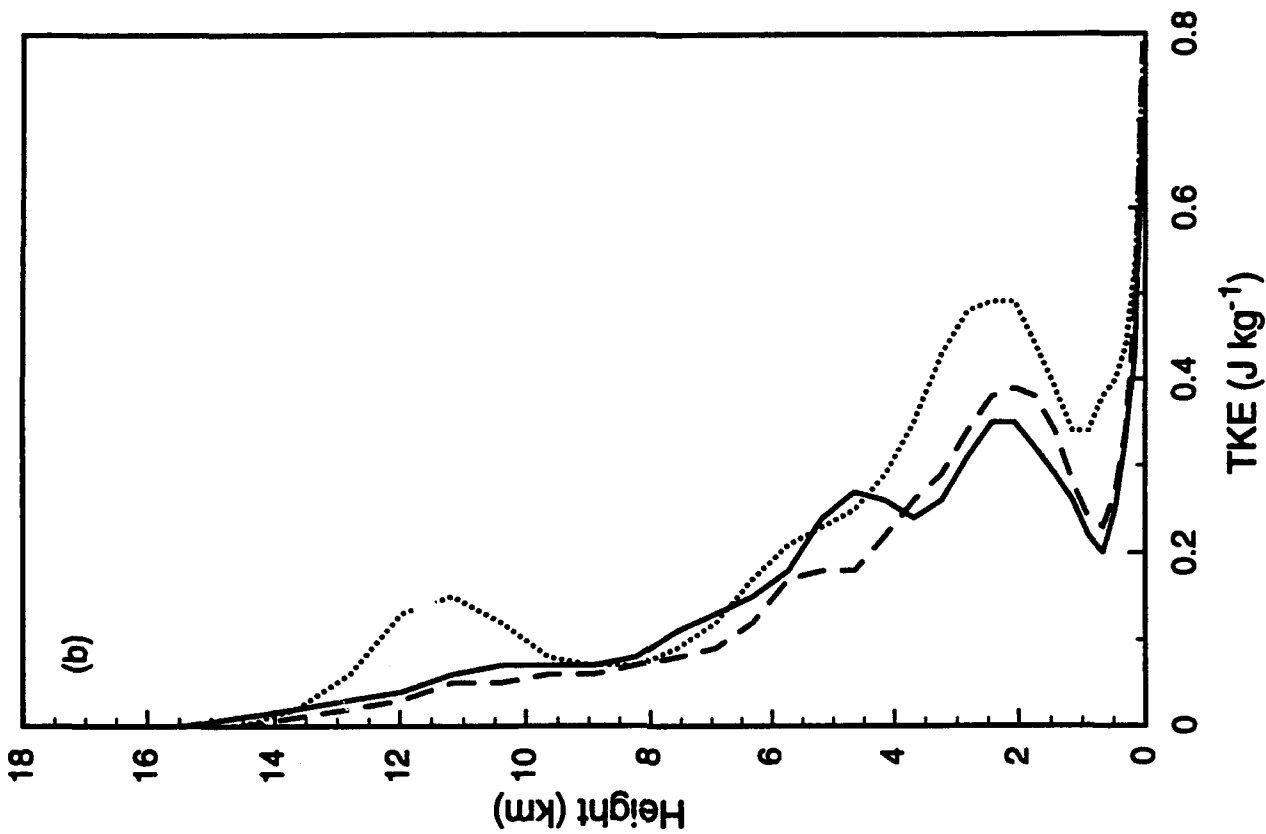
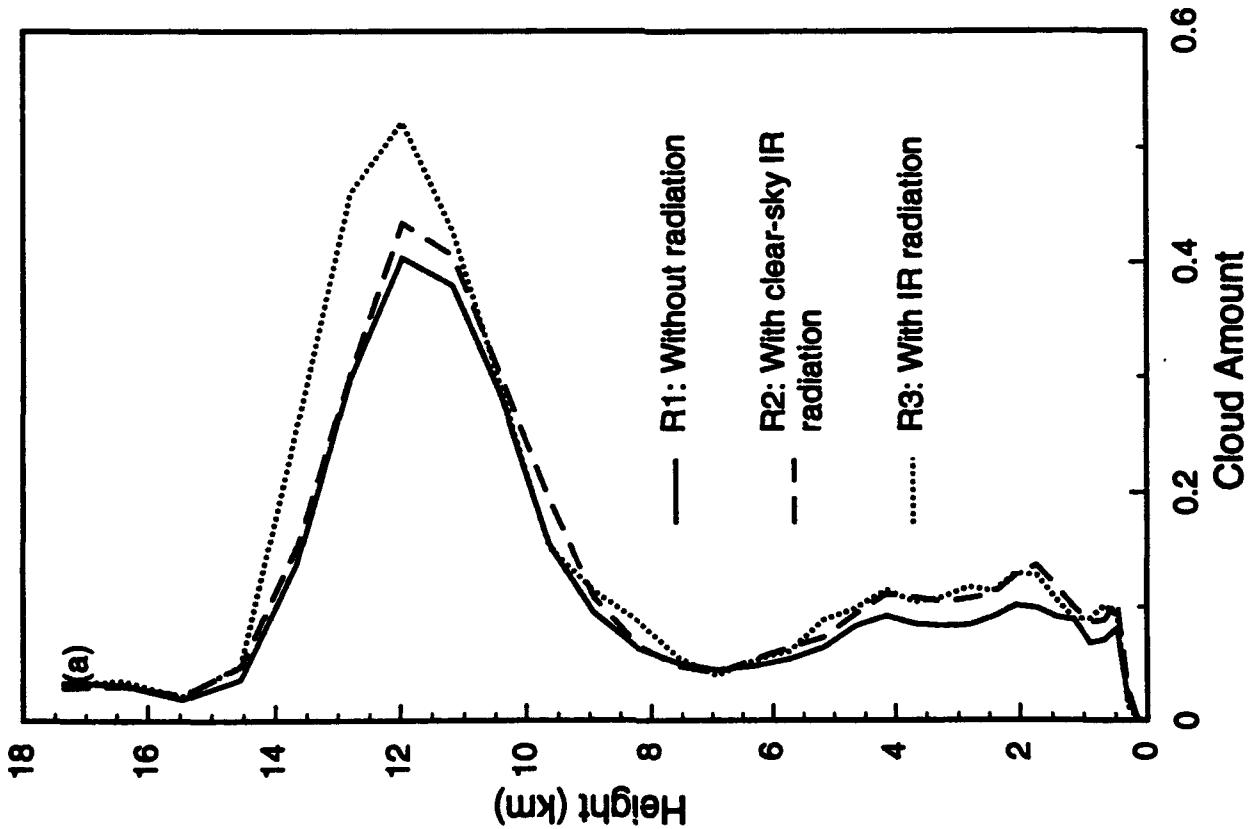


Fig. 8



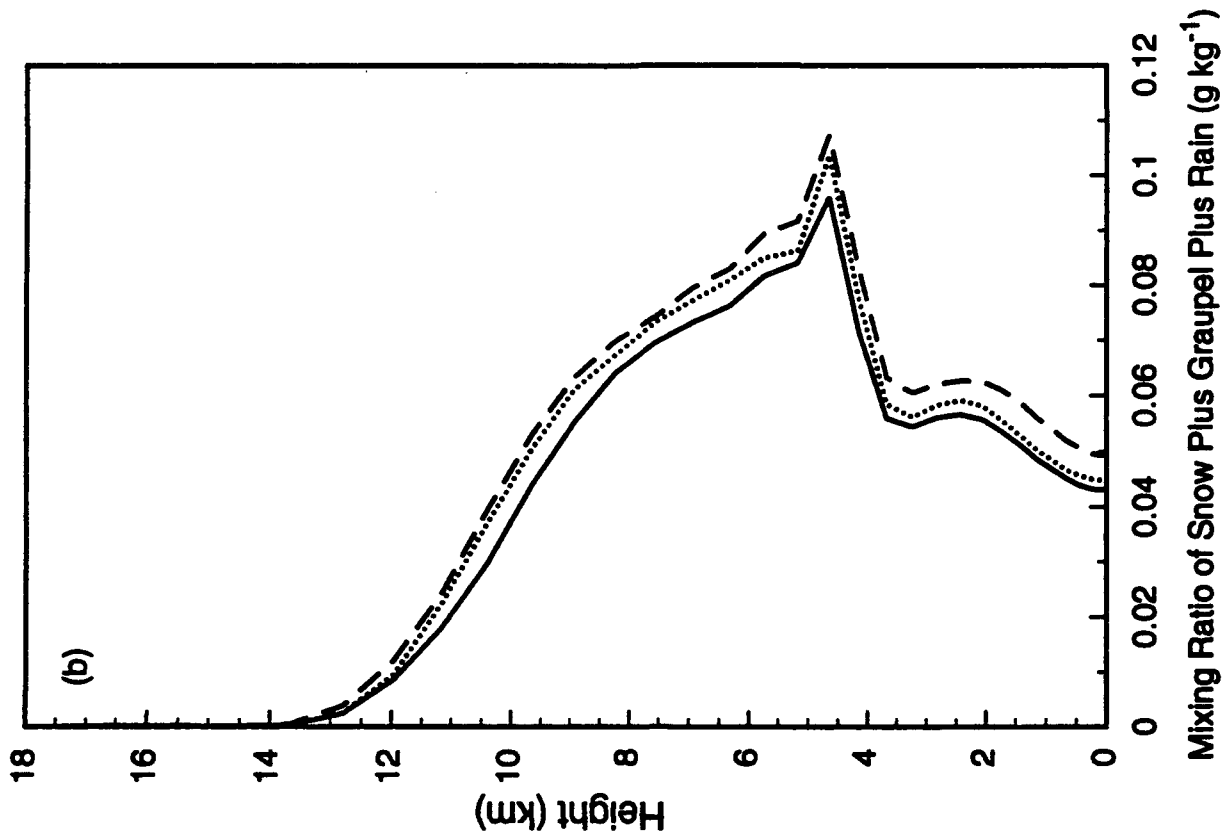
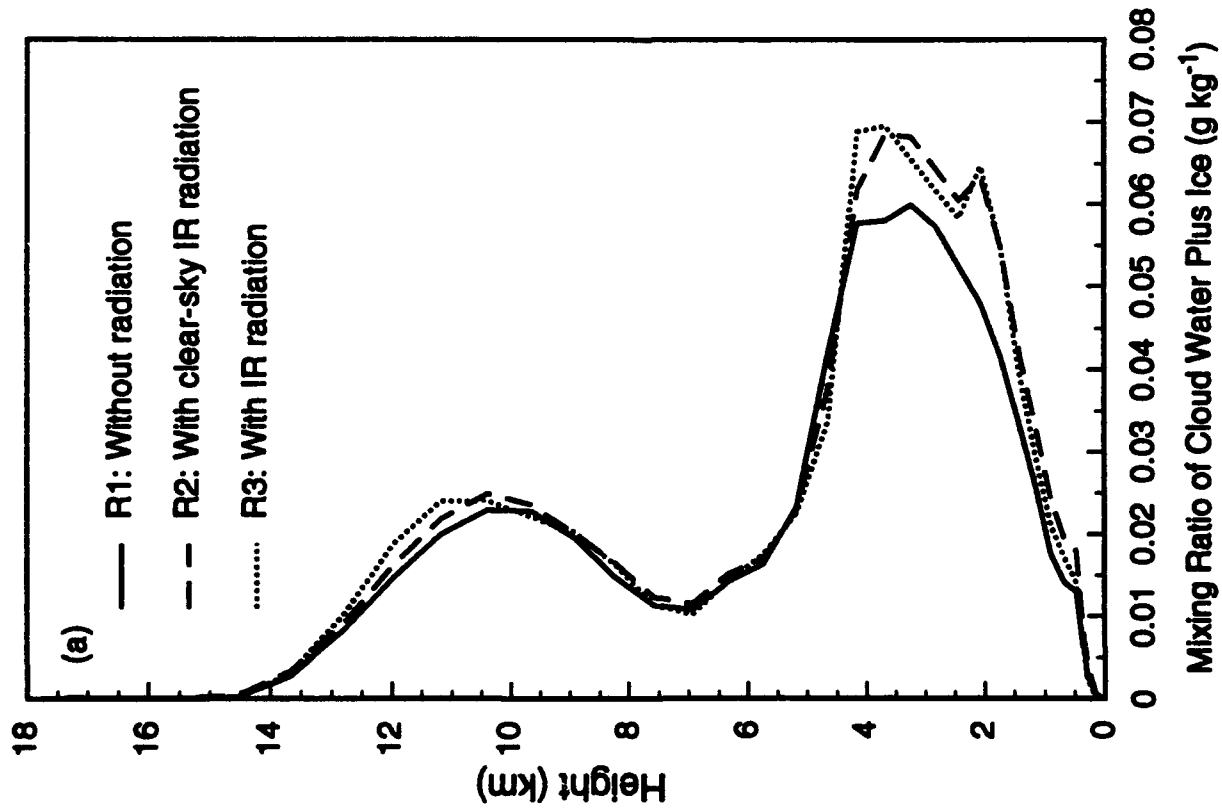


Fig. 10

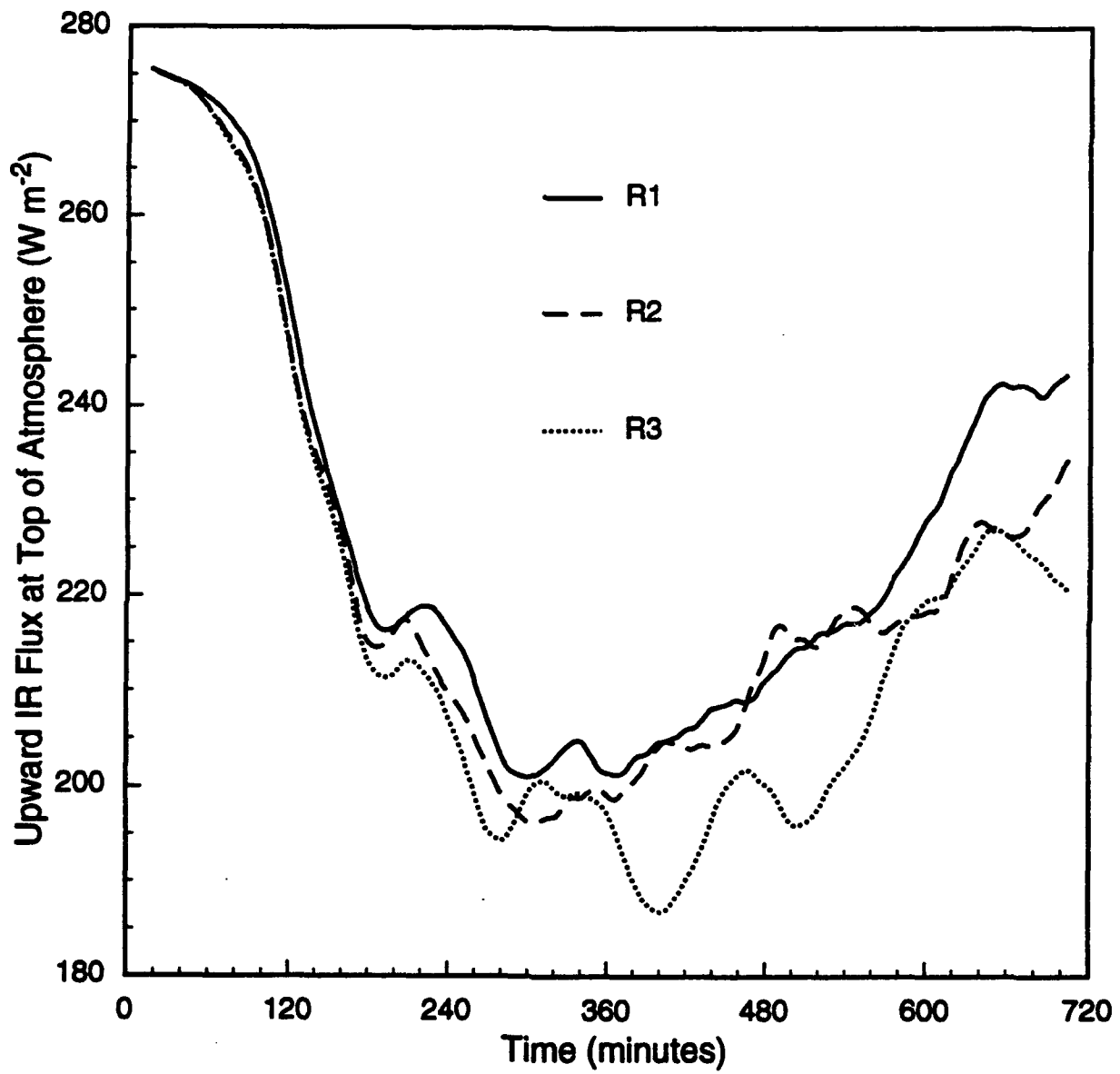


Fig. 11

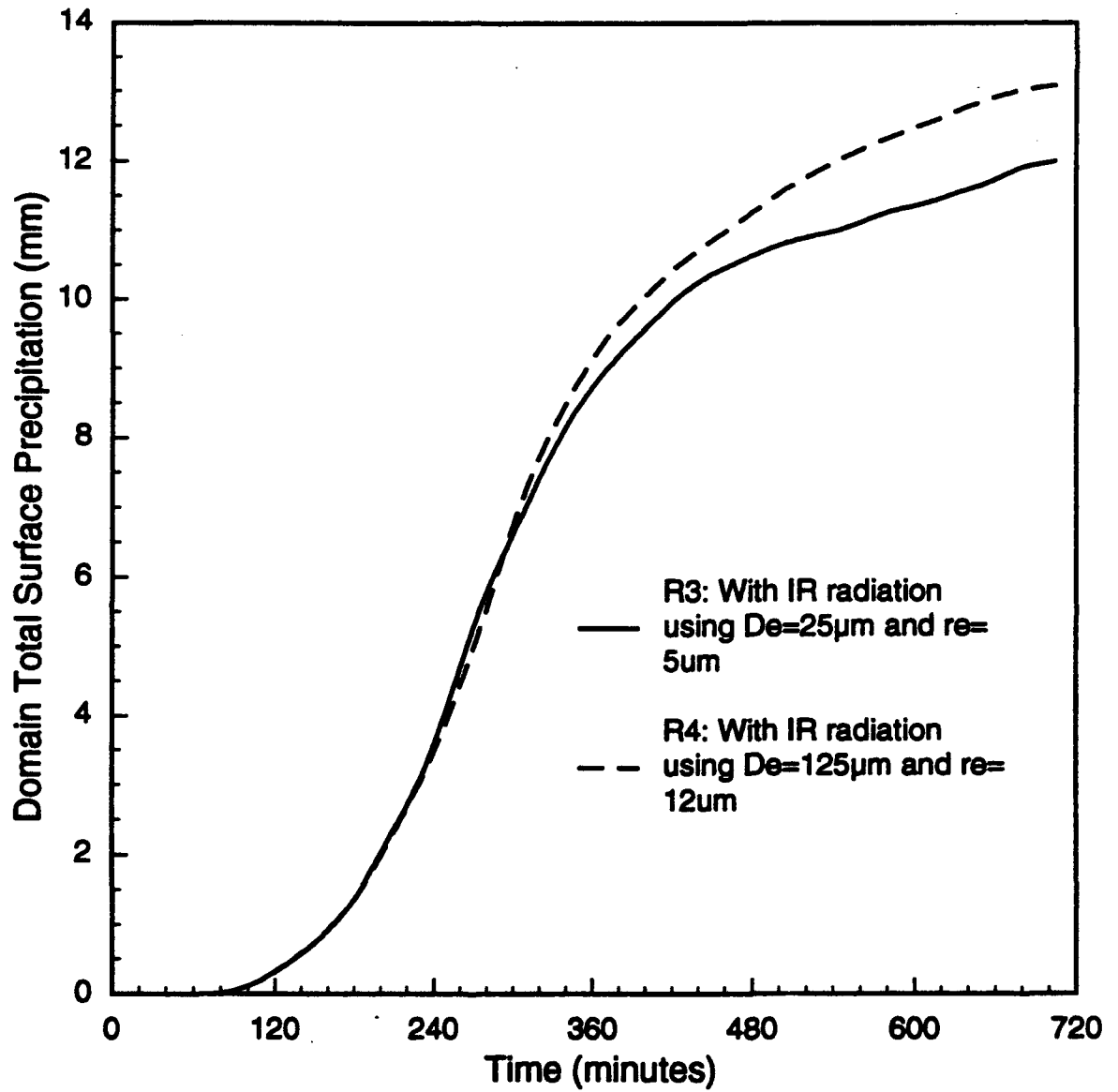


Fig. 12

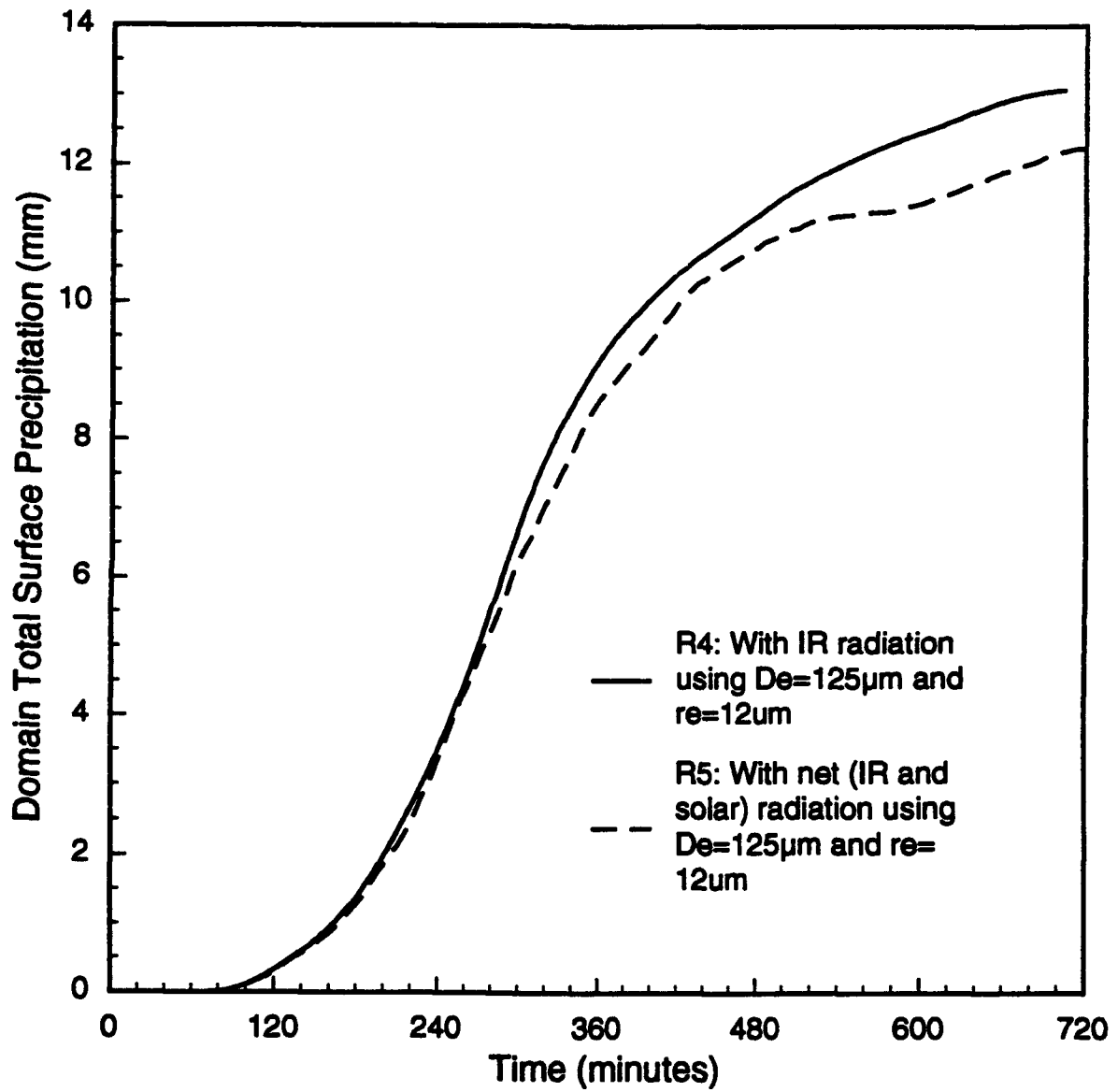


Fig. 13

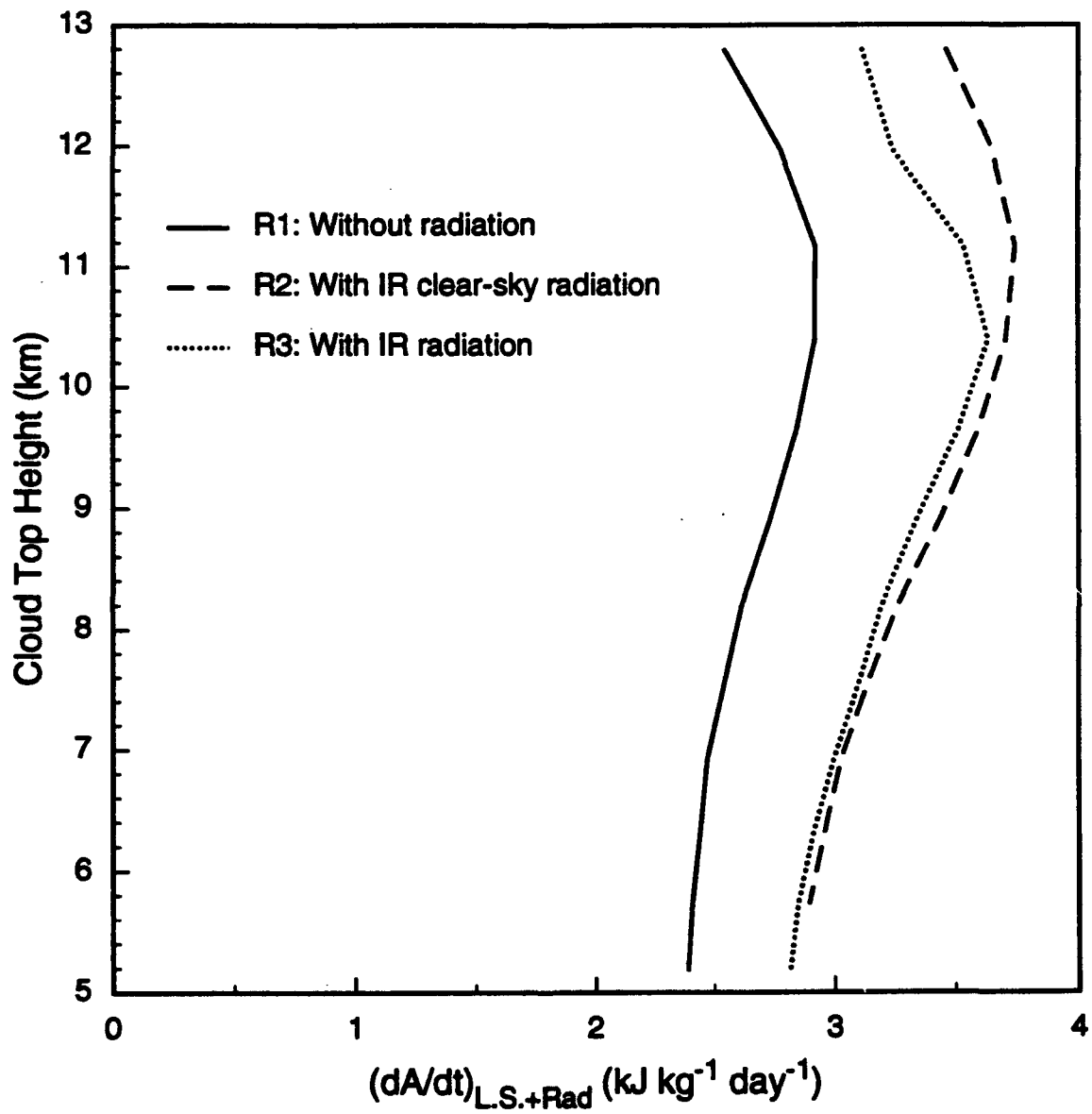


Fig. 14

